

Carbon dioxide activation and hydrogenation over copper-based catalysts studied by near-ambient pressure X-ray photoelectron spectroscopy

Présentée le 30 septembre 2021

Faculté des sciences de base
Laboratoire des matériaux pour les énergies renouvelables
Programme doctoral en chimie et génie chimique

pour l'obtention du grade de Docteur ès Sciences

par

Mo LI

Acceptée sur proposition du jury

Prof. B. Smit, président du jury
Prof. A. Züttel, W. Luo, directeurs de thèse
Prof. L. Lietti, rapporteur
Dr S. Zafeiratos, rapporteur
Prof. O. Kröcher, rapporteur

Acknowledgements

This thesis is finished with the support from my supervisors, colleagues, students, friends, and family members. I could not have gone this far with even one of them missing.

I would like to thank my thesis director, Prof. Andreas Züttel, for giving me the opportunity to complete my PhD project in his lab. It is not easy for a professor to decide to accept a PhD student who has changed his supervisor for the second time. However, Andreas showed not only his confidence in my potential, but also his trust in my capability, which allowed me to take care of the unique, brand-new NAP-XPS system with a value of 1.5 million CHF. Working with him, I benefit a lot from the advanced infrastructures, sufficient resources, scientific discussions, paper revisions, and group meetings where I learned how to present my work precisely in the form of achievements. He also creates a highly active and open atmosphere by group excursions, educational trips, and international conferences, which facilitated communication and enriched my research experience. What I learned from Andreas is invaluable because it both developed my visions on the society and get me ready for my future careers.

I also want to express my gratitude to my thesis co-director, Prof. Wen Luo, who offered me day-to-day guidance and supervision during my entire PhD study. He is the person who brings me to the beautiful field of surface science and helps me to get familiar with UHV technology. Collaborating with Wen, I have developed my knowledge on heterogeneous catalysis at both micro and macro scale. My experimental skills and scientific writing skills are significantly improved during our coworking. In addition, I was always impressed by his efforts and efficiency in revising my paper drafts which elevates the quality of the manuscripts. Wen is the key person who brings me to the success in my PhD.

As the jury members, Prof. Berend Smit, Prof. Luca Lietti, Dr. Spyridon Zafeiratos, and Prof. Oliver Kröcher carefully evaluated and corrected my thesis. During my oral exam, we had critical and constructive discussions on all related scientific topics. I appreciate their efforts in improving the quality of this thesis.

There are also countless helps from my colleagues and collaborators in my lab and EPFL. I thank them all.

During the preparation of this thesis and the oral exam presentation, Dr. Liping Zhong, Dr. Loris Lombardo, Mr. Jie Zhang, Mr. Youngdon Ko, Ms. Thi Ha My Pham, Mr. Cedric Koolen, and Ms. Pamela Canjura gave me many valuable suggestions and corrections. Mr. Alexandre Borsay helped me to translate the abstract to French.

Before joining EPFL, Dr. Kun Zhao and Dr. Shiqi Huang helped me to get the opportunity for an interview. Many experiments on Cu nanoparticles were finished by Mr. Alexandre Borsay. Dr. Kun Zhao, Dr. Mostapha Dakhchoune, Ms. Thi Ha My Pham, Mr. Youngdon Ko, Dr. Emad Oveisi, Dr. Lucie Navratilova, and Ms. Daniele Laub devoted great efforts in obtaining high-quality TEM images for my work. DRIFTS and ICP-OES

experiments were finished with the help of Dr. Kun Zhao and Dr. Natalia Gasilova, respectively. Many useful knowledge and good advices on XRD and XPS are from Dr. Pascal Schouwink and Dr. Mounir Mensi. Many high-quality customized parts, such as gaskets and crucibles, were machined by Mr. Stéphane Voeffray and Mr. Robin Délèze. For electronics, Mr. Patrick Favre and Mr. Dennis Ellersiek helped a lot in repairing and cabling. The IT support from Mr. Cédric Passerini and Jean Perruchoud was always fast and considerate. Ms. Ivana Suter, the secretary of our lab, offered great help not only in the complex administrative issues during the work but also in organizing all the events. She is the person who made my life in Sion easier.

There are also current and former members in our lab and EPFL, who did not contribute specifically to this thesis. I would also appreciate them for sharing knowledge, getting me involved in their projects, helping me in daily life, and all the happy moments we had together. They are Ms. Miriam Wischmann, Dr. Mariana Spodaryk, Dr. Heena Yang, Dr. Marco Calizzi, Dr. Emanuele Moioli, Dr. Robin Mutschler, Dr. Noris Gallandat, Ms. Valentina Waller, Mr. Yannick Baehler, Dr. Hiroyuki Kanda, and Ms. Yi Yang.

I thank as well my previous PhD supervisors in ETH Zürich, Prof. Christoph Müller and Prof. Sotiris Pratsinis. Although I was not able to finish my PhD with them, they provided positive references so I can get this unique opportunity here in EPFL.

I appreciate the support and encouragement from my friends and family members, especially my parents who sacrificed the company of a son for years. I hope I was able to show them that my choice is worthwhile.

The financial support from Swiss National Science Foundation (Grant No. 170736 and 179989) and China Scholarship Council (Grant No. 201506060156) are gratefully acknowledged.

Sion, 1st September 2021

Abstract

Carbon neutrality has been proposed as a commitment by the international communities for the well-being of humans. To achieve carbon neutrality, one practical approach is to synthesize fuels and chemicals through CO₂ hydrogenation to replace fossil fuels. Such an approach has two major advantages. First, it integrates renewable energy sources to the traditional carbon-based industries for easy storage and transportation. Second, CO₂ emitted by human activities is used as the feedstock, and thus, a closed carbon cycle can be realized to minimize the negative impact of CO₂ on global environment.

CO₂ hydrogenation in the industrial scale relies on the development of highly efficient catalysts, which, however, is still a challenging task due to the lack of fundamental knowledge on the catalytic mechanism. The aim of this thesis is to promote the understanding of the gas-surface interaction and the structure-performance relationships for Cu-based CO₂ hydrogenation catalysts. In specific, this thesis focuses on the following topics: (1) size- and support-dependent thermal stability of Cu nanoparticles under CO₂ hydrogenation atmosphere, (2) effects of Cu-In interactions on the activation and hydrogenation of CO₂ in Cu-In model catalyst, (3) the role of Cu and CeO_{2-x} and their interactions during CO₂ hydrogenation reaction over model and practical Cu/CeO_{2-x} catalysts, and (4) effect of ZrO₂ and CeO₂ supports on the structural properties and CO₂ hydrogenation performance of Cu-In catalysts.

To achieve these goals, advanced surface science technique, i.e., near-ambient pressure X-ray photoelectron spectroscopy (NAP-XPS), and conventional catalyst characterization and evaluation methods were applied. As a starting step, size-selected Cu nanoparticles (Cu NPs) were deposited on carbon and silica as model catalysts by magnetron sputtering, and their thermal stability was investigated by XPS and TEM. Under ultra-high vacuum (UHV) condition, Cu NPs were found to agglomerate through particle migration at 220 °C, and through Ostwald ripening at 320 and 460 °C. The Cu NPs with 8 nm size were found to be more stable than those with 4 nm due to their low migration kinetics. In addition, Cu NPs were better stabilized on SiO₂ support than carbon support due to the stronger interaction between SiO₂ and Cu. Moreover, the CO₂ hydrogenation environment also affects the sintering of Cu NPs, as it causes the redispersion and valorization of Cu species.

To expand the model catalyst study from single metal to bimetallic system, In/Cu model catalysts were synthesized and their chemical properties and CO₂ activation ability were investigated by NAP-XPS. It was found that the deposition of In on the surface of a Cu foil led to the formation of Cu-In alloy, whereas upon CO₂ exposure, In was partially oxidized to In₂O_{3-x} and Cu remains metallic. CO₂ was activated on the defective In₂O_{3-x} sites mainly in the form of carbonate. An easier CO₂ activation was observed on the In₂O_{3-x} sites adjacent to Cu-In alloys by quantifying the surface density of oxygen vacancies and carbonates.

Oxide supports are mostly required in industrial heterogeneous catalytic systems, where they not only serve as supporting materials but also involve in the reaction process. Therefore, in the third part of this thesis, practical and model Cu/CeO_{2-x} catalysts were synthesized and investigated for CO₂ hydrogenation. In the

entire temperature range of 300 - 600 °C, CO was the only carbon-containing product, indicating that the hydrogenation of CO₂ occurred over Cu/CeO_{2-x} catalysts through a reverse water gas shift (RWGS) process. NAP-XPS revealed that partially reduced ceria with oxygen vacancies is responsible for the CO₂ activation into carbonate. Meanwhile, H₂ can dissociate on metallic Cu and spillover to the ceria sites, facilitating the conversion of carbonate to CO via formate intermediate and the regeneration of the oxygen vacancies healed by CO₂. This way, it was revealed that at the Cu/CeO_{2-x} surface, the coupled Cu⁺/Cu⁰ and Ce⁴⁺/Ce³⁺ redox pairs on the metal-oxide interfaces are active sites for the RWGS reaction via the formate route.

Based on the findings above, a series of practical catalysts consist of Cu and Cu-In sites supported by ZrO₂ and CeO₂ supports were systematically characterized and evaluated for CO₂ hydrogenation. The structural properties and the catalytic performance of Cu and Cu-In based catalysts were found to be support dependent. The CO₂ conversion of the Cu-In/ZrO₂ catalyst was higher than that of the Cu/ZrO₂ catalyst, but it is the opposite for the Cu/CeO₂ and Cu-In/CeO₂ catalysts. With a variety of characterization techniques, the support dependent RWGS activity was found to correlate with different active sites: Cu-In alloys on ZrO₂ for promoted CO₂ activation, and separated Cu and In₂O₃ on CeO₂ for a suppressed the RWGS activity. These results demonstrate that the active center, metal-support interactions, and catalytic performance of Cu-based catalysts can be dramatically influenced by the oxide support.

In short, the understanding in the surface science of CO₂ hydrogenation on Cu-based catalysts was promoted in this thesis. The resulting knowledge can potentially be applied in both the interpretation of the behaviors of existing CO₂ hydrogenation catalysts and the rational design of novel catalysts with better performance. This thesis contributes fundamental insights to producing fuels and chemicals from CO₂ in the industrial scale.

Keywords

CO₂ hydrogenation, heterogeneous catalysis, model catalysts, surface science, near-ambient pressure X-ray photoelectron spectroscopy

Résumé

La neutralité carbone a été proposée comme un engagement des communautés internationales pour le bien-être des humains. Une approche pratique pour atteindre la neutralité carbone consiste à synthétiser des carburants et des produits chimiques par l'hydrogénation du CO_2 pour remplacer les combustibles fossiles. Une telle approche présente deux avantages importants. Premièrement, elle intègre des sources d'énergie renouvelables dans les industries traditionnelles à base de pétrole pour un stockage et un transport facile. Deuxièmement, le CO_2 émis par les activités humaines est utilisé comme matière première, et ainsi, le cycle du carbone peut être fermé pour minimiser l'impact négatif du CO_2 sur l'environnement.

L'hydrogénation du CO_2 à l'échelle industrielle repose sur le développement de catalyseurs hautement efficaces, ce qui reste cependant un défi en raison du manque de connaissances fondamentales sur le mécanisme catalytique. Cette thèse vise à comprendre l'interaction entre les gaz et la surface et les relations entre la structure et la performance des catalyseurs d'hydrogénation du CO_2 à base de Cu. En particulier, cette thèse se concentre sur les sujets suivants : (1) la stabilité thermique dépendante de la taille et du support des nanoparticules de Cu sous atmosphère d'hydrogénation de CO_2 , (2) les effets des interactions Cu-In sur l'activation et l'hydrogénation du CO_2 dans le catalyseur modèle Cu-In, (3) le rôle du Cu et CeO_{2-x} , et leurs interactions au cours de la réaction d'hydrogénation du CO_2 sur des catalyseurs Cu/ CeO_{2-x} modèles et pratiques, et (4) les effets du ZrO_2 et CeO_2 comme supports sur les propriétés structurales et les performances d'hydrogénation du CO_2 des catalyseurs Cu-In.

Pour atteindre ces objectifs, une technique avancée de science des surfaces, la spectroscopie photoélectronique à rayons X à pression presque ambiante (NAP-XPS), et des méthodes conventionnelles de caractérisation et d'évaluation des catalyseurs ont été appliquées. Dans un premier temps, des nanoparticules de Cu de taille définie (Cu NPs) ont été déposées sur du carbone et de la silice en tant que catalyseurs modèles par pulvérisation magnétron, et leur stabilité thermique a été étudiée à l'aide de caractérisations XPS et TEM. Dans des conditions d'ultravide (UHV), les NP de Cu s'agglomèrent par migration de particules à 220 °C et par « Ostwald ripening » à 320 et 460 °C. Les NP de Cu avec une taille de 8 nm se sont avérées plus stables que celles de 4 nm en raison de leur cinétique de migration plus lente. De plus, les NP de Cu étaient plus stables sous atmosphère d'hydrogénation de CO_2 sur support de SiO_2 que sur support de carbone en raison de l'interaction plus forte entre le SiO_2 et le Cu. De plus, l'environnement d'hydrogénation du CO_2 affectait également l'agglomération des NP de Cu, car il provoquait la redispersion et la valorisation des espèces de Cu.

Pour étendre l'étude du catalyseur modèle d'un métal unique à un système bimétallique, des catalyseurs modèles In/Cu ont été synthétisés et leurs propriétés chimiques et leurs performances catalytiques pour l'hydrogénation du CO_2 ont été étudiées par NAP-XPS. Il a été constaté que le dépôt d'In sur la surface d'une feuille de Cu conduisait à la formation d'un alliage Cu-In, alors que lors de l'exposition au CO_2 , l'In était partiellement oxydé en $\text{In}_2\text{O}_{3-x}$, et le Cu restait métallique. Le CO_2 était activé sur les sites $\text{In}_2\text{O}_{3-x}$ défectueux,

principalement sous forme de carbonate. Une activation plus facile du CO_2 a été observée sur les sites $\text{In}_2\text{O}_{3-x}$ adjacents aux alliages Cu-In en quantifiant la densité surfacique des lacunes d'oxygène et des carbonates.

Les supports en oxyde sont principalement requis dans les systèmes catalytiques hétérogènes industriels, où ils servent non seulement de matériaux de support mais participent également à la réaction. Par conséquent, dans la troisième partie de cette thèse, des catalyseurs de Cu/ CeO_{2-x} pratiques et modèles ont été synthétisés et étudiés pour l'hydrogénation du CO_2 . Le CO était le seul produit contenant du carbone dans tout l'intervalle de températures de 300 à 600 °C, ce qui indique que l'hydrogénation du CO_2 s'est produite sur des catalyseurs Cu/ CeO_{2-x} via la réaction du gaz à l'eau inverse (RWGS). L'analyse NAP-XPS a révélé que l'oxyde de cérium partiellement réduit avec des lacunes d'oxygène est responsable de l'activation du CO_2 en carbonate. Pendant ce temps, l' H_2 peut se dissocier sur le Cu métallique et migrer sur les sites de cérium, facilitant la conversion du carbonate en CO via l'intermédiaire formiate et la régénération des lacunes d'oxygène comblées par le CO_2 . Ainsi, à la surface du Cu/ CeO_{2-x} , les paires redox couplées Cu^+/Cu^0 et $\text{Ce}^{4+}/\text{Ce}^{3+}$ sur les interfaces métal-oxyde sont des sites actifs pour la réaction RWGS via la voie formiate.

Sur la base des résultats ci-dessus, une série de catalyseurs pratiques constitués de sites de Cu et de Cu-In soutenus par des supports ZrO_2 et CeO_2 ont été systématiquement caractérisés et évalués pour l'hydrogénation du CO_2 . Les propriétés structurales et les performances catalytiques des catalyseurs à base de Cu et de Cu-In se sont avérées dépendantes du support. La conversion du CO_2 du catalyseur Cu-In/ ZrO_2 était supérieure à celle du catalyseur Cu/ ZrO_2 , mais c'est l'inverse pour les catalyseurs Cu/ CeO_2 et Cu-In/ CeO_2 . Grâce à une variété de techniques de caractérisation, l'activité de la RWGS dépendante du support s'est avérée être en corrélation avec différents sites actifs : l'alliage de Cu-In sur ZrO_2 pour une activation du CO_2 favorisée, et le Cu et l' In_2O_3 séparés sur CeO_2 pour une suppression de l'activité de la RWGS. Ces résultats démontrent que le centre actif, les interactions métal-support et les performances catalytiques des catalyseurs à base de Cu peuvent être considérablement influencés par le support en oxyde.

En conclusion, la compréhension de la science de surface de l'hydrogénation du CO_2 sur des catalyseurs à base de Cu a été promue dans cette thèse. Les connaissances résultantes peuvent potentiellement être appliquées à la fois à l'interprétation des comportements des catalyseurs d'hydrogénation du CO_2 existants et à la conception rationnelle de nouveaux catalyseurs avec de meilleures performances. Cette thèse apporte des connaissances fondamentales sur la production de carburants et de produits chimiques à partir du CO_2 à l'échelle industrielle.

Mots-clés

Hydrogénation du CO_2 , catalyse hétérogène, catalyseur modèle, science des surfaces, spectroscopie photoélectronique à rayons X à pression presque ambiante

Contents

Acknowledgements	i
Abstract	iii
Keywords	iv
Résumé	v
Mots-clés	vi
List of Figures	x
List of Tables	xiii
List of Equations	xiii
Chapter 1 Introduction	15
1.1 Achieving carbon neutrality	15
1.1.1 World energy demands and CO ₂ emission	15
1.1.2 Renewable energy for CO ₂ utilization	17
1.2 CO ₂ hydrogenation catalysts	18
1.2.1 CO ₂ to CH ₄	19
1.2.2 CO ₂ to CO	20
1.2.3 CO ₂ to CH ₃ OH	21
1.2.4 CO ₂ to C ₂₊ hydrocarbons	23
1.3 Surface science of CO ₂ hydrogenation	24
1.3.1 Activation of CO ₂ on model catalysts at ultrahigh vacuum	25
1.3.2 Pressure gap and material gap	28
1.3.3 <i>In situ</i> study on CO ₂ hydrogenation mechanisms	29
1.4 Instrumental methods	33
1.4.1 Near-ambient pressure XPS	33
1.4.2 Preparation of model catalysts	35
1.4.3 Catalyst characterization and evaluation	36
1.5 Challenges and objectives of this thesis	38
1.6 Overview of the research work	39
1.7 References	41
Chapter 2 Thermal stability of size-selected copper nanoparticles: effect of size, support and CO₂ hydrogenation atmosphere	45

2.1	Introduction	46
2.2	Experimental section	47
2.2.1	Substrates	47
2.2.2	Deposition of size-selected Cu nanoparticles (Cu NPs)	47
2.2.3	Characterizations	47
2.2.4	Micrograph analysis	48
2.3	Results and discussion	48
2.3.1	Deposition of size-selected Cu NPs	48
2.3.2	Size-dependent thermal stability of Cu NPs	49
2.3.3	Effect of support on thermal stability of Cu NPs	52
2.3.4	Effect of CO ₂ hydrogenation atmosphere on thermal stability of Cu NPs	53
2.4	Conclusions	56
	References.....	57
	Supporting information.....	59
Chapter 3	Near ambient-pressure X-ray photoelectron spectroscopy study of CO₂ activation and hydrogenation on indium/copper surface	63
3.1	Introduction.....	64
3.2	Experimental section	65
3.3	Results	66
3.3.1	Surface properties of In/Cu model catalysts	66
3.3.2	NAP-XPS in the presence of CO ₂ at 300 K	68
3.3.3	NAP-XPS under CO ₂ hydrogenation conditions at 300-600 K.....	71
3.4	Discussion	73
3.5	Conclusions.....	75
	References.....	77
	Supporting Information.....	80
Chapter 4	Revealing the surface chemistry for CO₂ hydrogenation on Cu/CeO_{2-x} using near-ambient pressure X-ray photoelectron spectroscopy.....	87
4.1	Introduction.....	88
4.2	Experimental section	89
4.2.1	Preparation, characterization, and evaluation of Cu/CeO _{2-x} powder catalyst	89
4.2.2	Cu/CeO _{2-x} model catalyst for RWGS mechanism studies	89
4.3	Results and discussion	90
4.4	Conclusions.....	98
	References.....	100
	Supporting information.....	103
Chapter 5	Support-dependent Cu-In bimetallic catalysts for tailoring the activity of reverse water gas shift reaction	109
5.1	Introduction.....	110

5.2	Experimental section	111
5.2.1	Catalyst preparation	111
5.2.2	Catalyst characterizations	111
5.2.3	Catalyst tests	112
5.3	Results	113
5.3.1	Catalytic performance and kinetics	113
5.3.2	Structural properties.....	115
5.3.3	Reducibility and surface properties	118
5.3.4	Adsorption-desorption properties.....	121
5.4	Discussions.....	121
5.5	Conclusions.....	123
	References.....	125
	Supporting information.....	127
Chapter 6	Conclusion and perspectives.....	132
6.1	Achieved results	132
6.2	Perspectives.....	133
6.2.1	In-based model catalysts	133
6.2.2	Practical catalysts.....	134
	Curriculum vitae	135

List of Figures

Figure 1.1 Global energy consumption and CO ₂ emission over the years from 1800 to 2019. Data retrieved from Ref. 3,4.	16
Figure 1.2 Median earth surface temperature anomalies (HadCRUT4 dataset) and atmospheric CO ₂ concentration (Mauna Loa Observatory) from 1959 to 2020. Data retrieved from Ref. 7.....	16
Figure 1.3 Installed solar energy capacity worldwide and in some major countries and regions from 2000 to 2019. Data retrieved from Ref. 3.	17
Figure 1.4 Schematic illustration of a closed carbon cycle with CO ₂ as feedstock for fuel and chemical production. Permission from Ref. 12.....	18
Figure 1.5 Possible pathways for CO ₂ hydrogenation to form CO. *(X) indicates reactive species adsorbed on the catalyst surface. Permission from Ref. 30.	21
Figure 1.6 Reaction pathways for CO ₂ hydrogenation to CH ₃ OH via the RWGS + CO-Hydro and formate intermediates. *(X) indicates adsorbed species. Permission from Ref. 56.	23
Figure 1.7 Different possible routes for the production of value-added hydrocarbons from CO ₂ hydrogenation. Permission from Ref. 30.....	24
Figure 1.8 Physisorption and chemisorption pathways of CO ₂ . Permission from Ref. 60.	25
Figure 1.9 BEs of CO ₂ adsorption and activation products. Permission from Ref. 21.....	25
Figure 1.10 O 1s and C 1s regions of the photoelectron spectrum of a Cu(211) surface: initially clean, pre-oxidized (50 L, O ₂), exposed to 100 L CO ₂ at 80 K, and then subsequently warmed to the temperatures indicated. Permission from Ref. 64.....	26
Figure 1.11 XPS data collected upon stepwise annealing of the CO ₂ -covered Ni(110) surface and of the CO ₂ + H coadsorbed layer. Permission from Ref. 67.	27
Figure 1.12 C 1s XPS spectra recorded from ZnO(0001)-O following exposure to ~3 L HCOOH, ~700 L CO, and ~2 L CO ₂ . Permission from Ref. 68.	28
Figure 1.13 Graphical illustration of the pressure gap and material gap between surface science investigation on reaction mechanism and practical development of catalysts.....	29
Figure 1.14 (a) O 1s and (b) C 1s regions of the NAP-XPS spectra in the presence of CO ₂ at RT on the Cu(111) surface and the Cu(100) surface. Permission from Ref. 78.	30
Figure 1.15 Ni 2p XP spectra of NiO (A) and 5% Pt/NiO (B) under CO ₂ hydrogenation conditions and subsequent evacuation at 673 K. Permission from Ref. 91.....	31
Figure 1.16 AP-XPS spectra of the C 1s region of the Rh/CeO ₂ catalyst measured in situ during a temperature ramp from 515 to 625 K under CO ₂ /H ₂ mixture (a). The corresponding C 1s (b), Rh 3d (c), and Ce 4d (d) levels recorded in situ for the Rh/CeO ₂ catalyst after exposure to a CO ₂ /H ₂ mixture at 515 K. Permission from Ref. 92.	31
Figure 1.17 O 1s and C 1s spectra taken using different photon energies during the in situ CO ₂ RR on a surface oxygen-free Cu/TiO ₂ NPs/HOPG sample under CO ₂ (100 mTorr) and H ₂ (100 mTorr) at 350 K. Permission from Ref. 93.	32
Figure 1.18 Schematic illustration of photoemission process and its energy conservation.	34
Figure 1.19 Two possible schemes for a NAP-XPS setup for transiting from a near ambient pressure in the analysis chamber to UHV in the electron analyzer. Permission from Ref. 105.....	35
Figure 1.20 NAP-XPS system used in this thesis. Source: SPECS GmbH.	35

Figure 1.21 Schematic illustration of the nanoparticle deposition system for synthesizing size-selected model catalysts. Reproduced from Ref. 77.....	36
Figure 1.22 Schematic illustration of the e-beam evaporation process.	36
Figure 1.23 Schematic diagram of fixed-bed flow reactor for performance evaluation of catalysts. .	37
Figure 1.24 Timeline of NAP-XPS studies on model catalysts and supported catalysts for CO ₂ hydrogenation. Colored boxes are bulk or thin film model catalysts, and transparent boxes are supported nanoparticles. The composition of catalysts, gas atmosphere, and the authors are given.....	38
Figure 1.25 An overview of the structure and logic of this thesis.	40
Figure 2.1 Schematic illustration of the size-selective nanoparticle deposition system.	49
Figure 2.2 Representative TEM images and corresponding PSD histograms of Cu NPs size-selected at (a-d) 4 and (e-h) 8 nm deposited on carbon TEM grid. The mean particle diameter with standard deviation is given. The images correspond to Cu NPs (a, e) without heating, and (b-d, f-h) heated to 220, 320, and 460 °C for 30 min. Cu NPs with diameter larger than 14 nm are included in one bin (dark green) in the histogram.	50
Figure 2.3(a) TEM image, (b) HAADF-STEM image, and (c) local Cu elemental map by EDX of a representative region for 8 nm Cu NPs heated to 460 °C.....	51
Figure 2.4 Representative TEM images and corresponding PSD histograms of Cu NPs size-selected at 8 nm deposited on a silica TEM grid. The mean particle diameter with standard deviation is given. The images correspond to Cu NPs (a) without heating, and heated to (b) 320 and (c) 460 °C for 30 min. Cu NPs with diameter larger than 14 nm are included in one bin (dark green) in the histogram.	53
Figure 2.5 Representative TEM images and corresponding PSD histograms of Cu NPs size-selected at 7 nm and deposited on (a) carbon and (b) silica TEM grids after heating to 320 °C for 30 min in a CO ₂ /H ₂ mixture. A comparison of PSD fittings is also shown for Cu NPs supported by (c) carbon and (d) silica at room temperature, heated to 320 °C in vacuum and in a 1 mbar CO ₂ /H ₂ mixture.	54
Figure 2.6 Comparison of (a) particle density (number of particles per μm ²), (b) particle coverage calculated from TEM images, and (c) Cu/support (C or Si) XPS peak area ratio for 8 nm Cu NPs supported on carbon and SiO ₂ under different conditions. The Cu/support ratio is normalized to the results measured at room temperature under UHV for the comparison on different supports.	55
Figure 2.7 Schematic illustration of interplay of redispersion, agglomeration, and volatilization of Cu NPs supported by carbon and SiO ₂ under CO ₂ hydrogenation atmosphere. Step 1 is reverse water-gas shift reaction. Step 2 is the formation of Cu carbonyl species at high temperature in a CO environment. Step 3a and b represents the redispersion and the agglomeration of Cu NPs on carbon and SiO ₂ , respectively. Step 4 is the formation of carbonyl and carboxylate groups as additional anchoring sites for Cu NPs redispersion.	56
Figure 3.1(a, b) XPS spectra of the Cu 2p _{3/2} , In 3d _{5/2} regions and (c, d) X-ray excited Cu LMM and In MNN Auger peaks of Cu foil, In foil, and In/Cu samples with different surface In coverage. Spectra are unsmoothed data. The In coverage is indicated by monolayer (ML) calculated from the peak area ratio of In 3d _{5/2} and Cu 2p _{3/2} after a Shirley type background subtraction and correction by the corresponding RSFs.....	67
Figure 3.2 Schematic illustration of the Cu-In charge transfer model for Cu-In alloying on Cu foil surface.	68
Figure 3.3 NAP-XPS spectra of the (a) Cu 2p _{3/2} , (b) In 3d _{5/2} , (c) O 1s, and (d) C 1s regions of Cu foil, In foil, and In/Cu samples with different surface In coverage upon exposure to 0.2 mbar CO ₂ at 300 K.	69
Figure 3.4 (a) Peak area ratios of defective/lattice oxygen (O _i /O _{ll}) and carbon from the contribution of carbonate/defective oxygen (C from CO ₃ [*] /O _i) for In/Cu and In foil samples upon exposure to 0.2 mbar CO ₂ at 300 K, and (b) percentage of different oxygen species (O _{ll} , O _i , and O from CO ₃ [*]) in O 1s region of one In/Cu sample with 1.4 ML In and In foil upon exposure to 0.2 mbar CO ₂ or O ₂ at 300 K.	70
Figure 3.5 Comparison of NAP-XPS spectra of (a, d) Cu 2p _{3/2} , (b, e) In 3d _{5/2} , and (c, f) O 1s regions for the In/Cu sample with 1.4 ML In coverage upon exposure to 0.2 mbar CO ₂ (a, b, and c) and the mixture of 0.2 mbar CO ₂ + 0.6 mbar H ₂ (d, e, and f) at 300–600 K. Spectra are unsmoothed data.	72

Figure 3.6 Schematic illustration of the formation of Cu-In alloy, the partial oxidation of In/Cu surface to $\text{In}_2\text{O}_{3-x}$ with oxygen vacancies, and the activation of CO_2 on the $\text{In}_2\text{O}_{3-x}$ /Cu-In boundaries and proposed further hydrogenation as an initial step for methanol production.	75
Figure 4.1 (a) STEM-HAADF and corresponding EDX elemental maps of the reduced Cu/CeO _{2-x} catalyst (the scale bar is 100 nm), (b) XRD patterns of the calcined CuO/CeO ₂ precursor and the reduced Cu/CeO _{2-x} catalyst, (c) gas species detected by MS as a function of time for the Cu/CeO _{2-x} catalyst under RWGS conditions from 523 to 873 K, and (d) CO ₂ conversion over the Cu/CeO _{2-x} catalyst under the same conditions with (c).92	
Figure 4.2 C 1s, Ce 3d, and Cu LMM spectra of the Cu/CeO _{2-x} model surface under UHV and 0.2 mbar of CO ₂ at 300, 450, and 600 K. The difference in C 1s peaks for gas-phase CO ₂ originates from the different sample-aperture distances which are optimized for each measurement.	93
Figure 4.3 C 1s, Ce 3d, and Cu LMM spectra of the Cu/CeO _{2-x} model surface under UHV and 0.2 mbar of CO ₂ + 0.6 mbar of H ₂ at 300, 450, and 600 K.	94
Figure 4.4 Ce ³⁺ concentration determined by deconvolution of the Ce 3d XPS spectra as a function of temperature under reaction conditions. The error bars were the standard deviation of the Ce ³⁺ concentration obtained from the measurement of three separately prepared samples.	95
Figure 4.5 C 1s region spectra of (a) a CeO _{2-x} surface and (b) a Cu foil under UHV and 0.2 mbar of CO ₂ + 0.6 mbar of H ₂ at 300, 450, and 600 K.	96
Figure 4.6 (a) Surface SEM, (b) cross-sectional STEM-BF and STEM-HAADF images, and (c) corresponding EDX elemental map of the Cu/CeO _{2-x} model surface after exposure to 0.2 mbar of CO ₂ + 0.6 mbar of H ₂ at 600 K for 1 h.	97
Figure 4.7 (a) Schematic illustration for the activation of CO ₂ and regeneration of oxygen vacancies during the RWGS reaction over the Cu/CeO _{2-x} surface, and the interaction between CO ₂ /H ₂ and (b) CeO _{2-x} or (c) Cu surface.	98
Figure 5.1 CO ₂ conversion and CO selectivity of all studied Cu and Cu-In catalysts supported by ZrO ₂ (a and c) and CeO ₂ (b and d) as well as corresponding supports.	114
Figure 5.2 Arrhenius plot with the CO ₂ conversion experimental data (dots) at the kinetic temperature range for all catalysts supported by ZrO ₂ (filled dots and solid lines) or CeO ₂ (hollow dots and dash lines).115	
Figure 5.3 STEM-HAADF image and STEM/EDX element maps of Cu ₁₀ and Cu ₅ In ₅ catalysts supported by (a, b) ZrO ₂ and (c, d) CeO ₂	116
Figure 5.4 XRD patterns of all reduced catalysts supported by (a) ZrO ₂ and (b) CeO ₂	117
Figure 5.5 H ₂ -TPR profiles of the calcined Cu ₁₀ and Cu ₅ In ₅ catalysts supported by (a) ZrO ₂ and (b) CeO ₂ . 118	
Figure 5.6 XPS spectra of all ZrO ₂ - and CeO ₂ -supported Cu ₁₀ and Cu ₅ In ₅ catalysts after reduction (in 5 vol.% H ₂ , 400 °C, 1h) at different regions: (a) Cu 2p _{3/2} , (b) Cu LMM Auger, (c) In 3d _{5/2} , (d) O 1s, and (e) Ce 3d. For all core level region data, the gray solid lines are the raw data, and the colored solid lines are the fitted spectra. For the Auger region, the colored solid lines are the raw data.	119
Figure 5.7 CO ₂ -TPD profiles of all reduced Cu ₁₀ and Cu ₅ In ₅ catalysts supported by (a) ZrO ₂ and (b) CeO ₂ . 121	
Figure 5.8 Schematic illustration for the dependence of active phases, surface properties, reaction intermediates, and corresponding RWGS activities on different supports investigated in this work on Cu ₁₀ /ZrO ₂ , Cu ₅ In ₅ /ZrO ₂ , Cu ₁₀ /CeO ₂ , and Cu ₅ In ₅ /CeO ₂ catalysts.	123

List of Tables

Table 1.1 Thermodynamic consideration and catalysts of various CO ₂ hydrogenation reactions at 298 K, and the corresponding reaction conditions. Reproduced from Ref. 21.....	19
Table 1.2 Representative catalysts and proposed reaction mechanism for CO ₂ hydrogenation to CH ₄ .20	
Table 1.3 Representative catalysts and proposed reaction mechanism for CO ₂ hydrogenation to CO.21	
Table 1.4 Representative catalysts and proposed reaction mechanism for CO ₂ hydrogenation to CH ₃ OH. 23	
Table 1.5 Examples of catalysts for CO ₂ hydrogenation to C2+ hydrogenation via different routes. . 24	
Table 1.6 C 1s and O 1s BEs of the carbon species observed on representative pure model catalyst surfaces.	33
Table 3.1 Positions and relative intensities of different O 1s species on the In/Cu sample with 1.4 ML In coverage under different conditions.	73
Table 5.1 Kinetic temperature range ($X_{\text{CO}_2} < 10\%$) for the calculation of activation energy and the determined activation energy (E_a) for CO ₂ conversion.	115
Table 5.2 Quantitative XRD analysis of Cu ₁₀ and Cu ₅ In ₅ catalysts supported by ZrO ₂ and CeO ₂ obtained from Rietveld refinement.	117
Table 5.3 Specific surface areas (SSA) of all calcined samples determined by N ₂ adsorption.	118

List of Equations

Equation 1.1 Physisorption and chemisorption of CO ₂ on Cu(110) and O-preadsorbed Cu(211) surfaces. 26	
Equation 1.2 Direct decomposition of CO ₂ into adsorbed CO and atomic O.	26
Equation 1.3 The chemisorption of CO ₂ with the assistance of surface oxygen and the formation of carbonate.	27
Equation 1.4 The energy conservation during the photoemission process.	34
Equation 3.1 Quantification of thin film thickness using XPS.	65

Chapter 1 Introduction

1.1 Achieving carbon neutrality

Over the past few decades, the rapid development of human civilization relies on energy and commodities produced from fossil fuels, including coal, oil, and natural gas. Consumption of fossil fuels releases carbon, which has been stored underground for millions of years, in the form of carbon dioxide (CO₂) into the atmosphere. Overwhelming evidence has indicated that the emission of CO₂ is largely responsible for rapid global environmental changes such as land and ocean surface temperature increase, sea-level rise, glacier melt, and ocean acidification. Thus, there is an urgent need to reduce global CO₂ emissions in the short term and a need to modify the carbon-based energy structure in the long term without compromising our economic growth, national security, and living standards.¹ Based on the current situation of carbon emission and the development of renewable energy worldwide, **carbon neutrality** has been proposed as a goal or a commitment by a lot of countries, international communities, and the United Nations. For example, in September 2020 China pledges carbon neutrality by 2060, ahead of the major industrial countries all over the world.²

In the pursuit of achieving carbon neutrality, the reduction of CO₂ emission, and the integration of renewable energy into our traditional carbon-based industrial model, are two significant challenges. Hydrogenation of CO₂ using renewable energy is a promising technology that can solve both problems simultaneously. These worldwide energy challenges, as well as potential solutions with renewable energy, are discussed below.

1.1.1 World energy demands and CO₂ emission

The industrial revolution led to the rapid growth of the global population, and the wealth which is possessed and used by people to increase their living standards and develop future technologies. Such growth of population and wealth is accompanied by an increase in global energy consumption. Since the 1940s, the primary energy consumption has increased significantly, from 22,840 TWh in 1940 to 173,340 TWh in 2019.³ Until now, the global energy supply is still dominated by fossil fuels (coal, oil, and gas), which account for 84.3% of the energy consumption in 2019.³

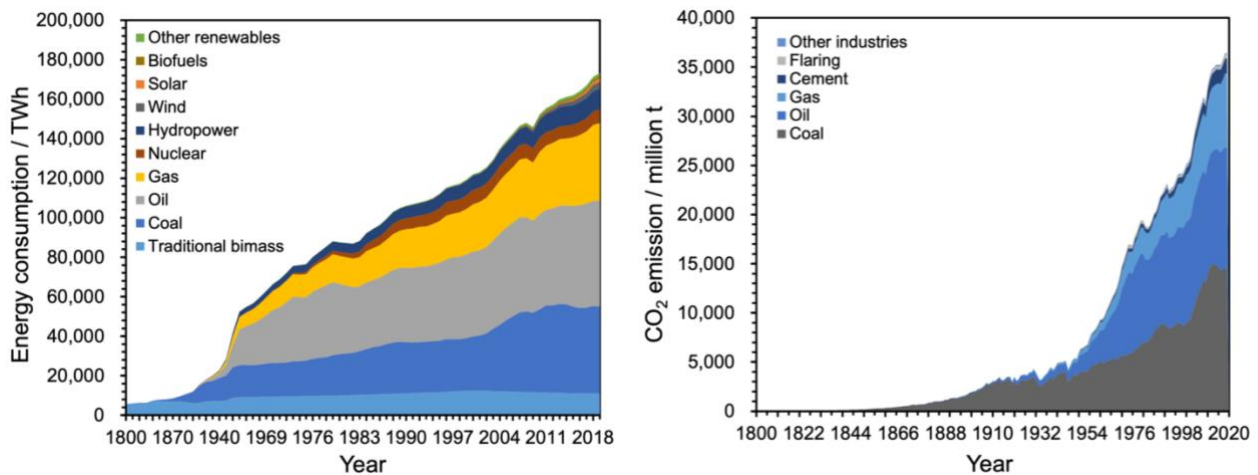


Figure 1.1 Global energy consumption and CO₂ emission over the years from 1800 to 2019. Data retrieved from Ref. 3,4.

Consequently, the CO₂ emission caused by human activities also increased dramatically over the same period. It is evident in Figure 1.1 that the majority of CO₂ emission happens after the 1940s, which is in parallel with the growth of global energy consumption.⁴ Such a huge amount of CO₂ emission led to an atmospheric CO₂ concentration as high as 416.06 ppm in February 2021 (measured at Mauna Loa Observatory), well exceeded the consistent fluctuations in CO₂ concentrations between 180 and 300 ppm caused by changes in the Earth's orbit around the sun over the past 800,000 years.⁵ The increased atmospheric CO₂ concentration brings many uncertainties to the Earth and the well-being of people. One of the best-known issues is climate change in the form of global warming. In Figure 1.2, the earth surface temperature anomalies obtained from the HadCRUT4 dataset⁶ and the atmospheric CO₂ concentration measured at Mauna Loa Observatory⁷ over the years from 1959 to 2020 are compared, where a clear global warming trend together with the increase of CO₂ concentration can be observed. Global warming has numerous negative impacts on people's livelihoods, such as desertification of agricultural lands, tidal flooding, storm intensification, heatwave intensification, etc. The World Bank estimates that climate change could drive over 120 million people into poverty by 2030.⁸

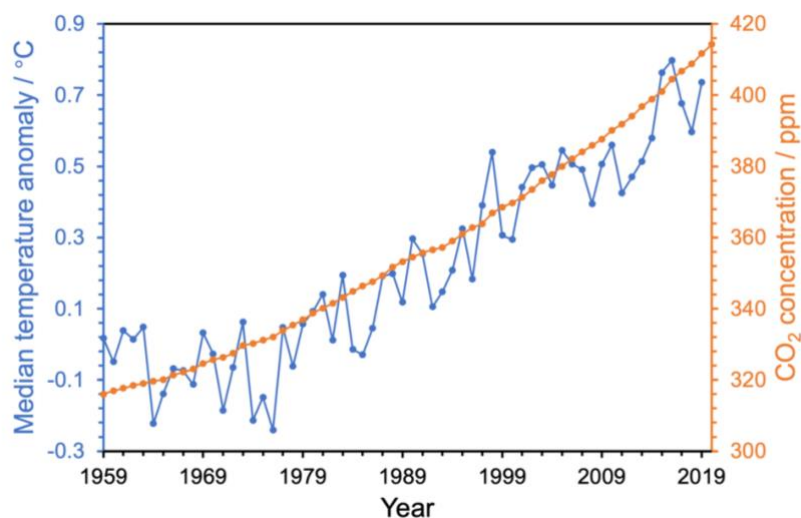


Figure 1.2 Median earth surface temperature anomalies (HadCRUT4 dataset) and atmospheric CO₂ concentration (Mauna Loa Observatory) from 1959 to 2020. Data retrieved from Ref. 7.

Thus, it is an urgent mission for people to mitigate the global warming caused by CO₂ emissions. To achieve carbon neutrality, both the increment of atmospheric CO₂ and the current atmospheric CO₂ level has to be reduced, which can be converted to two scientific and technologic topics: (1) reducing the consumption of fossil fuels, and (2) creating industrial processes without CO₂ emissions. However, one should always remember that billions of people worldwide, especially in Africa, Asia, and Latin America, are still living in poverty. The improvement of living standards relies heavily on industrialization, which requires a significant amount of energy consumption. Meanwhile, people living in industrialized areas are definitely not in favor of decreased life quality caused by activities aiming to reduce CO₂ emissions. We must anticipate an increased energy consumption and maintain a lot of necessary industrial processes with a huge amount of CO₂ emission (e.g., production of plastic, synthetic fibers, and rubbers, and the use of hydrocarbons in transportations). Based on the discussions above, the major scientific and technological challenges are clear:

- (1) Shifting from fossil fuels to renewable energy;
- (2) Integrating renewable energy into a carbon-based industrial model.

In the next section, based on a discussion on renewable energy's current status and future development, a closed carbon cycle with zero net CO₂ emission will be proposed.

1.1.2 Renewable energy for CO₂ utilization

People have devoted tremendous efforts to developing and deploying of renewable energy since the limitation of fossil fuels, and the issues of CO₂ emissions were realized. Aiming at minimizing the use of fossil fuels while meeting the increasing energy demand, renewable energy systems such as solar, wind, hydroelectric, geothermal, and modern biomass have been installed rapidly in the past two decades. Although renewable energy only contributed to 14.7% of the world energy consumption in 2019, we can be optimistic about the substitution of fossil fuels by renewable energy as the installed solar energy (mainly in the form of photovoltaic, PV) capacity has a near-exponential growth over the past 20 years (Figure 1.3).³ With such growth, one can expect a renewable energy production of 17 TW in 2050, which meets the global primary energy consumption of 2018.⁹

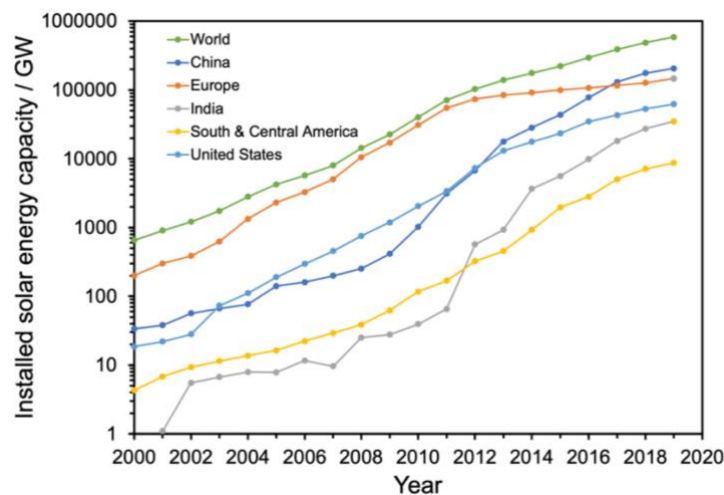


Figure 1.3 Installed solar energy capacity worldwide and in some major countries and regions from 2000 to 2019. Data retrieved from Ref. 3.

However, compared to fossil fuels, renewable energy sources suffer from drawbacks such as intermittency and a high degree of decentralization. These constraints limit the adaptation of renewable energy to modern industrial processes and people's daily life. Thus, an efficient energy carrier must be developed to store, transport, and integrate renewable energy. As modern renewable energy systems mainly generate energy in the form of electricity, the price of electricity is predicted to be very low in the future. Thus, sufficient electricity can be widely used for the generation of hydrogen, which is an ideal renewable energy carrier due to its high gravimetric energy density of 142 MJ/kg, and wide applications such as fuel and industrial processes require hydrogenation reactions.^{10,11}

More importantly, with sufficient hydrogen, CO₂ can also be used as a renewable energy carrier. Theoretically, CO₂ can be converted to various carbon-based fuels and chemicals (methane, ethylene, alcohols, gasoline, etc.) using hydrogenation reactions. This way, no significant changes to the modern carbon-based industrial mode will be required during the substitution of fossil fuels by renewable energy. And the cost of such an energy revolution can be minimized, as industrial production and people's lifestyle will not be greatly interfered. Furthermore, with the development of CO₂ capture technology, CO₂ generated by industrial processes and atmospheric CO₂ will be captured, purified, and used as carbon feedstock. In summary, with the introduction of renewable energy, a closed carbon cycle with zero net CO₂ emission (Figure 1.4) can be realized, which is the initial step for global carbon neutrality.¹² In this carbon cycle, the most critical step is the hydrogenation of CO₂ into fuels and chemicals in an industrial scale with acceptable cost, as it is a “two birds, one stone” approach toward solving the climate change and energy deficit for the future world.

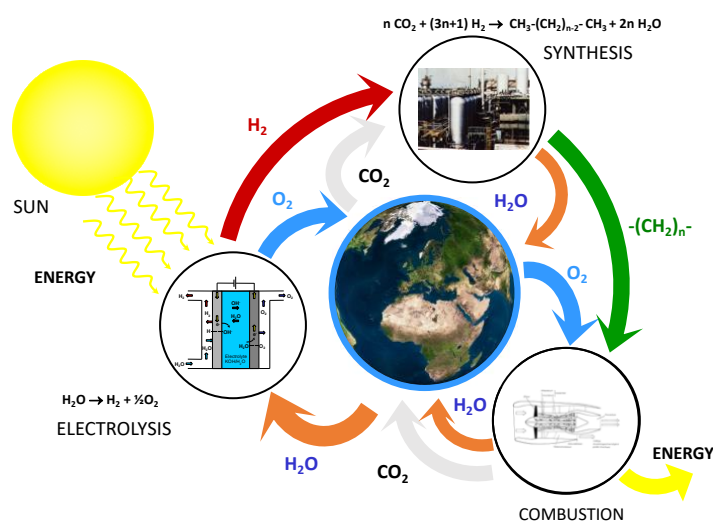


Figure 1.4 Schematic illustration of a closed carbon cycle with CO₂ as feedstock for fuel and chemical production. Permission from Ref. 12.

1.2 CO₂ hydrogenation catalysts

Hydrogenation of CO₂ can be carried out in conventional thermal catalytic processes, and novel electro- or photocatalytic processes.^{13–15} In this thesis, CO₂ hydrogenation is considered to be integrated into carbon-based industrial processes. As large-scale catalytic hydrogenation technology is only available in thermochemical processes, thermocatalytic CO₂ hydrogenation is discussed exclusively in this section. Once highly efficient catalysts for CO₂ hydrogenation are available, current technology and infrastructures for

catalytic hydrogenation in petroleum chemical engineering can adapt immediately without further obstacles for large-scale deployment.¹⁶

Several catalytic processes have been intensively studied in recent years to activate and upgrade CO₂ to value-added fuels and chemicals.^{17–20} Great efforts have been devoted to developing advanced catalysts to achieve high conversion and selectivity to desired products. Table 1.1 shows the most attractive reactions for CO₂ hydrogenation with corresponding thermodynamics considerations (ΔH and ΔG) and suitable heterogeneous catalysts suggested in the previous studies.²¹ As it is shown, CO₂ can be hydrogenated to various products, including CO, CH₃OH, and hydrocarbons, which can be further converted to liquid fuels or directly applied in industrial applications.

Table 1.1 Thermodynamic consideration and catalysts of various CO₂ hydrogenation reactions at 298 K, and the corresponding reaction conditions. Reproduced from Ref. 21.

Reactions	ΔH / kJ/mol	ΔG / kJ/mol	Catalysts	Reaction conditions
$\text{CO}_2 + \text{H}_2 \rightleftharpoons \text{CO} + \text{H}_2\text{O}$	41.2	28.6	Cu-, Cu/ZnO-, Fe-, and Ce-based catalysts	1 atm, > 500 °C
$\text{CO}_2 + \text{H}_2 \rightleftharpoons \text{HCOOH}$	-31.2	33	Rh-, Ru-, and Ir-based organometallic catalysts	40 ~140 atm, 60 ~80 °C
$\text{CO}_2 + 3\text{H}_2 \rightleftharpoons \text{CH}_3\text{OH} + \text{H}_2\text{O}$	-131	-9	Cu-, Cu/ZnO-, and In ₂ O ₃ -based catalysts	5 ~ 120 atm, 230 ~ 280 °C
$\text{CO}_2 + 4\text{H}_2 \rightleftharpoons \text{CH}_4 + 2\text{H}_2\text{O}$	-164.9	-113.5	Ni-based, supported Ru and Rh catalysts	1 atm, 150 ~ 450 °C
$n\text{CO}_2 + 3n\text{H}_2 \rightleftharpoons \text{C}_n\text{H}_{2n} + 2n\text{H}_2\text{O}$	N/A	N/A	Fe-, Co-, Zn-, Zr-, In-based supported catalysts	10 ~ 50 atm, 250 ~ 450 °C

Among all the reactions, a consensus seems to exist in the literature that the production of syngas, alcohols, and hydrocarbons is the most promising. To unveil the fundamental questions in the development of CO₂ hydrogenation catalysts, recent achievements and challenges heterogeneous catalysts converting CO₂ to CH₄, CO, methanol, and C₂₊ hydrocarbons are discussed briefly in this section.

1.2.1 CO₂ to CH₄

Well known as the Sabatier reaction²², CO₂ hydrogenation to CH₄ (Table 1.1) is the only catalytic hydrogenation process with industrial application, which dates back to the 1970s.²³ Currently, the Sabatier reaction gains interest again from researchers for the production of synthetic natural gas (SNG) due to the importance of CH₄ as a fuel and higher liquefaction temperature than H₂. Small-scale applications of Sabatier reaction have been demonstrated successful in LMER, EPFL.²⁴

Commercially available Ru/ γ -Al₂O₃ catalysts are highly active and stable for CO₂ hydrogenation to CH₄ under low operation temperatures.²⁵ Considering the current low price of natural gas, the cost and practical applicability of Ru impede its large-scale application. Thus, supported Ni-based catalysts have been extensively investigated as they have similar activity as Ru and much lower cost. However, Ni-based catalysts suffer from severe deactivation even at low temperatures due to the sintering of Ni particles, formation of nickel carbonyl compounds, and carbon deposits.²⁶ The research in this area focuses mainly on the elucidation of catalytic mechanisms, aiming to develop stable catalysts. Among all CO₂ hydrogenation catalysts, those for the Sabatier reaction have the least number of metal candidates and relatively clear

reaction mechanisms. Important catalysts and corresponding mechanistic studies for the Sabatier reaction are summarized in Table 1.2.

Table 1.2 Representative catalysts and proposed reaction mechanism for CO₂ hydrogenation to CH₄.

Catalyst	Reaction condition (fixed-bed reactor)	Conversion and selectivity	Mechanism (if available)	Ref.
3 wt.% Ru/ γ -Al ₂ O ₃	GHSV = 55000 h ⁻¹ ; H ₂ /CO ₂ = 5/1; 673 K; 1 atm	85%, 85%	via carbonates and formates	25
20 wt.% Ni/ γ -Al ₂ O ₃	6000 mL/g/h; H ₂ /CO ₂ = 4/1; 623 K; 1 atm	>95%, 100%		27
Ni/CeO ₂	H ₂ /CO ₂ = 4.6/1; 613 K; 1 atm	91.1%, 100%	via CO route	28
5 wt.% Ni/CeO ₂ -ZrO ₂	H ₂ /CO ₂ = 4/1; 623 K; 1 atm	80%, 100%	via carbonates and formates	29

1.2.2 CO₂ to CO

Conversion of CO₂ to CO is usually known as the reversed water gas shift (RWGS) reaction (Table 1.1). The importance of the RWGS reaction originates from CO as a flexible intermediate in CO₂ conversion in the form of syngas for multiple processes such as Fisher-Tropsch synthesis and hydroformylation.³⁰ So far, noble metals and transition metals supported by different oxides, and some metal oxides, have been applied as the catalysts for the RWGS reaction, with different proposed reaction mechanisms.

Noble-metal-based catalysts. Supported noble metals, especially Pt, are the most extensively studied catalysts for the RWGS reaction, due to their high intrinsic activity in hydrogenation reactions. The performance of the catalysts is highly dependent on the nature of the metal oxide supports. Hong et al. found that Pt/TiO₂ had a higher CO₂ conversion rate than the Pt/Al₂O₃ catalyst, due to the formation of highly electron-donating Pt-O_v-Ti³⁺ (O_v refers to oxygen vacancies) sites confirmed by H₂-TPR and FTIR studies.³¹ On these sites, the RWGS reaction can happen via the carbonate route, while carbonates cannot be formed on irreducible Al₂O₃ surfaces. Similarly, as another famous reducible support, CeO₂-supported Ir was also proven to achieve high CO selectivity because of the oxygen vacancies and strong metal-support interaction.³² On irreducible supports, alkali-metal promoters are used to increase the intrinsic activity of the noble metal catalysts. For example, with K as a promoter, the TOF of Pt/mullite catalyst for the RWGS reaction can be increased by seven times, as the interface between KO_x and Pt can serve as active sites for the decomposition of formate to form CO.³³

Transition-metal-based catalysts. The excellent hydrogenation activity of noble metals brings the drawback of the competitive methanation reaction. Meanwhile, their high cost hinders the application as catalysts for large-scale syngas production from CO₂. Thus, non-noble metal catalysts are also widely investigated in this field. A systematical study on Al₂O₃-supported Cu-ZnO catalysts unveiled that the Al₂O₃ support increased the dispersion of CuO and ZnO particles and thus, promoted the reaction rate.³⁴ Compared to irreducible supports, CeO₂ also showed its advantage as the support of Cu catalysts. Cu/CeO₂ catalyst showed 100% CO selectivity and four times higher activity than Cu/SiO₂ due to the formation of oxygen vacancies at a temperature as low as 300 °C, observed by in situ XRD and XAS studies.³⁵

Metal-oxide- and metal-carbide-based catalysts. Recently, various metal oxides and carbides were also found to be active for the RWGS reaction, avoiding the high cost of noble metals and the sintering issues of transition metals. Chen et al. prepared $\text{InO}_x/\text{ZrO}_2$ catalysts with over 80% CO selectivity.³⁶ With in situ DRIFTS and HCOOH-TPD, they found that with an In loading as low as 0.1 wt.%, highly dispersed $\text{InO}_x\text{-ZrO}_2$ interfaces were formed, which facilitated the decomposition of formate intermediates to CO and suppressed the further hydrogenation. Liu et al. synthesized polycrystalline hexagonal $\alpha\text{-Mo}_2\text{C}$ as a highly selective (>99%) catalyst for the RWGS reaction.³⁷ Combinational DFT calculations and TPD experiments showed that specific surface facets, such as $\text{Mo}_2\text{C}(101)\text{-Mo/C}$, exhibit binding properties and are responsible for the high selectivity.

Table 1.3 Representative catalysts and proposed reaction mechanism for CO_2 hydrogenation to CO.

Catalyst	Reaction condition (fixed-bed reactor)	Conversion and selectivity	Mechanism (if available)	Ref.
5 wt.% Ir/CeO ₂	H ₂ /CO ₂ = 4/1; 573 K; 1 MPa	6.8%, 99%		32
Pt-K/mullite	H ₂ /CO ₂ = 1/1; 823 K; 1 atm	30.9%, 99.2%	via formate pathway	33
Cu-ZnO/Al ₂ O ₃	H ₂ /CO ₂ = 1/1; 513 K; 1 atm	12%, 100%		34
5 wt.% Cu/CeO ₂ -nanorod	H ₂ /CO ₂ = 5/1; 623 K; 1 atm	50%, 100%		35
0.1 wt.% InO _x /ZrO ₂	H ₂ /CO ₂ = 4/1; 523 K; 5 MPa	not given, 80%	via formate pathway	36
$\alpha\text{-Mo}_2\text{C}$	H ₂ /CO ₂ = 5/1; 673 K; 1 atm	16%, >99%	direct C-O bond cleavage	37

In Table 1.3, representative catalysts for the RWGS reaction discussed above are compared. Meanwhile, the two possible reaction mechanisms, namely direct C-O bond cleavage (Path A) and the formate pathway (Path B) are shown in Figure 1.5.³⁰ In current studies, a clear recognition of the active sites and corresponding intermediates is still missing, which is crucial for the rational design of catalysts.

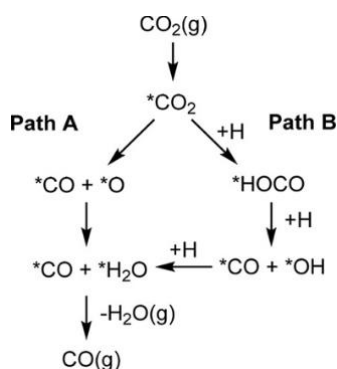


Figure 1.5 Possible pathways for CO_2 hydrogenation to form CO. *(X) indicates reactive species adsorbed on the catalyst surface. Permission from Ref. 30.

1.2.3 CO_2 to CH_3OH

The conversion of CO_2 to CH_3OH (Table 1.1) is the most studied among all catalytic CO_2 hydrogenation reactions, as CH_3OH is a highly demanded feedstock in chemical industries for the production of formaldehyde, acetic acid, dimethyl ether (DME), and methyl tertbutyl ether (MTBE).³⁸ Furthermore, the methanol-to-olefin (MTO) process has also gone into large-scale operation with the annual olefin production of over one million tons in China, which further extends the potential of CH_3OH as substituent feedstock of petroleum-based chemical engineering.³⁹ Huge efforts have been devoted to developing high-performance catalysts for CO_2 hydrogenation to CH_3OH , and the understanding of corresponding reaction mechanisms.

However, catalysts with good enough activity, selectivity, and stability for industrial application, and a conclusive mechanism about the nature of the catalytic activity, are still not available.

Cu-based catalysts. Based on the success of the Cu/ZnO/Al₂O₃ catalysts for the syngas-to-methanol process developed by Imperial Chemical Industries (ICI) in the 1960s, Cu-based catalysts, especially Cu-Zn combinations, have been extensively investigated for CO₂ hydrogenation to CH₃OH.³⁸ As an industrial benchmark, the commercially available Cu/ZnO/Al₂O₃ catalyst (ICI Katalco) has a productivity of 40 mol MeOH/(kg_{cat}·h) at 245 °C, and 4.5 MPa with the reaction gas composition of 70 vol% H₂, 24 vol% CO, and 6 vol% CO₂.⁴⁰ The performance of the Cu/ZnO/Al₂O₃ catalysts can be improved by ~30% after a comprehensive optimization of the composition and the preparation conditions. However, due to the sintering of Cu, the MeOH productivity undergoes substantial loss (44% in 100 h) during the operation, which prevents large-scale applications.⁴¹ With ZrO₂ as the support, the stability of the Cu-based catalysts can be significantly improved due to the formation of ZnO-ZrO₂ solid solution.⁴² An et al. used Zr-containing metal-organic frameworks (MOFs) to anchor ultrasmall Cu/ZnO_x NPs and achieved high stability over 100 h with 100% CH₃OH selectivity.⁴³

Not only the performance of Cu-based catalysts has been pushed to the limit, but numerous experiments were also done to understand the role of Cu and Zn as well as the evolution of the reaction intermediates. Several important observations and hypotheses have been published, such as the essential role of the steps at the Cu surface for high selectivity⁴⁴, the promotion effect originated from the migration of Zn atoms to the Cu surface⁴⁵, and the formation of highly active ZnCu bimetallic alloy during the reaction⁴⁶. However, arguments on these effects are still ongoing⁴⁷, and the real active site and the reaction pathway are still open questions.

In₂O₃-based catalysts. Based on the pioneering works predicted the potential of In₂O₃ for activating CO₂ theoretically^{48,49} and confirmed the activity of In₂O₃ for CO₂ hydrogenation to CH₃OH⁵⁰, In₂O₃ catalysts reported by Martin et al. attracted massive attention due to their extremely high CH₃OH selectivity (>99%) and superior stability.⁴¹ The defective In₂O_{3-x} sites are ideal for the stabilization and further hydrogenation of the formate intermediate.^{49,51} However, the CO₂ conversion over pure or supported In₂O₃ catalysts is rather low due to the lack of active sites for the dissociation and spillover of H₂.⁵¹ Thus, several strategies have been used to increase the activity of In₂O₃-based catalysts. Intuitively, the introduction of metal sites facilitates H₂ dissociation. Thus, supported catalysts, such as Au/In₂O₃, achieved a CO₂ conversion over 10% while maintaining the CH₃OH selectivity of ~70%.⁵² Alternatively, additional active sites can also be generated by the formation of bimetallic alloys containing In. As an example, both the activity and the selectivity of PtIn alloy NPs exceeded that of the Cu/ZnO/Al₂O₃ benchmark for CO₂ hydrogenation to methanol.⁵³

As a type of relatively new catalysts, the mechanism study on In₂O₃-based catalysts is still in its initial stage. Even though the formation of oxygen vacancies and the deactivation due to over-reduction have been observed by in situ XRD-XAS studies⁵⁴, the synergic effect between In and other metals, and the evolution of surface intermediates under reaction conditions still require in-depth experimental investigations using state-of-the-art techniques.

Other catalysts. Inspired by the idea of combining metallic sites for H₂ dissociation and oxides for CO₂ activation, novel catalysts such as PdZn/CeO₂, Au/CeO_x/TiO₂, and Pt/MoS₂ have also been developed. In these catalysts, either the oxygen vacancies from CeO_x or the Pt-S bonding were proposed to play an important role in activating CO₂ and the stabilization of formate intermediates.

Table 1.4 Representative catalysts and proposed reaction mechanism for CO₂ hydrogenation to CH₃OH.

Catalyst	Reaction condition (fixed-bed reactor)	Conversion and selectivity	Mechanism (if available)	Ref.
Cu/ZnO/Al ₂ O ₃ ⁴⁰	H ₂ /CO/CO ₂ = 6/3/1; 520 K; 4.5 MPa	30%, 85%	via formate or RWGS pathway	40
6.9 wt.% Cu/ZnO/UiO-bpy ⁴³	H ₂ /CO ₂ = 3/1; 523 K; 4 MPa	3.3%, 100%		43
9 wt.% In ₂ O ₃ /ZrO ₂ ⁴¹	H ₂ /CO ₂ = 4/1; 573 K; 5 MPa	5.2%, 99.8%	via formate pathway	41
Au/In ₂ O ₃ ⁵²	H ₂ /CO ₂ = 4/1; 573 K; 5 MPa	11.7%, 67.8%		52
PtIn alloy ⁵³	H ₂ /CO ₂ = 3/1; 543 K; 5 MPa	3%, 80%		53
Ca-doped PdZn/CeO ₂ ⁵⁵	H ₂ /CO ₂ = 3/1; 493 K; 3 MPa	7.7%, 100%	via formate pathway	55

In Table 1.4, representative catalysts for CO₂ hydrogenation to CH₃OH discussed above are compared. Meanwhile, the two possible reaction mechanisms corresponding to different catalysts, namely the RWGS + CO-Hydro pathways, and the formate pathways, are shown in Figure 1.6.⁵⁶ The RWGS + CO-Hydro pathway is featured by the CO intermediate produced from the RWGS reaction via the carboxyl (*HOCO) species, and its further hydrogenation to CH₃OH. The formate pathway is featured by the formate (*HCOO) intermediate and the following CH₃OH formation via C-O bond cleavage and *HCO/*H₂CO intermediates.

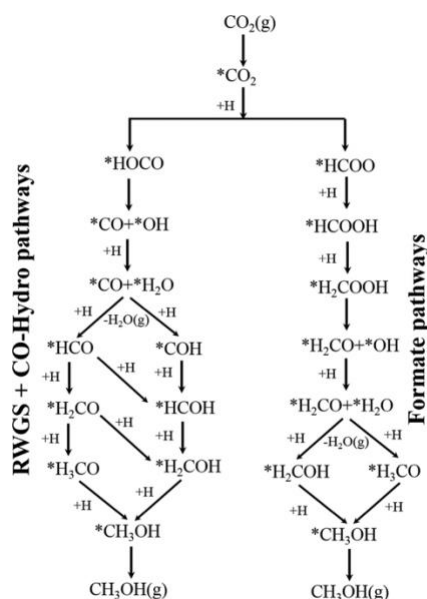


Figure 1.6 Reaction pathways for CO₂ hydrogenation to CH₃OH via the RWGS + CO-Hydro and formate intermediates. *(X) indicates adsorbed species. Permission from Ref. 56.

1.2.4 CO₂ to C₂₊ hydrocarbons

C₂₊ hydrocarbons, such as gasoline, kerosene, and diesel, are the most essential liquid fuel for transportation in daily life. There are two possibilities to produce multicarbon hydrocarbons from CO₂. One is Fischer-Tropsch like reaction (CO₂-FT) using standalone catalysts. The other is the tandem catalytic process consists of CO/CH₃OH production followed by the C-C coupling reaction catalyzed by various zeolites. Different

possible routes for the production of hydrocarbons from CO₂ hydrogenation are listed in Figure 1.7.³⁰ As the fundamental step of CO₂ conversion to C₂₊ hydrocarbons is the production of CO or CH₃OH, which has been discussed previously, and the catalysts and related mechanisms of the C-C coupling reactions will be beyond the scope of this thesis, this section will be relatively brief.

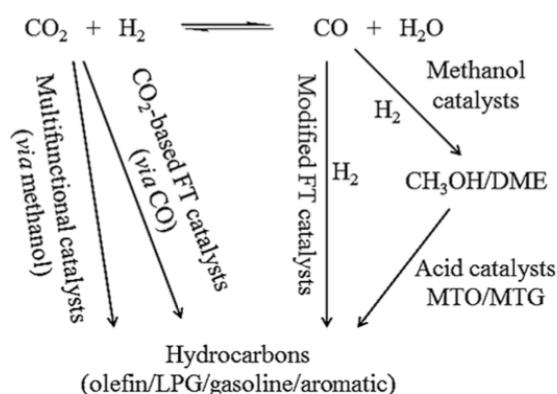


Figure 1.7 Different possible routes for the production of value-added hydrocarbons from CO₂ hydrogenation. Permission from Ref. 30.

One example of standalone catalysts is the K-promoted Fe/C catalyst.⁵⁷ Fe is known to be active for both the RWGS and the FT reactions, leading to the production of both CO and CH₄ in CO₂ hydrogenation. With K as the promoter, the olefin selectivity is enhanced significantly due to the increase of the basicity of the support. In tandem catalysts, zeolites play an important role in the redistribution of CO₂ hydrogenation products by catalyzing reactions such as hydrocracking, isomerization, aromatization, etc. The function of zeolites has been well understood based on massive studies in petrochemical industries. For example, HZSM-5 is an ideal catalyst for aromatization reactions, and SAPO-34 is highly selective to olefins in the MTO processes. Several examples of catalysts for CO₂ hydrogenation to C₂₊ products are listed in Table 1.5.

Table 1.5 Examples of catalysts for CO₂ hydrogenation to C₂₊ hydrogenation via different routes.

Catalyst	Reaction condition (fixed-bed reactor)	Reaction route	CO ₂ conversion	Selectivity		Ref.
				C ₂ -C ₄ ⁼	Aromatic	
K-promoted Fe/C ⁵⁷	593 K; 3 MPa	standalone	40%	38.8%	-	57
ZnFeO _x -Na/HZSM-5 ⁵⁸	593 K; 3 MPa	CO ₂ -FT	36.2%	2.8%	53.4%	58
In-Zr/SAPO-34 ⁵⁹	653 K; 3 MPa	MeOH	26.2%	26.9%	-	59

1.3 Surface science of CO₂ hydrogenation

In Section 1.2, catalysts for different CO₂ hydrogenation reactions have been discussed extensively. Despite the great efforts devoted to the development of catalysts, fundamental surface phenomena behind CO₂ hydrogenation should also be investigated thoroughly for the rational design of the catalysts rather than tediously exhausting all the possible combinations of the elements in the periodical table. Thus, molecular and atomic level surface fundamentals in CO₂ activation, such as the evolution of the intermediates, and the catalyst structure-activity relationships (e.g., the chemical state of the active sites, the dispersion of the metals, the bimetallic synergy, and the effect of the oxide supports), should be broadly investigated via both experimental and theoretical approaches. Specifically, in this section, experimental observations on surface

phenomena of CO₂ activation and corresponding characterization strategies are discussed. The importance of the well-defined model surfaces and surface science techniques under controlled temperature and pressure conditions will be highlighted.

1.3.1 Activation of CO₂ on model catalysts at ultrahigh vacuum

In order to gain a molecular-level understanding of the CO₂ activation, studies using surface sensitive techniques under ultrahigh vacuum (UHV) condition over model catalysts (mainly single crystals of metals and metal oxides) have been carried out in the last few decades. Among different UHV techniques, X-ray photoelectron spectroscopy (XPS) has been considered an appropriate and powerful technique to probe the chemical state of the catalyst and the nature of adsorbed species on the catalyst surface due to its high surface sensitivity. For CO₂ hydrogenation, the change of the core-level binding energies (BEs) indicates well the change in chemical bonding (environment) of carbon element. Thus, typical binding interactions of CO₂ on solid surfaces can be monitored using XPS, and the bonding information of adsorbed species can be obtained. It should be pointed out that the chemisorption of CO₂ is the prerequisite of CO₂ activation and further hydrogenation. Chemisorbed CO₂ species consist of various carbonates, as well as anionic bent CO₂^{δ-} species, depending on different surfaces and co-adsorbates, as summarized in Figure 1.8.⁶⁰

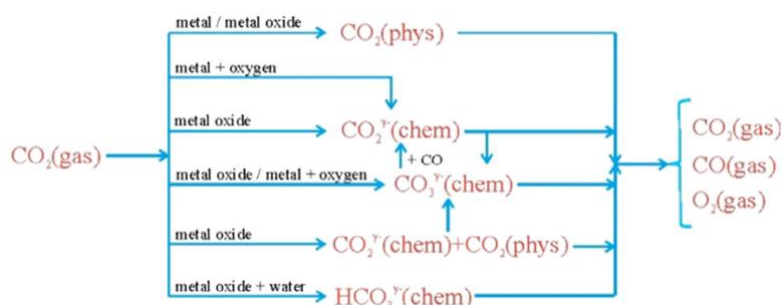


Figure 1.8 Physisorption and chemisorption pathways of CO₂. Permission from Ref. 60.

Figure 1.9 summarizes the C 1s core level BEs of the carbon species (including adsorbed CO, CO₃²⁻, carboxylate, oxalate, graphite/adventitious carbon, formate, and gas-phase CO and CO₂) related to the CO₂ surface chemistry.²¹ Representative studies have been carried over various metal and metal oxides single crystals, such as Cu, Ni, and ZnO.

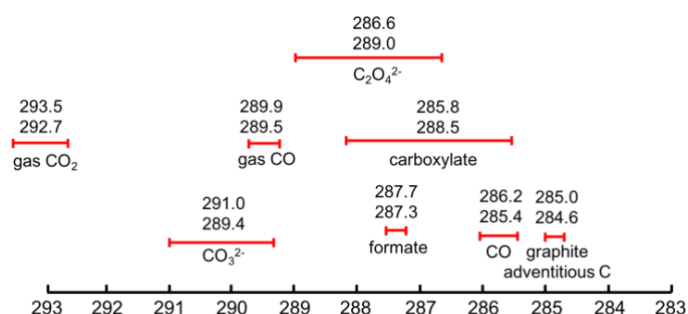
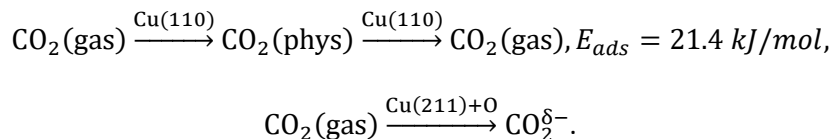


Figure 1.9 BEs of CO₂ adsorption and activation products. Permission from Ref. 21.

Cu surfaces. The surface chemistry of CO₂ on Cu surfaces attracts great interest due to the importance of Cu in CH₃OH synthesis. However, the reactivity of Cu crystals is low, and the adsorption of CO₂ is rather weak, as shown in Equation 1.1:



Equation 1.1 Physisorption and chemisorption of CO₂ on Cu(110) and O-preadsorbed Cu(211) surfaces.

On flat Cu(111) surfaces, even no CO₂ physisorption occurs unless alkali metals are coadsorbed.⁶¹ CO₂ physisorbs on “open” Cu(110) surfaces under low temperatures, but no dissociation or carbonate formation was evident.⁶² The reactivity of Cu increases as the surface becomes more stepped. For example, CO₂ physisorbs on clean Cu(211) surfaces and desorbs at a relatively high temperature of 130 K.⁶³ With pre-adsorption of oxygen, even chemisorbed CO₂ (CO₂^{δ-}) species were observed at 130 K through C 1s and O 1s peaks at 289 and 531.5 eV, respectively, as shown in Figure 1.10.⁶⁴ If the temperature was further increased to 295 K, no carbon species can be detected.

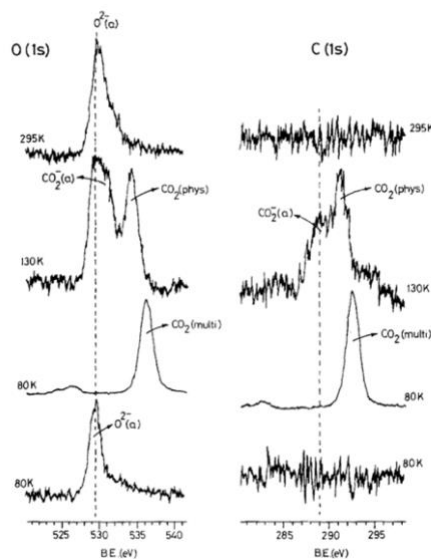
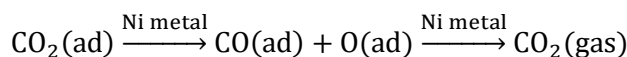


Figure 1.10 O 1s and C 1s regions of the photoelectron spectrum of a Cu(211) surface: initially clean, pre-oxidized (50 L, O₂), exposed to 100 L CO₂ at 80 K, and then subsequently warmed to the temperatures indicated. Permission from Ref. 64.

Ni surfaces. Ni-based catalysts are extensively studied for CO₂ hydrogenation to CH₄, and the Ni surfaces are known to be more reactive than Cu surfaces.^{65,66} CO₂ dissociation (Equation 1.2) and further hydrogenation at large rates have been clearly demonstrated.



Equation 1.2 Direct decomposition of CO₂ into adsorbed CO and atomic O.

Vesselli et al. provided a thorough description of the very initial steps of hydrogen reaction with CO₂ chemisorbed on Ni(110), as shown in Figure 1.11.⁶⁷ The physisorbed and chemisorbed CO₂ can be identified at C 1s regions with BEs of 290.6 and 286.2 eV at 90 K. The dissociation of CO₂ happens after annealing at

above 220 K, indicated by the appearance of CO peak at 285.1 eV. With the coadsorption of H, the formation of formate (C 1s at 288.0 eV) in a reversed “Y” configuration was observed at the temperature between 150 and 300 K. This result explained why the CO₂ hydrogenation barrier on Ni is much smaller than that on the Cu-based catalysts.

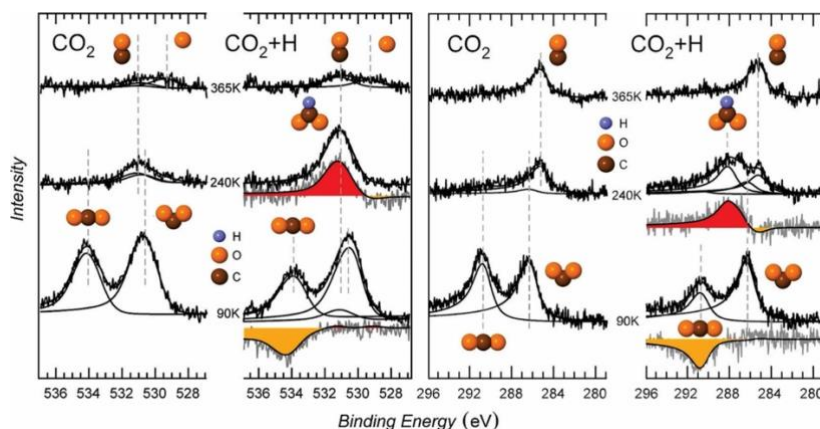
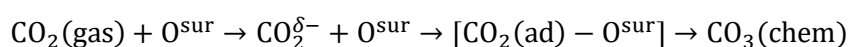


Figure 1.11 XPS data collected upon stepwise annealing of the CO₂-covered Ni(110) surface and of the CO₂ + H coadsorbed layer. Permission from Ref. 67.

Metal oxide surfaces. CO₂ adsorption on metal oxide surfaces can lead to direct carbonate formation without any coadsorption species (Equation 1.3), as the surface can provide the missing oxygen.⁶⁰



Equation 1.3 The chemisorption of CO₂ with the assistance of surface oxygen and the formation of carbonate.

Carbonate is an important intermediate in different CO₂ hydrogenation pathways because it is the stabilized form of the chemisorbed CO₂ and can be further converted to formate, which is essential for both CO and CH₃OH production. Due to its promoting role in CH₃OH synthesis to Cu-based catalysts, ZnO has been studied for CO₂ adsorption and activation. For example, on the O-terminated ZnO(0001) surface, carbonate species (C 1s peak at 290 eV, Figure 1.12) was observed upon exposure to ~2 Langmuir of CO₂ at 120 K.⁶⁸ Based on STM results, the formation of carbonates occurred on the oxygen vacancies at the edges. In addition, carbonate formation has also been observed on MgO⁶⁹ and CaO⁷⁰ single crystals due to their high basicity. In₂O₃-based catalysts have been discussed in detail in the previous section. Recent DFT studies showed that CO₂ adsorption on In₂O₃(110) surface also results in carbonate formation.^{48,49} However, XPS studies on the gas-solid interaction between CO₂ and In₂O₃ are still missing.

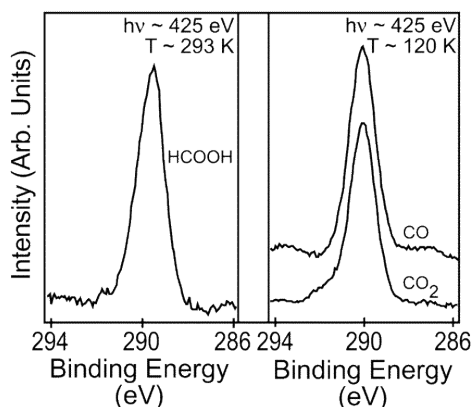


Figure 1.12 C 1s XPS spectra recorded from ZnO(0001)-O following exposure to ~ 3 L HCOOH, ~ 700 L CO, and ~ 2 L CO₂. Permission from Ref. 68.

1.3.2 Pressure gap and material gap

In practical processes of CO₂ hydrogenation, the reactions are typically carried out under elevated pressure and temperature (Table 1.1). Moreover, the catalysts always have complex compositions and structures, as discussed in Section 1.2. Naturally, one would expect that the surface chemistry of CO₂ during the catalytic processes of CO₂ hydrogenation cannot be adequately simulated by conventional UHV surface science techniques. In other words, the conclusions on the activation of CO₂ on clean single crystal surfaces could probably not be extrapolated to the practical catalytic processes. On top of that, the evolution of the catalyst surface properties, which is also critical in understanding the catalytic mechanism of CO₂ hydrogenation, cannot be observed under UHV pressures and cryogenic temperatures. Two major drawbacks of the conventional UHV-XPS studies on single crystal model catalysts have been pointed out.

First, there is a gap in the surface chemistry of CO₂ between the real catalytic reaction with continuous gas exposure at ≥ 1 bar and the UHV experiment with exposure to low pressure gas ($<10^{-6}$ mbar) for 10-1000 s, which is known as the **pressure gap**.⁷¹ For example, conventional XPS studies showed that, on the Ni(111) surface, CO₂ is only physisorbed under UHV conditions at cryogenic temperatures (<100 K).⁷² However, if the Ni(111) surface was exposed to 200 mTorr of CO₂, chemisorbed CO₂ can be observed in the form of carbonate.⁷³ Thus, information on the surface gained from conventional UHV techniques could be different from the authentic surface of the catalysts during the reactions.⁷⁴ Such an inconsistency generated from the pressure gap would impede the detection of the reaction intermediates and the understanding of the reaction pathway, as the knowledge obtained under UHV conditions cannot be directly extrapolated to the reaction conditions. With the application of conventional surface science techniques under reaction conditions, significant improvements in the investigations on CO₂ hydrogenation mechanisms will be achieved.

Second, conventional single crystal model catalysts are idealized catalysts and lack the complexity of real samples, such as metal-support interaction, particle size, and surface composition, which is dependent on a multitude of physical factors and even preparation methods. In specific, CO₂ hydrogenation reactions are widely agreed to be structure sensitive. Thus, conventional single crystal model catalysts can only provide the surface chemistry information of a particular site or set of sites. It has been argued that the structure-sensitive CO₂ activation process can currently be fully understood only in non-model catalysts, which is known as the **material gap**.⁷⁵ The structure sensitivity of CO₂ hydrogenation catalysts is distinguished in single

atom catalysts. Ni-based catalysts are ideal for CO₂ hydrogenation to CH₄, as discussed in Section 1.2.1. However, if Ni is dispersed on MgO lattice in the form of single atoms, the resulting catalyst was only active to the RWGS reaction but unable to further convert CO to CH₄.⁷⁶ TGA-MS and in situ FTIR results showed that the formate intermediate is highly stable on Ni single atoms and cannot be further hydrogenated to CH₄. This result indicates that the investigation of CO₂ surface chemistry cannot be limited to the bulk metal surface but should be extended to atomically dispersed scale. The preparation of size-selected metal nanoparticles, as well as the addition of metals on thin-film oxide supports, will be a powerful technology to narrow down the material gap.⁷¹

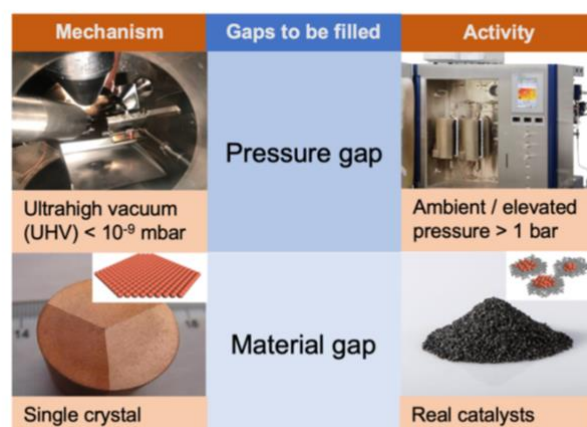


Figure 1.13 Graphical illustration of the pressure gap and material gap between surface science investigation on reaction mechanism and practical development of catalysts.

The pressure gap and material gap discussed above are summarized and graphically illustrated in Figure 1.13. To narrow down the material gap and pressure gap between model catalysts and “real-world” catalysts, it is necessary to (1) develop a model catalyst platform with flexibility in size and composition of both the active metal and the support, and (2) apply surface science techniques (especially XPS) under reaction atmosphere at near-ambient pressure (in several-mbar range). For the first requirement, the physical preparation method has advantages over wet chemistry techniques because it leads to clean materials without any contaminations during the sample transport.⁷⁷ For the second requirement, the near-ambient pressure XPS (NAP-XPS) technology should be appropriately applied to obtain authentic information on the surface under CO₂ hydrogenation conditions.

1.3.3 *In situ* study on CO₂ hydrogenation mechanisms

The development of NAP-XPS instrumentation enables the investigation of CO₂ surface chemistry under reaction conditions. Since 2008, in situ studies on CO₂ hydrogenation mechanisms using NAP-XPS has emerged and attracted the interests of researchers in the field of physical chemistry and heterogeneous catalysis. Typically, three types of information can be obtained in such studies: (1) activation of CO₂ on conventional model catalysts upon exposure to CO₂ gas in mbar range; (2) active surface sites evolution of more complex model catalysts or real catalysts under CO₂ hydrogenation conditions; and (3) surface adsorbates on real catalysts under CO₂ hydrogenation reactions. Representative research outcomes are summarized below.

Cu single crystals are the most studied model catalysts for CO₂ hydrogenation using NAP-XPS. Eren et al. compared the dissociation of CO₂ on Cu(100) and Cu(111) surfaces under various pressures.⁷⁸ It was found that the interaction between CO₂ and Cu is both structural- and pressure-sensitive. Cu(100) surface was more active in dissociating CO₂ than the Cu(111) surface, which is in agreement with the results of UHV-XPS studies. On Cu(100) surface, chemisorbed CO₂ (CO₂^{δ-}) was observed at 0.05 Torr CO₂ but not at 0.3 Torr and above, while the atomic oxygen coverage increased with CO₂ pressure (Figure 1.14). This result shows that no CO₂ can adsorb on a Cu surface after it is covered with atomic oxygen through CO₂ dissociation, which cannot be obtained from UHV-XPS studies. A very similar work comparing the Cu(110) and Cu(111) surfaces and the pressure dependence of CO₂ activation was recently published.⁷⁹

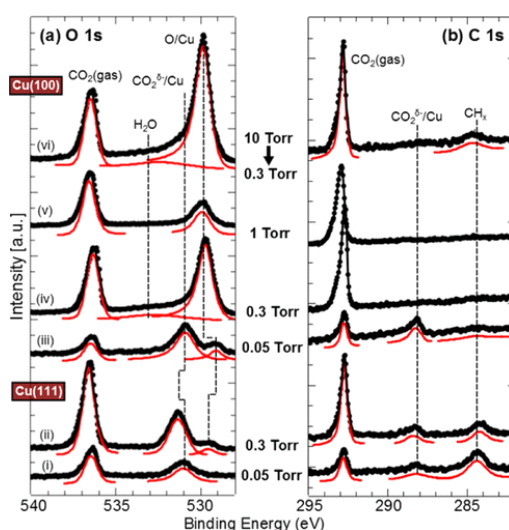


Figure 1.14 (a) O 1s and (b) C 1s regions of the NAP-XPS spectra in the presence of CO₂ at RT on the Cu(111) surface and the Cu(100) surface. Permission from Ref. 78.

Other Cu model catalysts, such as Cu(110) and Cu(997) single crystals, as well as polycrystalline Cu foils, have also been investigated upon exposure to CO₂ or mixtures between CO₂ and H₂, H₂O, or O₂.^{79–81} The effects of ZnO, ZrO₂, and Ni overlayers has also been studied.^{82–84} Besides, NAP-XPS studies on Ni(100), Ni(110), Ni(111), Pt(111), Rh(111), and polycrystalline Co foil surfaces were also reported.^{85–89} The review paper⁹⁰ by Zhong et al. thoroughly summarized the NAP-XPS studies on conventional model catalysts under CO₂ hydrogenation conditions. The carbon species observed on representative pure model catalyst surfaces by NAP-XPS are summarized in Table 1.6.

The unique advantage of NAP-XPS is the possibility to track the chemical state of the surface active sites during CO₂ hydrogenation over model catalysts with complex compositions or practical supported catalysts. Sapi et al. investigated the chemical state evolution of Ni and Pt of Pt nanoparticles supported on mesoporous NiO under reactive conditions.⁹¹ In Figure 1.15, the comparison between Ni 2p spectra of NiO and Pt/NiO catalysts for CO₂ hydrogenation highlighted the fact that the fraction of metallic Ni decreases during CO₂ hydrogenation for NiO but increases for Pt/NiO. This phenomenon shows an enhanced electron transfer property of Pt nanoparticles to NiO or Ni/NiO interface and that Pt assists nickel (Ni + NiO) enrichment on the surface. On the complex NiO_x/Ni/PtO_x/Pt surface, the formate intermediate may convert to formaldehyde and be further hydrogenated to CH₄, resulting in high CH₄ productivity.

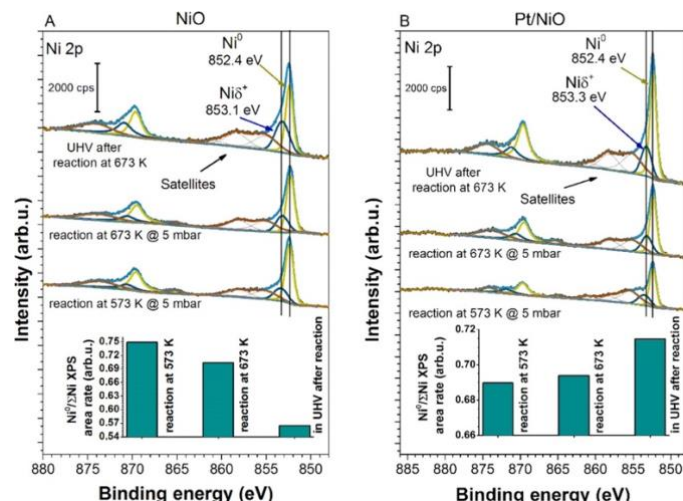


Figure 1.15 Ni 2p XPS spectra of NiO (A) and 5% Pt/NiO (B) under CO₂ hydrogenation conditions and subsequent evacuation at 673 K. Permission from Ref. 91.

In a more sophisticated example, the structure-activity relationship was even better elucidated by simultaneous NAP-XPS investigation on CO₂ activation and active sites evolution of Ru/CeO₂ catalyst for CO₂ hydrogenation to CH₄.⁹² In Figure 1.16, the strong peak at around 290 eV with a shoulder at 289.5 eV in C 1s region confirmed the formation of formate/carboxylate groups. In the Rh 3d and Ce 4d regions, the formation of RhO_x and partial reduction of ceria into Ce³⁺ was confirmed. This information indicated the presence of Rh-O species and oxygen vacancies in ceria in CO₂ hydrogenation to CH₄. Altogether, over the Ru/CeO₂ catalyst, CO₂ methanation occurs via the formate pathway, and the high CH₄ selectivity was attributed to the strong metal-support interaction.

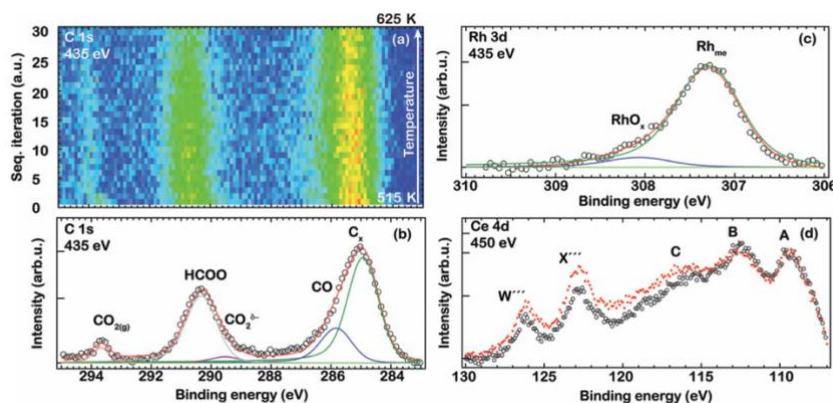


Figure 1.16 AP-XPS spectra of the C 1s region of the Rh/CeO₂ catalyst measured in situ during a temperature ramp from 515 to 625 K under CO₂/H₂ mixture (a). The corresponding C 1s (b), Rh 3d (c), and Ce 4d (d) levels recorded in situ for the Rh/CeO₂ catalyst after exposure to a CO₂/H₂ mixture at 515 K. Permission from Ref. 92.

Ferrah et al. showed another example on the NAP-XPS study on Cu-based nanoparticles supported on TiO₂ nanoparticles/HOPG for CO₂ hydrogenation.⁹³ This work is interesting because (1) the Cu NPs were prepared by wet chemistry and loaded on the support, and (2) the use of HOPG as support complicated the analysis of the C 1s region. The use of HOPG made the results from in situ NAP-XPS and ex situ TEM characterizations comparable with each other, as the TEM sample was prepared on the carbon-coated Cu grids. Figure 1.17 showed the intermediates of CO₂ hydrogenation over Cu/TiO₂/HOPG sample at different photon energies. Based on the difference of carbon species at various information depths, the authors proposed that the

activity toward CO, CH₄, and CH₃OH is strongly dependent on the percentage of oxygen present on the Cu NPs surfaces. However, it should be pointed out that the HOPG support mainly contributed the C 1s peaks, and a lot of assumptions were used for the peak fittings. In this case, the consistency of the peak fitting parameters should be carefully ensured during the data analysis for a reliable result. Thus, the understanding of data should be carried out with great caution.

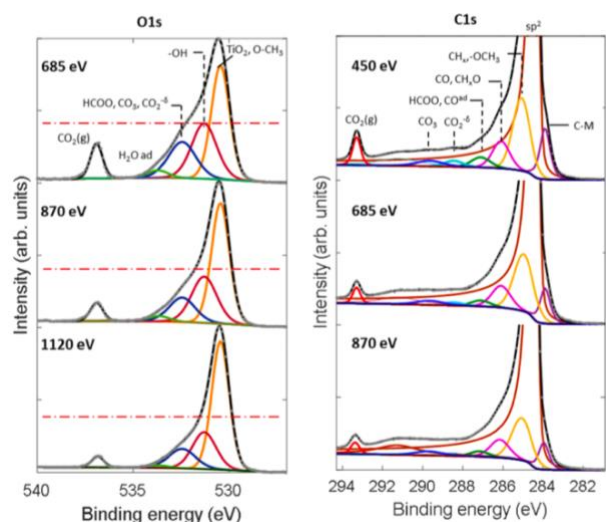


Figure 1.17 O 1s and C 1s spectra taken using different photon energies during the in situ CO₂RR on a surface oxygen-free Cu/TiO₂ NPs/HOPG sample under CO₂ (100 mTorr) and H₂ (100 mTorr) at 350 K. Permission from Ref. 93.

Comparing the catalysts developed for CO₂ hydrogenation in Section 1.2 and the mechanism studies in Section 1.3, one can observe a disparity between them. Significant progress has been achieved in the development of novel catalysts for CO₂ hydrogenation in recent years. However, there is a lack in the surface chemistry of CO₂ and the understanding of structure-performance relationships in these novel catalysts. The deficiency in the fundamental research impedes people's efforts to push the performance of CO₂ hydrogenation catalysts to the extent of industrial applications. For example, In₂O₃-based catalysts have extremely high selectivity towards CH₃OH⁴¹, while the experimental evidence of CO₂ activation on In₂O₃ surfaces remained absent. The CO₂ conversion of In₂O₃-based catalysts can be improved by introducing a second metal or selection of suitable supports⁵¹, but the evolution of active sites under reaction conditions is still unclear. Another example involves the well-studied Cu-based catalysts. Although the size and support sensitivity of Cu NPs has been proven in CH₃OH selectivity¹⁰⁹, the corresponding deactivation mechanism has not been thoroughly investigated. For the Cu/CeO₂ system, high activity towards RWGS reaction and CH₃OH production was attributed to the strong metal-support interaction¹¹⁰, while the relationship between the strong metal-support interactions (SMSI) and CO₂ activation is also in dispute. In summary, the important topics in NAP-XPS studies for understanding CO₂ hydrogenation mechanisms in this thesis are proposed as follows: (1) development of model catalysts with structural and compositional complexity that can simulate the state-of-the-art CO₂ hydrogenation catalysts. (2) simultaneous spectral and visual observation on the structure sensitivities of representative model catalysts; and (3) simultaneous investigation on CO₂ hydrogenation intermediates and the corresponding functions of active sites for the novel, promising catalysts.

Table 1.6 C 1s and O 1s BEs of the carbon species observed on representative pure model catalyst surfaces.

Surface	Gas	Temperature / K	C 1s and O 1s BEs / eV					Notes	Ref.
			CO ₂ (phys)	CO ₃	CO ₂ ^{δ-}	HCOO	C-O		
Poly-Cu	CO ₂	300	290.7 534.6	289.3 531.9	288.4 531.4	-	-		80, 94
	CO ₂ +H ₂ O	300	-	289.3 531.9	288.4 531.4	287.3	285.2	C-O from methoxy group	
Cu(111)	CO ₂	300	-	-	288.4 531.4	-	-		81
	CO ₂ +H ₂ O	300	-	289.4 531.8	287.9 530.8	287.3 530.8	286.3 530.8	Overlap of CO ₂ ^{δ-} , HCOO, and C-O	
Cu(997)	CO ₂	340	-	289.0 531.3	-	-	-		95
Cu(110)	CO ₂	300	-	-	288.1 531.6	-	-		79
Cu(100)	CO ₂	300	-	-	288.0 531.0	-	-		96
Ni(111)	CO ₂	300	-	288.9 531.1	-	-	-	No adsorption above 0.07 mbar	73
	CO ₂ +H ₂	300	-	-	-	-	285.2 531.1	After reaction at 573 K	
Ni(110)	CO ₂	300	-	288.4	286.6	-	285.5	Converted to C ₀ with H ₂	87
Poly-Co	CO ₂ +H ₂ O	300	-	288.9	-	287.0	285.2	C-O from methoxy group	86
				531.9		531.2	532.5		
Pt(111)	CO ₂	358	-	-	-	-	286.8 532.7	CO _{bridge} at 286.0 and 531.0 eV	88
Rh(111)	CO ₂ +CO	300	-	-	289.4	-	286.1	CO ₂ (ads.) at 285.5 eV	89

1.4 Instrumental methods

In this thesis, the state-of-the-art of in situ surface science techniques and model catalysts preparation methods are used. Besides, classical characterization methods, such as scanning electron microscopy (SEM), transmission electron microscopy (TEM), energy dispersive X-ray analysis (EDX), X-ray diffraction (XRD), N₂ adsorption, temperature-programmed techniques, thermogravimetric analysis (TGA), and diffuse infrared reflectance infrared Fourier transform spectroscopy (DRIFTS), and Raman spectroscopy, are also widely applied for further understanding of the catalysts. To evaluate the activity of the catalysts, a fixed-bed reactor with online mass spectroscopy (MS) was also built.

1.4.1 Near-ambient pressure XPS

XPS is one of the most common surface-sensitive techniques due to its powerful utility of combining atomic and chemical specificity with sub-monolayer quantitative sensitivity.⁹⁷ Since adsorption and dissociation of gas molecules on the surface of catalysts is the key step of heterogeneous catalytic reactions, such as NH₃ synthesis^{98,99}, and CO₂ hydrogenation, XPS is a fundamental tool to investigate the basic process on the gas-solid interface.

XPS is based on the photoelectric effect, i.e., emission of electrons following excitation of core level electrons by photons.¹⁰⁰ If a solid sample is exposed under an X-ray beam with large enough energy ($h\nu > E_b$), the electrons in certain orbitals can be excited. If the energy of the photoelectron is larger than the vacuum energy level, it can be removed from the solid surface and become a free electron (shown in Figure 1.18).

For solids, it is customary to define the binding energy relative to the Fermi level, which serves as a more practical reference.

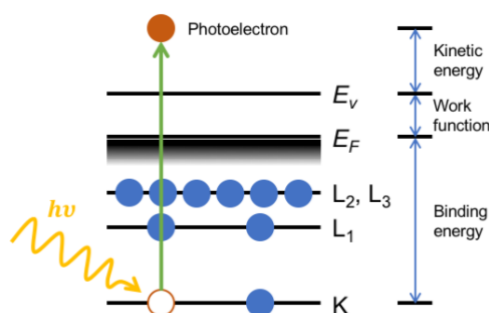


Figure 1.18 Schematic illustration of photoemission process and its energy conservation.

The energy conservation during the photoemission process of an isolated atom can be described in Equation 1.4.

$$E_b = h\nu - E_{kin} - \phi$$

Equation 1.4 The energy conservation during the photoemission process.

where $h\nu$ is the photon energy, E_{kin} is the kinetic energy of the photoelectron, ϕ is the work function of the surface where E_{kin} is measured at, and E_b is the binding energy of an electron in the atom.¹⁰¹

The binding energy of an electron depends mainly on the type of atom that it is bound to and its quantum state (*i.e.*, energy level, 1s, 2s, 2p, *etc.*). In addition, the measured binding energy is also a function of the chemical environment of the atom, which is referred as chemical shifts, and it is the power to resolve these subtle differences that makes XPS an excellent method for the investigation of surface chemistry.¹⁰¹ Specifically, for CO₂ hydrogenation, the intermediate species can be investigated with the chemical shift of C 1s and O 1s core levels by XPS as it has been reviewed Section 1.2-1.3.

The XPS apparatuses are maintained under UHV conditions (10^{-7} ~ 10^{-10} Pa) to minimize gas collisions of the emitted electrons after photoionization and to maintain the stability and long lifetime requirements of the spectrometer.¹⁰² However, further understanding of CO₂ hydrogenation processes under realistic conditions requires measurements at elevated pressures.¹⁰³ The investigation of surfaces using XPS at or near relevant pressures poses challenges due to the scattering of electrons by gas molecules, which have been overcome through the development of NAP-XPS.¹⁰⁴

To perform XPS measurements under elevated pressure, the ideal solution is to introduce a gas-impermeable but electron-permeable membrane between the sample and the spectrometer, such as graphene, which provides an abrupt pressure drop, from mbar range to UHV (Figure 1.19a). However, this approach has shown to be difficult to implement technically due to the stringent requirements on the mechanical stability of the ultrathin membranes.¹⁰⁵ Thus, the most commonly used scheme to transition from the ambient pressure in the analysis chamber to UHV in the electron analyzer is differential pumping, which creates a pressure gradient along the electron trajectory (Figure 1.19b). There are apertures between the pumping stages to

limit gas flow and allow electron transmission. To ensure the electrons can travel from the sample to the aperture, a sample-aperture distance of 0.1 to 1 mm is required for operation at 10 mbar.

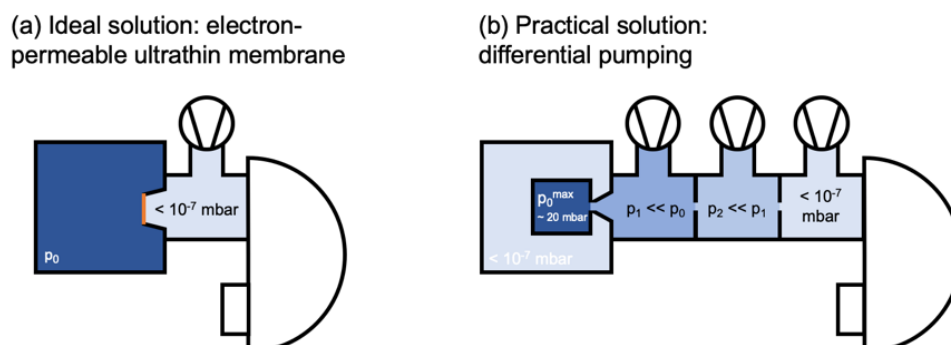


Figure 1.19 Two possible schemes for a NAP-XPS setup for transitioning from a near ambient pressure in the analysis chamber to UHV in the electron analyzer. Permission from Ref. 105.

In this thesis, a NAP-XPS system (Figure 1.20, SPECS GmbH) consists of an XR 50 X-ray gun, a uFocus 600 monochromator, and a Phoibos 150 NAP energy analyzer is used. Besides, the system is also equipped with a quadrupole mass spectrometer (QMS) to analyze the composition of off-gas in the analysis chamber.

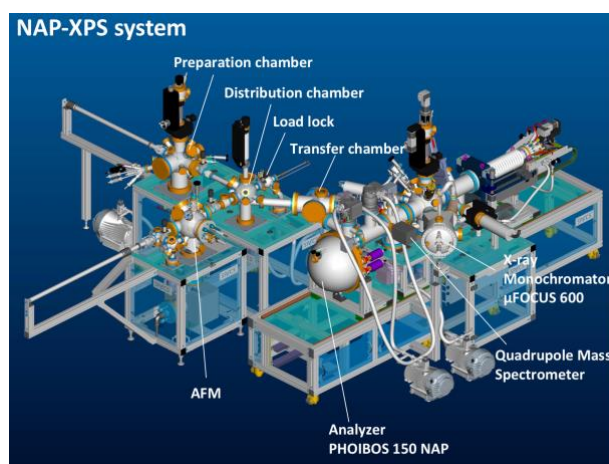


Figure 1.20 NAP-XPS system used in this thesis. Source: SPECS GmbH.

1.4.2 Preparation of model catalysts

In this thesis, two different methods were used to prepare model catalysts, depending on the expectation of the research outcomes.

Size-selected magnetron sputtering. Size-selected nanoparticle model catalysts are synthesized under vacuum using a nanoparticle deposition system (Nanogen Trio, Mantis Deposition Ltd.) which employs the Haberland concept of cluster formation.^{106,107}

The nanoparticle deposition system consists of magnetron sputtering, gas aggregation, and mass filtering, as illustrated in Figure 1.21. Up to 3 different metal targets can be mounted and sputtered by a DC plasma of argon, after which the sputtered material aggregated into nanoparticles in the gas phase by collisions with helium at relatively high pressure (several mbar) in a differentially pumped “aggregation zone”. After

aggregation, the particles undergo a supersonic expansion through an aperture, and subsequently, they do not grow further. The size distribution of the nanoparticles can be modified by varying the distance between the magnetron source at the exit aperture, the DC sputtering current, and the flowrate of Ar and He.⁷⁷ A significant fraction of the particles is negatively charged and could therefore be filtered according to their mass-to-charge ratio (m/z) in a quadrupole mass-filter (QMF, MesoQ, Mantis Deposition Ltd.). The particles can be deposited on various types of substrates for different purposes, *e.g.* (i) holey carbon/Cu grids for transmission electron microscopy (TEM) and (ii) metal oxides (SiO_2 , TiO_2 , Al_2O_3 , *etc.*) thin film prepared by natural oxidation or atomic layer deposition (ALD) on Si wafers.

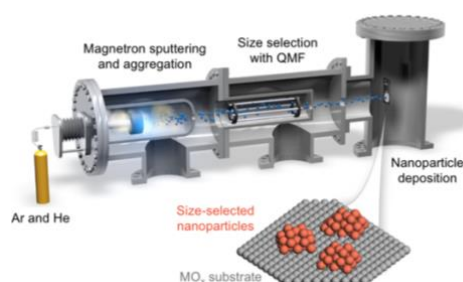


Figure 1.21 Schematic illustration of the nanoparticle deposition system for synthesizing size-selected model catalysts. Reproduced from Ref. 77.

Electron-beam evaporation. Thin film and bimetallic alloy model catalysts are prepared using e-beam evaporation under vacuum. Electron bombardment is used to produce intense localized heating, by which materials placed in small crucibles can be heated. The crucibles are placed inside a ring filament at ground potential. Electrons from the incandescent filament are attracted towards the crucibles, which is held at high positive potential. The evaporated materials are deposited on desired substrates, as shown in Figure 1.22. Thanks to the design of the instrument, up to 4 different materials can be evaporated simultaneously. By accelerating the electrons to 2 kV and allowing the emission up to 200 mA, total heating power of up to 400 W may be delivered into a very small area, allowing a temperature up to 3500 °C.

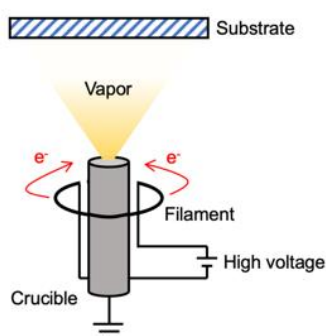


Figure 1.22 Schematic illustration of the e-beam evaporation process.

1.4.3 Catalyst characterization and evaluation

SEM and TEM are applied to characterize the size, morphology, and distribution of both “real world” catalysts and the model catalysts. Together with EDX, information on the elemental distribution on catalyst surfaces can also be obtained. TEM is important in determining the size distribution of model catalysts.

XRD is used to characterize the crystal structure, phase composition, and grain size of the samples (mostly the “real world” catalysts). The phases can be identified by direct comparison between the measured XRD patterns and the reference patterns in the database. The composition and grain size can be calculated by fitting the measured patterns with Rietveld refinement.¹⁰⁸

Temperature-programmed techniques heat the samples in carrier gas at a constant ramp and detect the change in the composition of the gas out of the samples. Such dynamic analysis is robust in investigating the physical and chemical properties of solid surfaces. For example, using temperature-programmed reduction (TPR), the precursor of the supported metal catalysts can be reduced, and the reduction temperature can be determined, which is an important reference for choosing the suitable reduction temperature of the catalysts. In H_2 and CO_2 temperature-programmed desorption (TPD), the amount of adsorption centers and the adsorption strength can be investigated. The information is commonly acknowledged by industrial catalysis researchers and is used to validate the results obtained by XPS.

DRIFTS and Raman spectroscopy measure the vibrational and rotational motions of molecules. They can be used to determine the surface composition of catalysts, and the interaction between the adsorbed molecules and the surface of catalysts. *In situ* DRIFTS can also be applied for cross-validating the surface species of CO_2 adsorption detected by NAP-XPS.

Conventionally prepared catalysts are evaluated in a fixed-bed flow reactor for their activity under real CO_2 hydrogenation conditions. The results can be used for validating the information obtained from NAP-XPS measurements and sieving good candidates for catalyst development. Figure 1.23 shows the flow reactor for performance evaluation. A certain mass of catalyst is placed in a quartz glass fix-bed reactor with an inner diameter of 7 mm. The as-prepared catalysts are firstly reduced, and a flow of CO_2/H_2 is passed through the fixed bed at certain temperatures. The temperature is measured with a thermocouple attached to the outside of the quartz glass reactor at the position of the fixed bed. The space velocity can be tuned by changing the gas flow using the mass flow controllers. The products are analyzed with a QMS.

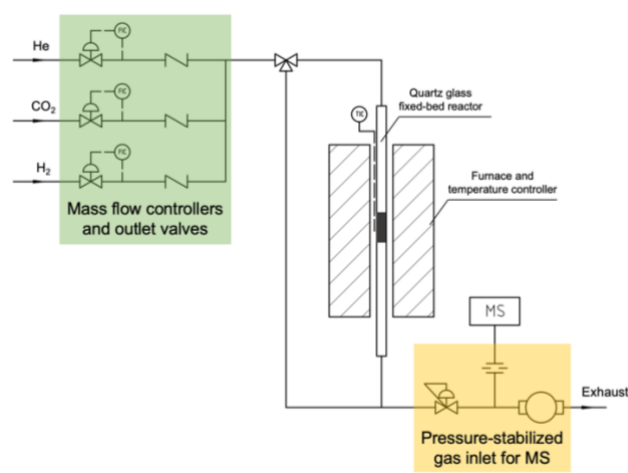


Figure 1.23 Schematic diagram of fixed-bed flow reactor for performance evaluation of catalysts.

1.5 Challenges and objectives of this thesis

Based on the comprehensive literature review in this chapter and the examples above, a timeline of major publications on NAP-XPS studies for understanding CO₂ hydrogenation mechanism is summarized in Figure 1.24. For pure metals, Cu and Ni have been investigated thoroughly, and recent publications turn to noble metals. However, pure metal model catalysts are less helpful in narrowing down the “material gaps”. On the other hand, supported nanoparticles are mostly real catalysts, but difficulties exist in monitoring CO₂ activation on their surface due to the contamination in sample synthesis and during sample transfer. Thin film and/or metal alloy model catalysts provide both flexibility in surface composition and possibility in reliable C 1s region XPS data analysis, and thus, are considered to be the promising subject in this thesis.

Accordingly, the challenges of mechanism study in CO₂ catalytic hydrogenation are summarized as follows: (1) the development of suitable model catalysts for the study on structure-performance relationships (e.g., size effects, bimetallic synergy, and metal-support interactions, etc.); (2) the monitoring of CO₂ activation process over novel catalyst surfaces under reaction conditions; (3) the development of NAP-XPS operation techniques for acquiring reliable data; and (4) the connection between the activities of the real catalysts and surface science information from the model catalysts.

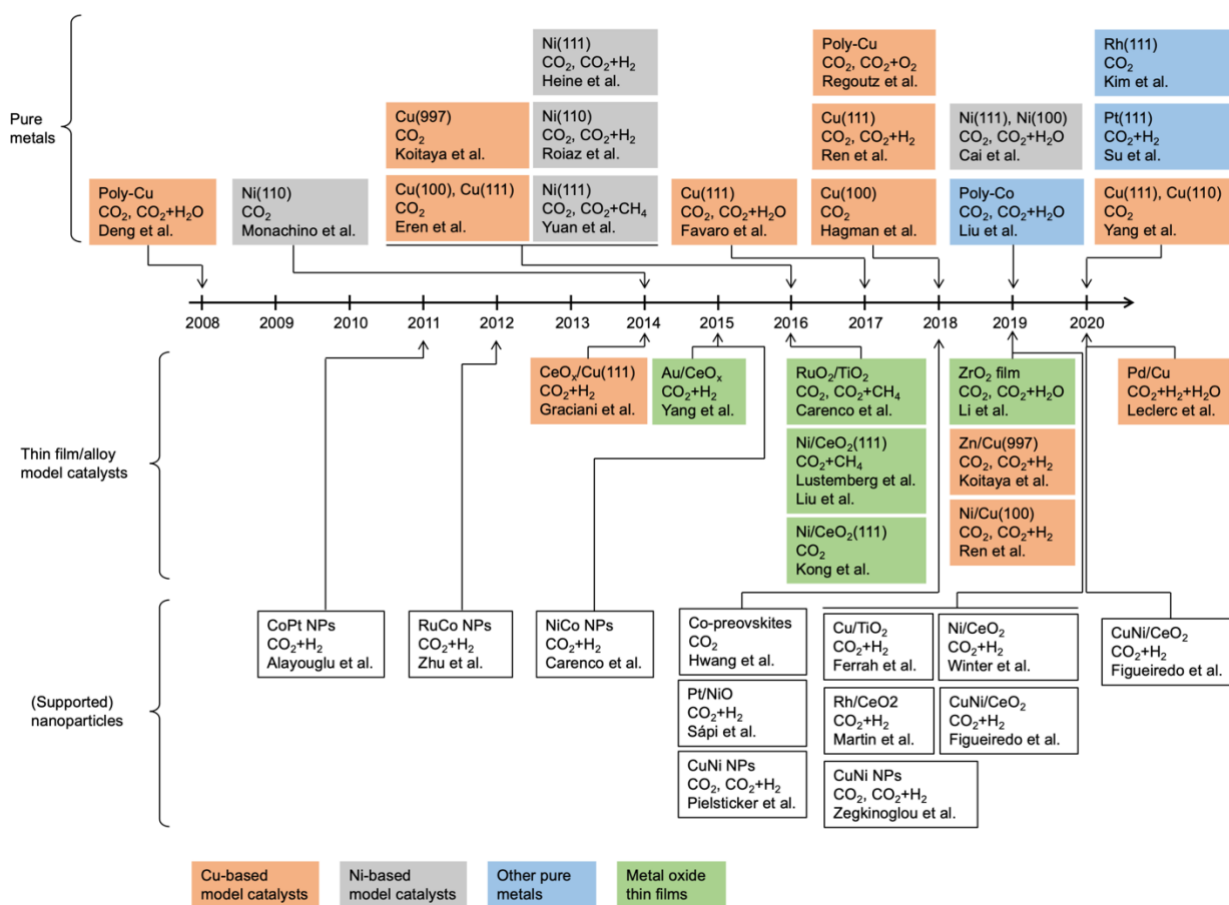


Figure 1.24 Timeline of NAP-XPS studies on model catalysts and supported catalysts for CO₂ hydrogenation. Colored boxes are bulk or thin film model catalysts, and transparent boxes are supported nanoparticles. The composition of catalysts, gas atmosphere, and the authors are given.

Therefore, in this thesis the author attempts to develop surface science models for Cu-based and Cu-In bimetallic catalysts and investigate the CO₂ hydrogenation processes using NAP-XPS and other techniques. Initially, size- and support- sensitivity of size-selected Cu NPs in catalysts deactivation was studied. Then, the Cu-In bimetallic synergy and the Cu/CeO₂ SMSI were investigated under CO₂ hydrogenation conditions with NAP-XPS. Based on the results from real catalysts, Cu and Cu-In catalysts with different supports were prepared and compared in terms of activity, bulk properties, and surface compositions.

1.6 Overview of the research work

This thesis focuses on understanding the gas-surface interaction and the structure-performance relationships for CO₂ hydrogenation catalysts. The author chose Cu and In as the main component of the model catalysts due to the general interests of researchers and the novelty in potential applications. By combining knowledge from heterogeneous catalysts prepared by conventional methods and newly developed model catalysts, CO₂ activation processes were investigated over the In/Cu and Cu/CeO₂ surfaces. The effects of size, composition, and metal-support interaction were also systematically studied by laboratory-based NAP-XPS system under CO₂ hydrogenation conditions. The structure of this PhD thesis is listed below and outlined in Figure 1.25.

In Chapter 2, the size and support-dependent thermal stability of Cu NPs was studied under CO₂ hydrogenation conditions. Size-selected Cu NPs were deposited by magnetron sputtering on different supports. The influence of particle size, support, temperature, and CO₂ hydrogenation atmosphere was systematically investigated. By simultaneous XPS and TEM characterizations, the sintering process and mechanism of 4 and 8 nm Cu NPs supported by carbon and SiO₂ were compared under both UHV and CO₂ hydrogenation conditions. Specifically, upon exposure to CO₂/H₂ mixture, the stability of Cu NPs is suggested to be influenced by the interplay of redispersion, agglomeration, and volatilization. These findings from model systems can offer new insights for understanding the deactivation of Cu-based catalysts.

In Chapter 3, the model catalyst was upgraded from monometallic Cu to bimetallic In/Cu surface. NAP-XPS was employed to investigate the chemical properties and the catalytic role of In/Cu model catalysts under CO₂ hydrogenation conditions. It was found that the deposition of In on the surface of a Cu foil led to the formation of Cu-In alloy, whereas upon CO₂ exposure, In was partially oxidized to In₂O_{3-x}, and Cu remains metallic. Due to the presence of In₂O_{3-x}, CO₂ was activated on the surface of In/Cu samples, mainly in the form of carbonate. The promotion effect of Cu-In alloy in the activation of CO₂ was explained by quantifying the surface density oxygen vacancies and carbonates. These results reveal the evolution of the active sites of indium/copper catalysts and inspire the design of advanced In-based bimetallic catalysts for CO₂ hydrogenation.

In Chapter 4, an active and inexpensive Cu/CeO_{2-x} catalyst for the hydrogenation of CO₂ was prepared. On a Cu/CeO_{2-x} model surface, the active phase and surface intermediates were observed simultaneously using NAP-XPS. Under atmospheric pressure, CO₂ hydrogenation occurred on the Cu/CeO_{2-x} surface via the RWGS reaction, leading to CO production. Partially reduced ceria with oxygen vacancies is responsible for CO₂ activation in the form of carbonate, and metallic Cu is the active site for H₂ dissociation and spillover to hydrogenate the carbonate intermediates and regenerate the oxygen vacancies. To elucidate the partially buried active surface, the cross-sectional structure and chemical composition of the Cu/CeO_{2-x} model catalyst

were visualized by STEM/EDX after the RWGS reaction. Combining the NAP-XPS and STEM/EDX results, an effective CO_2 activation and hydrogenation via carbonate/formate intermediates over the coupled Cu^+/Cu^0 and $\text{Ce}^{4+}/\text{Ce}^{3+}$ redox pairs on the metal-oxide interfaces are the main reasons for the high performance of the $\text{Cu}/\text{CeO}_{2-x}$ catalyst in the RWGS reaction.

In Chapter 5, the synergy between Cu and In for catalyzing RWGS reaction was demonstrated to be support dependent using heterogeneous Cu, In, and Cu-In catalysts supported by ZrO_2 and CeO_2 . By adding In, the CO_2 conversion was increased over ZrO_2 -supported catalysts but decreased over CeO_2 -supported catalysts. Characterizations revealed that different supports influence the active phases and the chemical states of the surface in a different way. Thus, for the design of bimetallic catalysts for CO_2 hydrogenation, the surface composition, the active phase, and the CO_2 adsorption ability of the support should be comprehensively considered for optimized performance.

Finally, a general conclusion and perspectives on this thesis are presented.

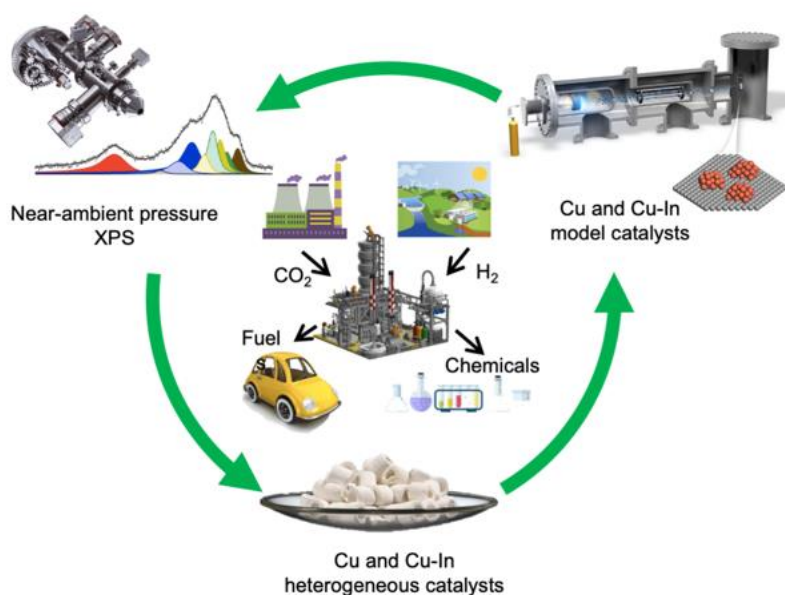


Figure 1.25 An overview of the structure and logic of this thesis.

1.7 References

1. Yu, K. M. K., Curcic, I., Gabriel, J. & Tsang, S. C. E. Recent Advances in CO₂ Capture and Utilization. *ChemSusChem* **1**, 893–899 (2008).
2. Mallapaty, S. How China could be carbon neutral by mid-century. *Nature* **586**, 482–483 (2020).
3. Statistical Review of World Energy. *bp global* <https://www.bp.com/en/global/corporate/energy-economics/statistical-review-of-world-energy.html>.
4. Data supplement to the Global Carbon Budget 2020. *ICOS* <https://www.icos-cp.eu/science-and-impact/global-carbon-budget/2020>.
5. Bereiter, B. *et al.* Revision of the EPICA Dome C CO₂ record from 800 to 600 kyr before present. *Geophys. Res. Lett.* **42**, 542–549 (2015).
6. Morice, C. P., Kennedy, J. J., Rayner, N. A. & Jones, P. D. Quantifying uncertainties in global and regional temperature change using an ensemble of observational estimates: The HadCRUT4 data set. *J. Geophys. Res. Atmospheres* **117**, (2012).
7. Keeling, R. F. & Keeling, C. D. Atmospheric Monthly In Situ CO₂ Data - Mauna Loa Observatory, Hawaii. (2017).
8. Hallegatte, S., Bangalore, M., Bonzanigo, L. & Fay, M. *Shock Waves : Managing the Impacts of Climate Change on Poverty. Climate Change and Development*. (World Bank, 2016).
9. Gielen, D. *et al.* The role of renewable energy in the global energy transformation. *Energy Strategy Rev.* **24**, 38–50 (2019).
10. Züttel, A., Remhof, A., Borgschulte, A. & Friedrichs, O. Hydrogen: the future energy carrier. *Philos. Trans. R. Soc. Math. Phys. Eng. Sci.* **368**, 3329–3342 (2010).
11. Schlapbach, L. & Züttel, A. Hydrogen-storage materials for mobile applications. *Nature* **414**, 353–358 (2001).
12. Züttel, A. *et al.* Storage of Renewable Energy by Reduction of CO₂ with Hydrogen. *Chim. Int. J. Chem.* **69**, 264–268 (2015).
13. Goeppert, A., Czaun, M., Jones, J.-P., Surya Prakash, G. K. & Olah, G. A. Recycling of carbon dioxide to methanol and derived products - closing the loop. *Chem. Soc. Rev.* **43**, 7995–8048 (2014).
14. Yan, T. *et al.* How to make an efficient gas-phase heterogeneous CO₂ hydrogenation photocatalyst. *Energy Environ. Sci.* **13**, 3054–3063 (2020).
15. Kibria, M. G. *et al.* Electrochemical CO₂ Reduction into Chemical Feedstocks: From Mechanistic Electrocatalysis Models to System Design. *Adv. Mater.* **31**, 1807166 (2019).
16. Ma, Z. & Porosoff, M. D. Development of Tandem Catalysts for CO₂ Hydrogenation to Olefins. *ACS Catal.* **9**, 2639–2656 (2019).
17. Li, W. *et al.* A short review of recent advances in CO₂ hydrogenation to hydrocarbons over heterogeneous catalysts. *RSC Adv.* **8**, 7651–7669 (2018).
18. V. Kondratenko, E., Mul, G., Baltrusaitis, J., O. Larrazábal, G. & Pérez-Ramírez, J. Status and perspectives of CO₂ conversion into fuels and chemicals by catalytic, photocatalytic and electrocatalytic processes. *Energy Environ. Sci.* **6**, 3112–3135 (2013).
19. Ma, J. *et al.* A short review of catalysis for CO₂ conversion. *Catal. Today* **148**, 221–231 (2009).
20. Zheng, Y. *et al.* Energy related CO₂ conversion and utilization: Advanced materials/nanomaterials, reaction mechanisms and technologies. *Nano Energy* **40**, 512–539 (2017).
21. Taifan, W., Boily, J.-F. & Baltrusaitis, J. Surface chemistry of carbon dioxide revisited. *Surf. Sci. Rep.* **71**, 595–671 (2016).
22. SABATIER, P. New Synthesis of Methane. *Comptes Rendus* **134**, 514–516 (1902).
23. Kopyscinski, J., Schildhauer, T. J. & Biollaz, S. M. A. Production of synthetic natural gas (SNG) from coal and dry biomass – A technology review from 1950 to 2009. *Fuel* **89**, 1763–1783 (2010).
24. Moiola, E., Mutschler, R. & Züttel, A. Renewable energy storage via CO₂ and H₂ conversion to methane and methanol: Assessment for small scale applications. *Renew. Sustain. Energy Rev.* **107**, 497–506 (2019).
25. Garbarino, G., Bellotti, D., Finocchio, E., Magistri, L. & Busca, G. Methanation of carbon dioxide on Ru/Al₂O₃: Catalytic activity and infrared study. *Catal. Today* **277**, 21–28 (2016).
26. Su, X. *et al.* Catalytic carbon dioxide hydrogenation to methane: A review of recent studies. *J. Energy Chem.* **25**, 553–565 (2016).
27. Rahmani, S., Rezaei, M. & Meshkani, F. Preparation of highly active nickel catalysts supported on mesoporous nanocrystalline γ -Al₂O₃ for CO₂ methanation. *J. Ind. Eng. Chem.* **20**, 1346–1352 (2014).
28. Zhou, G. *et al.* Role of surface Ni and Ce species of Ni/CeO₂ catalyst in CO₂ methanation. *Appl. Surf. Sci.* **383**, 248–252 (2016).
29. Aldana, P. A. U. *et al.* Catalytic CO₂ valorization into CH₄ on Ni-based ceria-zirconia. Reaction mechanism by operando IR spectroscopy. *Catal. Today* **215**, 201–207 (2013).
30. De, S., Dokania, A., Ramirez, A. & Gascon, J. Advances in the Design of Heterogeneous Catalysts and Thermocatalytic Processes for CO₂ Utilization. *ACS Catal.* **10**, 14147–14185 (2020).
31. Kim, S. S., Lee, H. H. & Hong, S. C. A study on the effect of support's reducibility on the reverse water-gas shift reaction over Pt catalysts. *Appl. Catal. Gen.* **423–424**, 100–107 (2012).
32. Li, S. *et al.* Tuning the Selectivity of Catalytic Carbon Dioxide Hydrogenation over Iridium/Cerium Oxide Catalysts with a Strong Metal–Support Interaction. *Angew. Chem.* **129**, 10901–10905 (2017).

33. Liang, B. *et al.* Promoting role of potassium in the reverse water gas shift reaction on Pt/mullite catalyst. *Catal. Today* **281**, 319–326 (2017).
34. Stone, F. S. & Waller, D. Cu–ZnO and Cu–ZnO/Al₂O₃ Catalysts for the Reverse Water-Gas Shift Reaction. The Effect of the Cu/Zn Ratio on Precursor Characteristics and on the Activity of the Derived Catalysts. *Top. Catal.* **22**, 305–318 (2003).
35. Lin, L. *et al.* In Situ Characterization of Cu/CeO₂ Nanocatalysts for CO₂ Hydrogenation: Morphological Effects of Nanostructured Ceria on the Catalytic Activity. *J. Phys. Chem. C* **122**, 12934–12943 (2018).
36. Chen, T. *et al.* Unraveling Highly Tunable Selectivity in CO₂ Hydrogenation over Bimetallic In–Zr Oxide Catalysts. *ACS Catal.* **9**, 8785–8797 (2019) doi:10.1021/acscatal.9b01869.
37. Liu, X. *et al.* Effective and Highly Selective CO Generation from CO₂ Using a Polycrystalline α -Mo₂C Catalyst. *ACS Catal.* **7**, 4323–4335 (2017).
38. Roy, S., Cherevotan, A. & Peter, S. C. Thermochemical CO₂ Hydrogenation to Single Carbon Products: Scientific and Technological Challenges. *ACS Energy Lett.* **3**, 1938–1966 (2018).
39. Tian, P., Wei, Y., Ye, M. & Liu, Z. Methanol to Olefins (MTO): From Fundamentals to Commercialization. *ACS Catal.* **5**, 1922–1938 (2015).
40. Baltes, C., Vukojević, S. & Schüth, F. Correlations between synthesis, precursor, and catalyst structure and activity of a large set of CuO/ZnO/Al₂O₃ catalysts for methanol synthesis. *J. Catal.* **258**, 334–344 (2008).
41. Martin, O. *et al.* Indium Oxide as a Superior Catalyst for Methanol Synthesis by CO₂ Hydrogenation. *Angew. Chem. Int. Ed.* **55**, 6261–6265 (2016).
42. Wang, J. *et al.* A highly selective and stable ZnO–ZrO₂ solid solution catalyst for CO₂ hydrogenation to methanol. *Sci. Adv.* **3**, e1701290 (2017).
43. An, B. *et al.* Confinement of Ultrasmall Cu/ZnOx Nanoparticles in Metal–Organic Frameworks for Selective Methanol Synthesis from Catalytic Hydrogenation of CO₂. *J. Am. Chem. Soc.* **139**, 3834–3840 (2017).
44. Behrens, M. *et al.* The Active Site of Methanol Synthesis over Cu/ZnO/Al₂O₃ Industrial Catalysts. *Science* **336**, 893–897 (2012).
45. Kuld, S. *et al.* Quantifying the promotion of Cu catalysts by ZnO for methanol synthesis. *Science* **352**, 969–974 (2016).
46. Kattel, S., Ramírez, P. J., Chen, J. G., Rodriguez, J. A. & Liu, P. Active sites for CO₂ hydrogenation to methanol on Cu/ZnO catalysts. *Science* **355**, 1296–1299 (2017).
47. Nakamura, J. *et al.* Comment on “Active sites for CO₂ hydrogenation to methanol on Cu/ZnO catalysts”. *Science* **357**, eaan8074 (2017).
48. Ye, J., Liu, C. & Ge, Q. DFT Study of CO₂ Adsorption and Hydrogenation on the In₂O₃ Surface. *J. Phys. Chem. C* **116**, 7817–7825 (2012).
49. Ye, J., Liu, C., Mei, D. & Ge, Q. Active Oxygen Vacancy Site for Methanol Synthesis from CO₂ Hydrogenation on In₂O₃(110): A DFT Study. *ACS Catal.* **3**, 1296–1306 (2013).
50. Sun, K. *et al.* Hydrogenation of CO₂ to methanol over In₂O₃ catalyst. *J. CO₂ Util.* **12**, 1–6 (2015).
51. Wang, J. *et al.* CO₂ Hydrogenation to Methanol over In₂O₃-Based Catalysts: From Mechanism to Catalyst Development. *ACS Catal.* **11**, 1406–1423 (2021).
52. Rui, N. *et al.* Hydrogenation of CO₂ to Methanol on a Au^{δ+}–In₂O₃–x Catalyst. *ACS Catal.* **10**, 11307–11317 (2020).
53. García-Trenco, A. *et al.* PdIn intermetallic nanoparticles for the Hydrogenation of CO₂ to Methanol. *Appl. Catal. B Environ.* **220**, 9–18 (2018).
54. Tsoukalou, A. *et al.* Structural Evolution and Dynamics of an In₂O₃ Catalyst for CO₂ Hydrogenation to Methanol: An Operando XAS–XRD and In Situ TEM Study. *J. Am. Chem. Soc.* **141**, 13497–13505 (2019).
55. Malik, A. S. *et al.* Development of highly selective PdZn/CeO₂ and Ca-doped PdZn/CeO₂ catalysts for methanol synthesis from CO₂ hydrogenation. *Appl. Catal. Gen.* **560**, 42–53 (2018).
56. Kattel, S., Yan, B., Yang, Y., Chen, J. G. & Liu, P. Optimizing Binding Energies of Key Intermediates for CO₂ Hydrogenation to Methanol over Oxide-Supported Copper. *J. Am. Chem. Soc.* **138**, 12440–12450 (2016).
57. Ramirez, A., Gevers, L., Bavykina, A., Ould-Chikh, S. & Gascon, J. Metal Organic Framework-Derived Iron Catalysts for the Direct Hydrogenation of CO₂ to Short Chain Olefins. *ACS Catal.* **8**, 9174–9182 (2018).
58. Cui, X. *et al.* Selective Production of Aromatics Directly from Carbon Dioxide Hydrogenation. *ACS Catal.* **9**, 3866–3876 (2019).
59. Wang, J., Zhang, A., Jiang, X., Song, C. & Guo, X. Highly selective conversion of CO₂ to lower hydrocarbons (C₂–C₄) over bifunctional catalysts composed of In₂O₃–ZrO₂ and zeolite. *J. CO₂ Util.* **27**, 81–88 (2018).
60. Burghaus, U. Surface chemistry of CO₂ – Adsorption of carbon dioxide on clean surfaces at ultrahigh vacuum. *Prog. Surf. Sci.* **89**, 161–217 (2014).
61. Hadenfeldt, S., Benndorf, C., Stricker, A. & Töwe, M. Adsorption of CO₂ on K-promoted Cu(111) surfaces. *Surf. Sci.* **352–354**, 295–299 (1996).
62. Funk, S. *et al.* Adsorption dynamics of CO₂ on Cu(110): A molecular beam study. *Surf. Sci.* **600**, 583–590 (2006).
63. Davies, P. R. & Keel, J. M. The reaction of carbon dioxide with amines at a Cu(211) surface. *Surf. Sci.* **469**, 204–213 (2000).

64. Copperthwaite, R. G., Davies, P. R., Morris, M. A., Roberts, M. W. & Ryder, R. A. The reactive chemisorption of carbon dioxide at magnesium and copper surfaces at low temperature. *Catal. Lett.* **1**, 11–19 (1988).
65. D'Evelyn, M. P., Hamza, A. V., Gdowski, G. E. & Madix, R. J. Dynamics of the dissociative adsorption of CO₂ on Ni(100). *Surf. Sci.* **167**, 451–473 (1986).
66. Ding, X. *et al.* Interaction of carbon dioxide with Ni(110): A combined experimental and theoretical study. *Phys. Rev. B* **76**, 195425 (2007).
67. Vesselli, E. *et al.* Carbon Dioxide Hydrogenation on Ni(110). *J. Am. Chem. Soc.* **130**, 11417–11422 (2008).
68. Lindsay, R. *et al.* Impact of Defects on the Surface Chemistry of ZnO(0001)–O. *J. Am. Chem. Soc.* **124**, 7117–7122 (2002).
69. Chakradhar, A. & Burghaus, U. Carbon dioxide adsorption on MgO(001)–CO₂ kinetics and dynamics. *Surf. Sci.* **616**, 171–177 (2013).
70. Doyle, C. S., Kendelewicz, T., Carrier, X. & Brown, G. E. THE INTERACTION OF CARBON DIOXIDE WITH SINGLE CRYSTAL CaO(100) SURFACES. *Surf. Rev. Lett.* **06**, 1247–1254 (1999).
71. Goodman, D. W. Correlations between Surface Science Models and “Real-World” Catalysts. *J. Phys. Chem.* **100**, 13090–13102 (1996).
72. Gordon, D. E. A. & Lambert, R. M. CO₂ adsorption on oxygen-modified Ni(111). *Surf. Sci.* **287–288**, 114–118 (1993).
73. Heine, C., Lechner, B. A. J., Bluhm, H. & Salmeron, M. Recycling of CO₂: Probing the Chemical State of the Ni(111) Surface during the Methanation Reaction with Ambient-Pressure X-Ray Photoelectron Spectroscopy. *J. Am. Chem. Soc.* **138**, 13246–13252 (2016).
74. Nguyen, L., Tao, F. F., Tang, Y., Dou, J. & Bao, X.-J. Understanding Catalyst Surfaces during Catalysis through Near Ambient Pressure X-ray Photoelectron Spectroscopy. *Chem. Rev.* **119**, 6822–6905 (2019).
75. Vogt, C. *et al.* Unravelling structure sensitivity in CO₂ hydrogenation over nickel. *Nat. Catal.* **1**, 127–134 (2018).
76. Millet, M.-M. *et al.* Ni Single Atom Catalysts for CO₂ Activation. *J. Am. Chem. Soc.* **141**, 2451–2461 (2019).
77. Vajda, S. & White, M. G. Catalysis Applications of Size-Selected Cluster Deposition. *ACS Catal.* **5**, 7152–7176 (2015).
78. Eren, B., Weatherup, R. S., Liakakos, N., Somorjai, G. A. & Salmeron, M. Dissociative Carbon Dioxide Adsorption and Morphological Changes on Cu(100) and Cu(111) at Ambient Pressures. *J. Am. Chem. Soc.* **138**, 8207–8211 (2016).
79. Yang, T. *et al.* Surface Orientation and Pressure Dependence of CO₂ Activation on Cu Surfaces. *J. Phys. Chem. C* (2020) doi:10.1021/acs.jpcc.0c08262.
80. Deng, X. *et al.* Surface Chemistry of Cu in the Presence of CO₂ and H₂O. *Langmuir* **24**, 9474–9478 (2008).
81. Favaro, M. *et al.* Subsurface oxide plays a critical role in CO₂ activation by Cu(111) surfaces to form chemisorbed CO₂, the first step in reduction of CO₂. *Proc. Natl. Acad. Sci.* **114**, 6706–6711 (2017).
82. Koitaya, T. *et al.* CO₂ Activation and Reaction on Zn-Deposited Cu Surfaces Studied by Ambient-Pressure X-ray Photoelectron Spectroscopy. *ACS Catal.* **9**, 4539–4550 (2019).
83. Ma, Y. *et al.* Reactivity of a Zirconia–Copper Inverse Catalyst for CO₂ Hydrogenation. *J. Phys. Chem. C* **124**, 22158–22172 (2020).
84. Ren, Y. *et al.* Probing the Reaction Mechanism in CO₂ Hydrogenation on Bimetallic Ni/Cu(100) with Near-Ambient Pressure X-Ray Photoelectron Spectroscopy. *ACS Appl. Mater. Interfaces* (2019) doi:10.1021/acsami.9b19523.
85. Cai, J. *et al.* CO₂ Activation on Ni(111) and Ni(100) Surfaces in the Presence of H₂O: An Ambient-Pressure X-ray Photoelectron Spectroscopy Study. *J. Phys. Chem. C* **123**, 12176–12182 (2019).
86. Liu, Q. *et al.* CO₂ Activation on Cobalt Surface in the Presence of H₂O: An Ambient-Pressure X-ray Photoelectron Spectroscopy Study. *Catal. Lett.* **148**, 1686–1691 (2018).
87. Roiaz, M. *et al.* Reverse Water–Gas Shift or Sabatier Methanation on Ni(110)? Stable Surface Species at Near-Ambient Pressure. *J. Am. Chem. Soc.* **138**, 4146–4154 (2016).
88. Su, H. *et al.* Probing the surface chemistry for reverse water gas shift reaction on Pt(111) using ambient pressure X-ray photoelectron spectroscopy. *J. Catal.* **391**, 123–131 (2020).
89. Kim, J. *et al.* How Rh surface breaks CO₂ molecules under ambient pressure. *Nat. Commun.* **11**, 5649 (2020).
90. Zhong, L., Chen, D. & Zafeirotos, S. A mini review of in situ near-ambient pressure XPS studies on non-noble, late transition metal catalysts. *Catal. Sci. Technol.* **9**, 3851–3867 (2019).
91. Sápi, A. *et al.* In Situ DRIFTS and NAP-XPS Exploration of the Complexity of CO₂ Hydrogenation over Size-Controlled Pt Nanoparticles Supported on Mesoporous NiO. *J. Phys. Chem. C* (2018) doi:10.1021/acs.jpcc.8b00061.
92. M. Martin, N. *et al.* Structure–function relationship for CO₂ methanation over ceria supported Rh and Ni catalysts under atmospheric pressure conditions. *Catal. Sci. Technol.* **9**, 1644–1653 (2019).
93. Ferrah, D. *et al.* Wet Chemical Growth and Thermocatalytic Activity of Cu-Based Nanoparticles Supported on TiO₂ Nanoparticles/HOPG: In Situ Ambient Pressure XPS Study of the CO₂ Hydrogenation Reaction. *ACS Catal.* **9**, 6783–6802 (2019).
94. Regoutz, A., Kerherve, G., Villar-Garcia, I., Williams, C. K. & Payne, D. J. The influence of oxygen on the surface interaction between CO₂ and copper studied by ambient pressure X-ray photoelectron spectroscopy. *Surf. Sci.* **677**, 121–127 (2018).

-
95. Koitaya, T. *et al.* Real-Time Observation of Reaction Processes of CO₂ on Cu(997) by Ambient-Pressure X-ray Photoelectron Spectroscopy. *Top. Catal.* **59**, 526–531 (2016).
 96. Hagman, B. *et al.* Steps Control the Dissociation of CO₂ on Cu(100). *J. Am. Chem. Soc.* **140**, 12974–12979 (2018).
 97. Arble, C., Jia, M. & Newberg, J. T. Lab-based ambient pressure X-ray photoelectron spectroscopy from past to present. *Surf. Sci. Rep.* **73**, 37–57 (2018).
 98. Bozso, F., Ertl, G., Grunze, M. & Weiss, M. Interaction of nitrogen with iron surfaces: I. Fe(100) and Fe(111). *J. Catal.* **49**, 18–41 (1977).
 99. Ertl, G., Lee, S. B. & Weiss, M. Kinetics of nitrogen adsorption on Fe(111). *Surf. Sci.* **114**, 515–526 (1982).
 100. Siegbahn, K. From X-Ray to Electron Spectroscopy. in *Nishina Memorial Lectures: Creators of Modern Physics* (ed. Foundation, N. M.) 137–228 (Springer Japan, 2008). doi:10.1007/978-4-431-77056-5_8.
 101. Hollander, J. M. & Jolly, W. L. X-ray photoelectron spectroscopy. *Acc. Chem. Res.* **3**, 193–200 (1970).
 102. Luo, W. & Zafeiratos, S. CHAPTER 5:XPS Characterization of Metal-free Functionalized Carbons. in *Metal-free Functionalized Carbons in Catalysis* 138–176 (2018). doi:10.1039/9781788013116-00138.
 103. Karslıoğlu, O. & Bluhm, H. Ambient-Pressure X-ray Photoelectron Spectroscopy (APXPS). in *Operando Research in Heterogeneous Catalysis* (eds. Frenken, J. & Groot, I.) 31–57 (Springer International Publishing, 2017). doi:10.1007/978-3-319-44439-0_2.
 104. Salmeron, M. & Schlögl, R. Ambient pressure photoelectron spectroscopy: A new tool for surface science and nanotechnology. *Surf. Sci. Rep.* **63**, 169–199 (2008).
 105. Wu, C. H., Weatherup, R. S. & Salmeron, M. B. Probing electrode/electrolyte interfaces in situ by X-ray spectroscopies: old methods, new tricks. *Phys. Chem. Chem. Phys.* **17**, 30229–30239 (2015).
 106. Haberland, H., Karrais, M. & Mall, M. A new type of cluster and cluster ion source. *Z. Für Phys. At. Mol. Clust.* **20**, 413–415 (1991).
 107. Haberland, H., Karrais, M., Mall, M. & Thurner, Y. Thin films from energetic cluster impact: A feasibility study. *J. Vac. Sci. Technol. A* **10**, 3266–3271 (1992).
 108. Rietveld, H. M. A profile refinement method for nuclear and magnetic structures. *J. Appl. Crystallogr.* **2**, 65–71 (1969).
 109. Liu, C. *et al.* Carbon Dioxide Conversion to Methanol over Size-Selected Cu₄ Clusters at Low Pressures. *J. Am. Chem. Soc.* **137**, 8676–8679 (2015).
 110. Graciani, J. *et al.* Highly active copper-ceria and copper-ceria-titania catalysts for methanol synthesis from CO₂. *Science* **345**, 546–550 (2014).

Chapter 2 Thermal stability of size-selected copper nanoparticles: effect of size, support and CO₂ hydrogenation atmosphere

Mo Li^{a,b}, Alexandre Borsay^{a,b}, Mostapha Dakhchoune^c, Kun Zhao^{a,b}, Wen Luo^{a,b,*}, Andreas Züttel^{a,b}

^a Laboratory of Materials for Renewable Energy (LMER), Institute of Chemical Sciences and Engineering (ISIC), Basic Science Faculty (SB), École Polytechnique Fédérale de Lausanne (EPFL) Valais/Wallis, Energypolis, Rue de l'Industrie 17, CH-1951 Sion, Switzerland

^b Empa Materials Science and Technology, CH-8600 Dübendorf, Switzerland

^c Laboratory of Advanced Separations (LAS), Institute of Chemical Sciences and Engineering (ISIC), Basic Science Faculty (SB), École Polytechnique Fédérale de Lausanne (EPFL) Valais/Wallis, Energypolis, Rue de l'Industrie 17, CH-1951 Sion, Switzerland

*Corresponding author: wen.luo@epfl.ch

Postprint version: this section has been published as a full-length article in *Applied Surface Science* **2020**, 510, 145439. DOI: 10.1016/j.apsusc.2020.145439.

Edit: caption numbers of figures, tables, and equations were edited to match the thesis chapter number.

Permission to reproduce: reproduced with permission from the publisher.

Abstract

Metal nanoparticles with a precisely controlled particle size distribution are ideal model catalysts for fundamental studies in catalysis. In this work, the thermal stability of size-selected Cu nanoparticles (Cu NPs) were deposited by magnetron sputtering, and their thermal stability was investigated using transmission electron microscopy and X-ray photoelectron spectroscopy. The influence of particle size, support, temperature, as well as CO₂ hydrogenation atmosphere was systematically studied. We found that at 220 °C in ultra-high vacuum (UHV), carbon-supported 4 nm Cu NPs sintered through particle migration while the 8 nm Cu NPs were relatively stable. As the temperature increased to 320 and 460 °C, both samples sintered severely, and Ostwald ripening was suggested to be the dominant mechanism. In addition, we observed that SiO₂ support can better stabilize Cu NPs upon heat treatment under both UHV and CO₂ hydrogenation atmosphere (1 mbar of 1:1 CO₂/H₂ mixture), due to the stronger interaction between SiO₂ and Cu compared to that between carbon and Cu. Furthermore, under a CO₂ hydrogenation atmosphere, the stability of Cu NPs is suggested to be influenced by the interplay of redispersion, agglomeration, and volatilization. These findings from model systems can offer new insights for understanding the deactivation of Cu-based catalysts.

2.1 Introduction

Supported metal nanoparticles (NPs) are widely used as heterogeneous catalysts for various industrial applications such as chemical production, energy conversion, and environmental protection.^{1,2} One of the major issues that limits their catalytic performance is the sintering of NPs due to their excess surface energy.³ At the microscopic level, the sintering of NPs is typically considered to follow two principal mechanisms^{4,5}: (i) particle migration, in which NPs diffuse and coalesce via Brownian motion, and (ii) Ostwald ripening, in which atomic species detach from smaller particles, diffuse on the support surface, and attach to larger particles. However, understanding the sintering behavior and determining the sintering mechanism of industrial catalysts is challenging, as detailed knowledge of their microscopic properties is precluded by their structural complexity, e.g., broad particle size distribution (PSD), highly irregular support structure, and different metal-support interactions.^{6,7}

To better understand the sintering mechanisms of NPs, well-defined model catalysts with metal NPs deposited on planar substrates have to be designed. Novel techniques, such as size selection using quadrupole or time-of-flight mass filter, enable the deposition of NPs with narrow PSDs and thus facilitate the understanding of catalyst stability.⁸ In combination with advanced microscopy and surface characterization techniques, important insights have been gained on the sintering behaviors of size-selected noble metal NPs (e.g. Pt^{9–11}, Pd^{12,13}, and Au^{14,15}). For instance, F. Yin et al.¹² compared the sintering of pinned (submonolayers on the edge of a substrate) and unpinned (multilayers in the center of a substrate) size-selected Pd NPs deposited on HOPG. They observed that pinned NPs were much more stable than unpinned ones and concluded that the sintering resistance is dependent on the particle deposition energy. Hu et al.¹⁵ studied the effects of the CO oxidation reaction on the sintering behavior of size-selected Au_{561±13}, Au_{923±20} and Au_{2057±45} clusters supported on amorphous carbon films. They found that under the same condition, the agglomeration of small clusters (Au_{561±13} and Au_{923±20}) was mediated by Ostwald ripening, whereas the larger Au_{2057±45} particles ripened through particle migration. However, K. Wettergren et al.⁹ demonstrated that Pt clusters with perfectly monomodal PSD are highly resistant to sintering due to the suppression of Ostwald ripening by the elimination of its main driving force (differences in chemical potential) via size-selection. While the important roles of particle size, support and reaction environment on the sintering of noble metal NPs have been successfully illustrated, systematic studies are still required for non-noble metals (e.g. Cu NPs).

Supported Cu catalysts have attracted great attention in recent years because of their potential to convert CO₂ to methanol, CO, and hydrocarbons via hydrogenation reactions.^{16–19} Specifically, size-selected Cu NPs have been developed not only as model catalysts for understanding reaction mechanisms but also as highly efficient catalysts for various reactions. Vajda et al.^{20,21} demonstrated that size-selected Cu₄ clusters were the most active low-pressure catalyst for catalytic hydrogenation of CO₂ to CH₃OH because of their low activation barriers for the key reaction steps. Vilar-Vidal et al.²² showed that Cu clusters with less than ≈10–13 atoms are highly active for reducing methylene blue, as they can mediate the electron transfer through the frontier orbital of their lowest unoccupied molecular orbital. Interestingly, Cu NPs of less than 5 nm size also showed a dramatic increase in CO₂ electrochemical reduction activity and selectivity.²³ However, the important details on catalyst deactivation,²⁴ in particular the impact of particle size, catalyst support, and reactive atmosphere on the thermal stability of Cu NPs, have not yet been resolved.

Herein, we prepared Cu NPs with different size distributions on carbon and SiO₂ supports using a nanoparticle deposition system which consists of a DC magnetron sputtering source and a quadrupole mass filter, and investigated their thermal stability under both ultra-high vacuum (UHV) and CO₂ hydrogenation conditions by means of transmission electron microscopy (TEM) and X-ray photoelectron spectroscopy (XPS). The thermal stability of Cu NPs with two different size distributions (4 and 8 nm) supported on carbon substrates was firstly studied under UHV to understand the size-dependent sintering mechanism. Subsequently, the

influence of carbon and SiO₂ supports were revealed. Finally, we discussed the effects of a CO₂ hydrogenation atmosphere on the stability of Cu NPs.

2.2 Experimental section

2.2.1 Substrates

Carbon- (150 mesh) and silica-coated copper TEM grids (200 mesh) were purchased from Electron Microscopy Sciences (PA, U.S.A.) and SPI Supplies (PA, U.S.A.), respectively. For STEM/EDX, carbon-coated gold TEM grids (300 mesh, from Electron Microscopy Sciences, PA, U.S.A.) were used instead of copper grids. Graphite foil (0.1 mm thickness) was obtained from Goodfellow (Cambridge, U.K.) and cut into 10 mm × 12 mm size before use. Boron-doped Si(100) wafers (resistivity of 0.1 ~ 0.5 Ω·cm, diced into 10 mm × 12 mm) was provided by EPFL-CMi (Lausanne, Switzerland). A SiO₂ layer of approximately 8 nm was deposited on the surface of a Si wafer using a Beneq TFS200 atomic layer deposition (ALD) system with bis(t-butylamino) silane and ozone as precursors at 300 °C.

2.2.2 Deposition of size-selected Cu nanoparticles (Cu NPs)

Size-selected Cu NPs were synthesized using a UHV nanoparticle deposition system (Mantis Deposition Ltd., Cambridge, U.K.) with a base pressure of 2×10^{-9} mbar following the Haberland concept of nanoparticle formation.²⁵ Briefly, Cu NPs were generated from a Cu target (99.99% pure, Kurt J. Lesker, U.S.A.) by a DC magnetron sputtering source (NanogenTrio, Mantis Deposition Ltd., Cambridge, U.K.) with Ar plasma and size-selected using a quadrupole mass filter (QMF, MesoQ, Mantis Deposition Ltd., Cambridge, U.K.) with a mass limit of 10⁶ amu. Next, the Cu NPs were deposited on substrates mounted on a sample holder with a rotatory manipulator under soft-landing conditions, i.e., with deposition energy lower than 1 eV per nanoparticle. The as-deposited samples were heated directly in the deposition chamber to 220, 320, and 460 °C for 30 min with a ramp of 10 °C/min. The heating temperature was measured by a K-type thermocouple attached to the radiative heating plate, after calibration using an infrared pyrometer (PUA2, spectral range of 2.0 to 2.6 μm, Calex Electronics Ltd., U.K.) which measured the temperature of the sample surface through a glass window on the deposition chamber. This method was used to prepare size-selected Cu NPs with or without heat treatment under UHV conditions. Following preparation, the samples were transferred out of UHV via a load lock with a pneumatic gate valve for further characterization.

2.2.3 Characterizations

TEM images of the Cu NPs deposited on carbon- or silica-coated copper grids were obtained from a FEI Tecnai Spirit microscope operating at 120 kV. STEM/EDX was performed with FEI Tecnai Osiris operating at 200 kV. The STEM images were recorded using a high-angle annular dark field (HAADF) detector, and the EDX elemental map was acquired using Bruker Super-X SDD EDX detectors. The XPS analysis was carried out in a UHV chamber (base pressure 1×10^{-9} mbar) equipped with a Mg Kα (1253.6 eV) X-ray source and Phoibos 100 (SPECS GmbH) hemispherical energy analyzer with a multichanneltron detector. The XPS spectra were recorded in the fixed analyzer transmission (FAT) mode using pass energies of 90 eV for the survey and 20 eV for the narrow scans. For near ambient pressure (NAP) XPS, a system equipped with a monochromatic Al Kα (1486.6 eV) X-ray source and Phoibos 150 NAP (SPECS GmbH) hemispherical energy analyzer with a 1-D delayed-line detector were used. The samples were fixed in the NAP cell of the system and heated to 320 °C in 1:1 CO₂/H₂ mixture at a total pressure of 1 mbar before XPS measurement. The XPS spectra were recorded in the FAT mode using pass energies of 30 eV for the survey and 10 eV for the narrow scans. The data were analyzed using CasaXPS software. Binding energies

were referenced to the Si 2p binding energy of SiO₂ (103.3 eV) or C1s binding energy of graphite (284.5 eV) for silica or carbon supported samples, respectively. Symmetric peaks were fitted with a mixture of Gaussian (70%) – Lorentzian (30%) (GL30) line shape, and asymmetric peaks with a Voigt-like A(0.4, 0.38, 20)GL(20) line shape (for the C1s peak of graphite), or an exponential-modified GL(30)T(1.5) line shape (for the Cu2p peaks of metallic Cu). The atomic ratio of different elements was calculated based on the corresponding peak area ratio after correction with the atomic sensitivity factors.

2.2.4 Micrograph analysis

The TEM images were firstly processed with an in-house Matlab code to uniform the background. Subsequently, ImageJ software²⁶ was used to convert the images to binary and perform particle analysis. The threshold to segment the binary image into features of interest and background was manually adjusted for each image, and the original and processed images were compared visually to eliminate the artifacts occurring during the process. For the statistics of Cu NPs, a circularity of 0.5 was allowed and the particles on the edges and corners were not counted.

For each sample, at least 4 different regions of the TEM grid were imaged at different magnifications. The average density of Cu NPs (number of CuNPs per μm^2) and the corresponding standard deviation of the density was evaluated using all micrographs at the same magnification for a given sample. The diameter of the Cu NPs was calculated from the measured projection area assuming the NPs are spherical. The particle coverage was calculated using the sum of the projection area of all particles in one region divided by the area of TEM imaging region. The average diameter and the related standard deviation were obtained from the total number of Cu NPs measured over at least 4 images taken from a single sample.

2.3 Results and discussion

2.3.1 Deposition of size-selected Cu NPs

A schematic illustration of the deposition system for synthesizing size-selected Cu NPs is shown in Figure 2.1. The Cu target was sputtered in Ar atmosphere (~ 0.1 mbar) to generate atomic Cu species, which underwent collisional condensation in the gas phase and aggregated to form nanoparticles in an aggregation zone with adjustable length. As Ar gas flow carries the Cu species away from the sputtering source, increasing the Ar flow rate decreases the size of Cu NPs by decreasing the residence time of the Cu species in the aggregation zone. During this process, He, an inert gas with high thermal conductivity, can also be introduced into the aggregation zone to reduce the size of Cu NPs by removing the heat in the aggregation zone and decreasing the probability of Cu collisions. Thus, by changing the flow rate of Ar and He, as well as the length of the aggregation zone, the production rate and the size distribution of the Cu NPs can be optimized. After an adiabatic expansion through a nozzle into the vacuum, Cu NPs stopped growing. As a substantial fraction of the generated Cu NPs were negatively charged,²⁵ filtering by the QMF could be performed based on their mass-to-charge ratio (m/z). Thus, by changing the parameters of the QMF, Cu NPs with the desired size were selected and deposited. For this work, 4 and 8 nm Cu NPs were deposited on different substrates using the deposition parameters listed in Table S2.1.

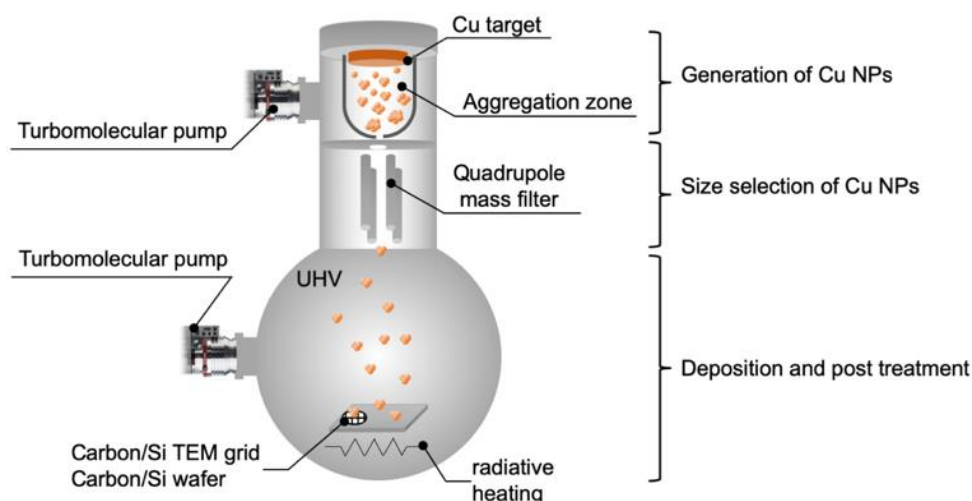


Figure 2.1 Schematic illustration of the size-selective nanoparticle deposition system.

2.3.2 Size-dependent thermal stability of Cu NPs

To study the influence of particle size on the sintering behavior, Cu NPs with an average size of ~ 4 and ~ 8 nm were deposited onto distinct carbon supports, and the coverage was controlled to be below one monolayer to avoid agglomeration and coalescence during the deposition. Carbon supports were selected based on the following considerations: (i) it is one of the most commonly used catalyst supporting materials, and (ii) the weak interactions between carbon and Cu NPs can preserve particle morphology under soft-landing conditions. The successful deposition of Cu NPs was confirmed by XPS and TEM. Compared to the XP spectrum of a blank carbon support, Cu 2p photoelectron peaks were clearly observed from both Cu NP samples (Figure S2.1). Figure 2.2 shows the TEM images and the corresponding PSD histograms of the as-prepared Cu NP samples, as well as images of the samples after annealing at different temperatures. For the 4 nm sample (Figure 2.2a), the average diameter determined from TEM images is 3.9 nm with a standard deviation of 1.4 nm. The relatively large standard deviation mainly results from the existence of particles larger than 4 nm shown as a shoulder at the larger diameter part of the histogram. These large particles were deposited due to the limits of QMF resolution²⁷ and the existence of neutral Cu NPs, which cannot be size-selected.^{28–30} Figure 2e shows results for the as-deposited 8 nm particles (which have a more uniform distribution than the 4 nm particles shown in Figure 2.2a), and the histogram has a Gaussian shape, rather than a lognormal distribution. Overall, the PSDs of 4 nm and 8 nm samples barely overlap and the Cu NPs appear to be randomly distributed on the support with no obvious coalescence, which is suitable for further thermal stability studies.

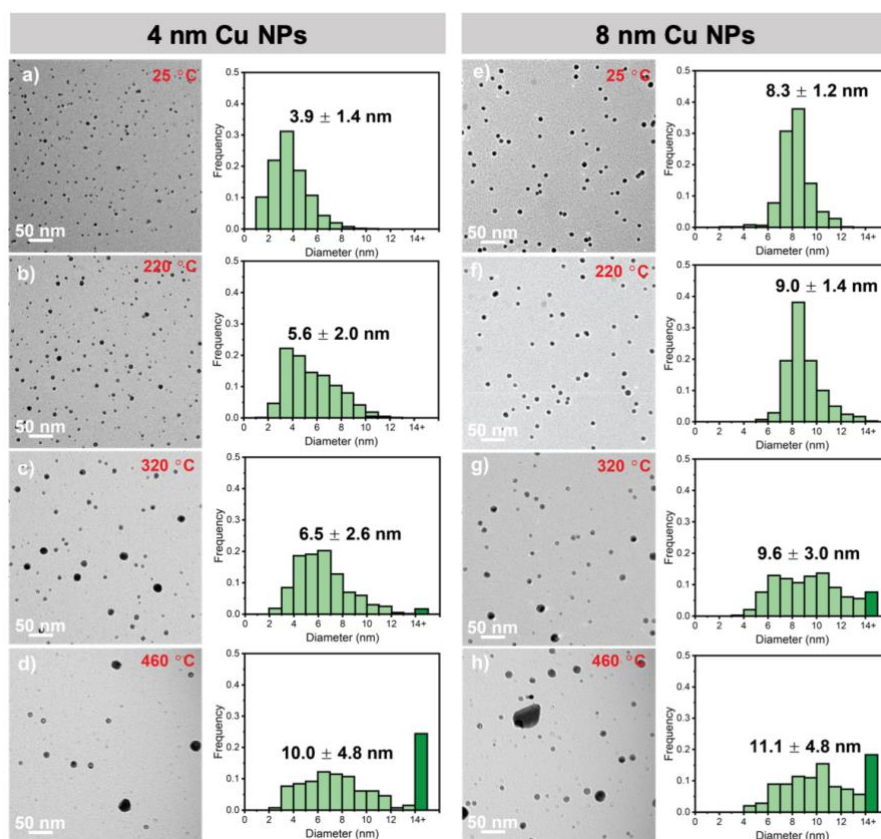


Figure 2.2 Representative TEM images and corresponding PSD histograms of Cu NPs size-selected at (a-d) 4 and (e-h) 8 nm deposited on carbon TEM grid. The mean particle diameter with standard deviation is given. The images correspond to Cu NPs (a, e) without heating, and (b-d, f-h) heated to 220, 320, and 460 °C for 30 min. Cu NPs with diameter larger than 14 nm are included in one bin (dark green) in the histogram.

After deposition, the 4 and 8 nm Cu NPs were heated to 220, 320, and 460 °C for 30 min, in the deposition chamber under UHV condition. The changes in particle morphology, size distribution, and coverage were firstly characterized using TEM. As shown in Figure 2.2b and f, at 220 °C the average diameter of the 4 nm sample increased by 44% (from 3.9 to 5.6 nm) and many more particles larger than 6 nm appeared compared to the sample at room temperature. In contrast, the 8 nm sample was relatively stable (<10% increase in the average diameter). The sintering of the 4 nm sample at this step should be attributed to migration and coalescence of small NPs, as Cu NPs with particle size smaller than 2 nm completely disappeared (Figure 2.2b). Moreover, Ostwald ripening is not expected to take place at 220 °C, since the energy required to move a Cu atom from a Cu particle to the surface of the support is very high — about the same as the heat of sublimation of Cu (337.4 kJ/mol).^{31,32} After further heating to 320 and 460 °C, both 4 nm (Figure 2.2c and d) and 8 nm (Figure 2.2g and h) samples sintered severely, as demonstrated by the significant increase in average diameter and large ratio of particles larger than 14 nm. To further understand the sintering mechanism, the histograms of the 4 and 8 nm samples were fitted using lognormal and Gaussian functions, respectively (Figure S2.2). The PSD curves of the 4 and 8 nm samples share a common feature: as the temperature increases, the distributions broaden and shift to larger sizes. However, for the 8 nm sample, smaller particles (4 ~ 6 nm) also appear at higher temperatures (Figure 2.2g, h, and Figure S2.2b). This indicates that the sintering of 8 nm Cu NPs is mediated by Ostwald ripening and the observed small particles result from the disintegration of particles. In this circumstance, the 4 nm sample may follow the same sintering mechanism, as the sublimation temperature decreases with a decrease in particle size.³³

Detailed morphological features of the Cu NPs are also important for the interpretation of the sintering mechanism. As shown in Figure 2.2c, d, g, and h, hollow particles appeared in both samples after annealing

at 320 and 460 °C. To gain further information about these hollow particles, STEM/EDX was carried out on a representative region of the 8 nm sample annealed at 460 °C. Figure 2.3 shows the TEM image, HAADF-STEM image, and the EDX elemental map, where a solid particle, a hollow particle, and two dark gray traces are marked for comparison. The solid particle shows clear contrast in the TEM and HAADF-STEM images and highly intense Cu signals in the EDX spectra (Figure S2.3), demonstrating that it is a Cu NP. On the other hand, despite that the Cu signal in the EDX elemental map and spectra (Figure 2.3c and Figure S2.3, respectively) is very weak for the hollow particle and the two dark gray traces, contrast features observed in the HAADF-STEM image indicate that these species are also Cu NPs. Therefore, these marked particles should be the different states of the Cu NP during the Ostwald ripening: the solid particle is a Cu NP after agglomeration, and the hollow particle and traces are the residues of Cu NPs that lose their atomic Cu species. Thus, the presence of these hollow particles confirms that at a high annealing temperature (> 320 °C), Ostwald ripening dominates the sintering of Cu NPs for both samples.

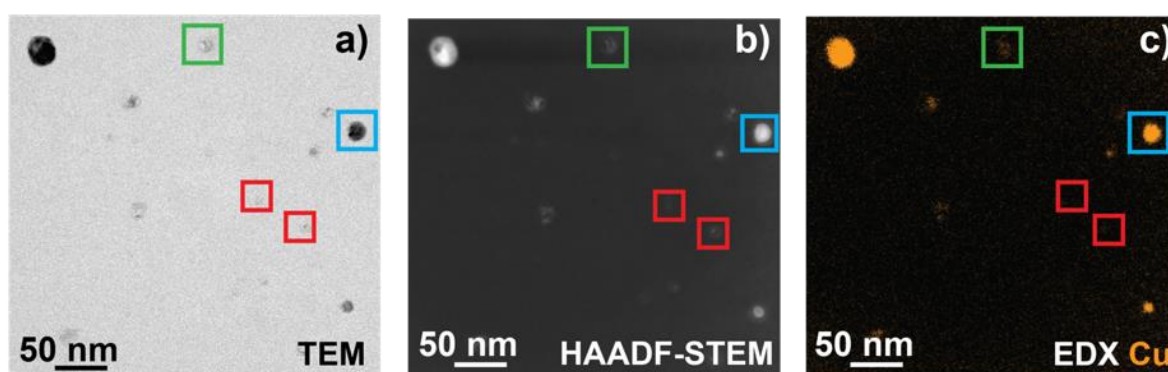


Figure 2.3(a) TEM image, (b) HAADF-STEM image, and (c) local Cu elemental map by EDX of a representative region for 8 nm Cu NPs heated to 460 °C.

Overall, the above results show the strong influence of particle size on the sintering behavior of Cu NP supported by carbon. These findings from the model system can also be adapted to real catalysts. For example, the absence of Cu NPs smaller than 2 nm after 30 min of annealing at only 220 °C suggests that, at the initial stage of the reaction, the deactivation of the Cu NPs supported on a weak-interaction support (e.g. carbon) may arise from the sintering of very small NPs, which are in many cases the most active and selective. On the other hand, although large particles are less efficient than the small particles due to their lower ratio of surface atoms, they are more stable (Figure 2.2f). Moreover, the disintegration of large Cu NPs can result in the formation of a certain number of small NPs (Figure 2.2e). Therefore, Cu NP catalysts with optimized particle size should be designed to achieve a balance between activity and stability. In addition, increasing the heating temperature led to dramatically faster sintering processes. Particularly, we observed high ratios of nanoparticles larger than 14 nm after annealing at 460 °C for 30 min, independent of the initial size of Cu NPs. As the formation of abnormally large particles significantly decreased the number of small nanoparticles and thus the active surface area, this could be the main reason for the deactivation of supported Cu catalysts during long-term and high-temperature operations.

2.3.3 Effect of support on thermal stability of Cu NPs

To investigate the influence of catalyst support on the thermal stability, 8 nm Cu NPs were deposited on SiO₂-coated TEM grids at room temperature and heated for 30 min in UHV at 320 and 460 °C, respectively. Figure 2.4 shows the corresponding TEM images and PSD histograms. By comparing Figure 2.4b and c with Figure 2.4a, we can observe that, upon heating, particles with a diameter larger than 14 nm appear, and the ratio of particles with a diameter smaller than 6 nm increases, indicating that SiO₂-supported Cu NPs also follow the Ostwald ripening mechanism. However, in stark contrast to the carbon-supported NPs, the average sizes of the SiO₂-supported ones decrease from 8.2 nm to 7.3 and 7.4 nm after heating to 320 and 460 °C, respectively. The difference in the standard deviation of the particle diameter for SiO₂-supported samples heated at different temperatures is also smaller compared to those of the carbon-supported samples, which is in agreement with the visual observation that the Cu NPs are still evenly distributed after annealing at 460 °C. The increased thermal stability of Cu NPs on SiO₂ supports could be attributed to a stronger metal-support interaction, despite that both of the carbon and SiO₂ support are considered to interact weakly with the NPs as they hardly react with the NPs at relatively low temperature.^{34–37} At high annealing temperatures (> 600 °C), Van den Oetelaar et al. found that Cu could diffuse into a thin layer of SiO₂ (10 nm) or form Cu silicide with a thick layer of SiO₂ (400-500 nm).^{35,36} In our case, high density of Cu NPs can still be observed on the surface of SiO₂, and no Cu silicide signal can be detected by XPS (Figure S2.4), indicating that 460 °C annealing did not lead to the diffusion of Cu or the formation of Cu silicide. Therefore, we expect that with stronger Cu-Si (2.1 eV) or Cu-O-Si bond energy (2.83 eV)³⁸ than the Cu-C bond energy (0.3 eV)³⁹, SiO₂ could better stabilize Cu NPs, as well as slow down the migration of Cu atoms/clusters on the support, thereby leading to the formation of nanoparticles with reduced size.⁴⁰

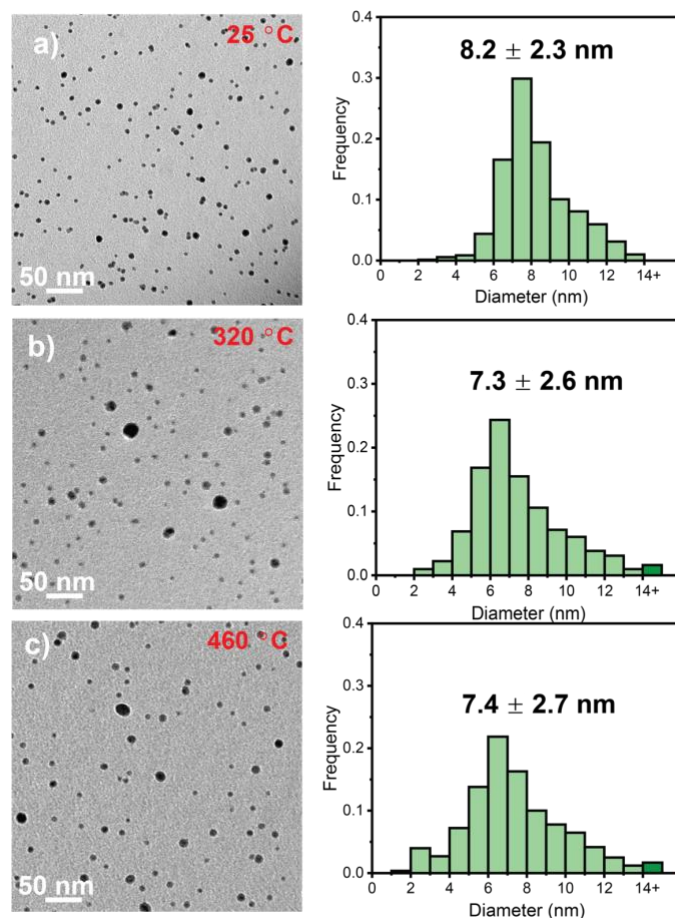


Figure 2.4 Representative TEM images and corresponding PSD histograms of Cu NPs size-selected at 8 nm deposited on a silica TEM grid. The mean particle diameter with standard deviation is given. The images correspond to Cu NPs (a) without heating, and heated to (b) 320 and (c) 460 °C for 30 min. Cu NPs with diameter larger than 14 nm are included in one bin (dark green) in the histogram.

2.3.4 Effect of CO₂ hydrogenation atmosphere on thermal stability of Cu NPs

To study the stability of Cu NPs under reaction conditions, carbon- and SiO₂-supported 8 nm samples were exposed to 1 mbar CO₂/H₂ (1:1) mixture at 320 °C in the NAP-cell of the NAP-XPS system. The TEM images and XPS data are summarized in Figures 2.5 and 2.6. Surprisingly, annealing in the CO₂ hydrogenation condition leads to a decrease in the average size of Cu NPs supported on both carbon and SiO₂, despite that particles larger than 14 nm are also present. Specifically, for the carbon-supported Cu NPs, after annealing in the CO₂/H₂ mixture at 320 °C, the PSD histogram is subject to a lognormal-like distribution with the highest frequency at 4 ~ 5 nm (Figure 2.5a and c). The average diameter of the particles is therefore only 5.6 nm, much smaller than the average diameter of 9.6 nm obtained for the sample annealed under UHV condition. For the SiO₂-supported Cu NPs, annealing at 320 °C in the CO₂/H₂ mixture leads to a similar PSD but with a slightly larger average diameter and standard deviation (7.7 ± 3.0 nm in Figure 2.5b) than the same sample annealed in UHV (7.3 ± 2.6 nm in Figure 4b). However, the histogram in Figure 2.5b has a more Gaussian-like distribution compared to carbon-supported samples annealed in UHV (Figure 2.2g) and the CO₂/H₂ mixture (Figure 2.5a). This implies that under the CO₂ hydrogenation atmosphere, SiO₂ can still better stabilize Cu NPs and preserve the PSD to the largest extent.

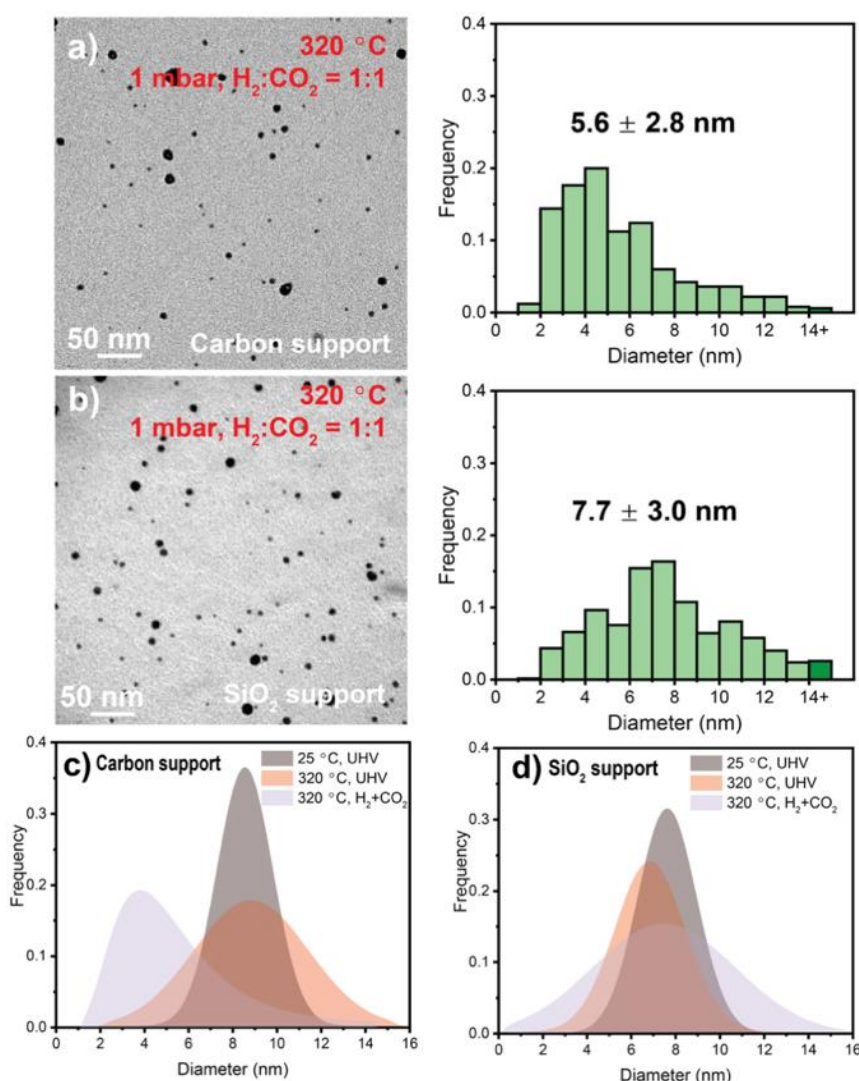


Figure 2.5 Representative TEM images and corresponding PSD histograms of Cu NPs size-selected at 7 nm and deposited on (a) carbon and (b) silica TEM grids after heating to 320 °C for 30 min in a CO₂/H₂ mixture. A comparison of PSD fittings is also shown for Cu NPs supported by (c) carbon and (d) silica at room temperature, heated to 320 °C in vacuum and in a 1 mbar CO₂/H₂ mixture.

The chemical state and the surface coverage of the two samples after annealing at 320 °C in the CO₂/H₂ mixture were characterized using XPS. Figure S2.5 shows the XP spectra of both samples: no difference in the Cu valence state is found for the two samples and the samples before and after annealing in the CO₂/H₂ mixture. In Figure 2.6, the Cu NP density and coverage calculated from TEM image analysis, and the Cu fractions on the support surface calculated from the Cu/support XPS peak area ratio, are compared for both carbon- and SiO₂-supported samples at different conditions (25 °C UHV, 320 °C UHV, and 320 °C CO₂/H₂ mixture). In both supports, the Cu NP coverage decreases as the temperature increases from 25 to 320 °C in UHV, and the CO₂ hydrogenation atmosphere further lowers the particle coverage, as shown in Figure 2.6b. This trend agrees well with the decreasing trends of normalized Cu fractions shown in Figure 2.6c. In addition, the decrease in the Cu fraction is smaller on the SiO₂ support than on the carbon support (Figure 2.6c), further confirming that Cu NPs are more stable on SiO₂. However, it should be noted that the CO₂ hydrogenation atmosphere has different effects on the Cu NP density for different supports. For the carbon-supported

sample, the CO₂/H₂ mixture leads to an increase in particle density and a decrease in particle coverage. In contrast, for the SiO₂-supported samples, both particle density and coverage decrease with the introduction of the CO₂/H₂ mixture.

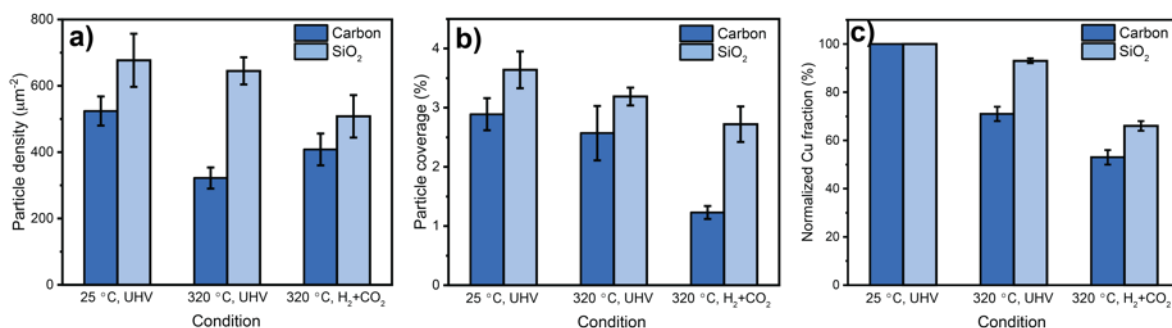


Figure 2.6 Comparison of (a) particle density (number of particles per μm²), (b) particle coverage calculated from TEM images, and (c) Cu/support (C or Si) XPS peak area ratio for 8 nm Cu NPs supported on carbon and SiO₂ under different conditions. The Cu/support ratio is normalized to the results measured at room temperature under UHV for the comparison on different supports.

It is well-known that the presence of reactants could significantly influence the sintering and re-dispersion of supported metal particles, as illustrated in Figure 2.7. For instance, it was found that the presence of O₂ or NO can accelerate the sintering of Pt NPs through the formation of volatile Pt-oxide species.⁴¹ Similarly, metal-gas species have also been found to assist ripening and disintegration in other systems, such as Rh-CO⁴², Pt-H⁴³, and Ni-OH³¹. For supported Cu catalysts, it is reported that Cu is structurally flexible under a CO₂ hydrogenation atmosphere, and the CO product from the reverse water-gas shift reaction (Figure 2.7, Step 1) could also promote the growth of crystalline Cu and lead to more severe sintering than annealing in UHV.^{44,45} Meanwhile, the formation of Cu carbonyl at high temperature in a CO environment (Figure 2.7, Step 2) was suggested to drive the evaporation of Cu.⁴⁶ In some cases, reactants can also interact with supports, further complicating the sintering process. For carbon-based supports, carbonyl and carboxylate groups could form on the surface of the carbon support due to the oxidization by CO₂,⁴⁷ which can serve as anchoring sites for metal atoms/clusters (Figure 2.7, Step 4).^{48,49} Therefore, the detached Cu atoms/clusters from the NPs on the carbon support may be redispersed (Figure 2.7, Step 3a), agglomerated and/or volatilized. While redispersion can lead to the smaller average diameter (Figure 2.5c) and the higher particle density (Figure 2.6a) of Cu NP samples annealed at 320 °C in the CO₂/H₂ mixture compared to samples annealed in UHV, the volatilization and agglomeration can result in the decrease of both particle coverage (Figure 2.6b) and the surface Cu fraction (Figure 2.6c). On the other hand, as SiO₂ is stable under the CO₂ hydrogenation environment, additional anchoring sites of Cu NPs is not expected. Therefore, agglomeration (Figure 2.7, Step 3b) and volatilization of Cu species may lead to the overall decreased particle coverage and particle density. Together, these results indicate that under the CO₂ hydrogenation atmosphere, the interplay of redispersion, agglomeration and volatilization drive the Cu NPs to the final states. These results also suggest that interactions between reactant and support should be considered when attempting to understand the sintering mechanisms. Moreover, our findings imply that functionalization of catalyst support with reactive gas can be an interesting method to improve nanoparticle dispersion.⁵⁰

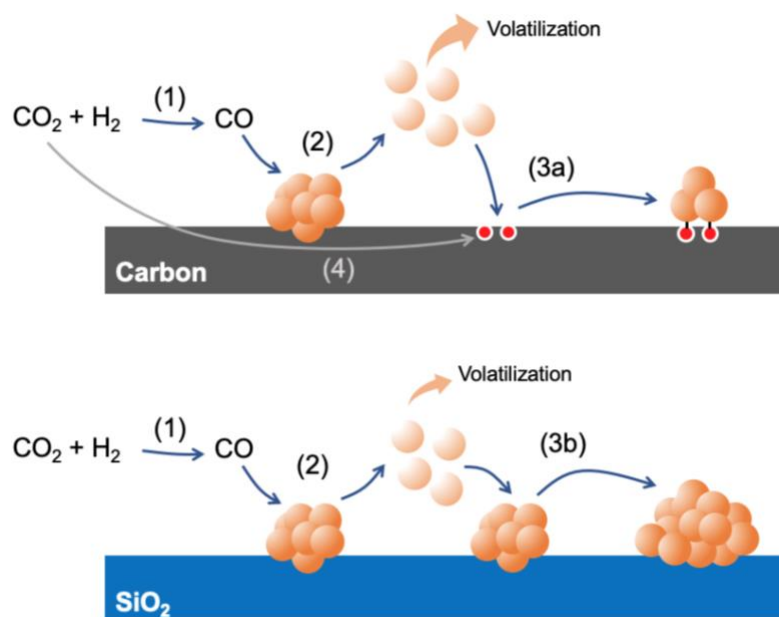


Figure 2.7 Schematic illustration of interplay of redispersion, agglomeration, and volatilization of Cu NPs supported by carbon and SiO_2 under CO_2 hydrogenation atmosphere. Step 1 is reverse water-gas shift reaction. Step 2 is the formation of Cu carbonyl species at high temperature in a CO environment. Step 3a and b represents the redispersion and the agglomeration of Cu NPs on carbon and SiO_2 , respectively. Step 4 is the formation of carbonyl and carboxylate groups as additional anchoring sites for Cu NPs redispersion.

2.4 Conclusions

In summary, we successfully prepared well-defined Cu model catalysts with narrow size distributions supported by carbon and SiO_2 using size-selective magnetron sputtering, and we investigated their thermal stability under both UHV and a CO_2 hydrogenation atmosphere. For carbon-supported Cu NPs, at 220 °C in UHV, the sintering of 4 nm Cu NPs appears to follow the particle migration mechanism while the 8 nm Cu NPs were found to be relatively stable. At 320 and 460 °C, the sintering of both samples was mainly mediated by Ostwald ripening. For Cu NPs on SiO_2 , their average particle size decreased upon heating in UHV due to the formation of small particles during the Ostwald ripening. The CO_2 hydrogenation atmosphere was found to induce the redispersion, agglomeration and valorization of Cu species and led to the decrease of Cu NP coverage on both substrates. We believe our results are of great importance for understanding the sintering of Cu-based catalysts and can provide guidelines for designing well-dispersed and stable catalysts.

References

1. Bell, A. T. The Impact of Nanoscience on Heterogeneous Catalysis. *Science* **299**, 1688–1691 (2003).
2. J. White, R., Luque, R., L. Budarin, V., H. Clark, J. & J. Macquarrie, D. Supported metal nanoparticles on porous materials. Methods and applications. *Chemical Society Reviews* **38**, 481–494 (2009).
3. Dai, Y., Lu, P., Cao, Z., Campbell, C. T. & Xia, Y. The physical chemistry and materials science behind sinter-resistant catalysts. *Chem. Soc. Rev.* **47**, 4314–4331 (2018).
4. Wynblatt, P. & Gjostein, N. A. Particle growth in model supported metal catalysts—I. Theory. *Acta Metallurgica* **24**, 1165–1174 (1976).
5. Hansen, T. W., DeLaRiva, A. T., Challa, S. R. & Datye, A. K. Sintering of Catalytic Nanoparticles: Particle Migration or Ostwald Ripening? *Acc. Chem. Res.* **46**, 1720–1730 (2013).
6. Goodman, D. W. Correlations between Surface Science Models and “Real-World” Catalysts. *J. Phys. Chem.* **100**, 13090–13102 (1996).
7. St.Clair, T. P. & Goodman, D. W. Metal nanoclusters supported on metal oxide thin films: bridging the materials gap. *Topics in Catalysis* **13**, 5–19 (2000).
8. Fischer, A., Kruk, R. & Hahn, H. A versatile apparatus for the fine-tuned synthesis of cluster-based materials. *Review of Scientific Instruments* **86**, 023304 (2015).
9. Wettergren, K. *et al.* High Sintering Resistance of Size-Selected Platinum Cluster Catalysts by Suppressed Ostwald Ripening. *Nano Lett.* **14**, 5803–5809 (2014).
10. Quinson, J. *et al.* Electrochemical stability of subnanometer Pt clusters. *Electrochimica Acta* **277**, 211–217 (2018).
11. Schweinberger, F. F. *et al.* Cluster Size Effects in the Photocatalytic Hydrogen Evolution Reaction. *J. Am. Chem. Soc.* **135**, 13262–13265 (2013).
12. Yin, F., Lee, S., Abdela, A., Vajda, S. & Palmer, R. E. Communication: Suppression of sintering of size-selected Pd clusters under realistic reaction conditions for catalysis. *J. Chem. Phys.* **134**, 141101 (2011).
13. Mao, B.-H. *et al.* Oxidation and reduction of size-selected subnanometer Pd clusters on Al₂O₃ surface. *J. Chem. Phys.* **138**, 214304 (2013).
14. Lim, D. C., Dietsche, R., Bubek, M., Ganteför, G. & Kim, Y. D. Oxidation and Reduction of Mass-Selected Au Clusters on SiO₂/Si. *ChemPhysChem* **7**, 1909–1911 (2006).
15. Hu, K.-J. *et al.* Atomic Resolution Observation of a Size-Dependent Change in the Ripening Modes of Mass-Selected Au Nanoclusters Involved in CO Oxidation. *J. Am. Chem. Soc.* **137**, 15161–15168 (2015).
16. Porosoff, M. D., Yan, B. & Chen, J. G. Catalytic reduction of CO₂ by H₂ for synthesis of CO, methanol and hydrocarbons: challenges and opportunities. *Energy Environ. Sci.* **9**, 62–73 (2016).
17. Su, X., Yang, X., Zhao, B. & Huang, Y. Designing of highly selective and high-temperature endurable RWGS heterogeneous catalysts: recent advances and the future directions. *Journal of Energy Chemistry* **26**, 854–867 (2017).
18. Saeidi, S., Amin, N. A. S. & Rahimpour, M. R. Hydrogenation of CO₂ to value-added products—A review and potential future developments. *Journal of CO₂ Utilization* **5**, 66–81 (2014).
19. Ronda-Lloret, M., Rothenberg, G. & Shiju, N. R. A Critical Look at Direct Catalytic Hydrogenation of Carbon Dioxide to Olefins. *ChemSusChem* **0**.
20. Liu, C. *et al.* Carbon Dioxide Conversion to Methanol over Size-Selected Cu₄ Clusters at Low Pressures. *J. Am. Chem. Soc.* **137**, 8676–8679 (2015).
21. Yang, B. *et al.* Copper Cluster Size Effect in Methanol Synthesis from CO₂. *J. Phys. Chem. C* **121**, 10406–10412 (2017).
22. Vilar-Vidal, N., Rivas, J. & López-Quintela, M. A. Size Dependent Catalytic Activity of Reusable Subnanometer Copper(0) Clusters. *ACS Catal.* **2**, 1693–1697 (2012).
23. Reske, R., Mistry, H., Behafarid, F., Roldan Cuenya, B. & Strasser, P. Particle Size Effects in the Catalytic Electroreduction of CO₂ on Cu Nanoparticles. *J. Am. Chem. Soc.* **136**, 6978–6986 (2014).
24. Prašnikar, A., Pavličič, A., Ruiz-Zepeda, F., Kovač, J. & Likozar, B. Mechanisms of Copper-Based Catalyst Deactivation during CO₂ Reduction to Methanol. *Ind. Eng. Chem. Res.* **58**, 13021–13029 (2019).
25. Haberland, H., Karrais, M. & Mall, M. A new type of cluster and cluster ion source. *Z Phys D - Atoms, Molecules and Clusters* **20**, 413–415 (1991).
26. Schneider, C. A., Rasband, W. S. & Eliceiri, K. W. NIH Image to ImageJ: 25 years of image analysis. *Nature Methods* **9**, 671–675 (2012).
27. Kunz, S. *et al.* Size-selected clusters as heterogeneous model catalysts under applied reaction conditions. *Phys. Chem. Chem. Phys.* **12**, 10288–10291 (2010).
28. Landi, G. T., Romero, S. A. & Santos, A. D. High density flux of Co nanoparticles produced by a simple gas aggregation apparatus. *Review of Scientific Instruments* **81**, 033908 (2010).

29. Kiss, L. B., Söderlund, J., Niklasson, G. A. & Granqvist, C. G. New approach to the origin of lognormal size distributions of nanoparticles. *Nanotechnology* **10**, 25–28 (1999).
30. Gojdka, B. *et al.* Study of cobalt clusters with very narrow size distribution deposited by high-rate cluster source. *Nanotechnology* **22**, 465704 (2011).
31. Sehested, J. Sintering of nickel steam-reforming catalysts. *Journal of Catalysis* **217**, 417–426 (2003).
32. *NIST Chemistry WebBook, NIST Standard Reference Database Number 69.* (National Institute of Standards and Technology).
33. Xiong, S. *et al.* Universal relation for size dependent thermodynamic properties of metallic nanoparticles. *Phys. Chem. Chem. Phys.* **13**, 10652–10660 (2011).
34. Fu, Q. & Wagner, T. Interaction of nanostructured metal overlayers with oxide surfaces. *Surface Science Reports* **62**, 431–498 (2007).
35. van den Oetelaar, L. C. A., Partridge, A., Toussaint, S. L. G., Flipse, C. F. J. & Brongersma, H. H. A Surface Science Study of Model Catalysts. 2. Metal–Support Interactions in Cu/SiO₂ Model Catalysts. *J. Phys. Chem. B* **102**, 9541–9549 (1998).
36. van den Oetelaar, L. C. A., van den Oetelaar, R. J. A., Partridge, A., Flipse, C. F. J. & Brongersma, H. H. Reaction of nanometer-sized Cu particles with a SiO₂ substrate. *Appl. Phys. Lett.* **74**, 2954–2956 (1999).
37. Backhaus-Ricoult, M., Samet, L., Thomas, M., Trichet, M.-F. & Imhoff, D. Changes in Cu–silica interfacial chemistry with oxygen chemical potential. *Acta Materialia* **50**, 4191–4204 (2002).
38. Ferullo, R. M. & Castellani, N. J. NCO adsorption over SiO₂ and Cu/SiO₂ cluster models from density functional theory. *Journal of Molecular Catalysis A: Chemical* **221**, 155–162 (2004).
39. Apai, G., Hamilton, J. F., Stohr, J. & Thompson, A. Extended X-Ray–Absorption Fine Structure of Small Cu and Ni Clusters: Binding-Energy and Bond-Length Changes with Cluster Size. *Phys. Rev. Lett.* **43**, 165–169 (1979).
40. Ruckenstein, E. Role of wetting in sintering and redispersion of supported metal crystallites. *Journal of Crystal Growth* **47**, 666–670 (1979).
41. Loof, P., Stenbom, B., Norden, H. & Kasemo, B. Rapid Sintering in NO of Nanometer-Sized Pt Particles on γ -Al₂O₃ Observed by CO Temperature-Programmed Desorption and Transmission Electron Microscopy. *Journal of Catalysis* **144**, 60–76 (1993).
42. Evans, J., Hayden, B., Mosselmans, F. & Murray, A. Adsorbate induced phase changes of rhodium on TiO₂(110). *Surface Science Letters* **279**, L159–L164 (1992).
43. Horch, S. *et al.* Enhancement of surface self-diffusion of platinum atoms by adsorbed hydrogen. *Nature* **398**, 134–136 (1999).
44. Sun, J. T., Metcalfe, I. S. & Sahibzada, M. Deactivation of Cu/ZnO/Al₂O₃ Methanol Synthesis Catalyst by Sintering. *Ind. Eng. Chem. Res.* **38**, 3868–3872 (1999).
45. Wang, Z.-Q. *et al.* High-Performance and Long-Lived Cu/SiO₂ Nanocatalyst for CO₂ Hydrogenation. *ACS Catal.* **5**, 4255–4259 (2015).
46. Bloom, H. Evidence for the Formation of a Copper Carbonyl. *Nature* **159**, 539–539 (1947).
47. Kelemen, S. R. & Freund, H. XPS characterization of glassy-carbon surfaces oxidized by O₂, CO₂, and HNO₃. *Energy Fuels* **2**, 111–118 (1988).
48. García-García, F. R., Gallegos-Suarez, E., Fernández-García, M., Guerrero-Ruiz, A. & Rodríguez-Ramos, I. Understanding the role of oxygen surface groups: The key for a smart ruthenium-based carbon-supported heterogeneous catalyst design and synthesis. *Applied Catalysis A: General* **544**, 66–76 (2017).
49. Bowden, B. *et al.* The deposition of metal nanoparticles on carbon surfaces: the role of specific functional groups. *Faraday Discuss.* **208**, 455–470 (2018).
50. Yao, Y. *et al.* High temperature shockwave stabilized single atoms. *Nat. Nanotechnol.* **14**, 851–857 (2019).

Supporting information

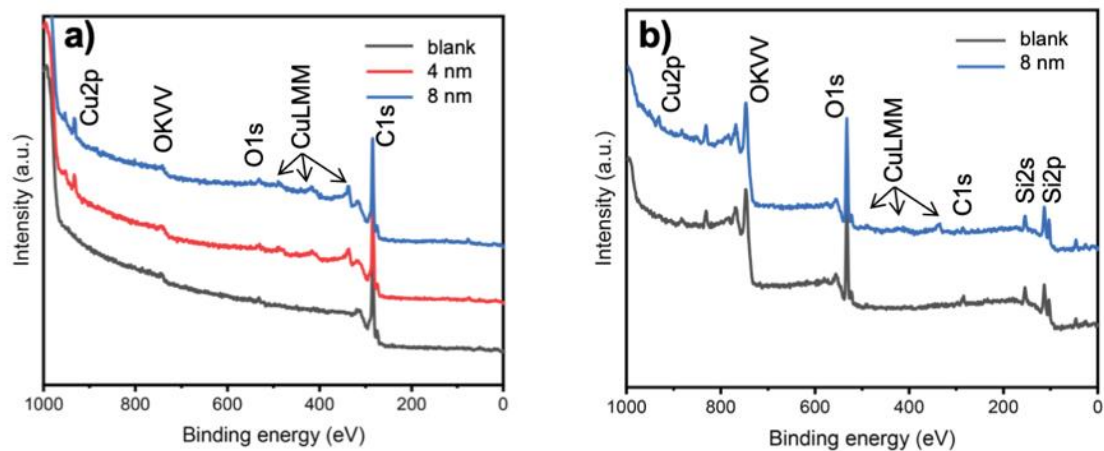


Figure S2.1 (a) Survey XP-spectra of CuNPs size-selected at 3 and 7 nm and deposited on graphite sheet. (b) Survey XP-spectra of CuNPs size-selected 7 nm and deposited on SiO₂/Si(100).

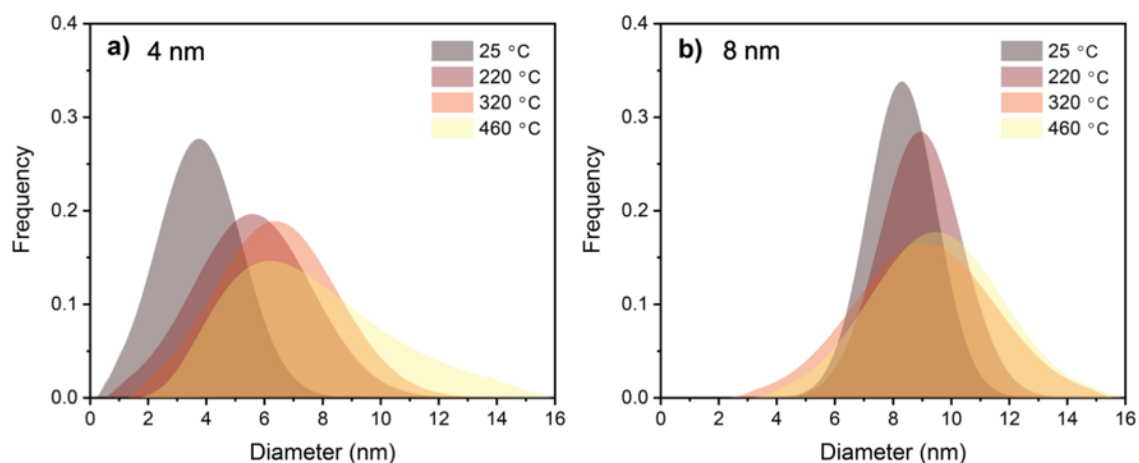


Figure S2.2 PSD fittings of Cu NPs size-selected at (a) 4 and (b) 8 nm heated to different temperatures. The 4 nm Cu NPs are fitted with a lognormal function while the 8 nm Cu NPs are fitted with a Gaussian function. Particles larger than 14 nm are excluded for the fittings.

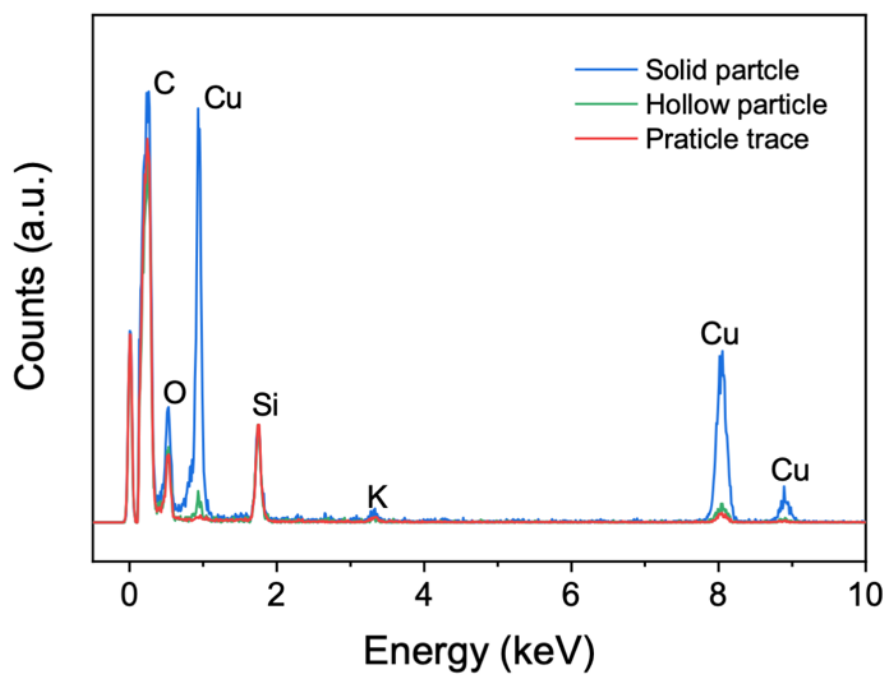


Figure S2.3 EDX spectra of the solid particle, hollow particle, and one gray particle trace shown in Figure 3. The spectra are normalized by the intensity of Si.

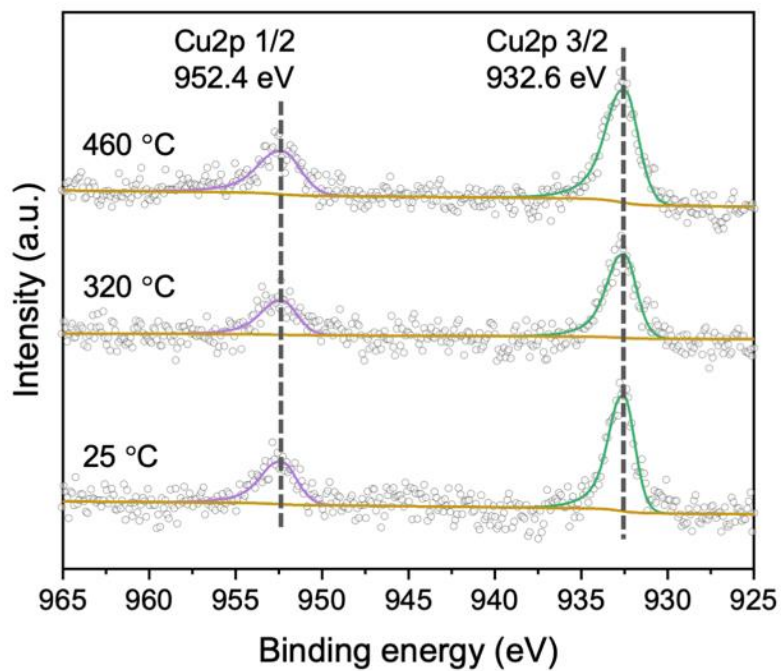


Figure S2.4 Cu₂p XP spectra of CuNPs supported by SiO₂/Si(100) at room temperature and after heated to 320 and 460 °C for 30 min under UHV.

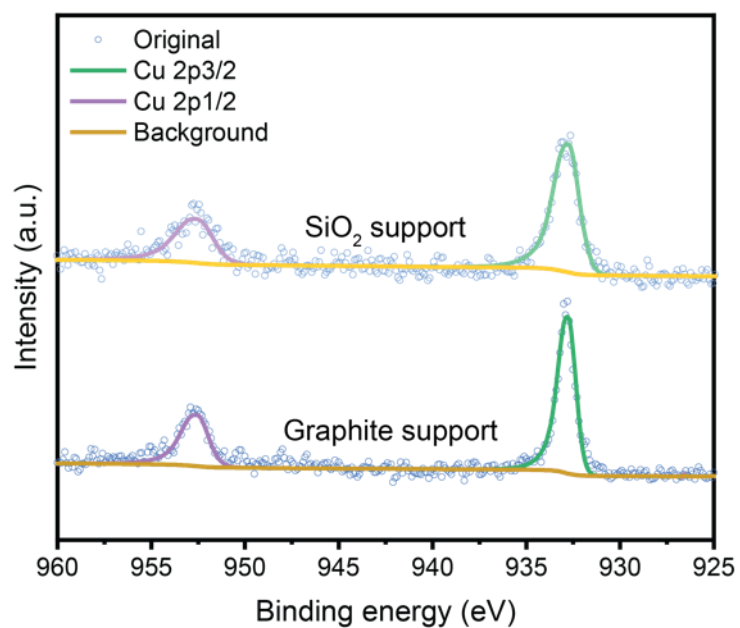


Figure S2.5 Cu2p XP spectra of 8 nm Cu NPs supported by graphite and SiO₂/Si(100) after heated to 320 °C for 30 min under CO₂/H₂ mixture.

Table S2.1 Operational parameters for the deposition of 4 and 8 nm CuNPs.

Sample	Sputtering source				QMF		
	Current/ mA	Ar flow rate/mLmin ⁻¹	He flow rate/mLmin ⁻¹	Target distance/mm	DC voltage/V	AC voltage/V	Frequency/kHz
4 nm	50	60	80	40	1.06	106.45	13.787
8 nm	50	50	0	46	1.06	106.45	3.864

Chapter 3 Near ambient-pressure X-ray photoelectron spectroscopy study of CO₂ activation and hydrogenation on indium/copper surface

Mo Li^{a,b}, Wen Luo^{a,b,c,*}, Andreas Züttel^{a,b}

^a Laboratory of Materials for Renewable Energy (LMER), Institute of Chemical Sciences and Engineering (ISIC), Basic Science Faculty (SB), École Polytechnique Fédérale de Lausanne (EPFL) Valais/Wallis, Energypolis, Rue de l'Industrie 17, CH-1951 Sion, Switzerland

^b Empa Materials Science and Technology, CH-8600 Dübendorf, Switzerland

^c School of Environmental and Chemical Engineering, Shanghai University, 99 Shangda Road, Shanghai 200444, China

* Corresponding author: wen.luo@epfl.ch

Postprint version: this section has been published as a full-length article in *Journal of Catalysis* **2021**, 395, 315-324. DOI: 10.1016/j.jcat.2021.01.010.

Edit: caption numbers of figures, tables, and equations were edited to match the thesis chapter number.

Permission to reproduce: reproduced with permission from the publisher.

Abstract

Indium-based catalysts exhibit excellent performance for CO₂ hydrogenation to methanol, yet their nature and chemical evolution under reaction conditions are still elusive, thus hindering an understanding of their reaction mechanism. In this work, near ambient-pressure X-ray photoelectron spectroscopy (NAP-XPS) is employed to investigate the chemical properties and the catalytic role of indium/copper model catalysts under CO₂ hydrogenation conditions. We found that the deposition of In on the surface of a Cu foil led to the formation of Cu-In alloy, whereas upon CO₂ exposure, In was partially oxidized to In₂O_{3-x} and Cu remains metallic. Due to the presence of In₂O_{3-x}, CO₂ was activated on the surface of In/Cu samples mainly in the form of carbonate. In addition, compared with the pure In foil reference, both the fraction of oxygen vacancies and the coverage density of carbonate were higher on the In/Cu samples, indicating the promotion effect of Cu-In alloy in the activation of CO₂. These results reveal the evolution of the active sites of indium/copper catalysts and inspire the design of advanced In-based bimetallic catalysts for CO₂ hydrogenation.

3.1 Introduction

In the framework of research devoted to meeting the growing energy demands, the catalytic conversion of CO₂ to value-added chemicals and fuels with the assistance of H₂ has been proven to be a feasible and promising approach, as it both mitigates global warming caused by conventional fossil fuels and provides a solution to the storage of renewable energy.^{1–3} Although the process is attractive, its scale-up remains a great challenge due to the lack of efficient and selective catalysts, as well as its unclear reaction mechanism. Thus, understanding the activation and reduction of CO₂ on a catalyst surface is imperative for the development of advanced catalyst and the eventual industrialization of CO₂ hydrogenation.

Recently, In₂O₃ has emerged as a promising material for converting CO₂ to methanol via hydrogenation.^{4–7} For example, using pure In₂O₃ as catalyst, the reverse water-gas shift (RWGS) reaction can be completely suppressed, leading to a nearly 100% methanol selectivity (5 MPa, 16 000 h^{–1} GHSV, 200–300 °C). Density functional theory (DFT) calculations have suggested that the presence of oxygen vacancies on the In₂O₃ surface favors the methanol synthesis pathway.^{8,9} The existence of oxygen vacancies has also been proven experimentally using electron paramagnetic resonance (EPR), temperature-programmed desorption (CO₂-TPD), and Raman spectroscopy, *etc.*^{5,7,10} Recently, an *operando* XRD-XAS study directly correlated the activation of In₂O₃ catalysts to the formation of oxygen vacancies, and deactivation to the appearance of over reduced metallic In.¹¹ Nevertheless, surface-sensitive studies are still required to reveal the chemical state of In₂O₃ and adsorbates under reaction conditions.

Although In₂O₃ is highly selective and durable for CO₂ hydrogenation, its low H₂-splitting ability limits its CO₂ conversion rate. Therefore, metals such as Cu^{12–15}, Pd^{16–19}, Ni²⁰, and Au²¹ have been integrated with In₂O₃-based catalysts, with the intention to enhance the H₂-splitting ability. However, the formation of alloys between In and other metals (*e.g.*, Cu or Pd) makes it difficult to identify the catalytic sites and the reaction mechanism under the CO₂ reduction environment. For example, Shi *et al.* suggested that the formation of Cu₁₁In₉ improves the dissociation of H₂ to atomic hydrogen, which then participates in CO₂ hydrogenation to methanol.¹³ However, Yao *et al.* proposed that metallic Cu sites adsorb and dissociate H₂ for the hydrogenation of adsorbed CO₂ on the surface of In₂O₃.¹⁵ Similar arguments also hold for Pd-In₂O₃ catalytic systems. These arguments for the function of the bimetallic phase might originate from the extensively employed *ex situ* characterization techniques on these bimetallic catalysts after exposure to air, which is exclusively undesirable for bimetallic alloy phases and oxygen vacancies due to the potential oxidation. Therefore, it is important to investigate In₂O₃-based bimetallic catalysts (*i.e.*, Cu-In) under CO₂ hydrogenation conditions using *in situ* techniques to understand the structural and compositional evolution of the catalysts.

In this work, the activation of CO₂ on bimetallic In/Cu model catalysts were systematically studied using near ambient-pressure X-ray photoelectron spectroscopy (NAP-XPS). We prepared a series of samples by depositing In on Cu foil, and then probed their surface properties upon exposure to CO₂ and CO₂/H₂ mixtures at different temperatures. We quantified the relative amount of lattice and defect oxygen under different conditions, and observed that the Cu-In alloy corresponded to a higher density of oxygen vacancies, which resulted in a higher coverage density of activated CO₂ in the form of carbonate compared with the pure In reference. Furthermore, we revealed the stability of the oxygen vacancies on In/Cu surfaces at up to 600 K. Based on our experimental observations, we discussed the synergy between the Cu-In alloy phase and the

oxygen vacancies from $\text{In}_2\text{O}_{3-x}$ sites for highly active CO_2 hydrogenation reactions. Overall, our study provides fundamental details of the relationship between the surface property and the performance of Cu-In bimetallic catalysts for CO_2 hydrogenation.

3.2 Experimental section

In/Cu model catalysts were prepared in the preparation chamber (base pressure 2×10^{-10} mbar) of a laboratory-based NAP-XPS system (SPECS GmbH). A polycrystalline Cu foil (Goodfellow, purity 99.9%, 0.125 mm thick, size 1 cm^2) was cleaned by electrochemical polishing in 85 wt.% H_3PO_4 solution at 40 mA for 60 s with another Cu foil as counter electrode before being introduced into the NAP-XPS system. Prior to the In deposition, at least three cycles of Ar^+ sputtering (1.5×10^{-5} mbar Ar, 1 keV, 15 min) and vacuum annealing (850 K, 15 min) were applied to the Cu foil until the level of impurities (O 1s and C 1s) was below the XPS detection limit. In was deposited on the Cu foil from a molybdenum crucible filled with In pellets (Alfa Aesar, purity 99.99%) using an e-beam evaporator (EBE-4, SPECS GmbH) by electron bombardment. The deposition rate was kept constant by maintaining a constant flux current monitored using a built-in flux electrode. A flux current of 10 nA roughly corresponds to a deposition rate of 0.003 ML/s. The morphology of the samples was characterized by a FEI Teneo scanning electron microscope (SEM) operating at a high voltage of 1 kV and a 25 pA beam current, with a working distance of 5–7 mm.

All UHV- and NAP-XPS measurements were carried out in an analysis chamber (base pressure 2×10^{-10} mbar) equipped with a microfocus, monochromatic Al $K\alpha$ ($h\nu = 1486.74$ eV) X-ray source, and a differentially pumped hemispherical energy analyzer (PHOIBOS 150 NAP, SPECS GmbH) with a series of electrostatic lenses. For NAP-XPS measurements, the sample is placed in a NAP cell with an X-ray transparent Si_3N_4 window and a 300 μm aperture for the photoelectrons to pass through. With this configuration, XPS measurements can be performed in gas environments up to 25 mbar. Research-grade CO_2 (4.5, PanGas) and H_2 (5.0, PanGas) were used for all experiments and the flowrates were regulated with precise mass flow controllers (GF40, Brooks). The purity of the gases was confirmed with a residual gas analyzer (MKS e-Vision 2) installed on the pre-lens stage. The pressure in the NAP cell was measured with a gas-independent capacitance gauge (CMR361, Pfeiffer Vacuum). An e-beam heater was placed on the back of the NAP cell, allowing sample heating up to 600 K. After each sample loading, the position of the sample was optimized to maximize the intensity of the signal. For all core level regions, a pass energy of 20 eV was used. As the samples were conductive, no charge compensation was required. For all clean samples (before NAP-XPS measurements), the valence band (VB) region spectra were also measured for energy scale calibration with Fermi-edge. The XPS spectra were analyzed with CasaXPS software after Shirley or linear type background subtraction. Symmetric peaks were fitted using a Gaussian/Lorentzian product formula with suitable G/L ratios, and asymmetric peaks were fitted with the three-parameter Lorentzian asymmetric line shape. For quantitative analysis, Scofield relative sensitivity factors (RSFs) were used for correcting the peak areas.²² The coverage of In was estimated using Equation 3.1²³ based on quantification of XPS results.

$$\frac{I_o}{I_s} = \frac{I_o^\infty}{I_s^\infty} \frac{1 - \exp(-t/\lambda_{\text{In}}^I(E_o) \cos \theta)}{\exp(-t/\lambda_{\text{In}}^I(E_s) \cos \theta)}$$

Equation 3.1 Quantification of thin film thickness using XPS.

Where I_o and I_s are the intensities of the In overlayer and the Cu substrate, given by corresponding XPS core-level peak areas corrected by the RSFs. I_o^∞ and I_s^∞ are the signal intensities for infinitely thick layer of In and Cu, respectively. $\lambda_{in}^l(E_o)$ and $\lambda_{in}^l(E_s)$ are the inelastic mean free path of the photoelectrons moving through the In layer with energies E_o and E_s , obtained from the NIST Electron Inelastic-Mean-Free-Path Database.²⁴ θ is the photoelectron emission angle and t is the thickness of In overlayer.

3.3 Results

3.3.1 Surface properties of In/Cu model catalysts

To investigate the interactions between Cu and In, we first prepared four model samples with varied coverage of In from 0.2 to 2.0 monolayer (ML) on Cu foil, along with pure Cu and In foils as references. The SEM images (Figure S3.1) show that, by means of e-beam evaporation, In initially (0.2 ML) aggregated on the defective edge of the Cu surface, and did not present on the flat surface. As the In coverage increases to 0.9 ML, In nanoparticles can be observed on the flat surface but still distribute mainly on the slightly grooved areas (formed during the electrochemical polishing). On the sample with 1.4 ML In, In nanoparticles are homogeneously distributed. With further increase of In coverage up to 2.0 ML, the In domains interconnected with each other. This growth behavior is similar to that of many other bimetallic systems^{25–27}. Figure 3.1 shows the Cu 2p_{3/2} and In 3d_{5/2} XPS spectra from the Cu, In and In/Cu surfaces taken at room temperature under UHV. With the increase in the amount of deposited In, the binding energy (BE) of the Cu 2p_{3/2} peaks gradually increased from 932.7 eV for Cu foil to 933.06 eV for a sample with 2.0 ML In (Figure 3.1a). The primary LMM Auger transition of Cu, which originates from the 3d⁸ configuration due to a single L₃ (2p_{3/2}) core-hole decay involving two M₄₅ (3d) electrons²⁸, is shown in Figure 3.1c. The final state splitting components, namely ³F, ¹D, ¹G and ¹S, can be clearly identified, while the ³P is not visible due to its low intensity. Furthermore, another Auger peak arising from the L₂L₃M₄₅ Coster-Kronig transitions is also observed.²⁹ Because we did not observe any O 1s peak after the In deposition (Figure S3.2), and the peak shape of Cu 2p and Cu LMM Auger peaks (Figure 3.1a and c) remained the same as those of metallic Cu, we can exclude the oxidation of Cu as the reason for the BE shift. In accordance with the results in Figure 1a, Figure 3.1b shows that decreasing the amount of In leads to a decrease in the BEs of In 3d_{5/2}: from 443.8 eV for pure In foil to 443.6 eV for 0.2 ML In on Cu. In addition, the valence band spectra (Figure S3.3) show the variation of the density of states (DOS) for Cu with different In coverages compared to the pure elements. The Cu d band peak shifts gradually from 2.8 eV to 3.2 eV with the increase of In coverage. This trend is similar to that of the Au-In and Au-Sn alloys systems and has been suggested as the result of the s-d hybridization of the s and d orbitals of Au with s and p orbitals of the main-group atoms upon alloying.^{30,31} These results, along with the observations in the core-level BE shifts, can confirm the formation of Cu-In alloys. Although this phenomenon was not reported for Cu-In samples, the BE shifts of the Pd and In peaks due to the formation of Pd-In alloys have been observed.³² Additionally, one may also notice that the bulk plasmon loss peak associated with the In 3d_{5/2} core level at ~455.5 eV (Figure S3.4) of the pure In sample^{33,34} does not exist on any In 3d spectra of the In/Cu samples. This implies that In exists in a highly dispersed form after deposition on Cu, which further supports the formation of Cu-In alloy. The In MNN Auger peaks in Figure 3.1d result from two different final states with a 4d⁸ configuration, namely M₅ (3d_{5/2}) and M₄ (3d_{3/2}) core-hole decay involving two N₄₅ (4d) electrons. Both Auger transitions consist of one strong line corresponding to the

(1D_2)(1G_4) electron configuration and weak asymmetric peaks on the high energy side.³⁵ The weak peaks in the $M_5N_{45}N_{45}$ line can be assigned to 3P_2 and $^3F_{2,3}$ configurations, while in the $M_4N_{45}N_{45}$ line, the can be assigned to $^3F_{2,3}$ and 3F_4 configurations.³⁵ Similar to Cu, the shape of the In MNN Auger peaks remains unchanged for all samples, further confirming the metallic state of In.

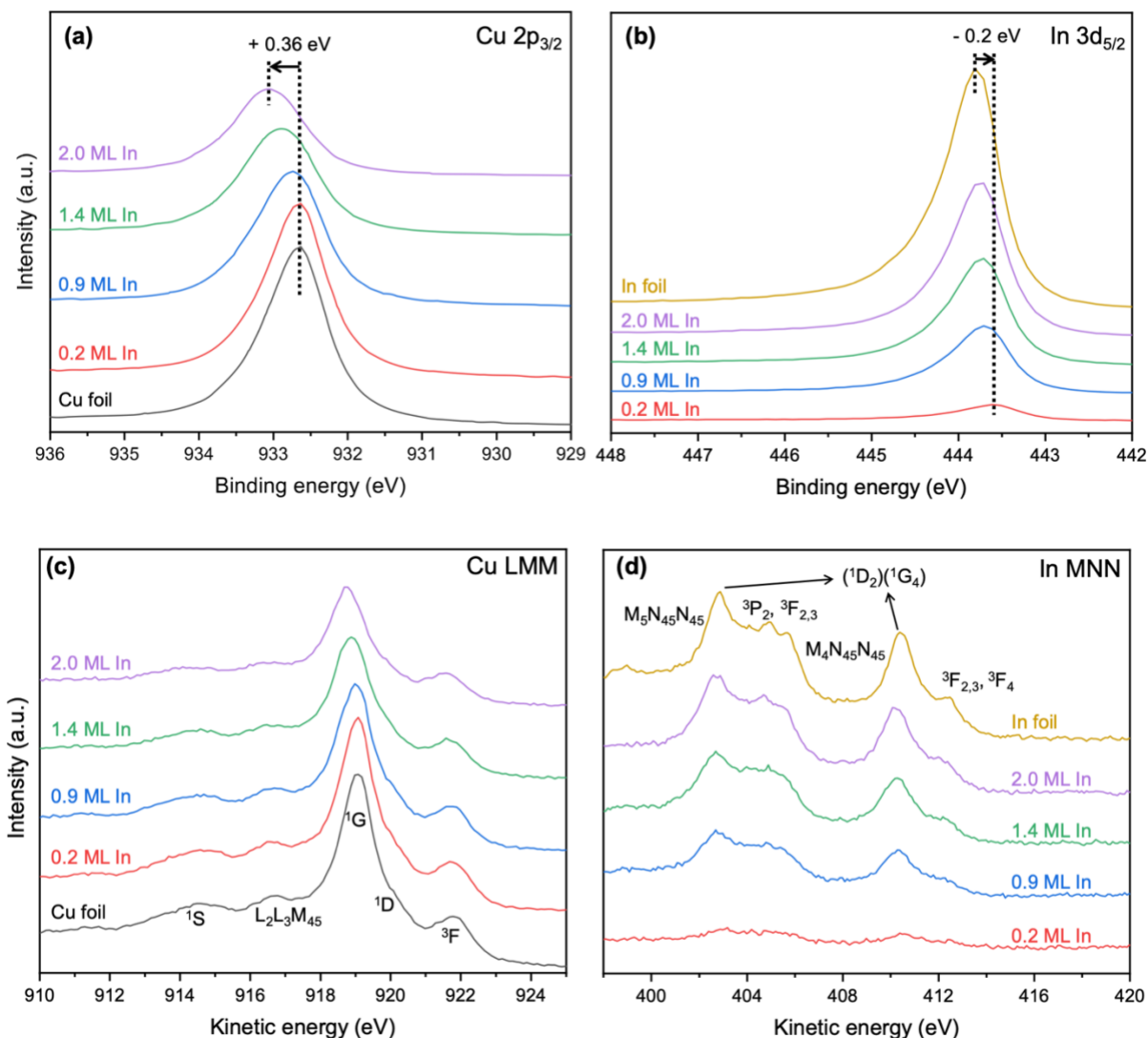


Figure 3.1(a, b) XPS spectra of the Cu 2p_{3/2}, In 3d_{5/2} regions and (c, d) X-ray excited Cu LMM and In MNN Auger peaks of Cu foil, In foil, and In/Cu samples with different surface In coverage. Spectra are unsmoothed data. The In coverage is indicated by monolayer (ML) calculated from the peak area ratio of In 3d_{5/2} and Cu 2p_{3/2} after a Shirley type background subtraction and correction by the corresponding RSFs.

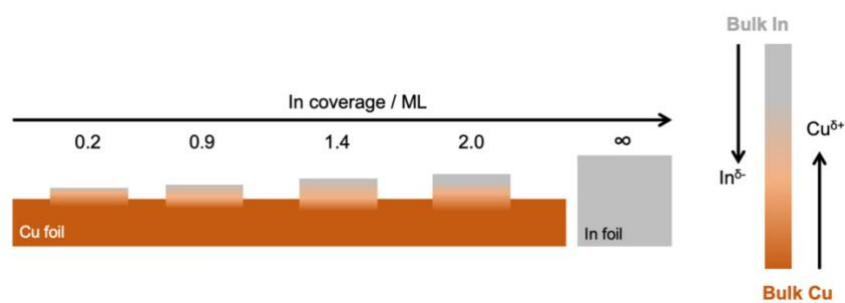


Figure 3.2 Schematic illustration of the Cu-In charge transfer model for Cu-In alloying on Cu foil surface.

To qualitatively interpret the relative BE shifts with the change in In surface coverage, a simple charge transfer model of Cu-In coordination near the surface is proposed (Figure 3.2). With the deposition of In, Cu was more positively charged in the In-coordinated state relative to the “pure Cu” state and thus showed an increased Cu 2p BE. In turn, increasing the In coverage resulted in the decreased ratio of Cu-In coordination, thus the In 3d BE value of high In coverage sample approached that of the In foil. This model indicates that the formation of Cu-In surface alloy induces a flow of electrons from Cu to In. Notably, the electronegativity of Cu (1.90) is slightly higher than that of In (1.78), therefore electron flow from In to Cu is expected. Such counterintuitive results were explained earlier by Goodman *et al.*: the charge transfer in surface alloys can be contrary to that of bulk alloys due to the anisotropic character of a surface that changes the relative electronegativities of metal atoms.³⁶ Furthermore, the BE shifts of surface alloys can also be influenced by other factors during the photoelectron emission process. For example, the geometric contribution caused by lower effective coordination of surface adlayer than the bulk material could decrease the BE of the adlayer element³⁷, orbital rehybridization may decrease the BEs of both adlayer and substrate elements^{38,39}, and the final state effects partially cancel the abovementioned initial state contributions^{40,41}. Overall, these factors lead to the observed BE shifts of Cu and In.

3.3.2 NAP-XPS in the presence of CO₂ at 300 K

Next we exposed the clean Cu, In and In/Cu surfaces to 0.2 mbar CO₂ at 300 K to investigate the effect of CO₂ on the surface properties. The Cu 2p_{3/2} and In 3d_{5/2} spectra collected from the different surfaces are shown in Figure 3.3a and b. Compared with the spectra obtained under UHV, introducing CO₂ did not change the peak shape of Cu 2p_{3/2} (Figure 3.3a) or Cu LMM (Figure S3.5a), indicating that Cu can maintain its metallic state.⁴² In contrast, the peak shape of In 3d_{5/2} was significantly changed upon CO₂ exposure: additional peaks contributed by In oxides can be observed at a higher BE (Figure 3.3b). The deconvolution of the In 3d_{5/2} region using a multipeak fitting indicates that the fraction of the oxidized In is dependent on the amount of deposited In. As shown in Figure 3.2b, a small amount of In (0.2 ML) was completely oxidized, whereas the increased the deposition amount of In led to an increase in the remaining ratio of metallic In from ~47% for the 0.9 ML In sample to ~65% for the In foil sample. Meanwhile, the Auger peaks in Figure S3.5b also exhibited hybridized characteristics of metallic and oxidized In.⁴³ Notably, as In is oxidized by CO₂, the In concentration in the Cu-In alloy should be smaller than that before CO₂ introduction. Such a phase separation can be confirmed by the slight shift in the Cu 2p_{3/2} peak to a lower BE (Figure 3.3a). Nevertheless, the metallic phase of Cu and In remains to be alloyed, as the peak shifts of Cu 2p_{3/2} to a higher BE and In 3d_{5/2} to a lower BE

compared with the pure metal references are consistent with the results from UHV measurement. Together, these results indicate that at room temperature, Cu can maintain its metallic state upon CO₂ exposure while In can be partially oxidized, leading to the partial de-alloying of Cu-In alloys.

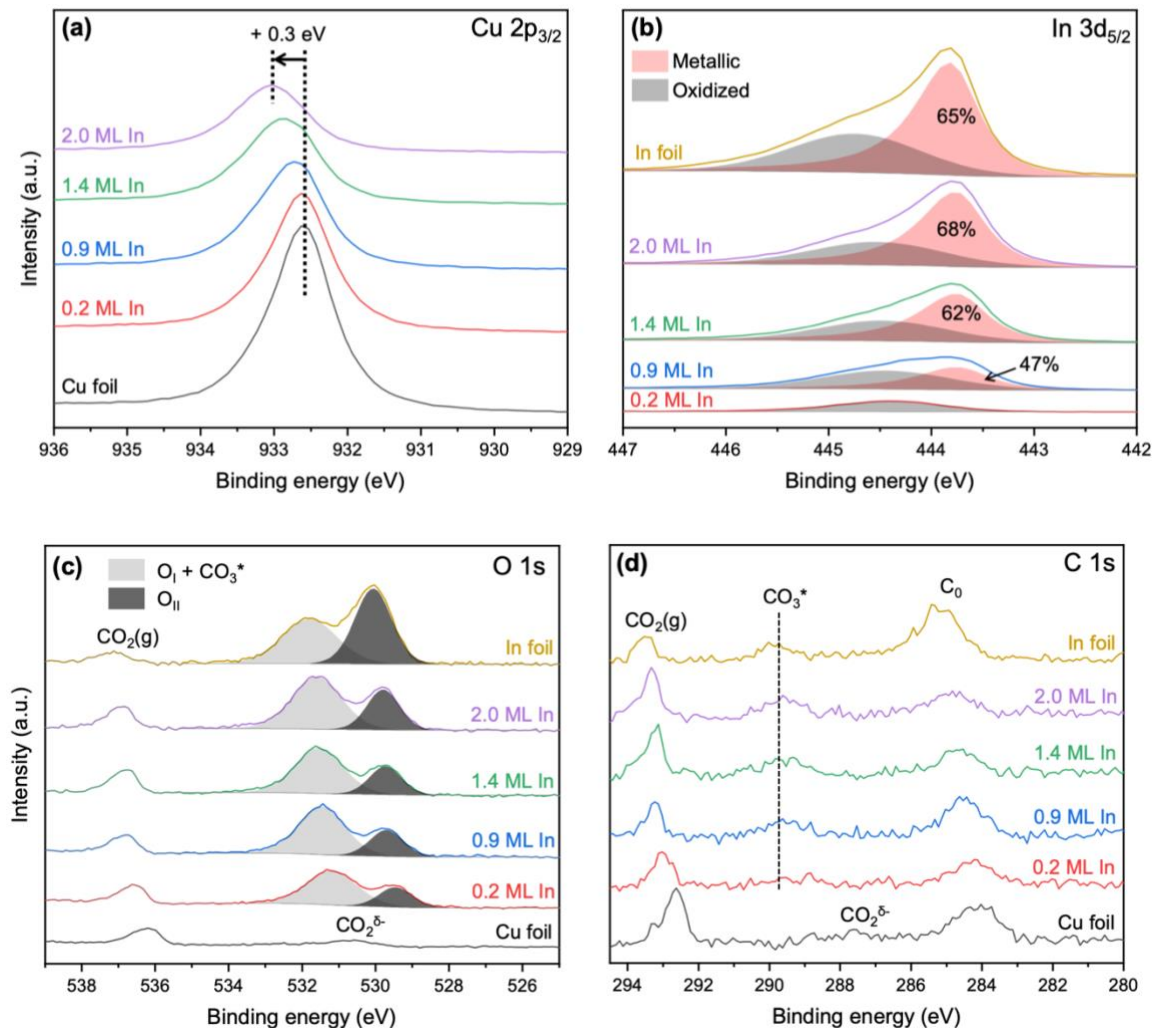


Figure 3.3 NAP-XPS spectra of the (a) Cu 2p_{3/2}, (b) In 3d_{5/2}, (c) O 1s, and (d) C 1s regions of Cu foil, In foil, and In/Cu samples with different surface In coverage upon exposure to 0.2 mbar CO₂ at 300 K.

Apart from the surface properties of In/Cu samples, we also monitored the adsorption states of CO₂. Figure 3c and d shows a series of C 1s and O 1s spectra collected from different surfaces at 300 K under 0.2 mbar CO₂. Gas-phase CO₂ was clearly detected in the O 1s region (~536.5 eV) and C 1s region (~293.0 eV). In C 1s region, an additional peak can be observed at ~284.5 eV for all five samples, and is assigned to neutral carbon impurity (C₀)⁴⁴ as this peak also appears after the sample is placed in NAP cell without exposure to any gases (Figure S6). Here, the slight variation in the positions of gas-phase CO₂ and C₀ peaks on different samples is due to the change of sample work function and vacuum level after In alloying with Cu. As the gas phase is not electrically contacted with the sample surface and the energy analyzer, its energy scale is referenced to the vacuum level of the gas ($E_{\text{vac-gas}}$), which is between the vacuum level of the sample and the aperture.⁴⁵ Besides, the sample position, which also affects the gas-phase peak position⁴⁵, was optimized individually for each measurement. Thus, the gas-phase peak positions are different for samples with different In coverage.

Similarly, the C_0 peak positions are also dependent on the work function of the sample and vary for different samples.⁴⁶ As we tried to use identical sample position in each experiment, the these peaks shifted systematically as In coverage increases. On the Cu foil surface, a weak peak at ~ 288.0 eV can be observed in addition to the C_0 peak. This peak can be assigned to the chemisorbed, negatively charged CO_2 .⁴⁷ In contrast, an additional peak at 289–290 eV can be observed for the samples containing In. This peak is assigned to the adsorbed CO_3 according to previous studies.^{42,44,47,48} Thus, the different adsorption species on Cu and In/Cu samples clearly indicates that the deposition of In changes the activation mechanism of CO_2 .

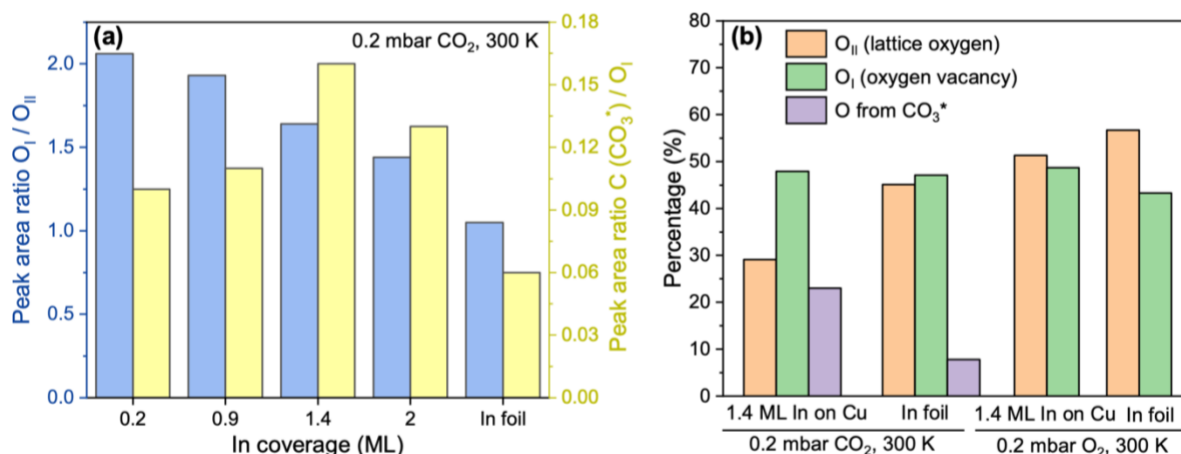


Figure 3.4 (a) Peak area ratios of defective/lattice oxygen (O_I/O_{II}) and carbon from the contribution of carbonate/defective oxygen (C from CO_3^*/O_I) for In/Cu and In foil samples upon exposure to 0.2 mbar CO_2 at 300 K, and (b) percentage of different oxygen species (O_{II} , O_I , and O from CO_3^*) in O 1s region of one In/Cu sample with 1.4 ML In and In foil upon exposure to 0.2 mbar CO_2 or O_2 at 300 K.

In the O 1s region, the Cu foil sample shows a weak peak at ~ 530.5 eV, which corresponds to the chemisorbed CO_2 . However, for the In-containing samples, high-intensity doublet O 1s peaks are observed at 528–534 eV. The double O 1s peaks are characteristic of indium oxides and common for oxides with cations in multiple valence states.^{49–51} This spectrum can be deconvoluted into two peaks: a lower BE peak at 529.8 eV, assigned to the lattice oxygen of In_2O_3 (O_{II}), and a higher BE one at 531.5 eV, assigned to the defective In_2O_{3-x} (O_I). The higher BE of O_I relative to O_{II} can be well explained well by the fact that oxygen vacancies change the distribution of the negative charge density.⁵²

Here, it should be noted that the O 1s peak from carbonate overlaps with that from the O_I species of indium oxides. Thus, the peaks at ~ 531.4 eV in Figure 3.3c are contributed by the oxygen from both O_I species and carbonate. To identify the ratio of oxygen species, the contribution of carbonate to the O 1s peak at ~ 531.4 eV was calculated from the area of the C 1s peak at ~ 289.5 eV using the C:O ratio of 1:3 and the corresponding RSFs for all In/Cu and In foil samples, respectively. The calculated O_I/O_{II} ratio is shown in Figure 3.4a. Obviously, a decreasing trend in the O_I/O_{II} ratio is observed with an increase of In coverage, and the In foil sample corresponds to the lowest fraction of oxygen vacancies. The ratios of C 1s peak area contributed by carbonate, and the O_I peak area for all samples are also compared in Figure 3.4a. With the lowest O_I/O_{II} ratio, the In foil sample adsorbs the least amount of CO_2 in the form of carbonate. In contrast, all In/Cu samples show a CO_3/O_I ratio at least 1.5 time higher than that of the In foil sample, and the highest CO_3/O_I ratio is observed for the sample with 1.4 ML of In. These results imply that, compared with In, the Cu-In alloy also enhances the adsorption of CO_3 on the In_2O_{3-x} surface.

To further investigate the oxidation behavior of In/Cu samples, additional NAP-XPS measurements were taken for the In/Cu sample with 1.4 ML In and In foil under 0.2 mbar O₂ at 300 K, and the corresponding In 3d and O 1s spectra are shown in Figure S3.7. Figure 3.4b shows that for both In/Cu and In foil samples, the fraction of oxidized In calculated from the In 3d_{5/2} spectra is higher in O₂ than in CO₂, as O₂ is a much stronger oxidant. Moreover, the ratio of defective oxygen (O_i) species is higher than lattice oxygen (O_{ll}) in CO₂ (Figure 3.4b). Overall, we conclude that CO₂ tends to oxidize In with a relatively high fraction of oxygen vacancies and this effect is more distinct on Cu-In alloy than pure In.

3.3.3 NAP-XPS under CO₂ hydrogenation conditions at 300-600 K

Providing the essential information on the interaction between the CO₂ and In/Cu surfaces, we further investigated the evolution of the chemical states of Cu and In, as well as the surface O and C species under CO₂ hydrogenation conditions. Figure S3.1 shows that the 1.4 ML In samples exhibits the most homogeneous In particle distribution on Cu foil and the highest particle density ($1.4 \times 10^{10} \text{ cm}^{-2}$) compared with other In/Cu samples (Figure S3.1), offering the highest Cu-In interface area. Thus, the In/Cu sample with 1.4 ML In was used for the following study. The spectra were acquired under 0.2 mbar CO₂, or the mixture of 0.2 mbar CO₂ and 0.6 mbar H₂, at 300, 450, and 600 K, respectively.

The evolution of Cu 2p_{3/2} BE upon exposure to CO₂ and CO₂+H₂ at different temperatures is shown in Figure 3.5a and d, respectively. Obviously, as the temperature increases, the position of the Cu 2p_{3/2} peak shifts to a lower BE by ~0.3 eV (from 300 K under UHV to 600 K with gases), which is independent of the gas atmosphere. As discussed earlier, the BE shift can be attributed to the de-alloying of the Cu-In alloy due to the oxidation of In (Figure S3.7a and b). As confirmed in Figure 3.5b and e, the In is progressively oxidized from 100% metallic In (under the UHV condition at 300 K) to 100% In₂O_{3-x} (under CO₂ and CO₂+H₂ conditions at 600 K). This trend is further confirmed by the change in the In MNN Auger peaks (Figure S3.8c and d). It is necessary to note that the existence of H₂ in the gas atmosphere did not influence the oxidation of In by CO₂ (Figure 3.5e and f). The reduction of In₂O₃ powder by 1.0 bar H₂ has been reported to be limited to the surface without any detectable structural change below 500 K, and a deep reduction to metallic In was observed above 573 K.⁵³ It was also reported that the reduction of In₂O₃ layer on metallic In was as slow as 1 nm/h at 623 K in 40 mbar H₂.⁵⁴ With H₂ partial pressure of 0.6 mbar and the co-existence of CO₂ in this work, it is reasonable that the kinetics of oxidation by CO₂ would prevail over the reduction by H₂, resulting in less metallic In at 450 K, and no metallic In left at 600 K upon exposure to CO₂/H₂ mixture. In addition, the SEM image (Figure S3.9a) of the In/Cu sample with 1.4 ML In coverage was also taken after exposure to the CO₂/H₂ mixture at 600 K. In the particle size distribution histogram of samples before and after exposure the CO₂/H₂ mixture at 600 K (Figure S3.9b), no significant sintering of In nanoparticles is observed, thus the influence of the slow diffusion of gas in large particles can be excluded.

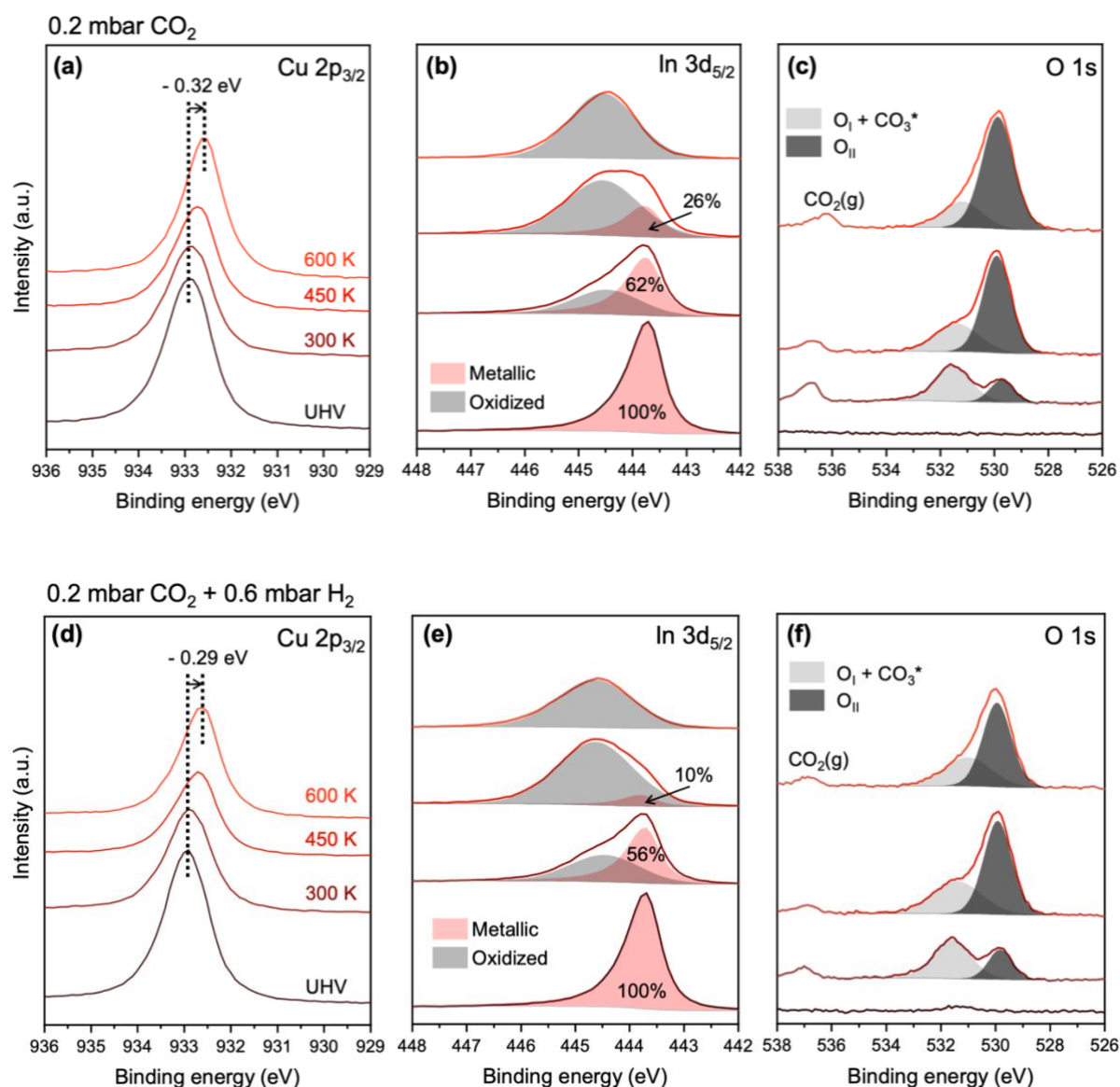


Figure 3.5 Comparison of NAP-XPS spectra of (a, d) Cu 2p_{3/2}, (b, e) In 3d_{5/2}, and (c, f) O 1s regions for the In/Cu sample with 1.4 ML In coverage upon exposure to 0.2 mbar CO₂ (a, b, and c) and the mixture of 0.2 mbar CO₂ + 0.6 mbar H₂ (d, e, and f) at 300–600 K. Spectra are unsmoothed data.

Figure 3.5c and f show that with the increase in temperature, a clear increasing trend of the O_{II}/O_I peak ratio, together with an overall building of the O 1s peaks can be observed. The relative intensities of O_I and O_{II} peaks are summarized in Table 1. Meanwhile, it should be pointed out that at 600 K, even though all the In on the sample surface is oxidized, O_I still accounts for 22% (for CO₂ exposure) or 36% (for CO₂+H₂ exposure) of the O 1s peaks. This means that the oxygen vacancies on the In/Cu sample are stable at up to 600 K upon exposure to CO₂ and CO₂+H₂, and thus, can function as the active sites for CO₂ activation under such conditions. In addition, it can also be observed that with the increase in temperature, the fraction of O 1s peak area contributed by carbonate adsorbed on the sample surface (Table 3.1 and C 1s region in Figure S3.10) decreases. By comparing the relative intensities of O_I and CO₃ under different atmospheres, it is also obvious that the mixture of CO₂ and H₂ leads to a higher fraction of oxygen vacancies and a lower fraction of carbonates than pure CO₂, indicating that the reduction atmosphere may preserve more oxygen vacancies, and that H₂ may react with adsorbed carbonates to form CO₂ hydrogenation products. In Figure S3.10, it is

shown that the carbon deposition is substantially higher when the sample is exposed to CO₂/H₂ mixture at 600 K, which can be attributed to (1) longer heating time due to the existence of highly thermal conductive gas H₂ and (2) formation of carbon from the reduction of CO₂ by H₂.^{44,47,55} Other intermediates of CO₂ hydrogenation, such as HCOO*, HCO*/H₂CO*, and CH₃O groups have been previously observed using synchrotron-based NAP-XPS.^{44,47,48,56} Although we could also deconvolute our C 1s region to identify these intermediates based on previous studies (Figure S3.11), it should be noted that a reliable peak fitting for C 1s region should be in consistent with the O 1s region counterpart, which is not realistic in this work as the majority of O 1s region species are from metal oxides and the contribution of carbon species is as small as 2-3%. Thus, details of other CO₂ hydrogenation intermediates are not discussed as we try not to overinterpret the results.

Table 3.1 Positions and relative intensities of different O 1s species on the In/Cu sample with 1.4 ML In coverage under different conditions.

Gases	Temperature (K)	Positions (eV) and relative intensities				
		O _I + CO ₃ *	O _I	CO ₃ *		O _{II}
CO ₂	300	531.5	63%	8%	529.7	29%
	450	531.4	29%	2%	529.9	69%
	600	531.2	22%	0%	529.9	78%
CO ₂ +H ₂	300	531.6	63%	4%	529.8	33%
	450	531.4	35%	3%	529.9	62%
	600	531.0	36%	0%	530.0	64%

3.4 Discussion

In this work, we investigated the reactivity of CO₂ on In/Cu samples with different In coverages on Cu foil, as well as on polycrystalline Cu and In foils. By means of e-beam evaporation, the In readily formed a surface alloy with the polycrystalline Cu substrate. This is an ideal model catalyst as the formation of Cu-In alloys is widely observed in different Cu-In bimetallic catalysts. However, as soon as CO₂ was introduced onto the sample, In was oxidized and consequently de-alloyed from the Cu-In alloy (Figure 3.3 and S3.4). Under the same conditions, Cu remained in a metallic state, in agreement with the recent NAP-XPS and NEXAFS studies on Cu foil and Cu single crystals.^{42,57} The selective oxidation of In is consistent with the fact that In₂O₃ ($\Delta H_f^\circ = -923.5$ kJ/mol) is thermodynamically more stable than CuO ($\Delta H_f^\circ = -56.06$ kJ/mol) or Cu₂O ($\Delta H_f^\circ = -170.71$ kJ/mol) under standard conditions.^{58,59} Meanwhile, we observed O 1s peaks from both defective and lattice oxygen atoms of the indium oxide, and the ratio of defective oxygen was much higher for the indium oxides from In/Cu samples than that from the In foil, which agrees well with previous observations that oxygen vacancies tend to be concentrated on the topmost surface layers of In₂O₃, rather than in the bulk.^{60,61} According to the theoretical and experimental studies, defective In₂O_{3-x} sites are prone to activate CO₂ and assist the hydrogenation.^{4,8} With NAP-XPS, we observed the formation of more defective In₂O_{3-x} sites on In/Cu than on In surfaces upon CO₂ exposure. Such findings from our In/Cu model catalysts may partially explain the previous observations that Cu-In catalysts show better performance than pure In-based catalysts.¹²⁻¹⁴

Next, the activation of CO₂ on Cu, In, and In/Cu surfaces at 300 K are discussed. On the polycrystalline Cu surface, we observed negatively charged, chemisorbed CO₂^{δ-} from both O 1s and C 1s regions (Figure 3.3c and d), which is in agreement with the widely reported chemisorption of CO₂ as the initial activation step on polycrystalline Cu⁴⁷, as well as on Cu(111) surfaces^{48,57,62}. However, the further reaction between CO₂ and

$\text{CO}_2^{\delta-}$ which leads to the formation of carbonate was not observed in our experiments, nor were the results from Ren *et al.*⁶², possibly due to the relatively slow reaction rate.⁴⁷ In contrast, on the In/Cu and polycrystalline In surfaces, a substantial build-up of carbonate peak were observed (Figure 3.3d). According to previous DFT studies on CO_2 adsorption on the In_2O_3 surface, CO_2 is activated in the form of carbonate upon adsorption by combining with surface oxygen on O-In-O sites with low coordination numbers of their constituent atoms.⁹ This theoretically explained our observation from NAP-XPS measurements that the oxygen vacancies from $\text{In}_2\text{O}_{3-x}$ sites directly corresponded to the formation of carbonate. In addition, the depletion of $\text{CO}_2^{\delta-}$ peaks implies that the $\text{In}_2\text{O}_{3-x}$ sites may also facilitate the stabilization of the carbonate originating from $\text{CO}_2^{\delta-}$ on the Cu surfaces, similar to the function of ZnO sites.^{44,47} Overall, our NAP-XPS results demonstrate experimentally the activation of CO_2 on In/Cu surfaces and the importance of defective $\text{In}_2\text{O}_{3-x}$ sites for CO_2 hydrogenation.

In addition, on In/Cu samples, the density of carbonate adsorbed on oxygen vacancies is increased by at least a factor of 1.5 compared with In foil (Figure 3.4a). This indicates a potential synergy between the Cu-In alloy and $\text{In}_2\text{O}_{3-x}$ sites, where CO_2 tends to be more easily activated on the oxygen vacancies adjacent to the Cu-In alloy sites (*i.e.*, on the boundaries between Cu-In alloys and $\text{In}_2\text{O}_{3-x}$). Such a synergy can be further supported by the peak area ratio of $\text{C}(\text{CO}_3^*)/\text{O}_\text{i}$ on the different In/Cu samples shown in Figure 3.4a. Although it is difficult to obtain a precise particle density for the sample with 0.9 ML In due to the inhomogeneous particle distribution, we estimated a particle density ranging from 9.2×10^8 to $2.9 \times 10^9 \text{ cm}^{-2}$ for this sample from several representative SEM images. While for the 1.4 ML In sample the particle density is around $1.4 \times 10^{10} \text{ cm}^{-2}$. Thus, the $\text{C}(\text{CO}_3^*)/\text{O}_\text{i}$ ratio increases and reaches its maximum at 1.4 ML In coverage, as the highest density of $\text{In}_2\text{O}_{3-x}/\text{Cu-In}$ sites is expected. However, a further increase in the In coverage to 2.0 ML leads to a continuous In overlayer (Figure S3.1), resulting in a decreased $\text{C}(\text{CO}_3^*)/\text{O}_\text{i}$ ratio. Previously, Shi *et al.* prepared a $\text{Cu}_{11}\text{In}_9\text{-In}_2\text{O}_3$ catalyst with superior activity and selectivity for CO_2 hydrogenation to methanol, and proposed that $\text{Cu}_{11}\text{In}_9$ interacts closely with In_2O_3 and thus affects the adsorption strength of CO_2 .¹³ Similarly, the CO_2 -TPD results from Gao *et al.* also suggested that Cu-In alloy corresponds to additional CO_2 adsorption sites and thus higher methanol selectivity compared with pure Cu or In-based catalysts.¹⁴ In addition, it has also been widely proposed for bimetallic In_2O_3 -based catalysts that the metallic (Cu, Pd, Ni or Au) sites provide active hydrogen atoms to the activated CO_2 on $\text{In}_2\text{O}_{3-x}$ sites so that the initial step of hydrogenation can occur.^{12,15,16,20,21,63} Our results not only supports the previous findings but, more importantly, offer direct evidence of the activation of CO_2 on oxygen vacancies and justify the synergy between the Cu-In alloy and the $\text{In}_2\text{O}_{3-x}$ sites in In_2O_3 -based catalysts. These results obtained from In/Cu samples may also be adapted for the purpose of understanding other bimetallic catalysts for CO_2 hydrogenation.

The oxidation state of the In/Cu surfaces and the adsorption of CO_2 change significantly with the gas composition and the temperature, as summarized in Figure 3.5 and Table 3.1. In both CO_2 and CO_2/H_2 mixtures, the metallic In atoms are further oxidized to $\text{In}_2\text{O}_{3-x}$ at 450 and 600 K, and the quantification of O_i species indicates that oxygen vacancies were preserved under all conditions in our NAP-XPS experiments. However, with the presence of H_2 , the $\text{In}_2\text{O}_{3-x}$ sites were slightly reduced at elevated temperatures, as indicated by the higher ratio of O_i species. In a recent study on an $\text{Au}/\text{In}_2\text{O}_3$ catalyst, In_2O_3 was also found to be oxidized by CO_2 and partially reduced by H_2 , which is consistent with our findings.²¹ The reduction of In_2O_3 by H_2 has been found to be limited on the surface at $< 500 \text{ K}$.⁵³ Furthermore, the *in operando* XAS-XRD study

on In_2O_3 catalyst for CO_2 hydrogenation also considered the reduction by H_2 as a necessary step for catalyst activation due to the formation of oxygen vacancies.¹¹ Combining the results from published studies on supported catalysts and our In/Cu model system, it can be inferred that oxygen vacancies from $\text{In}_2\text{O}_{3-x}$ are stable under typical CO_2 hydrogenation conditions, and the reduction process by H_2 can activate the In-based catalyst.

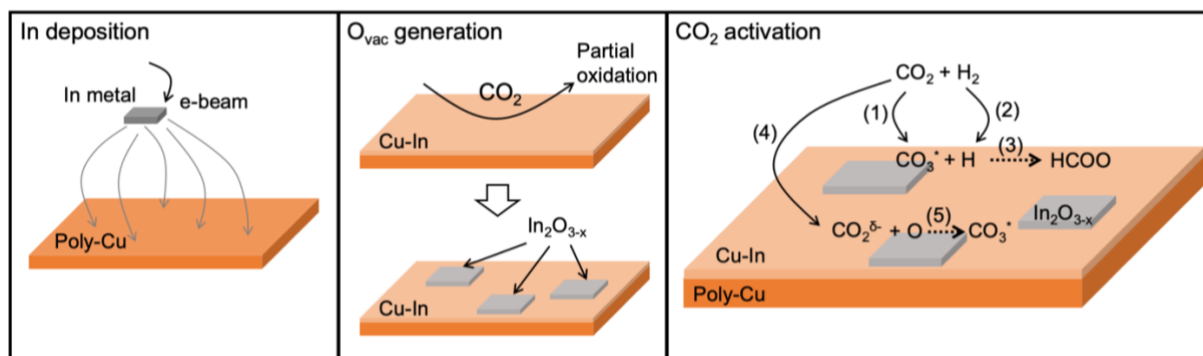


Figure 3.6 Schematic illustration of the formation of Cu-In alloy, the partial oxidation of In/Cu surface to $\text{In}_2\text{O}_{3-x}$ with oxygen vacancies, and the activation of CO_2 on the $\text{In}_2\text{O}_{3-x}$ /Cu-In boundaries and proposed further hydrogenation as an initial step for methanol production.

On the basis of the discussion above, a full schematic for the In/Cu phase evolution and the hydrogenation of CO_2 is summarized in Figure 3.6. Upon the deposition of In metal on a Cu substrate, In and Cu alloy immediately at the surface. In the presence of CO_2 , the Cu-In alloy is partially oxidized with the formation of defective $\text{In}_2\text{O}_{3-x}$ sites. During CO_2 hydrogenation, both the Cu-In alloy phase and $\text{In}_2\text{O}_{3-x}$ sites are involved in different reactions. Under CO_2 hydrogenation conditions, the majority of the Cu-In alloy works as the precursor of the highly active $\text{In}_2\text{O}_{3-x}$ sites, and H_2 dissociates on the remaining Cu-In alloy and metallic Cu. Reaction (1) is the activation of CO_2 to carbonate on the boundary of the $\text{In}_2\text{O}_{3-x}$ site and Cu-In alloy, and reaction (2) is the adsorption of atomic hydrogen on the Cu-In surface. As the H_2 -splitting ability of $\text{In}_2\text{O}_{3-x}$ is limited⁶⁴, the H atoms dissociate from H_2 by Cu and Cu-In alloy sites can spill-over to the adjacent $\text{In}_2\text{O}_{3-x}$ sites to react with the activated CO_2 . This way, further hydrogenation to formate can occur as the initial step for the formation of methanol, which is shown as reaction (3). In addition, reactions (4) and (5) indicate the formation and stabilization of carbonate on the Cu-In alloy surface facilitated by oxygen atoms with low coordination number from the $\text{In}_2\text{O}_{3-x}$ site. We believe that the combination of the CO_2 activation by oxygen vacancies on the $\text{In}_2\text{O}_{3-x}$ /Cu-In boundary and the enhanced hydrogen adsorption on In/Cu surface is the potential origin of the superior activity and selectivity of the Cu-In bimetallic catalysts for CO_2 hydrogenation.

3.5 Conclusions

A series of In/Cu model samples with In coverage from 0.2 to 2.0 ML were prepared on a Cu foil substrate by e-beam evaporation of metallic In. NAP-XPS studies were carried out to understand the evolution of the surface structure and composition as well as solid-gas interactions under CO_2 hydrogenation conditions. After deposition, In was found to form an alloy with the Cu substrate showing clear core-level binding energy shifts. Upon exposure to CO_2 at 300 K, the alloyed Cu-In surface was partially oxidized to $\text{In}_2\text{O}_{3-x}$ /Cu-In. CO_2 was found to be better activated on the surface In/Cu samples than on the Cu foil reference in the form of carbonate because of the existence of oxygen vacancies on $\text{In}_2\text{O}_{3-x}$. The quantification of the carbonate and

oxygen vacancies revealed that the Cu-In alloy promoted the utilization of defective $\text{In}_2\text{O}_{3-x}$ sites for activating CO_2 . Further investigations at elevated temperatures up to 600 K and upon exposure to a CO_2/H_2 mixture revealed that 36% of the oxygen species remained as oxygen vacancies and were stable under such conditions. A synergy between Cu-In alloy and oxygen vacancies from $\text{In}_2\text{O}_{3-x}$ was proposed, in which CO_2 was activated on the $\text{In}_2\text{O}_{3-x}/\text{Cu-In}$ boundaries and further hydrogenated by atomic hydrogen adsorbed on the Cu-In alloy surface. Overall, the obtained results provide fundamental insights into the surface evolution of the In/Cu model catalysts under reaction conditions, and indicate a direct relationship between the existence of surface oxygen vacancies and the enhanced activity of bimetallic Cu-In catalysts for CO_2 hydrogenation.

References

1. Züttel, A. *et al.* Storage of Renewable Energy by Reduction of CO₂ with Hydrogen. *Chim. Int. J. Chem.* **69**, 264–268 (2015).
2. Amouroux, J. *et al.* Carbon dioxide: A new material for energy storage. *Prog. Nat. Sci. Mater. Int.* **24**, 295–304 (2014).
3. International Energy Agency. *World Energy Outlook 2016*. (Head of Communication and Information Office, 2016).
4. Sun, K. *et al.* Hydrogenation of CO₂ to methanol over In₂O₃ catalyst. *J. CO₂ Util.* **12**, 1–6 (2015).
5. Martin, O. *et al.* Indium Oxide as a Superior Catalyst for Methanol Synthesis by CO₂ Hydrogenation. *Angew. Chem. Int. Ed.* **55**, 6261–6265 (2016).
6. Frei, M. S. *et al.* Mechanism and microkinetics of methanol synthesis via CO₂ hydrogenation on indium oxide. *J. Catal.* **361**, 313–321 (2018).
7. Dang, S. *et al.* Rationally designed indium oxide catalysts for CO₂ hydrogenation to methanol with high activity and selectivity. *Sci. Adv.* **6**, eaaz2060 (2020).
8. Ye, J., Liu, C., Mei, D. & Ge, Q. Active Oxygen Vacancy Site for Methanol Synthesis from CO₂ Hydrogenation on In₂O₃(110): A DFT Study. *ACS Catal.* **3**, 1296–1306 (2013).
9. Ye, J., Liu, C. & Ge, Q. DFT Study of CO₂ Adsorption and Hydrogenation on the In₂O₃ Surface. *J. Phys. Chem. C* **116**, 7817–7825 (2012).
10. Wang, W. *et al.* Reverse water gas shift over In₂O₃–CeO₂ catalysts. *Catal. Today* **259**, 402–408 (2016).
11. Tsoukalou, A. *et al.* Structural Evolution and Dynamics of an In₂O₃ Catalyst for CO₂ Hydrogenation to Methanol: An Operando XAS-XRD and In Situ TEM Study. *J. Am. Chem. Soc.* **141**, 13497–13505 (2019).
12. Shi, Z., Tan, Q. & Wu, D. A novel Core–Shell structured CuIn@SiO₂ catalyst for CO₂ hydrogenation to methanol. *AIChE J.* **65**, 1047–1058 (2019).
13. Shi, Z. *et al.* CO₂ hydrogenation to methanol over Cu–In intermetallic catalysts: Effect of reduction temperature. *J. Catal.* **379**, 78–89 (2019).
14. Gao, J. *et al.* Cu₂In nanoalloy enhanced performance of Cu/ZrO₂ catalysts for the CO₂ hydrogenation to methanol. *Ind. Eng. Chem. Res.* (2020) doi:10.1021/acs.iecr.9b06956.
15. Yao, L., Shen, X., Pan, Y. & Peng, Z. Synergy between active sites of Cu–In–Zr–O catalyst in CO₂ hydrogenation to methanol. *J. Catal.* **372**, 74–85 (2019).
16. Rui, N. *et al.* CO₂ hydrogenation to methanol over Pd/In₂O₃: effects of Pd and oxygen vacancy. *Appl. Catal. B Environ.* **218**, 488–497 (2017).
17. García-Trenco, A. *et al.* PdIn intermetallic nanoparticles for the Hydrogenation of CO₂ to Methanol. *Appl. Catal. B Environ.* **220**, 9–18 (2018).
18. Frei, M. S. *et al.* Atomic - scale engineering of indium oxide promotion by palladium for methanol production via CO₂ hydrogenation. *Nat. Commun.* **10**, 1–11 (2019).
19. Snider, J. L. *et al.* Revealing the Synergy between Oxide and Alloy Phases on the Performance of Bimetallic In–Pd Catalysts for CO₂ Hydrogenation to Methanol. *ACS Catal.* 3399–3412 (2019) doi:10.1021/acscatal.8b04848.
20. Jia, X., Sun, K., Wang, J., Shen, C. & Liu, C. Selective hydrogenation of CO₂ to methanol over Ni/In₂O₃ catalyst. *J. Energy Chem.* **50**, 409–415 (2020).
21. Rui, N. *et al.* Hydrogenation of CO₂ to Methanol on a Au_δ+–In₂O₃-x Catalyst. *ACS Catal.* (2020) doi:10.1021/acscatal.0c02120.
22. Scofield, J. H. Hartree-Slater subshell photoionization cross-sections at 1254 and 1487 eV. *J. Electron Spectrosc. Relat. Phenom.* **8**, 129–137 (1976).
23. Powell, C. J. & Jablonski, A. Progress in quantitative surface analysis by X-ray photoelectron spectroscopy: Current status and perspectives. *J. Electron Spectrosc. Relat. Phenom.* **178–179**, 331–346 (2010).
24. C. J. Powell & A. Jablonski. *NIST Electron Inelastic-Mean-Free-Path Database - Version 1.2*. (National Institute of Standards and Technology, 2010).
25. Sano, M., Adaniya, T., Fujitani, T. & Nakamura, J. Formation Process of a Cu–Zn Surface Alloy on Cu(111) Investigated by Scanning Tunneling Microscopy. *J. Phys. Chem. B* **106**, 7627–7633 (2002).
26. Flores, T., Junghans, S. & Wuttig, M. Atomic mechanisms of the formation of an ordered surface alloy: an STM investigation of MnCu(100). *Surf. Sci.* **371**, 14–29 (1997).
27. Raeker, T. J. & DePristo, A. E. Alloy formation energetics and dynamics in the Ni/Cu(100) and Ni/Cu(111) systems. *J. Vac. Sci. Technol. A* **10**, 2396–2399 (1992).
28. Pauly, N., Tougaard, S. & Yubero, F. LMM Auger primary excitation spectra of copper. *Surf. Sci.* **630**, 294–299 (2014).
29. Antonides, E., Janse, E. C. & Sawatzky, G. A. LMM Auger spectra of Cu, Zn, Ga, and Ge. I. Transition probabilities, term splittings, and effective Coulomb interaction. *Phys. Rev. B* **15**, 1669–1679 (1977).
30. Sham, T. K., Perlman, M. L. & Watson, R. E. Electronic behavior in alloys: Gold-non-transition-metal intermetallics. *Phys. Rev. B* **19**, 539–545 (1979).

31. Sadhukhan, P. *et al.* Electronic structure of Au-Sn compounds grown on Au(111). *Phys. Rev. B* **100**, 235404 (2019).
32. Rameshan, C. *et al.* CO₂-selective methanol steam reforming on In-doped Pd studied by in situ X-ray photoelectron spectroscopy. *J. Catal.* **295**, 186–194 (2012).
33. Tougaard, S. Energy loss in XPS: Fundamental processes and applications for quantification, non-destructive depth profiling and 3D imaging. *J. Electron Spectrosc. Relat. Phenom.* **178–179**, 128–153 (2010).
34. Maira, G. K., Orton, B. R. & Riviere, J. C. An XPS study of indium through the melting point. *J. Phys. F Met. Phys.* **17**, 1999–2006 (1987).
35. Aksela, S. High resolution MNN Auger spectra of Ag, Cd, In, Sb, Te, and I. *Z. Für Phys. Hadrons Nucl.* **244**, 268–274 (1971).
36. Rodriguez, J. A. & Goodman, D. W. The Nature of the Metal-Metal Bond in Bimetallic Surfaces. *Science* **257**, 897–903 (1992).
37. Rodriguez, J. A., Campbell, R. A. & Goodman, D. W. Interaction of ultrathin films of copper with rhodium(100) and ruthenium(0001): an XPS study. *J. Phys. Chem.* **95**, 2477–2483 (1991).
38. Jeroro, E., Hyman, M. P. & Vohs, J. M. Ensemble vs. electronic effects on the reactivity of two-dimensional Pd alloys: a comparison of CO and CH₃OH adsorption on Zn/Pd(111) and Cu/Pd(111). *Phys. Chem. Chem. Phys.* **11**, 10457–10465 (2009).
39. Khanuja, M., Mehta, B. R. & Shivaprasad, S. M. Geometric and electronic changes during interface alloy formation in Cu/Pd bimetal layers. *Thin Solid Films* **516**, 5435–5439 (2008).
40. Liu, G., St. Clair, T. P. & Goodman, D. W. An XPS Study of the Interaction of Ultrathin Cu Films with Pd(111). *J. Phys. Chem. B* **103**, 8578–8582 (1999).
41. Ganduglia-Pirovano, M. V., Kudrnovský, J. & Scheffler, M. Adlayer Core-Level Shifts of Random Metal Overlayers on Transition-Metal Substrates. *Phys. Rev. Lett.* **78**, 1807–1810 (1997).
42. Regoutz, A., Kerherve, G., Villar-Garcia, I., Williams, C. K. & Payne, D. J. The influence of oxygen on the surface interaction between CO₂ and copper studied by ambient pressure X-ray photoelectron spectroscopy. *Surf. Sci.* **677**, 121–127 (2018).
43. Rosnagel, S. M., Dylla, H. F. & Cohen, S. A. AES study of the adsorption of O₂, CO, CO₂, and H₂O on indium. *J. Vac. Sci. Technol.* **16**, 558–561 (1979).
44. Koitaya, T. *et al.* CO₂ Activation and Reaction on Zn-Deposited Cu Surfaces Studied by Ambient-Pressure X-ray Photoelectron Spectroscopy. *ACS Catal.* **9**, 4539–4550 (2019).
45. Nguyen, L., Tao, F. F., Tang, Y., Dou, J. & Bao, X.-J. Understanding Catalyst Surfaces during Catalysis through Near Ambient Pressure X-ray Photoelectron Spectroscopy. *Chem. Rev.* **119**, 6822–6905 (2019).
46. Greczynski, G. & Hultman, L. Reliable determination of chemical state in x-ray photoelectron spectroscopy based on sample-work-function referencing to adventitious carbon: Resolving the myth of apparent constant binding energy of the C 1s peak. *Appl. Surf. Sci.* **451**, 99–103 (2018).
47. Deng, X. *et al.* Surface Chemistry of Cu in the Presence of CO₂ and H₂O. *Langmuir* **24**, 9474–9478 (2008).
48. Favaro, M. *et al.* Subsurface oxide plays a critical role in CO₂ activation by Cu(111) surfaces to form chemisorbed CO₂, the first step in reduction of CO₂. *Proc. Natl. Acad. Sci.* **114**, 6706–6711 (2017).
49. Bonnelle, J. P., Grimblot, J. & D’huysser, A. Influence de la polarisation des liaisons sur les spectres ESCA des oxydes de cobalt. *J. Electron Spectrosc. Relat. Phenom.* **7**, 151–162 (1975).
50. Gurlo, A., Ivanovskaya, M., Pfau, A., Weimar, U. & Göpel, W. Sol-gel prepared In₂O₃ thin films. *Thin Solid Films* **307**, 288–293 (1997).
51. Janowitz, C. *et al.* Experimental electronic structure of In₂O₃ and Ga₂O₃. *New J. Phys.* **13**, 085014 (2011).
52. Fan, J. C. C. & Goodenough, J. B. X-ray photoemission spectroscopy studies of Sn-doped indium-oxide films. *J. Appl. Phys.* **48**, 3524–3531 (1977).
53. Bielz, T. *et al.* Hydrogen on In₂O₃: Reducibility, Bonding, Defect Formation, and Reactivity. *J. Phys. Chem. C* **114**, 9022–9029 (2010).
54. Schoeller, H. & Cho, J. Oxidation and reduction behavior of pure indium. *J. Mater. Res.* **24**, 386–393 (2009).
55. Ren, Y. *et al.* Probing the Reaction Mechanism in CO₂ Hydrogenation on Bimetallic Ni/Cu(100) with Near-Ambient Pressure X-Ray Photoelectron Spectroscopy. *ACS Appl. Mater. Interfaces* (2019) doi:10.1021/acsami.9b19523.
56. Roiaz, M. *et al.* Reverse Water–Gas Shift or Sabatier Methanation on Ni(110)? Stable Surface Species at Near-Ambient Pressure. *J. Am. Chem. Soc.* **138**, 4146–4154 (2016).
57. Eren, B., Weatherup, R. S., Liakakos, N., Somorjai, G. A. & Salmeron, M. Dissociative Carbon Dioxide Adsorption and Morphological Changes on Cu(100) and Cu(111) at Ambient Pressures. *J. Am. Chem. Soc.* **138**, 8207–8211 (2016).
58. Cordfunke, E. H. P., Konings, R. J. M. & Ouweltjes, W. The standard enthalpy of formation of In₂O₃. *J. Chem. Thermodyn.* **23**, 451–454 (1991).
59. *NIST Chemistry WebBook, NIST Standard Reference Database Number 69.* (National Institute of Standards and Technology).
60. Walsh, A. Surface oxygen vacancy origin of electron accumulation in indium oxide. *Appl. Phys. Lett.* **98**, 261910 (2011).
61. Lany, S. *et al.* Surface Origin of High Conductivities in Undoped $\text{In}_{2}\text{O}_{3}$ Thin Films. *Phys. Rev. Lett.* **108**, 016802 (2012).

-
62. Ren, Y. *et al.* Catalytic Intermediates of CO₂ Hydrogenation on Cu(111) Probed by In Operando Near-Ambient Pressure Technique. *Chem. – Eur. J.* **24**, 16097–16103 (2018).
 63. Ye, J., Ge, Q. & Liu, C. Effect of PdIn bimetallic particle formation on CO₂ reduction over the Pd–In/SiO₂ catalyst. *Chem. Eng. Sci.* **135**, 193–201 (2015).
 64. Ye, J., Liu, C., Mei, D. & Ge, Q. Methanol synthesis from CO₂ hydrogenation over a Pd₄/In₂O₃ model catalyst: A combined DFT and kinetic study. *J. Catal.* **317**, 44–53 (2014).

Supporting Information

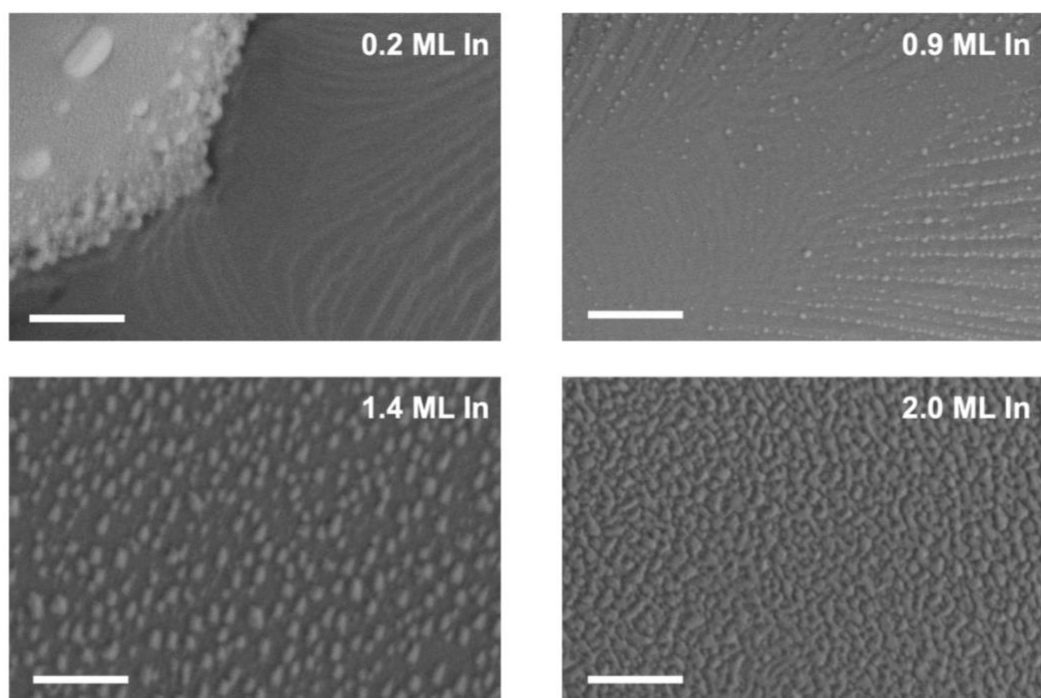


Figure S3.1 SEM images of Cu foil substrate with 0.2-2.0 ML In deposited on surface. The scale bar is 500 nm.

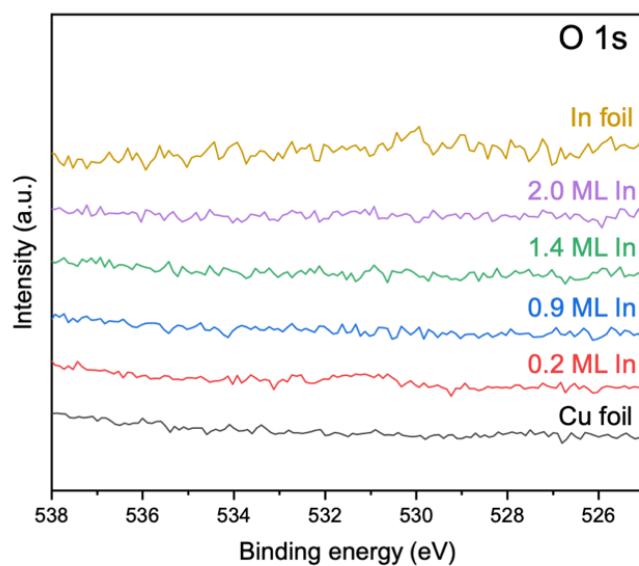


Figure S3.2 XPS spectra of the O 1s regions of Cu foil, In foil, and In/Cu samples with different surface In coverage. Spectra are unsmoothed data with original scale.

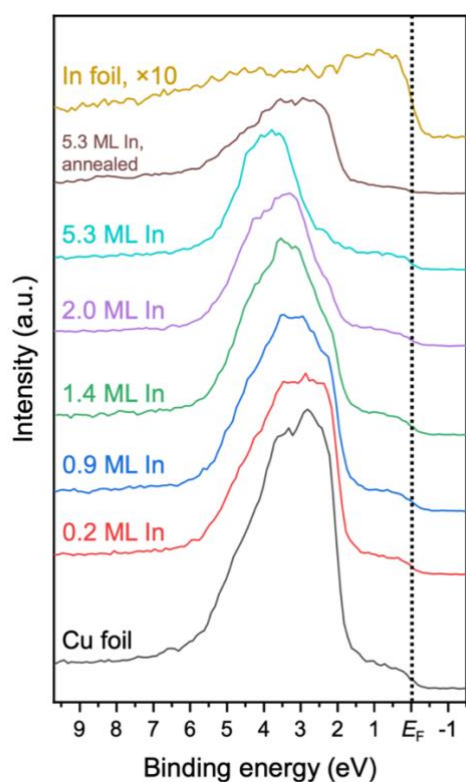


Figure S3.3 X-ray excited valence band region spectra of Cu foil, In foil, and In/Cu samples with different surface In coverage. An additional sample with 5.3 ML In coverage was also prepared and further confirmed this peak shift. After this sample was annealed in 0.2 mbar CO_2 at 600 K, the valence band feature is similar to that of pure Cu, indicating the dealloying of Cu and In.

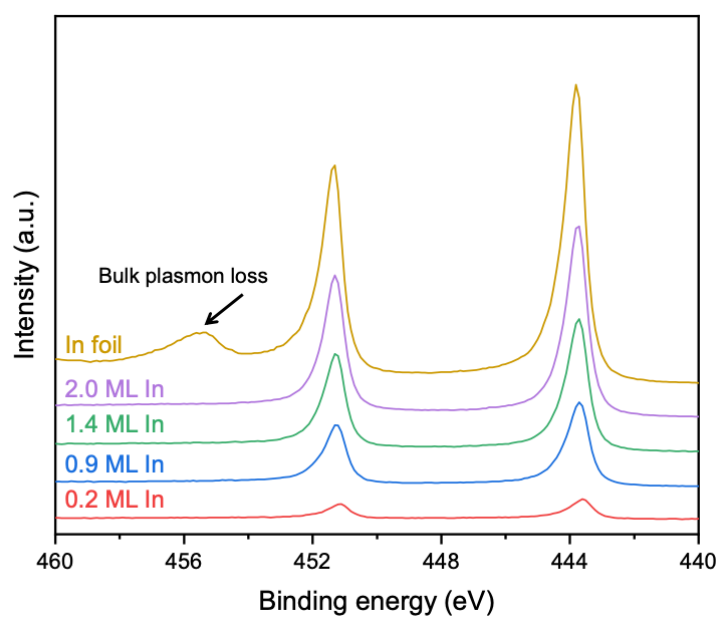


Figure S3.4 Full In 3d region of all In/Cu samples with different In coverage in UHV at 300 K. Cu-In alloy is confirmed to be highly dispersed on Cu substrate surface due to the absence of the bulk plasmon loss peak exclusive for In foil sample.

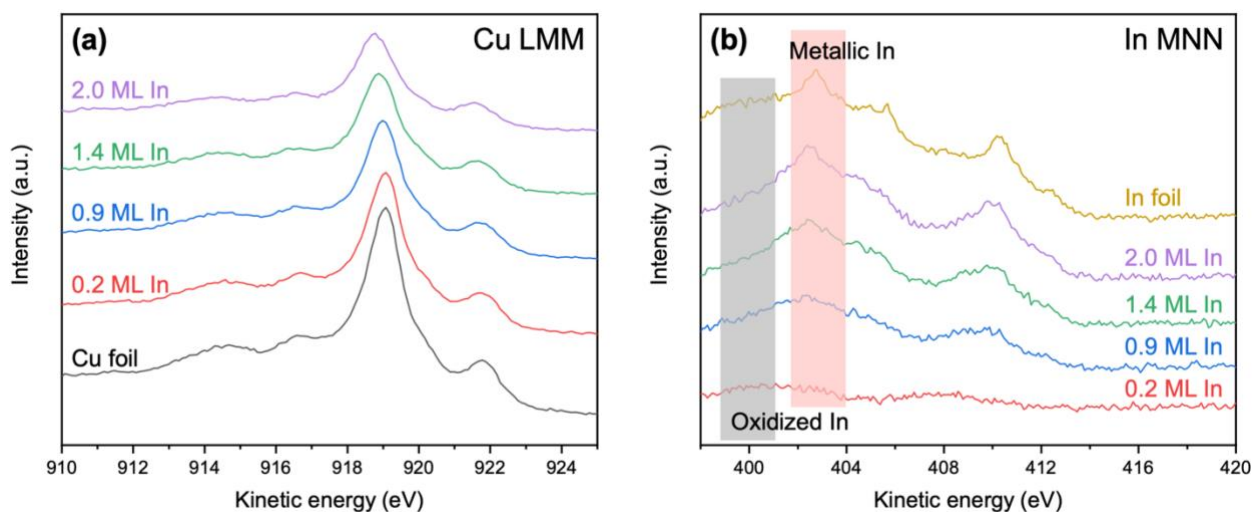


Figure S3.5 X-ray excited (a) Cu LMM and (b) In MNN Auger peaks of Cu foil, In foil, and In/Cu samples with different In coverage upon exposure to 0.2 mbar CO₂ at 300 K. Spectra are unsmoothed data.

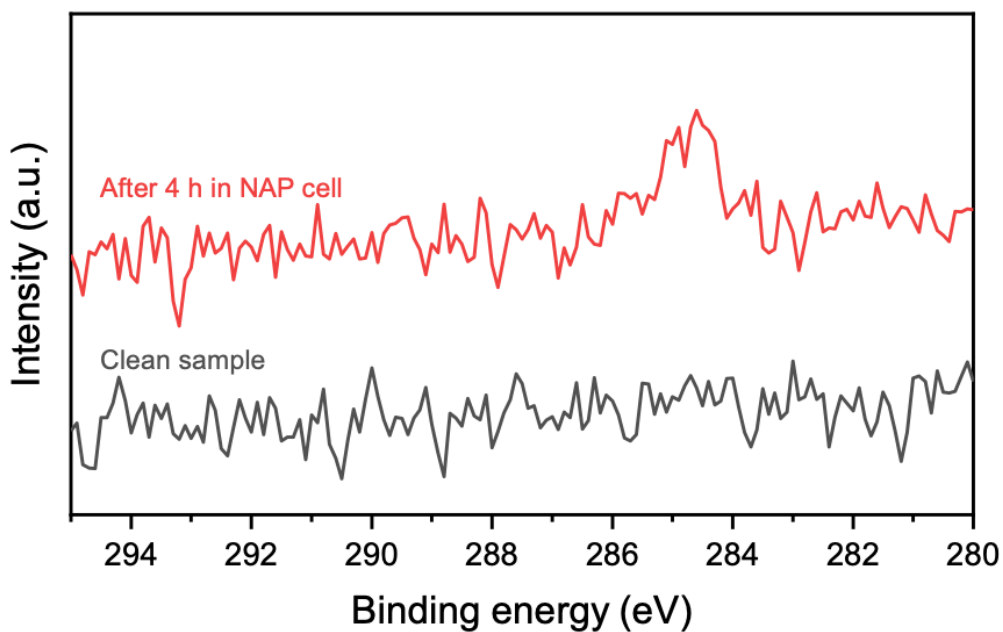


Figure S3.6 C 1s region XPS spectra of a clean In/Cu sample with 1.4 ML In placed in the NAP cell without exposure to any gases measured immediately after sample insertion and after 4 hours. It confirms that the neutral carbon impurity in the NAP cell does not affect the analysis of other carbon intermediates.

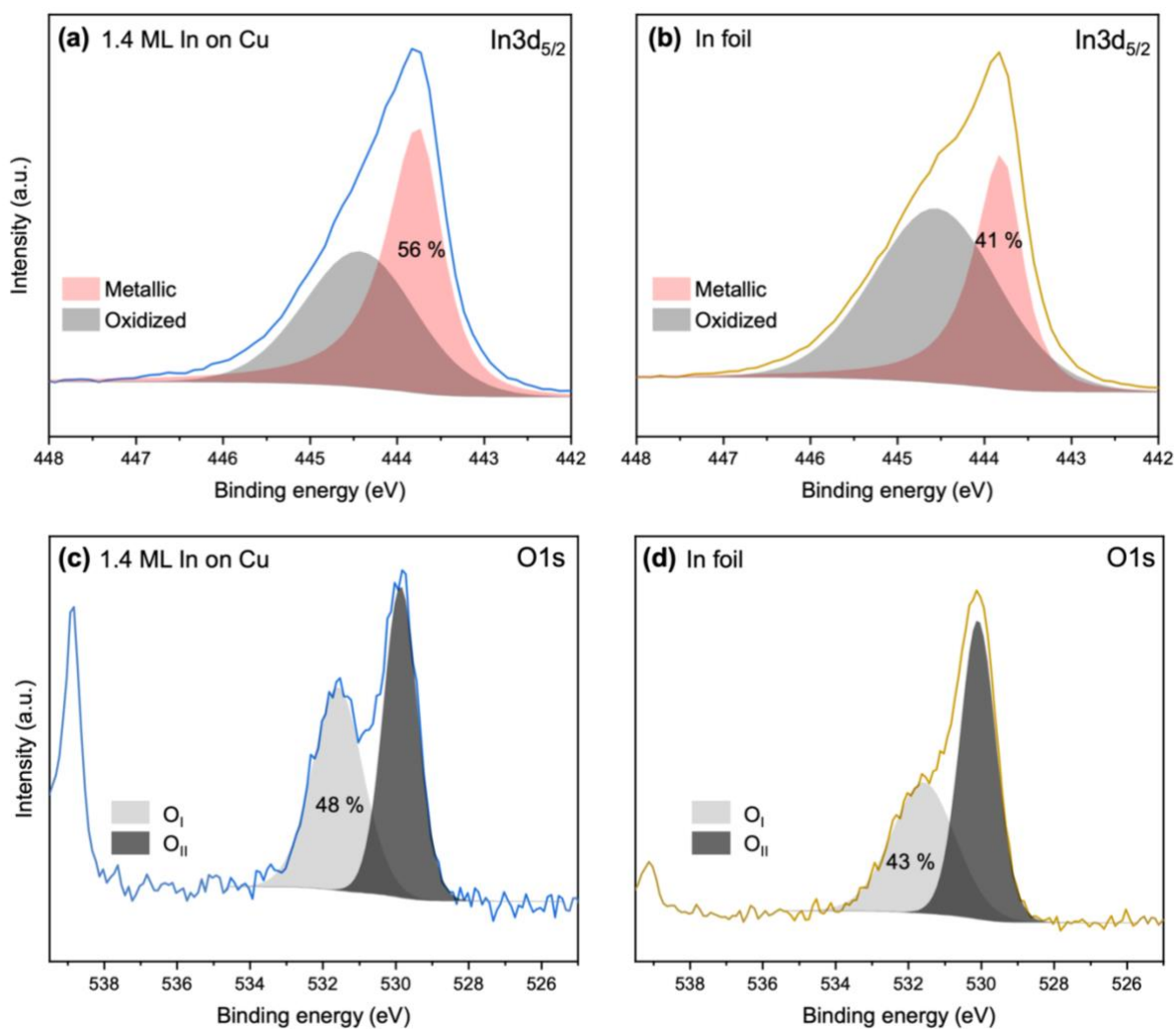


Figure S3.7 NAP-XPS spectra of (a, b) In 3d_{5/2} and (c, d) O1s regions of the In/Cu sample with (a, c) 1.4 ML In on Cu and (b, d) In foil upon exposure to 0.2 mbar O₂ at 300 K. Spectra are unsmoothed data.

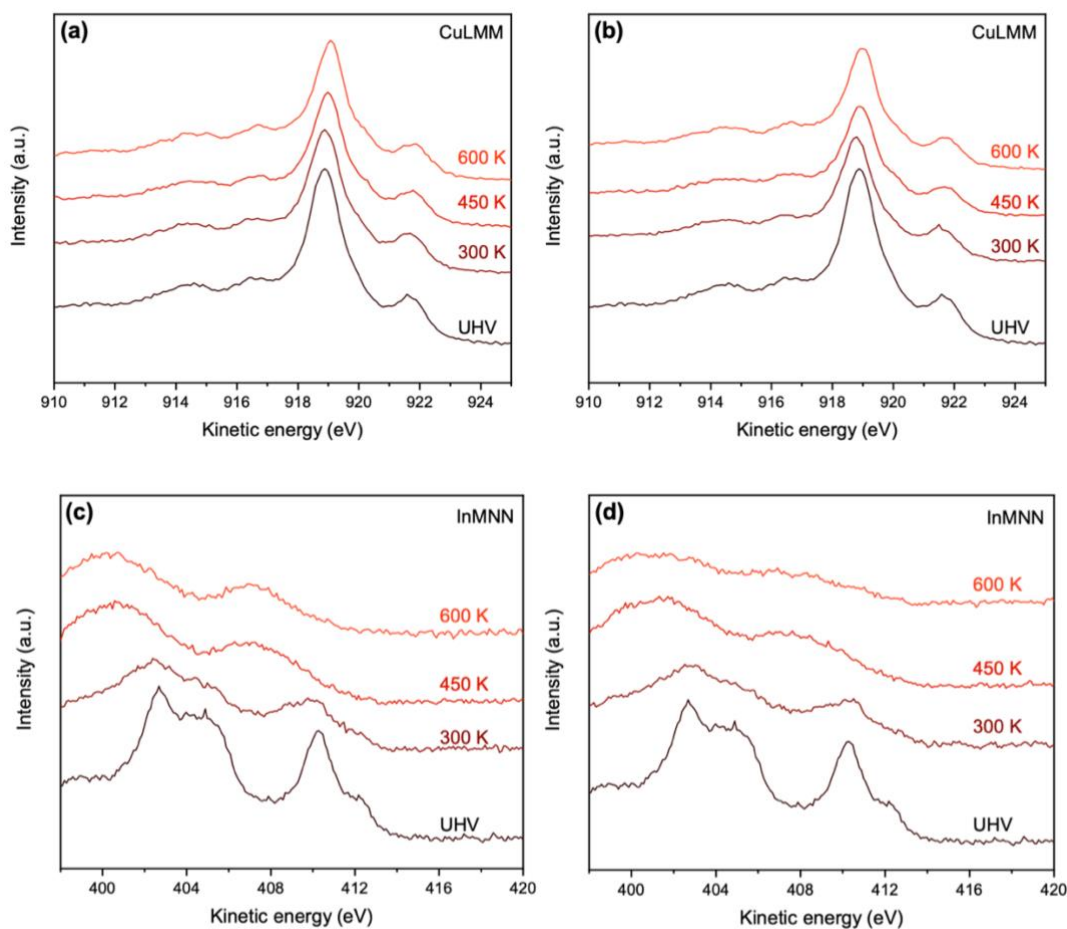


Figure S3.8 X-ray excited (a, b) Cu LMM and (c, d) In MNN Auger peaks of the In/Cu sample with 1.4 ML In on Cu upon exposure to (a, c) 0.2 mbar CO_2 and (b, d) mixture of 0.2 mbar CO_2 and 0.6 mbar H_2 at different temperatures. Spectra are unsmoothed data.

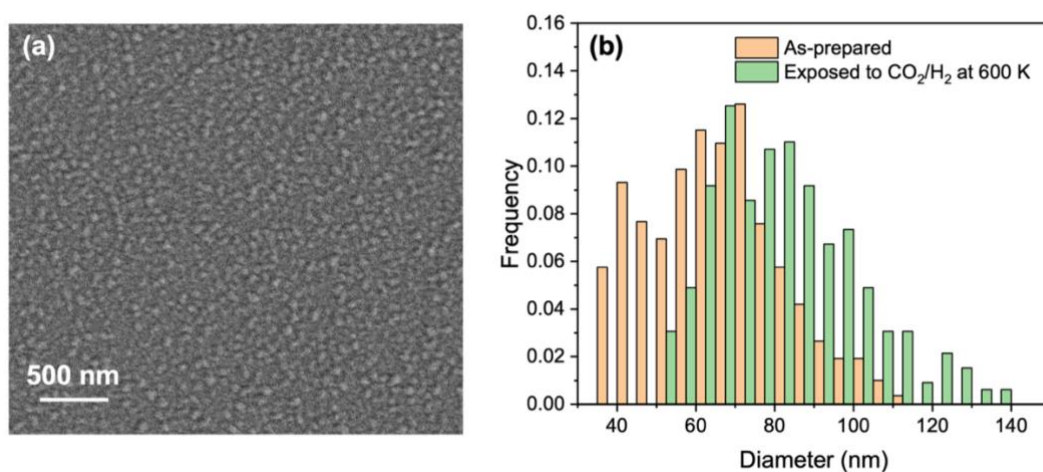


Figure S3.9 (a) SEM image of In/Cu sample with 1.4 ML In coverage upon exposure to CO_2/H_2 mixture at 600 K for 1 h, and (b) particle size distribution histogram for In/Cu sample with 1.4 ML In coverage before and after exposure to CO_2/H_2 mixture at 600 K for 1 h. It should be noted that for the sample after exposure to CO_2/H_2 at 600 K, there are a considerable number of particles with diameters smaller than 30 nm that were not counted due to the limited resolution of the SEM. If these particles are considered, the size distribution before and after CO_2/H_2 exposure will be more similar.

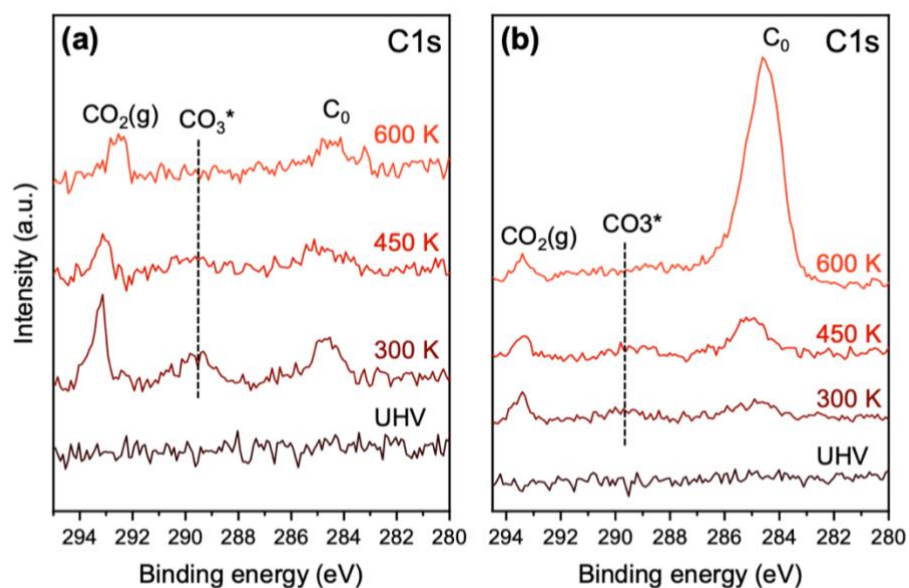


Figure S3.10 NAP-XPS spectra of C 1s regions of the In/Cu sample with 1.4 ML In on Cu upon exposure to (a) 0.2 mbar CO_2 and (b) mixture of 0.2 mbar CO_2 and 0.6 mbar H_2 at different temperatures. Spectra are unsmoothed data.

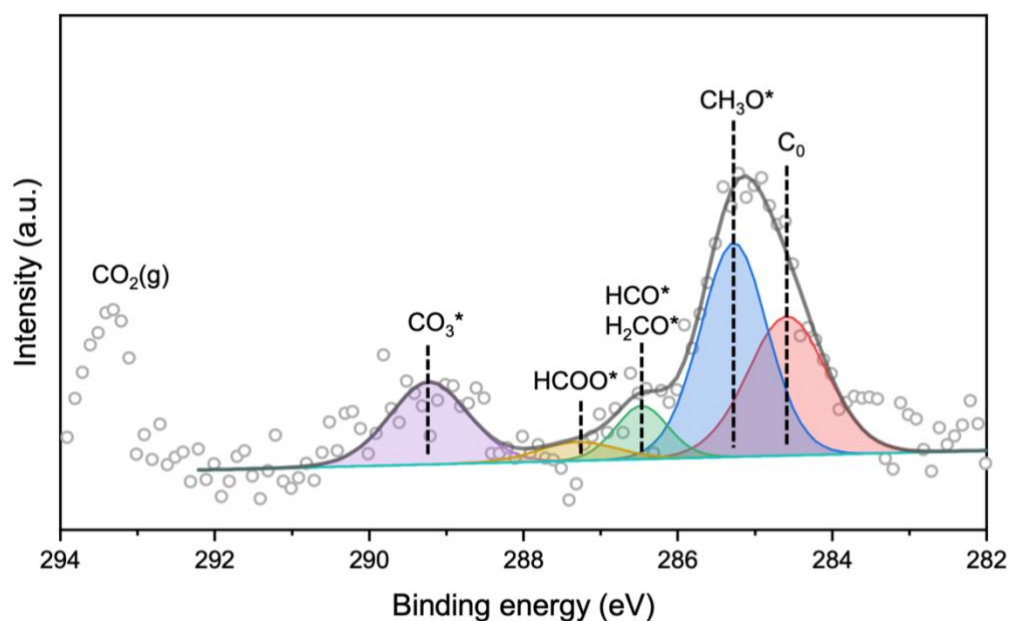


Figure S3.11 NAP-XPS spectrum of C 1s regions of the In/Cu sample with 1.4 ML In on Cu upon exposure to the mixture of 0.2 mbar CO_2 and 0.6 mbar H_2 at 450 K. The identification of CO_2 hydrogenation intermediates has been done by peaks deconvolution. The peak at 284.6 eV is assigned to the neutral carbon impurity (C_0), while the peak at 285.3 eV can be assigned to the single bond C-O* species, especially methoxy (CH_3O^*) group based on previous studies of CO_2 hydrogenation on Cu-based model catalysts.[1–3] The peak at 289.2 eV is assigned to the adsorbed carbonate. The assignment of the peaks at 287.3 and 286.5 eV are less uncertain, because formate (HCOO^*) and adsorbed CO overlap at the region of 287.3–287.5 eV[4,5], and the region of 286.1–286.5 eV corresponds to various C-O and C=O species such as C-O(H), HCO^* , or H_2CO^* on Cu-based surfaces[6,7]. As CO_2 is mainly activated as carbonate on $\text{In}_2\text{O}_{3-x}$ sites and further hydrogenated to methanol along the formate pathway[8], we assign the peak at 287.3 and 286.5 eV as formate and H_2CO^* , respectively.

References

- [1] X. Deng, A. Verdager, T. Herranz, C. Weis, H. Bluhm, M. Salmeron, Surface Chemistry of Cu in the Presence of CO₂ and H₂O, *Langmuir*. 24 (2008) 9474–9478. <https://doi.org/10.1021/la8011052>.
- [2] T. Koitaya, S. Yamamoto, Y. Shiozawa, Y. Yoshikura, M. Hasegawa, J. Tang, K. Takeuchi, K. Mukai, S. Yoshimoto, I. Matsuda, J. Yoshinobu, CO₂ Activation and Reaction on Zn-Deposited Cu Surfaces Studied by Ambient-Pressure X-ray Photoelectron Spectroscopy, *ACS Catal.* 9 (2019) 4539–4550. <https://doi.org/10.1021/acscatal.9b00041>.
- [3] D. Ferrah, A.R. Haines, R.P. Galhenage, J.P. Bruce, A.D. Babore, A. Hunt, I. Waluyo, J.C. Hemminger, Wet Chemical Growth and Thermocatalytic Activity of Cu-Based Nanoparticles Supported on TiO₂ Nanoparticles/HOPG: In Situ Ambient Pressure XPS Study of the CO₂ Hydrogenation Reaction, *ACS Catal.* 9 (2019) 6783–6802. <https://doi.org/10.1021/acscatal.9b01419>.
- [4] M. Favaro, H. Xiao, T. Cheng, W.A. Goddard, J. Yano, E.J. Crumlin, Subsurface oxide plays a critical role in CO₂ activation by Cu(111) surfaces to form chemisorbed CO₂, the first step in reduction of CO₂, *Proc. Natl. Acad. Sci.* 114 (2017) 6706–6711. <https://doi.org/10.1073/pnas.1701405114>.
- [5] M. Leclerc, A. Etxebarria, Y. Ye, E.J. Crumlin, G.M. Brisard, An APXPS Probe of Cu/Pd Bimetallic Catalyst Surface Chemistry of CO₂ Toward CO in the Presence of H₂O and H₂, *J. Phys. Chem. C*. 124 (2020) 17085–17094. <https://doi.org/10.1021/acs.jpcc.0c04717>.
- [6] Y. Ren, K. Yuan, X. Zhou, H. Sun, K. Wu, S.L. Bernasek, W. Chen, G.Q. Xu, Catalytic Intermediates of CO₂ Hydrogenation on Cu(111) Probed by In Operando Near-Ambient Pressure Technique, *Chem. – Eur. J.* 24 (2018) 16097–16103. <https://doi.org/10.1002/chem.201802931>.
- [7] Y. Ma, J. Wang, K.R. Goodman, A.R. Head, X. Tong, D.J. Stacchiola, M.G. White, Reactivity of a Zirconia–Copper Inverse Catalyst for CO₂ Hydrogenation, *J. Phys. Chem. C*. 124 (2020) 22158–22172. <https://doi.org/10.1021/acs.jpcc.0c06624>.
- [8] J. Ye, C. Liu, Q. Ge, DFT Study of CO₂ Adsorption and Hydrogenation on the In₂O₃ Surface, *J. Phys. Chem. C*. 116 (2012) 7817–7825. <https://doi.org/10.1021/jp3004773>.

Chapter 4 Revealing the surface chemistry for CO₂ hydrogenation on Cu/CeO_{2-x} using near-ambient pressure X-ray photoelectron spectroscopy

Mo Li^{a,b}, Thi Ha My Pham^{a,b}, Emad Oveisi^c, Wen Luo^{a,b*}, Andreas Züttel^{a,b}

a. Laboratory of Materials for Renewable Energy (LMER), Institute of Chemical Sciences and Engineering (ISIC), Basic Science Faculty (SB), École Polytechnique Fédérale de Lausanne (EPFL) Valais/Wallis, Energypolis, Rue de l'Industrie 17, CH-1951 Sion, Switzerland

b. Empa Materials Science and Technology, CH-8600 Dübendorf, Switzerland

c. Interdisciplinary Centre for Electron Microscopy (CIME), École Polytechnique Fédérale de Lausanne (EPFL), Lausanne CH-1015, Switzerland

*Corresponding author: wen.luo@epfl.ch

Preprint version: preprint version of this manuscript has been accepted by *ACS Applied Energy Materials*.

Edit: caption numbers of figures, tables, and equations were edited to match the thesis chapter number.

Abstract

Catalytic reduction of CO₂ to valuable products is an attractive route for CO₂ recycling. CeO₂-supported Cu catalysts have shown their high activity and selectivity for the hydrogenation of CO₂ to CO. To uncover the origin of their high performance, we prepared a practical and a well-defined model Cu/CeO_{2-x} catalysts with Cu nanoparticles dispersed on CeO_{2-x} thin film. We studied the structure and catalytic activity of the practical catalyst, and the evolution of the active phase and surface intermediates using near-ambient pressure X-ray photoelectron spectroscopy (NAP-XPS) over the model catalyst under CO₂ hydrogenation condition. The results indicated that strong interaction between Cu and CeO_{2-x} was favored during CO₂ hydrogenation, showing partial covering of Cu by CeO_{2-x} and diffusion of Cu into CeO_{2-x}. Metallic copper and partially reduced ceria with oxygen vacancies were found to be active sites for the reduction of CO₂ to CO. Specifically, the C 1s and Ce 3d core level spectra showed clearly the effective activation of CO₂ on the CeO_{2-x} surface in the form of carbonate by filling the oxygen vacancies. After H₂ was introduced, the carbonates were hydrogenated to formate, and the formate decomposed to CO at elevated temperatures. The role of Cu was revealed by the Cu LMM Auger spectra, and the quantification of the Ce³⁺ fraction on a Cu/CeO_{2-x} and a CeO_{2-x} thin film during the RWGS reaction. Cu was found responsible for H₂ dissociation and spillover to the CeO_{2-x} surface. This way, the dissociated H can effectively convert the carbonate intermediates to formates and regenerate the oxygen vacancies on the CeO_{2-x} surface, keeping the catalytic active sites continuously renewed. This work provides direct experimental evidence on the surface properties of Cu and ceria during the RWGS reaction, and the successive activation process of CO₂ to carbonate and formate on the Cu/CeO_{2-x} surface for a high RWGS catalytic performance.

4.1 Introduction

The activation and hydrogenation of CO₂ using renewable energy can mitigate the negative effects of CO₂ emission and provide an effective way to integrate renewable energy development into conventional carbon-based industrial processes, achieving a zero-emission carbon cycle for the production of fuels and chemicals.^{1–4} At atmospheric pressure, CO₂ can be converted to CO through the reverse water-gas shift (RWGS, CO₂ + H₂ = CO + H₂O, ΔH = 41.3 kJ/mol) reaction, which is highly promising because the product, CO, can be further converted to gasoline via the Fischer–Tropsch process or used as the feedstock of olefin synthesis via the methanol route.^{5–7} The industrial-scale application of the RWGS process is a challenging task because of the chemical inertness of CO₂ and the highly endothermic nature of the reaction.^{4,6,8,9} The scientific question behind the challenge is a thorough understanding of CO₂ activation on catalyst surfaces and developing highly active RWGS catalysts to accelerate the reaction under mild conditions.

As a reducible oxide, CeO₂ is a good candidate as the support of catalysts for the RWGS reaction.^{6,10,11} It has been proposed that the highly active Ce⁴⁺/Ce³⁺ redox pair and the resulting oxygen vacancies play an important role in the activation of CO₂.^{9,12,13} By dispersing another nano-sized redox-active metal, such as Cu, the performance of the subsequent catalyst can be positively tailored for not only the RWGS reaction¹⁴ but also CO preferential oxidation¹⁵, steam reforming¹⁶, and methanol synthesis from CO₂.^{17,18} *In situ* characterizations pointed out that the unique electronic and chemical properties of Cu/CeO₂ catalysts, in which the Cu⁺/Cu⁰ and Ce⁴⁺/Ce³⁺ redox pairs are coupled, could be the origin of their high catalytic performance.^{14,18,19} However, a whole picture of the mechanistic insights into the RWGS activity of the Cu/CeO₂ catalysts is still vague due to the limitations of current *in situ* investigations. For example, *in situ* X-ray diffraction (XRD) and X-ray adsorption spectroscopy (XAS) provide bulk information about the active phase of the catalysts^{20,21}, while *in situ* diffuse reflectance infrared Fourier transform spectroscopy (DRIFTS) examines only the surface intermediates.²² A simultaneous investigation of both the active phase and the surface species of Cu/CeO₂ during the RWGS reaction, ideally along with a comparable activity measurement, should be made for both academic and practical reasons.

Near-ambient pressure X-ray photoelectron spectroscopy (NAP-XPS) is a powerful technique that can monitor both the surface chemical state and surface adsorbents of a catalyst under reaction conditions.^{23,24} This method is proven reliable and successful when combined with well-defined model catalysts with uniform surface structures.^{25,26} Previously, we prepared In/Cu model catalysts and investigated the active phase, which contains numerous oxygen vacancies promoted by the Cu-In alloy, and surface intermediates under CO₂ hydrogenation conditions, using NAP-XPS.²⁷ This study synthesized a practical powder Cu/CeO_{2-x} catalyst and a corresponding planar Cu/CeO_{2-x} model sample for the RWGS reaction. The structure-performance relationship of the practical and model catalysts was found highly consistent. With the help of NAP-XPS, we show that partially reduced ceria with oxygen vacancies is responsible for CO₂ activation in the form of carbonate, and metallic Cu is the active site for H₂ dissociation and spillover to hydrogenate the carbonate intermediates and regenerate the oxygen vacancies. More importantly, catalytic activity for the RWGS was observed over the Cu/CeO_{2-x} model surface during the NAP-XPS measurements under mild conditions at as low as 450 K, establishing a correlation between the activity investigation on the real catalyst and the surface

investigation on the model catalyst. We also visualized the cross-sectional structure and chemical composition of the Cu/CeO_{2-x} model catalyst by scanning transmission electron microscopy coupled with energy-dispersive X-ray spectroscopy (STEM-EDX) after the RWGS reaction and confirmed the numerous metal-oxide interfaces where CO₂ hydrogenation occurred.

4.2 Experimental section

4.2.1 Preparation, characterization, and evaluation of Cu/CeO_{2-x} powder catalyst

The CuO/CeO₂ powder catalyst precursor was prepared by the wet impregnation method. First, the metal precursor solution was obtained by dissolving 0.76 g of Cu(NO₃)₂·3H₂O (Sigma-Aldrich) in 5 mL of deionized water. Next, sonication was used to disperse 2 g of CeO₂ (Sigma-Aldrich, 50 nm nanoparticles) support in the precursor solution followed by continuous stirring at 353 K until a homogeneous slurry was formed. The slurry were then dried at 353 K overnight and calcined at 873 K for 4 h in air with a ramp of 10 K/min.

X-ray diffraction (XRD) patterns of the powder Cu/CeO_{2-x} catalysts were obtained from a Bruker D8 Advance instrument (40 kV, 40 mA, Cu K α radiation, λ = 0.154 nm). The lattice constant of the components was calculated using the Rietveld refinement with TOPAS 5 software at an accuracy of 10%. Transmission electron microscopy (TEM) images of the CuO/CeO₂ precursors were obtained using a Thermo-Scientific Tecnai G2 Spirit microscope operated at 120 kV. High-resolution TEM (HR-TEM) and high-angle annular dark-field (HAADF) STEM imaging were performed on a Thermo-Scientific Osiris at 200 kV. STEM-EDX measurement was carried out on the same machines using Super-X EDX system comprised of four silicon-drift detectors. EDX data were collected in the form of spectrum images, in which a focused electron probe was scanned in raster (1024 \times 1024 pixels) across a region of interest in the STEM mode. For each scan point, structural information was obtained from the electron scattering incident on a HAADF detector. The samples were dispersed on carbon-supported Cu and Ni grids for TEM and STEM-EDX measurements, respectively.

For the catalytic testing of RWGS reaction, ~100 mg of catalyst precursor was placed in a quartz fixed-bed reactor and reduced by 10 vol.% H₂/He at 673 K and cooled below 373 K. Under the mixture of CO₂, H₂, and He (1:4:10), the catalyst was heated to 873 K with a ramp of 10 K/min. The total gas flow rate was kept at 15 mL/min and thus the space velocity was 3000 h⁻¹ assuming a voidage of 0.4. The temperature was measured with a K-type thermocouple positioned in the center of the catalyst bed. The outlet pipeline of the reactor was kept above 373 K to avoid water condensation. The products were analyzed with a quadrupole mass spectrometer (QMS, Pfeiffer Vacuum, OmniStar GSD 320) using a Faraday detector under multi-concentration detection (MCD) mode, which had been previously calibrated using standard gas mixtures previously.

4.2.2 Cu/CeO_{2-x} model catalyst for RWGS mechanism studies

To prepare the Cu/CeO_{2-x} model catalyst, metallic Ce (99.9%, Alfa Aesar) was evaporated (EBE-4 e-beam evaporator, SPECS GmbH) onto an Au foil (0.1 mm thick, 99.9975%, abcr GmbH) in the presence of 1 \times 10⁻⁷ mbar O₂, and then annealed at 800 K for 20 min under the same O₂ pressure. Before the evaporation, the Au foil was cleaned by cycles of Ar⁺ sputtering (1 keV, 5 \times 10⁻⁵ mbar Ar, 15 min) and vacuum annealing (800 K, 5 min) until the C 1s and O 1s signals were below the XPS detection limit. The resulting polycrystalline ceria

thin film was estimated to be > 10 nm thick based on the attenuation of the Au 4f XPS signal. Cu (99.99%, Alfa Aesar) was evaporated on the as-prepared ceria thin film at 300 K under vacuum. Cu was deposited onto the as-prepared CeO_{2-x}/Au surface at a deposition rate of 0.18 monolayer (ML) per minute and the nominal Cu coverage is estimated to be 0.9 ML. The evaporation was performed in the preparation chamber of the NAP-XPS system, and the sample was transferred to inside the system without exposure to air.

The sample was placed in a NAP cell with an X-ray transparent Si₃N₄ window and a 300 μm aperture for the photoelectrons to pass through. Research-grade CO₂ (4.5, PanGas) and H₂ (5.0, PanGas) were used for all experiments and the flowrates were regulated with precise mass flow controllers (GF40, Brooks). The gases flow over the surface of the Cu/CeO_{2-x} model catalyst, and the RWGS reactivity was monitored with a residual gas analyzer (RGA, MKS e-Vision 2) installed on the pre-lens stage of the energy analyzer. The volume of the NAP cell is 400 mL, corresponding to the gases residence time of 670 s at the flowrate of 0.6 mL/min. The pressure in the NAP cell was measured with a gas-independent capacitance gauge (CMR361, Pfeiffer Vacuum). An e-beam heater was placed on the back of the NAP cell without exposure to the gas phase, allowing sample heating to 600 K.

NAP-XPS measurements were carried out in operando. A monochromatic Al Kα (hν = 1486.74 eV) X-ray source and a differentially pumped hemispherical energy analyzer (PHOIBOS 150 NAP, SPECS GmbH) were used for X-ray generation and photoelectron collection, respectively. The power of the X-ray source was set to 45 W to eliminate the X-ray induced sample reduction. The base pressure of the NAP-XPS system is 1×10⁻⁹ mbar. After each sample loading, the position of the sample was optimized to maximize the intensity of the signal, which could change the vacuum level and thus the binding energy of the gas phase. A pass energy of 20 eV was used for all core level regions. As the samples were conductive, no charge compensation was required. The Ce 3d photoemission line at 916.9 eV of CeO₂ was used for binding energy calibration. The C 1s region spectra were normalized with the background intensity to distinguish the peaks of carbon species from the Ce 4s peak.²⁸ The quantification of Ce³⁺ and Ce⁴⁺ follows the peak model and procedures described elsewhere.^{29,30} The results are reproducible for samples with Ce³⁺ concentration as low as ~2%.

The surface morphology of the Cu/CeO_{2-x} model catalyst was characterized by a Thermo-Scientific Teneo scanning electron microscope (SEM) at an acceleration voltage of 15 kV and a working distance of 7 mm. For STEM-EDX analysis of the Cu/CeO_{2-x} model catalyst, a cross-sectional TEM lamella was extracted from one Cu/CeO₂ sample via conventional focused ion beam (FIB) lift-out with a Zeiss NVision-40. The sample surface was protected with carbon deposited inside the microscope. A small volume around the region of interest was cut as the lamella, lifted out in situ by the Kleindiek manipulator, glued on a Mo TEM grid, and thinned to electron transparency. EDX data were acquired using a Thermo-Scientific Titan Themis 60-300 at an acceleration voltage of 200 kV. This microscope is equipped with a high-brightness Schottky X-FEG gun and a Super-X EDX system.

4.3 Results and discussion

We prepared a powder Cu/CeO_{2-x} catalyst with a CeO_{2-x}-supported-Cu configuration using the impregnation method to bridge the material gap between the model catalyst and the practical catalyst. The calcined catalyst precursor was pre-reduced in 5% H₂/He at 673 K for 1 h. Figure 4.1a shows the EDX element maps

for a selected area of the catalyst after reduction. The catalyst contains polycrystalline CeO_2 nanoparticles with a diameter of ~ 50 nm (TEM, HRTEM, and HAADF-STEM images shown in Figure S4.1) with well-distributed Cu. XRD patterns of the calcined and reduced catalyst (Figure 4.1b) showed the complete reduction of CuO to metallic Cu. The CeO_2 support was also partially reduced as indicated by the lattice expansion of ceria: the increase of the ceria lattice constant (obtained by Rietveld refinement) from 5.4156 Å for the calcined catalyst to 5.4306 Å for the reduced catalyst, which is due to the replacement of the Ce^{4+} ions (ionic radius 0.970 Å) by the Ce^{3+} ions (1.143 Å).^{31–33} Figure 4.1c shows the mass spectrometry MS data for the RWGS process over this Cu/CeO_{2-x} catalyst from 523 to 873 K with a 50 K increment.

Upon exposure to the reactants, we observe a steady state right after the desired temperature was reached, and the production of CO and H_2O remained constant at corresponding temperatures. The CO_2 conversion increased from $\sim 4\%$ at 523 K to $\sim 62\%$ at 873 K and is close to the calculated thermodynamic limit in the temperature range of 673–873 K (Figure 4.1d). In addition, only CO and H_2O were detected as reaction products, demonstrating the high selectivity of Cu/CeO_{2-x} for RWGS. These results indicate that metallic Cu nanoparticles dispersed on partially reduced CeO_2 are highly active and selective for RWGS. While ex-situ characterization techniques (i.e., XRD and TEM) have provided us the crystal structure and elemental distribution of the Cu/CeO_{2-x} catalyst, the surface chemical state of Cu and CeO_{2-x} under the reaction condition and their roles in the activation and hydrogenation of CO_2 are still elusive. Thus, a simultaneous investigation of the activate phase, reaction intermediates, and activity is needed to thoroughly understand of the RWGS mechanisms over the Cu/CeO_{2-x} catalyst.

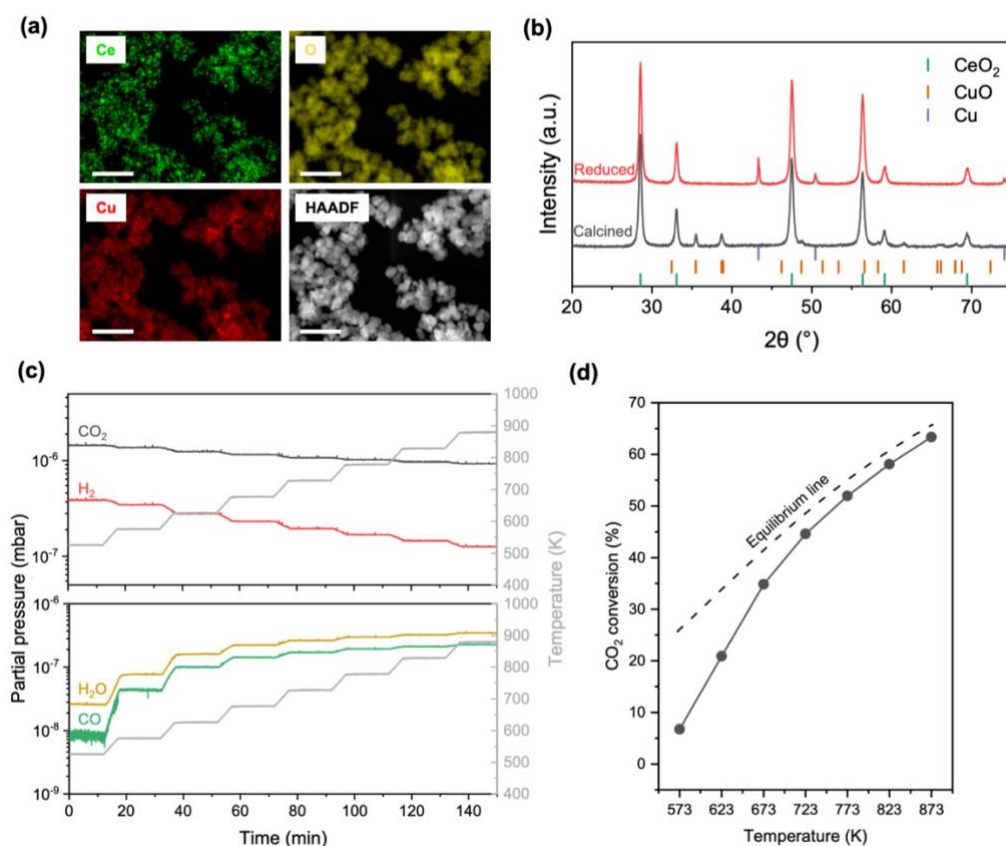


Figure 4.1 (a) STEM-HAADF and corresponding EDX elemental maps of the reduced Cu/CeO_{2-x} catalyst (the scale bar is 100 nm), (b) XRD patterns of the calcined CuO/CeO₂ precursor and the reduced Cu/CeO_{2-x} catalyst, (c) gas species detected by MS as a function of time for the Cu/CeO_{2-x} catalyst under RWGS conditions from 523 to 873 K, and (d) CO₂ conversion over the Cu/CeO_{2-x} catalyst under the same conditions with (c).

To better understand the surface chemistry of the RWGS process on a Cu/CeO_{2-x} catalyst, we prepared a CeO_{2-x}-supported-Cu thin-film sample as a simplified model of the powder Cu/CeO_{2-x} catalyst. Metal clusters supported on ultra-thin oxide films are excellent models for the corresponding bulk catalysts in terms of structural, electronic, and chemical properties.³⁴ Using a model sample instead of a powder catalyst also allows us to obtain contamination-free surfaces with electrical conductivity which is desirable in NAP-XPS investigations. Therefore, the Cu/CeO_{2-x} model sample was prepared in the UHV chamber using a physical vapor deposition method, and CeO_{2-x} thin film and Cu nanoparticles were sequentially deposited on an Au foil. A Cu/CeO_{2-x} sample with ~25% of the CeO_{2-x} substrate covered by metallic Cu was prepared by optimizing the deposition time. The Cu was proven to be fully metallic by comparing the Cu 2p core level and the Cu LMM Auger region with a sputter-cleaned metallic Cu foil (Figure S4.2a and b). No apparent charge transfer from Cu to CeO_{2-x} was observed in the valence band spectra (Figure S4.2d), which agrees the previous quantification of Cu chemical state on CeO₂(111) thin film.³⁵

We then investigated the interaction of CO₂ and CO₂/H₂ mixture with the model Cu/CeO_{2-x} surfaces using NAP-XPS. X-ray induced chemical reactions of the gas molecules can be excluded based on our previous blank experiment on an inactive Cu foil under the same conditions used in this study.²⁷ Figure 4.2 shows a series of XPS spectra collected from the Cu/CeO_{2-x} model sample under the UHV condition and exposure to 0.2 mbar of CO₂ at 300–600 K. Under UHV conditions, no carbon species can be observed in the C 1s region except a broad Ce 4s peak, indicating the clean surface of the as-prepared Cu/CeO_{2-x} model sample. As CeO₂ and Ce₂O₃ have different line shapes in the Ce 3d region, the Ce 3d spectra in Figure 4.2 can be deconvoluted to quantify the amount of Ce⁴⁺ and Ce³⁺ in the Cu/CeO_{2-x} sample according to published protocols.^{30,36,37} Compared to a fully oxidized CeO₂ reference sample (Figure S4.2c), the ceria thin film in the as-prepared Cu/CeO_{2-x} sample is slightly reduced with ~2.5% of Ce³⁺, as the maximum O₂ pressure (1×10⁻⁷ mbar) allowed in our evaporator is not enough to fully oxidize CeO₂.¹⁰ Due to the very close Cu 2p binding energy of Cu⁰ and Cu⁺, Cu LMM Auger spectra were used to understand the oxidation state of Cu. On the as-prepared Cu/CeO_{2-x} surface, Cu is fully metallic showing the characteristic Cu LMM Auger feature with the strongest peak at 918.6 eV (Figure S4.2b), indicating that there is no chemical reaction between Cu and ceria during the deposition process.

After 0.2 mbar CO₂ was introduced to the NAP cell, a sharp peak for CO₂ gas at ~293 eV can be observed. A strong peak at 289.3 eV can be assigned to O-C=O from carbonate (CO₃²⁻) or formate (HCOO⁻) adsorbed on the ceria surfaces^{9,27,38,39}, and a wide feature between 284–286 eV probably comes from neutral carbon (C₀) resulting from CO₂ dissociation.^{40,41} The contribution of formate to the C 1s peak at 289.3 eV is rather small due to the small fraction of its O 1s counterpart at 532.3 eV compared to the carbonate/carboxylate peak at 531.6 eV (inset of Figure S4.3).^{12,42–44} Correspondingly, CeO_{2-x} was oxidized to CeO₂, showing as the disappearance of the Ce³⁺ features, and Cu was slightly oxidized to Cu₂O, shown by the increase of the Cu⁺ Auger peak at 916.8 eV.⁴⁵ When heating to 450 and 600 K, metallic Cu was oxidized to Cu₂O shown by the shift of the Cu LMM Auger peak from 918.6 to 916.8 eV. The appearance of an O 1s peak at 530.3 eV corresponds to Cu₂O.^{46,47} At the same time, all carbonate/formate and C₀ species desorbed from the Cu/CeO_{2-x} model surface, and a shoulder peak at 288.3 eV that can be attributed to carboxylate (chemisorbed

CO₂, CO₂^{δ-}) appeared, in agreement with the fact that chemisorbed CO₂ can be stabilized on oxidized Cu surfaces.⁴⁸ Previous studies observed the formation of strongly bound carbonate by healing the surface oxygen vacancies upon exposure to CO₂ on a defective ceria surface.^{28,49} However, CO₂ was found to only weakly chemisorb on polycrystalline Cu surfaces.^{27,40} Combined NAP-XPS and IRRAS investigation on a CeO_x/Cu(111) model catalyst showed the simultaneous existence of carbonates and carboxylates after the introduction of CO₂. Thus, the ceria-Cu interfaces were concluded to activate CO₂.⁹ Our findings on the interaction between CO₂ and the Cu/CeO_{2-x} surface provide further evidence that both ceria and metallic Cu contribute to the activation of CO₂, as exposure to CO₂ induces the changes in the oxidation state of both Ce and Cu atoms. More importantly, our results indicate that CO₂ is activated on the Cu/CeO_{2-x} model surface, forming carbonate and formate as essential intermediates of the RWGS reaction via the formate pathway.^{9,19}

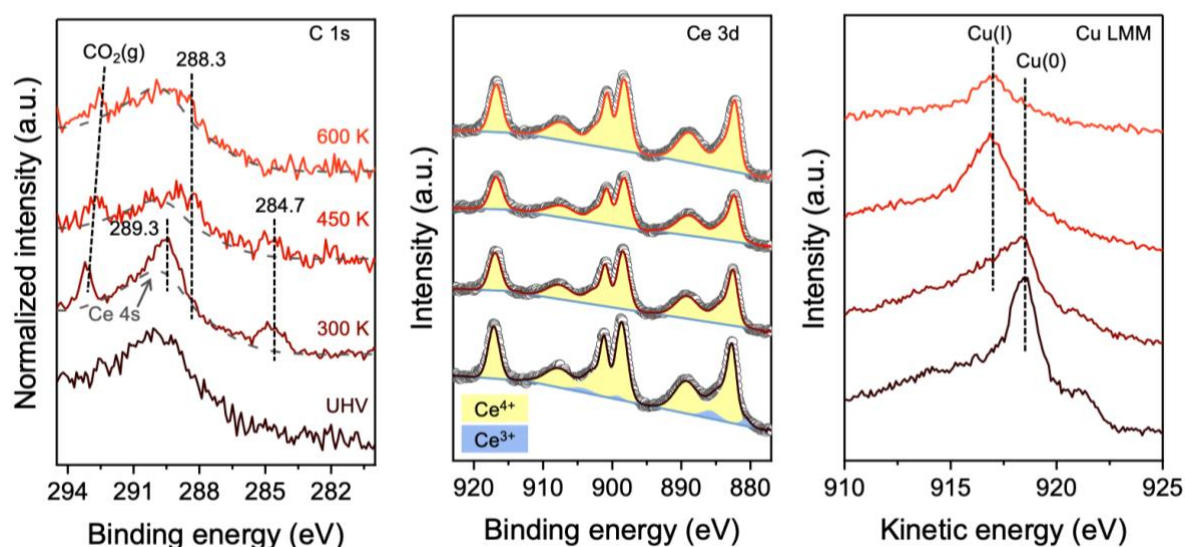


Figure 4.2 C 1s, Ce 3d, and Cu LMM spectra of the Cu/CeO_{2-x} model surface under UHV and 0.2 mbar of CO₂ at 300, 450, and 600 K. The difference in C 1s peaks for gas-phase CO₂ originates from the different sample-aperture distances which are optimized for each measurement.

Upon simultaneous exposure to CO₂ and H₂, significant changes are observed in the adsorbates and chemical states of the Cu/CeO_{2-x} model surface. Figure 4.3 shows a set of XPS spectra collected for a Cu/CeO_{2-x} model surface under the mixture of 0.2 mbar of CO₂ and 0.6 mbar of H₂ at 300–600 K. At 300 K, the C 1s region shows the presence of peaks from CO₂ gas, adsorbed carbonate/formate, and C₀ species. Although the intensity of the peak at 298.5 eV remains almost unchanged, there may be a conversion from carbonate to formate in the presence of H₂. Such a conversion is indicated by the increase of the HCOO⁻/CO₃²⁻ peak area ratio from 0.22:1 in CO₂ to 0.48:1 in CO₂/H₂ mixture, as shown in the inset of Figure S4.3. Thus, a further step in the RWGS reaction is revealed as the hydrogenation of carbonate to formate. Some early studies argued that formate species accumulate on the catalyst surfaces and may be a spectator in CO₂ hydrogenation process.⁵⁰ However, theoretical calculations proved that formate is a reactive intermediate for CO₂ conversion to methanol, rather than a spectator, even though it accumulates on Cu/ZrO₂ surface.⁵¹ Furthermore, DRIFTS, IRRAS, NAP-XPS studies, and theoretical calculations also showed that the activation barrier for the rate-limiting step in the carbonate, formate, and carbonyl pathways is dependent on the catalysts, and the Cu/CeO_{2-x} interface can lower the activation barrier for the formate pathway.^{9,10,48,52–55}

Thus, in our NAP-XPS study, the RWGS route on the Cu/CeO_{2-x} surface via CO₂ dissociation in the form of carbonate, the conversion of carbonate to formate, and the decomposition of formate to CO becomes feasible.

Both the preserved Ce³⁺ features in the Ce 3d region and a slight growth of the Cu⁺ feature as shown in the Cu LMM region accompany the transformation of carbonate to formate at 300 K. These results suggest that Cu⁺ species may also be involved in the CO₂ hydrogenation process at low reaction temperatures, in agreement with the observation of Cu⁺-CO intermediate proposed in a combined XAS and DRIFTS study on a Cu/CeO_{2-x} catalyst for CO₂ hydrogenation.¹⁴ Upon heating to 450 and 600 K, the formate and carbonate peaks disappear, and the C₀ species continuously accumulate due to the complete decomposition of CO₂ and deposition of adventitious carbon during a prolonged heating period due to the existence of H₂.^{9,41,56,57} In addition, the fraction of Ce³⁺ on the model catalyst surface increased slightly from 2.7% at 300 K to 4.6% at 450 K. The Cu species, which was partially oxidized at 300 K, was mostly reduced at 450 K. As the temperature was increased to 600 K, ceria and Cu were further reduced, resulting in 9.4% Ce³⁺ and 100% of metallic Cu. With online RGA, we also detected decreased CO₂ and H₂ signals and increased CO and H₂O signals (Figure S4.4), indicating the model surface became catalytically active from 450 to 600 K, agreeing well with the activity of the powder catalyst. It should be noted here that the geometry of the NAP cell and the location of the RGA are not designed for accurate reactivity measurement, and total pressure (0.8 mbar) in the NAP cell is much smaller than that in the activity measurement (~1000 mbar) of the powder catalyst. With the RGA data in Figure S4.4, we can only qualitatively conclude that the Cu/CeO_{2-x} model surface is active for the RWGS reaction, but the determination of CO₂ conversion is not reliable. In addition, the CO₂ conversion over the Cu/CeO_{2-x} powder catalyst is as low as ~10% at the highest NAP-XPS experiment temperature (600 K). The CO₂ conversion over the model surface is expected to be even smaller. The CO₂ peak in the C 1s region can be observed in all the NAP-XPS conditions without significant change in the intensity. Thus, we concluded that the influence of mass transfer limitation is not critical in our NAP-XPS measurements.

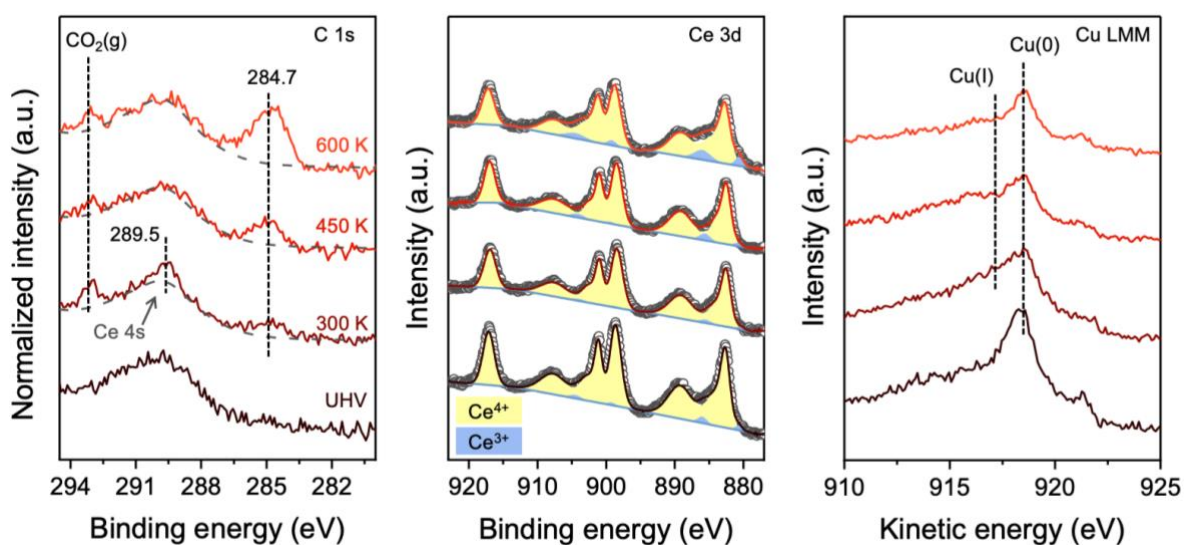


Figure 4.3 C 1s, Ce 3d, and Cu LMM spectra of the Cu/CeO_{2-x} model surface under UHV and 0.2 mbar of CO₂ + 0.6 mbar of H₂ at 300, 450, and 600 K.

We performed NAP-XPS measurements for a CeO_{2-x} thin film and a sputter-cleaned Cu foil under the same RWGS condition to elucidate the role of Cu. On the CeO_{2-x} thin film, we observed a slight reduction on the surface, but the amount of Ce^{3+} formed at 600 K ($\sim 4\%$) was much smaller than that formed on the Cu/CeO_{2-x} surface under similar conditions, as seen in Figure 4.4. Thus, we infer that the reduction of CeO_{2-x} surface and the generation of oxygen vacancies under the RWGS condition is promoted in the presence of Cu. As H_2 continuously dissociates on Cu and spillovers to the oxide support, a defective CeO_{2-x} surface favors CO_2 dissociation is maintained. This way, the high RWGS activity is achieved exclusively on the Cu/CeO_{2-x} surface.

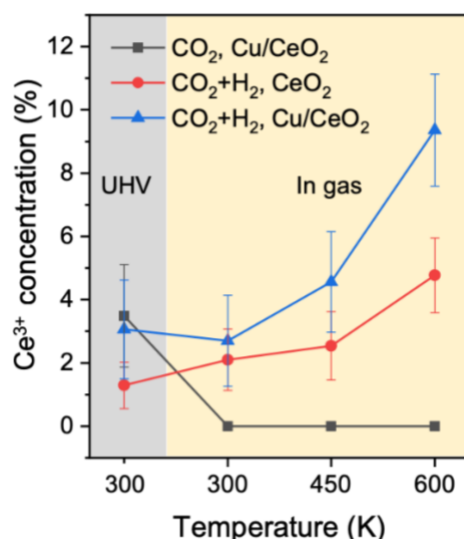


Figure 4.4 Ce^{3+} concentration determined by deconvolution of the Ce 3d XPS spectra as a function of temperature under reaction conditions. The error bars were the standard deviation of the Ce^{3+} concentration obtained from the measurement of three separately prepared samples.

The C 1s region spectra for the CeO_{2-x} and the Cu foil surface were also recorded under the RWGS condition and shown in Figure 4.5. We observed that in the C 1s region a much smaller amount of CO_2 was activated in the form of formate on the CeO_{2-x} surface than the Cu/CeO_{2-x} surface. On the Cu foil, the adsorption and dissociation of CO_2 were too weak to be clearly observed in the C 1s region. Thus, CO_2 cannot be activated on either the CeO_{2-x} or the Cu surface. The high activity of Cu/CeO_{2-x} catalysts for the RWGS reaction results from the dispersion of Cu on CeO_{2-x} , which creates abundant interfaces between Cu and defective ceria. Such a close proximity of Cu and CeO_{2-x} largely facilitates the interaction between H_2 and the model surface, as H_2 could dissociate on Cu surface and spillover to the CeO_{2-x} support, leading to the formation of Cu^0 and Ce^{3+} .^{14,19} Upon exposure to CO_2 , carbonate and Cu^+-CO intermediates formed due to the oxidation of Ce^{3+} to Ce^{4+} and Cu^0 to Cu^+ by CO_2 . When H_2 is also introduced, the conversion from carbonate to formate occurs. At elevated temperatures, the intermediates are rapidly hydrogenated and desorbed as CO, and the reduced sites (Cu^0 and Ce^{3+}) are regenerated, resulting in stable catalytic performance. Altogether, we conclude that the metal-oxide interface of Cu/CeO_{2-x} assists the formation of oxygen vacancies and adsorbs and activates CO_2 for the RWGS reaction.

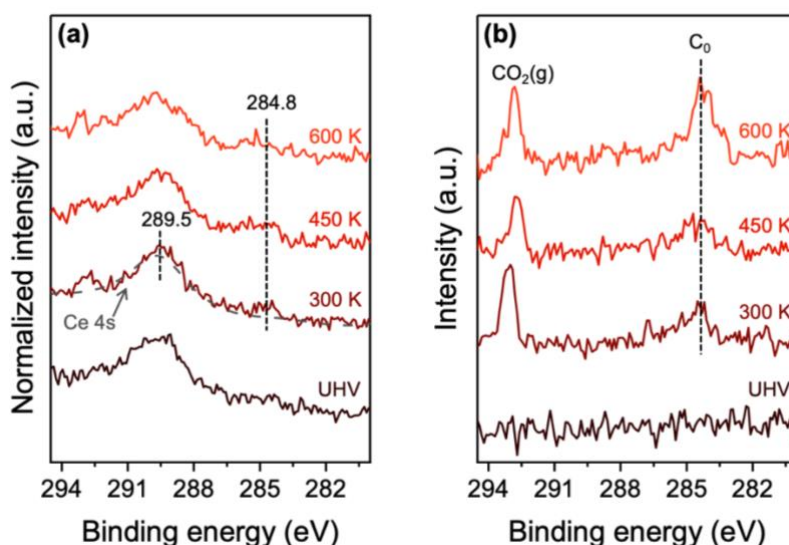


Figure 4.5 C 1s region spectra of (a) a CeO_{2-x} surface and (b) a Cu foil under UHV and 0.2 mbar of CO_2 + 0.6 mbar of H_2 at 300, 450, and 600 K.

To further confirm the existence of interfaces between Cu and CeO_{2-x} under the RWGS conditions, we performed SEM and TEM measurements on the planar Cu/ CeO_{2-x} model sample. The SEM image of the as-prepared Cu/ CeO_{2-x} sample (Figure S4.5) shows a rough surface composed of ceria islands⁵⁸. After exposure to the RWGS reaction atmosphere at 600 K, homogeneously distributed Cu nanoparticles can be observed (Figure 4.6a), indicating the agglomeration of Cu nanoparticles, which agrees with the decrease of Cu/Ce atomic ratio from 0.85 of the as-prepared sample to 0.17 of the reacted sample (Figure S4.6).

To further access the structure and chemistry of the abovementioned metal-oxide interface, we prepared a cross-sectional lamella (Figure S4.7) of the Cu/ CeO_{2-x} model sample after the RWGS reaction gain insight into the partially buried interfaces between Cu and ceria using STEM-EDX. The bright-field (BF) STEM and HAADF-STEM images of the Cu/ CeO_{2-x} sample (Figure 4.6b) clearly show a uniform ceria film of ~ 20 nm thick on the Au foil. The Cu nanoparticles are on the ceria film, in agreement with the SEM image. The elemental map of Cu, Ce, O, and Au obtained by EDX (Figure 4.6c) further confirms the chemical distribution of the Cu/ CeO_{2-x} model catalyst. The Cu nanoparticles with diameters of ~ 10 nm are anchored in the ceria overlayer, creating many metal-oxide interfaces for the activation and hydrogenation of CO_2 .

Notably, a small amount of Cu also diffuses into the ceria and Au substrates (Figure 4.6c and Figure S4.8). Such a phenomenon can associate with the strong metal-support interactions (SMSI) between Cu and ceria during the RWGS reaction. SMSI has been observed previously on metal nanoparticles supported on reducible supports (TiO_2 , CeO_2 , etc.) and been assigned to the origin of improved CO_2 hydrogenation performance.^{55,59,60} In this work, we show direct evidence of SMSI on a model Cu/ CeO_{2-x} catalyst and reveal that Cu nanoparticles are still well dispersed on CeO_{2-x} in both powder (Figure 4.1a) and model catalysts (Figure 4.6c). These results also demonstrate that Cu/ CeO_{2-x} catalysts are of good stability under CO_2 hydrogenation conditions, which is crucial in industrial applications.

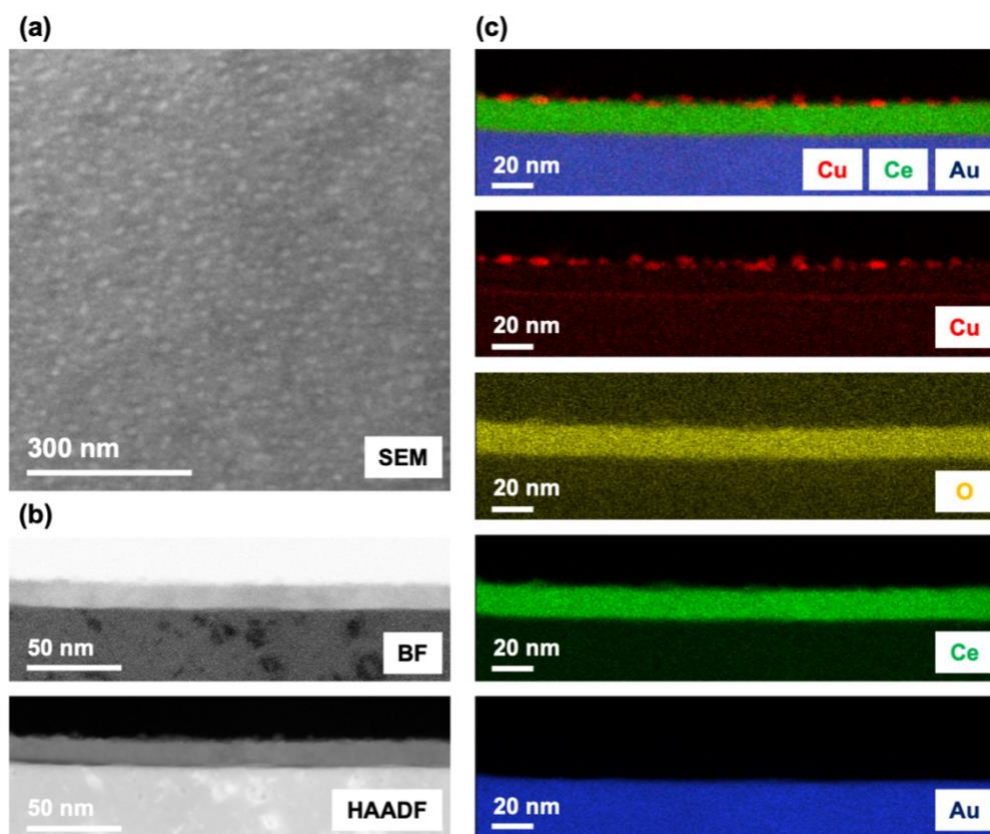


Figure 4.6 (a) Surface SEM, (b) cross-sectional STEM-BF and STEM-HAADF images, and (c) corresponding EDX elemental map of the Cu/CeO_{2-x} model surface after exposure to 0.2 mbar of CO₂ + 0.6 mbar of H₂ at 600 K for 1 h.

Next, the activation and hydrogenation mechanism of CO₂ at the interface of Cu and CeO_{2-x} is discussed. Previously, the reaction mechanism and intermediates of the RWGS reaction have been investigated using DRIFTS and MS over different powder catalysts. On Pt/CeO₂ surface, formate, Pt-carbonyl, and carbonate were all proposed as possible main reaction intermediates, and thus, a conclusive reaction route was not achieved.⁶¹ At the same time, in situ DRIFTS study on powder Cu/CeO₂ catalysts^{14,19} and density function theory (DFT) calculations^{62,63} suggested that the transformation from carbonate to formate facilitated by H adatoms is the crucial step for highly efficient RWGS reaction. However, the chemical states evolution of the metal and support was characterized in separate experiments by XRD, XAS, or Raman spectroscopy, which are all decoupled from the characterization of surface intermediates and the activity test. Consequently, the combined effects of H₂ and CO₂, i.e., reduction of Cu and CeO₂ by H₂ and oxidation of Cu and CeO₂ by oxygen during CO₂ activation, were not clearly elucidated.

In this work, we monitored reaction intermediates and surface chemical states simultaneously using in operando NAP-XPS. And combined with the results obtained from practical powder sample, a comprehensive rationalization of the reaction mechanisms of the RWGS reaction is graphically illustrated in Figure 4.7a. First, CO₂ is activated on the Cu/CeO_{2-x} surface in the form of carbonate on the Ce³⁺ sites with oxygen vacancies. With the addition of H₂, the carbonate is converted to formate and further decomposes to CO with the assistance of surface hydroxyl groups. Meanwhile, Cu is partially oxidized to Cu⁺ and reduced. Although the Cu⁺-CO intermediate cannot be observed by NAP-XPS, we do not exclude the potential carbonyl route as a

result of direct C-O bond cleavage. At elevated temperatures (450–600 K), the metallic Cu is regenerated, ensuring the dissociation and spillover of H₂. Meanwhile, the ceria surface is not re-oxidized, preserving the oxygen vacancies. Therefore, the Cu/Cu⁺ pairs and Cu/CeO_{2-x} interfaces work individually and cooperatively as active sites for converting CO₂ to CO through different mechanisms, namely direct C-O bond cleavage and the formate route, leading to high CO₂ conversion.

In comparison, on a pure CeO_{2-x} surface, no conversion from carbonate to formate was observed (Figure 4.5a), indicating that the formation of CO directly from carbonate is not the main reaction route (Figure 4.7b). On the Cu surface, CO₂ is very difficult to be activated in any form (Figure 4.5b), and thus the catalytic hydrogenation of CO₂ is not favored (Figure 4.7c). Moreover, cross-sectional STEM images confirms that Cu nanoparticles are stable on defective CeO_{2-x} under RWGS conditions because of SMSI. Meanwhile, the Cu/CeO_{2-x} model surface was proven to be catalytic active. Thus, a bridge between the model catalysts and practical catalysts and information about the surface and bulk characterizations is established. Overall, the continuously renewed metal-oxide interfaces composing Cu and oxygen-deficient ceria explains the preferential formation of formate intermediate, and thus, the origin of the high RWGS activity of Cu/CeO_{2-x} catalysts.

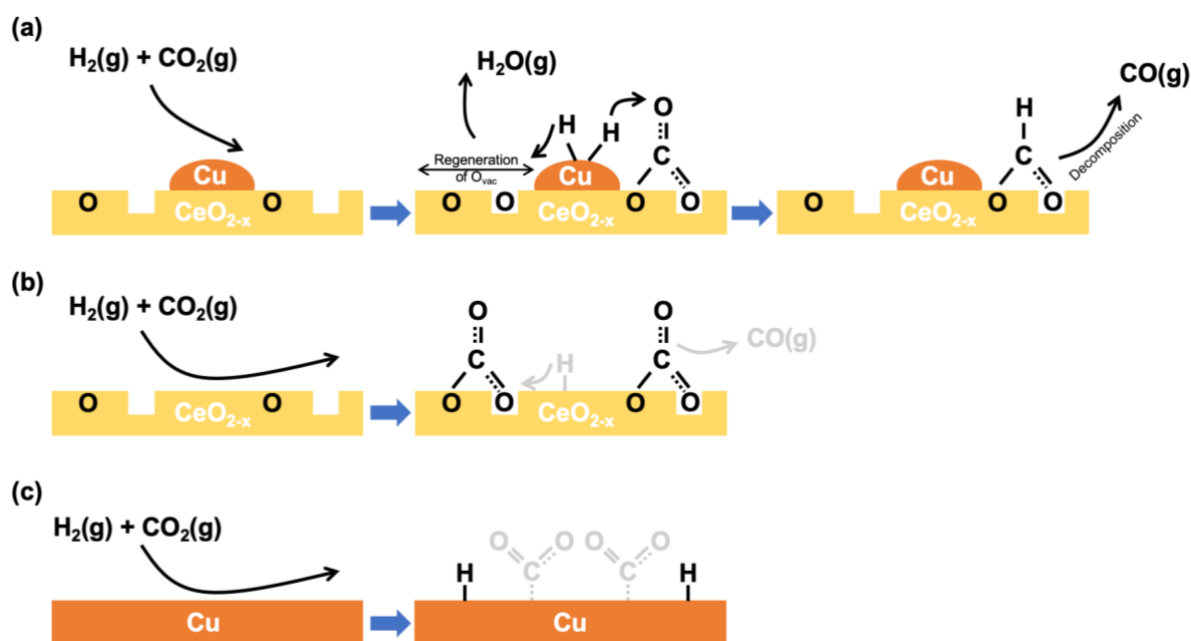


Figure 4.7 (a) Schematic illustration for the activation of CO₂ and regeneration of oxygen vacancies during the RWGS reaction over the Cu/CeO_{2-x} surface, and the interaction between CO₂/H₂ and (b) CeO_{2-x} or (c) Cu surface.

4.4 Conclusions

An active Cu/CeO_{2-x} catalyst for the RWGS reaction was synthesized and a comprehensive mechanistic insight was achieved over the corresponding Cu/CeO_{2-x} model surface using NAP-XPS. The cross-sectional structure and chemical composition of the Cu/CeO_{2-x} model catalyst were visualized by STEM-EDX after the RWGS reaction and confirmed the presence of metal-oxide interfaces where the CO₂ hydrogenation occurred. We show a detailed description of the RWGS reaction on the surface of the Cu/CeO_{2-x} model catalyst. CO₂ was activated in the form of carbonate by partially reduced ceria with oxygen vacancies. Meanwhile, H₂

dissociated on metallic Cu, converted the carbonate intermediates to formates, and the formates decomposed to CO at elevated temperatures. During this process, the dissociated H can keep the Cu sites reduced and regenerate the CeO_{2-x} sites with oxygen vacancies under the RWGS conditions. Due to the rich interfaces between Cu and CeO_{2-x} , a highly efficient RWGS reaction was maintained, and the active sites are continuously renewed. The synergy between Cu and CeO_{2-x} was proven to be the origin of a stable and effective conversion from CO_2 to CO. The Cu/ CeO_{2-x} model surface showed RWGS activity under mild conditions at as low as 450 K, establishing a correlation between the activity investigation on the real catalyst and the surface investigation on the model catalyst. Our results showed a simultaneous observation of the active sites and the surface intermediates during the RWGS reaction over Cu/ CeO_{2-x} catalyst, providing complementary insights into the roles of copper and ceria during CO_2 hydrogenation.

References

1. Goeppert, A., Czaun, M., Jones, J.-P., Surya Prakash, G. K. & Olah, G. A. Recycling of carbon dioxide to methanol and derived products - closing the loop. *Chemical Society Reviews* 43, 7995–8048 (2014).
2. Züttel, A. et al. Storage of Renewable Energy by Reduction of CO₂ with Hydrogen. *CHIMIA International Journal for Chemistry* 69, 264–268 (2015).
3. Zheng, Y. et al. Energy related CO₂ conversion and utilization: Advanced materials/nanomaterials, reaction mechanisms and technologies. *Nano Energy* 40, 512–539 (2017).
4. De, S., Dokania, A., Ramirez, A. & Gascon, J. Advances in the Design of Heterogeneous Catalysts and Thermocatalytic Processes for CO₂ Utilization. *ACS Catal.* 10, 14147–14185 (2020).
5. Tian, P., Wei, Y., Ye, M. & Liu, Z. Methanol to Olefins (MTO): From Fundamentals to Commercialization. *ACS Catal.* 5, 1922–1938 (2015).
6. Su, X., Yang, X., Zhao, B. & Huang, Y. Designing of highly selective and high-temperature endurable RWGS heterogeneous catalysts: recent advances and the future directions. *Journal of Energy Chemistry* 26, 854–867 (2017).
7. Roy, S., Cherevotan, A. & Peter, S. C. Thermochemical CO₂ Hydrogenation to Single Carbon Products: Scientific and Technological Challenges. *ACS Energy Lett.* 3, 1938–1966 (2018).
8. Behrens, M. et al. The Active Site of Methanol Synthesis over Cu/ZnO/Al₂O₃ Industrial Catalysts. *Science* 336, 893–897 (2012).
9. Graciani, J. et al. Highly active copper-ceria and copper-ceria-titania catalysts for methanol synthesis from CO₂. *Science* 345, 546–550 (2014).
10. Rodriguez, J. A., Grinter, D. C., Liu, Z., Palomino, R. M. & Senanayake, S. D. Ceria-based model catalysts: fundamental studies on the importance of the metal–ceria interface in CO oxidation, the water–gas shift, CO₂ hydrogenation, and methane and alcohol reforming. *Chem. Soc. Rev.* 46, 1824–1841 (2017).
11. Zhang, Y. et al. Unraveling the physical chemistry and materials science of CeO₂-based nanostructures. *Chem* 0, (2021).
12. Senanayake, S. D. et al. Hydrogenation of CO₂ to Methanol on CeO_x/Cu(111) and ZnO/Cu(111) Catalysts: Role of the Metal–Oxide Interface and Importance of Ce³⁺ Sites. *J. Phys. Chem. C* 120, 1778–1784 (2016).
13. Winter, L. R. et al. Elucidating the roles of metallic Ni and oxygen vacancies in CO₂ hydrogenation over Ni/CeO₂ using isotope exchange and in situ measurements. *Applied Catalysis B: Environmental* 245, 360–366 (2019).
14. Yang, S.-C. et al. Synergy between Ceria Oxygen Vacancies and Cu Nanoparticles Facilitates the Catalytic Conversion of CO₂ to CO under Mild Conditions. *ACS Catalysis* (2018) doi:10.1021/acscatal.8b04219.
15. Gamarra, D. et al. Structure–Activity Relationship in Nanostructured Copper–Ceria-Based Preferential CO Oxidation Catalysts. *J. Phys. Chem. C* 111, 11026–11038 (2007).
16. Liu, Y. et al. Highly active copper/ceria catalysts for steam reforming of methanol. *Applied Catalysis A: General* 223, 137–145 (2002).
17. Yang, B., Deng, W., Guo, L. & Ishihara, T. Copper-ceria solid solution with improved catalytic activity for hydrogenation of CO₂ to CH₃OH. *Chinese Journal of Catalysis* 41, 1348–1359 (2020).
18. Zhu, J. et al. Mechanism and Nature of Active Sites for Methanol Synthesis from CO/CO₂ on Cu/CeO₂. *ACS Catal.* 10, 11532–11544 (2020).
19. Lin, L. et al. In Situ Characterization of Cu/CeO₂ Nanocatalysts for CO₂ Hydrogenation: Morphological Effects of Nanostructured Ceria on the Catalytic Activity. *J. Phys. Chem. C* 122, 12934–12943 (2018).
20. Lukashuk, L. et al. Operando XAS and NAP-XPS studies of preferential CO oxidation on Co₃O₄ and CeO₂-Co₃O₄ catalysts. *Journal of Catalysis* 344, 1–15 (2016).
21. Tsoukalou, A. et al. Structural Evolution and Dynamics of an In₂O₃ Catalyst for CO₂ Hydrogenation to Methanol: An Operando XAS-XRD and In Situ TEM Study. *J. Am. Chem. Soc.* 141, 13497–13505 (2019).
22. Zhao, K., Wang, L., Calizzi, M., Moiola, E. & Züttel, A. In Situ Control of the Adsorption Species in CO₂ Hydrogenation: Determination of Intermediates and Byproducts. *J. Phys. Chem. C* 122, 20888–20893 (2018).
23. Prosvirin, I. P., Bukhtiyarov, A. V., Bluhm, H. & Bukhtiyarov, V. I. Application of near ambient pressure gas-phase X-ray photoelectron spectroscopy to the investigation of catalytic properties of copper in methanol oxidation. *Applied Surface Science* 363, 303–309 (2016).
24. Nguyen, L., Tao, F. F., Tang, Y., Dou, J. & Bao, X.-J. Understanding Catalyst Surfaces during Catalysis through Near Ambient Pressure X-ray Photoelectron Spectroscopy. *Chem. Rev.* 119, 6822–6905 (2019).
25. Wu, H. et al. Dynamic nanoscale imaging of enriched CO adlayer on Pt(111) confined under h-BN monolayer in ambient pressure atmospheres. *Nano Res.* 12, 85–90 (2019).
26. Wang, C., Tissot, H., Soldemo, M., Lu, J. & Weissenrieder, J. Inverse single-site Fe¹(OH)X/Pt(111) model catalyst for preferential oxidation of CO in H₂. *Nano Res.* (2021) doi:10.1007/s12274-021-3551-4.

27. Li, M., Luo, W. & Züttel, A. Near ambient-pressure X-ray photoelectron spectroscopy study of CO₂ activation and hydrogenation on indium/copper surface. *Journal of Catalysis* (2021) doi:10.1016/j.jcat.2021.01.010.
28. Liu, Z. et al. Dry Reforming of Methane on a Highly-Active Ni-CeO₂ Catalyst: Effects of Metal-Support Interactions on C–H Bond Breaking. *Angewandte Chemie International Edition* 55, 7455–7459 (2016).
29. Skála, T., Šutara, F., Prince, K. C. & Matolín, V. Cerium oxide stoichiometry alteration via Sn deposition: Influence of temperature. *Journal of Electron Spectroscopy and Related Phenomena* 169, 20–25 (2009).
30. Kato, S. et al. Quantitative depth profiling of Ce³⁺ in Pt/CeO₂ by in situ high-energy XPS in a hydrogen atmosphere. *Phys. Chem. Chem. Phys.* 17, 5078–5083 (2015).
31. Kim, D.-J. Lattice Parameters, Ionic Conductivities, and Solubility Limits in Fluorite-Structure MO₂ Oxide [M = Hf⁴⁺, Zr⁴⁺, Ce⁴⁺, Th⁴⁺, U⁴⁺] Solid Solutions. *Journal of the American Ceramic Society* 72, 1415–1421 (1989).
32. Hong, S. J. & Virkar, A. V. Lattice Parameters and Densities of Rare-Earth Oxide Doped Ceria Electrolytes. *Journal of the American Ceramic Society* 78, 433–439 (1995).
33. Bishop, S. R., Duncan, K. L. & Wachsman, E. D. Defect equilibria and chemical expansion in non-stoichiometric undoped and gadolinium-doped cerium oxide. *Electrochimica Acta* 54, 1436–1443 (2009).
34. Santra, A. K. & Goodman, D. W. Oxide-supported metal clusters: models for heterogeneous catalysts. *J. Phys.: Condens. Matter* 15, R31–R62 (2002).
35. Li, G., Hu, S., Xu, Q. & Zhu, J. Interaction between Cu Nanoparticles and CeO₂(111) Film Surfaces. *J. Phys. Chem. C* 123, 23563–23571 (2019).
36. Luches, P., Pagliuca, F. & Valeri, S. Morphology, Stoichiometry, and Interface Structure of CeO₂ Ultrathin Films on Pt(111). *J. Phys. Chem. C* 115, 10718–10726 (2011).
37. Paparazzo, E. Use and mis-use of x-ray photoemission spectroscopy Ce3d spectra of Ce₂O₃ and CeO₂. *J. Phys.: Condens. Matter* 30, 343003 (2018).
38. Mudiyanse, K. et al. Importance of the Metal–Oxide Interface in Catalysis: In Situ Studies of the Water–Gas Shift Reaction by Ambient-Pressure X-ray Photoelectron Spectroscopy. *Angewandte Chemie International Edition* 52, 5101–5105 (2013).
39. Li, H. et al. CO₂ activation on ultrathin ZrO₂ film by H₂O co-adsorption: In situ NAP-XPS and IRAS studies. *Surface Science* 679, 139–146 (2019).
40. Deng, X. et al. Surface Chemistry of Cu in the Presence of CO₂ and H₂O. *Langmuir* 24, 9474–9478 (2008).
41. Koitaya, T. et al. CO₂ Activation and Reaction on Zn-Deposited Cu Surfaces Studied by Ambient-Pressure X-ray Photoelectron Spectroscopy. *ACS Catal.* 9, 4539–4550 (2019).
42. Palomino, R. M. et al. Hydrogenation of CO₂ on ZnO/Cu(100) and ZnO/Cu(111) Catalysts: Role of Copper Structure and Metal–Oxide Interface in Methanol Synthesis. *The Journal of Physical Chemistry B* (2017) doi:10.1021/acs.jpbc.7b06901.
43. Hagman, B. et al. Steps Control the Dissociation of CO₂ on Cu(100). *J. Am. Chem. Soc.* 140, 12974–12979 (2018).
44. Ren, Y. et al. Probing the Reaction Mechanism in CO₂ Hydrogenation on Bimetallic Ni/Cu(100) with Near-Ambient Pressure X-Ray Photoelectron Spectroscopy. *ACS Appl. Mater. Interfaces* (2019) doi:10.1021/acsami.9b19523.
45. Poulston, S., Parlett, P. M., Stone, P. & Bowker, M. Surface Oxidation and Reduction of CuO and Cu₂O Studied Using XPS and XAES. *Surface and Interface Analysis* 24, 811–820 (1996).
46. Vasquez, R. P. Cu₂O by XPS. *Surface Science Spectra* 5, 257–261 (1998).
47. Zhu, C., Osherov, A. & Panzer, M. J. Surface chemistry of electrodeposited Cu₂O films studied by XPS. *Electrochimica Acta* 111, 771–778 (2013).
48. Favaro, M. et al. Subsurface oxide plays a critical role in CO₂ activation by Cu(111) surfaces to form chemisorbed CO₂, the first step in reduction of CO₂. *PNAS* 114, 6706–6711 (2017).
49. Li, C. et al. Carbon monoxide and carbon dioxide adsorption on cerium oxide studied by Fourier-transform infrared spectroscopy. Part 1.—Formation of carbonate species on dehydroxylated CeO₂, at room temperature. *J. Chem. Soc., Faraday Trans. 1* 85, 929–943 (1989).
50. Zhao, Y.-F. et al. Insight into methanol synthesis from CO₂ hydrogenation on Cu(111): Complex reaction network and the effects of H₂O. *Journal of Catalysis* 281, 199–211 (2011).
51. Hong, Q.-J. & Liu, Z.-P. Mechanism of CO₂ hydrogenation over Cu/ZrO₂(Z12) interface from first-principles kinetics Monte Carlo simulations. *Surface Science* 604, 1869–1876 (2010).
52. Yang, X. et al. Low Pressure CO₂ Hydrogenation to Methanol over Gold Nanoparticles Activated on a CeO_x/TiO₂ Interface. *J. Am. Chem. Soc.* 137, 10104–10107 (2015).
53. Eren, B., Weatherup, R. S., Liakakos, N., Somorjai, G. A. & Salmeron, M. Dissociative Carbon Dioxide Adsorption and Morphological Changes on Cu(100) and Cu(111) at Ambient Pressures. *J. Am. Chem. Soc.* 138, 8207–8211 (2016).
54. Yang, T. et al. Surface Orientation and Pressure Dependence of CO₂ Activation on Cu Surfaces. *J. Phys. Chem. C* (2020) doi:10.1021/acs.jpcc.0c08262.

-
55. Parastaev, A. et al. Boosting CO₂ hydrogenation via size-dependent metal–support interactions in cobalt/ceria-based catalysts. *Nature Catalysis* 3, 526–533 (2020).
 56. Ma, Y. et al. Reactivity of a Zirconia–Copper Inverse Catalyst for CO₂ Hydrogenation. *J. Phys. Chem. C* 124, 22158–22172 (2020).
 57. Su, H. et al. Probing the surface chemistry for reverse water gas shift reaction on Pt(111) using ambient pressure X-ray photoelectron spectroscopy. *Journal of Catalysis* 391, 123–131 (2020).
 58. Zhou, Y., Perket, J. M., Crooks, A. B. & Zhou, J. Effect of Ceria Support on the Structure of Ni Nanoparticles. *J. Phys. Chem. Lett.* 1, 1447–1453 (2010).
 59. Fan, L. & Fujimoto, K. Promotive SMSI Effect for Hydrogenation of Carbon Dioxide to Methanol on a Pd/CeO₂ Catalyst. *Journal of Catalysis* 150, 217–220 (1994).
 60. Bahmanpour, A. M. et al. Cu–Al Spinel as a Highly Active and Stable Catalyst for the Reverse Water Gas Shift Reaction. *ACS Catal.* 9, 6243–6251 (2019).
 61. Goguet, A., Meunier, F. C., Tibiletti, D., Breen, J. P. & Burch, R. Spectrokinetic Investigation of Reverse Water-Gas-Shift Reaction Intermediates over a Pt/CeO₂ Catalyst. *J. Phys. Chem. B* 108, 20240–20246 (2004).
 62. Yang, Y., Evans, J., Rodriguez, J. A., White, M. G. & Liu, P. Fundamental studies of methanol synthesis from CO₂ hydrogenation on Cu(111), Cu clusters, and Cu/ZnO(000). *Phys. Chem. Chem. Phys.* 12, 9909–9917 (2010).
 63. Kattel, S., Ramírez, P. J., Chen, J. G., Rodriguez, J. A. & Liu, P. Active sites for CO₂ hydrogenation to methanol on Cu/ZnO catalysts. *Science* 355, 1296–1299 (2017).

Supporting information

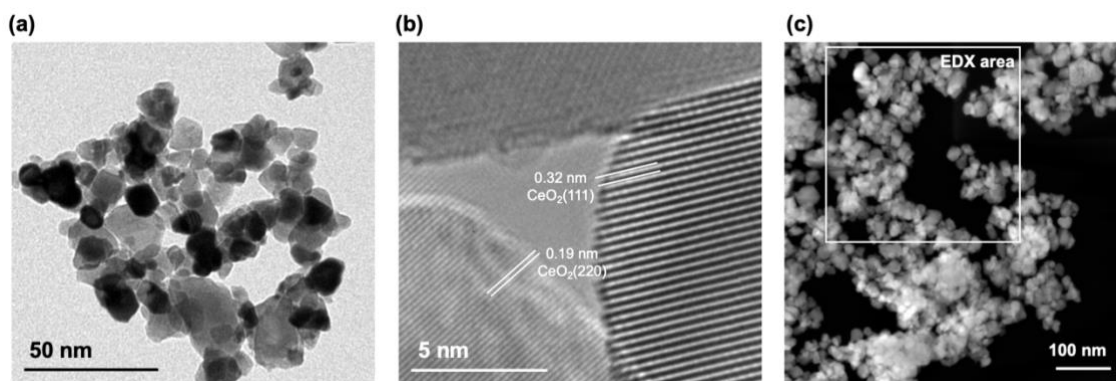


Figure S4.1 Representative (a) TEM, (b) HRTEM, (c) HAADF-STEM images of the Cu/CeO_{2-x} catalyst. The area for EDX element map is shown in (c).

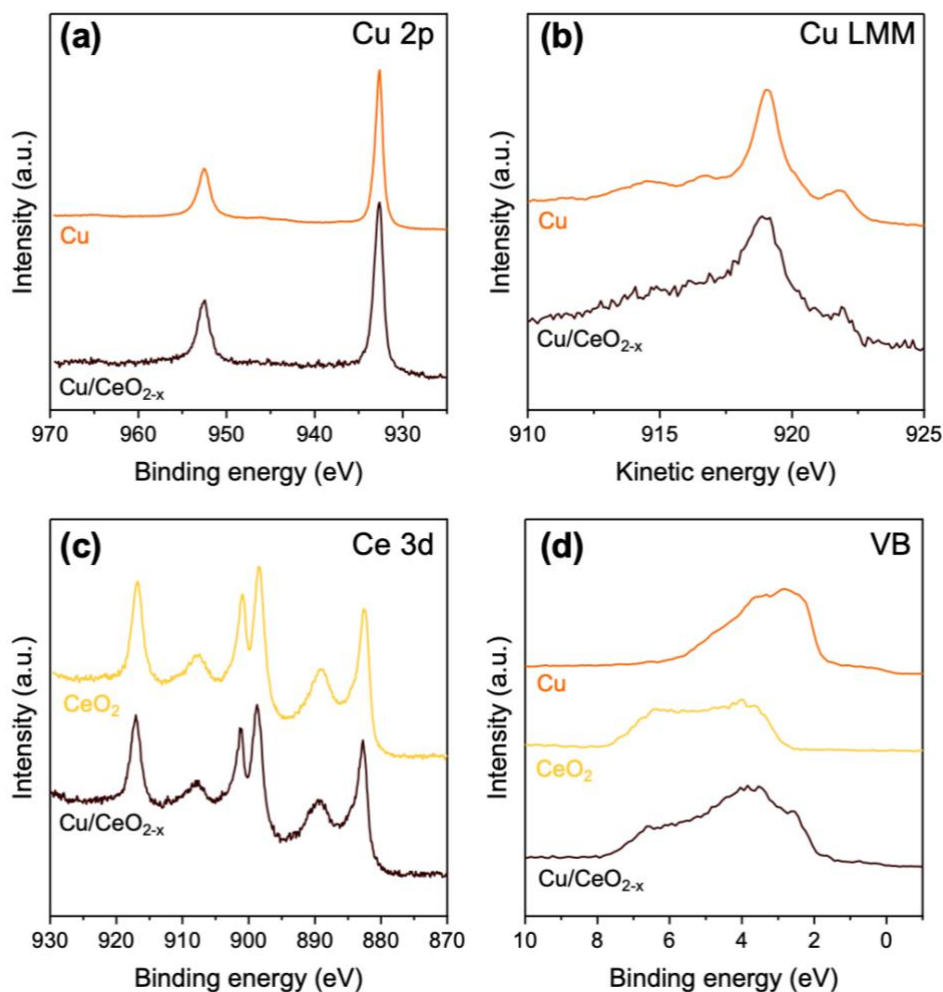
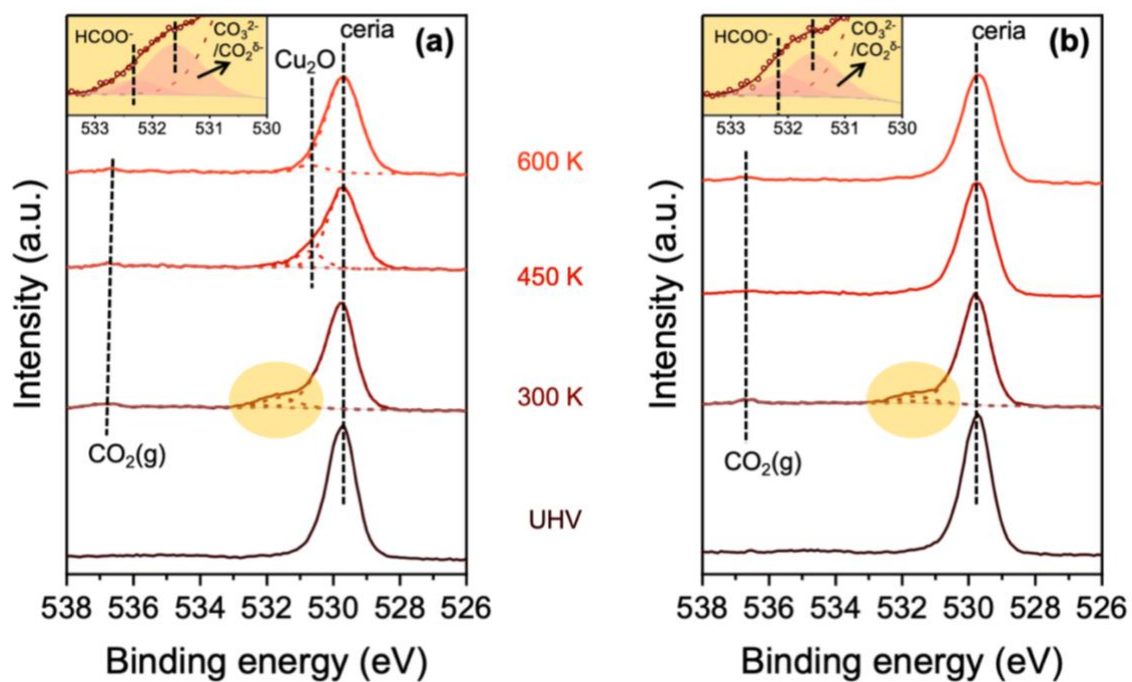


Figure S4.2 (a) Cu 2p, (b) Cu LMM Auger, (c) Ce 3d region XPS spectra, and (d) X-ray excited valence band spectra of the Cu/CeO_{2-x} model surface, a fully oxidized CeO₂ thin film sample prepared by oxidation (0.5 mbar O₂, 423 K, 60 min) of the reactive deposited ceria thin film, and a sputter-cleaned metallic Cu foil.



Peak assignment	Peak position		FWHM/eV		Peak area	
	CO ₂	CO ₂ +H ₂	CO ₂	CO ₂ +H ₂	CO ₂	CO ₂ +H ₂
CO ₃ ²⁻ /CO ₂ ^{δ-}	531.6	531.6	1.1	1.1	726	461
HCOO ⁻	532.3	532.1	1.0	1.0	159	221

Figure S4.3 O 1s spectra of the Cu/CeO_{2-x} model surface under UHV and (a) 0.2 mbar of CO₂, and (b) 0.2 mbar CO₂ + 0.6 mbar of H₂ at 300, 450, and 600 K. The peak positions and FWHMs used in the deconvolution is shown in the table below the figures.

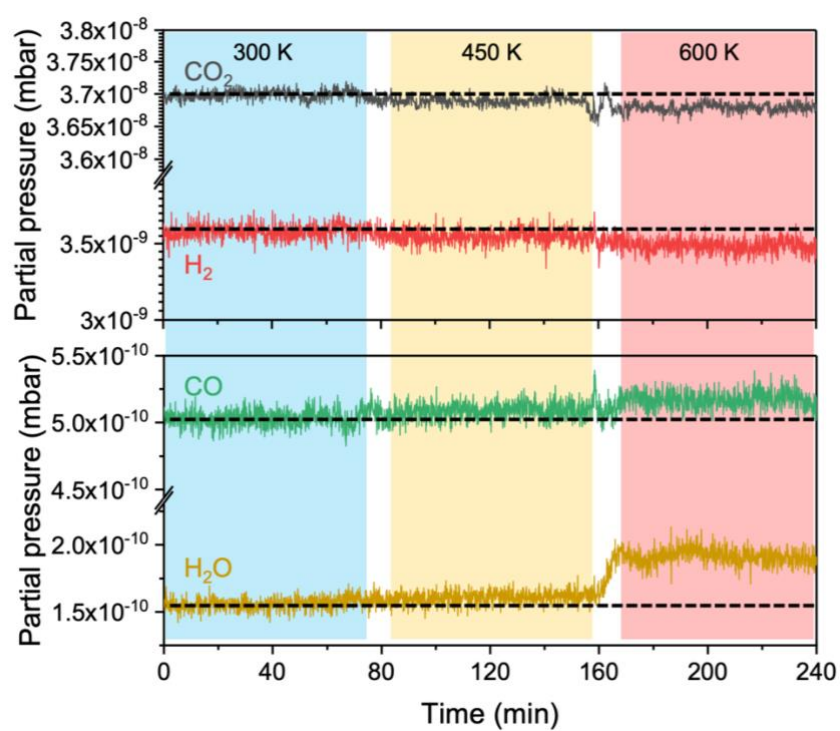


Figure S4.4 Gas species detected by MS at the pre-lens stage of the NAP-XPS during measurements of the Cu/CeO_{2-x} model surface under 0.2 mbar CO₂ + 0.6 mbar of H₂ at 300, 450, and 600 K.

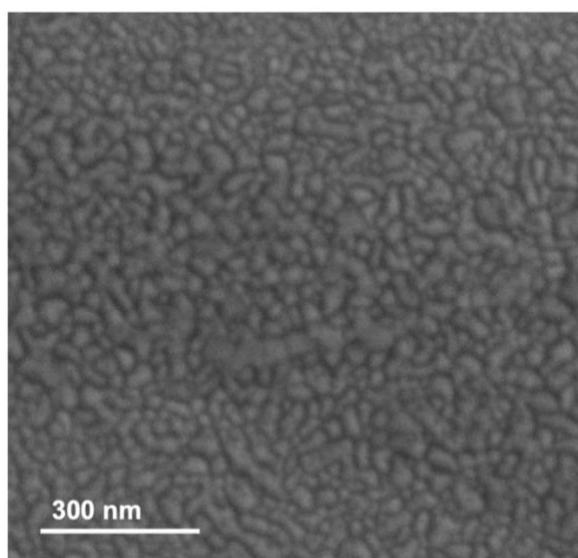


Figure S4.5 SEM image of as-prepared Cu/CeO_{2-x} model surface.

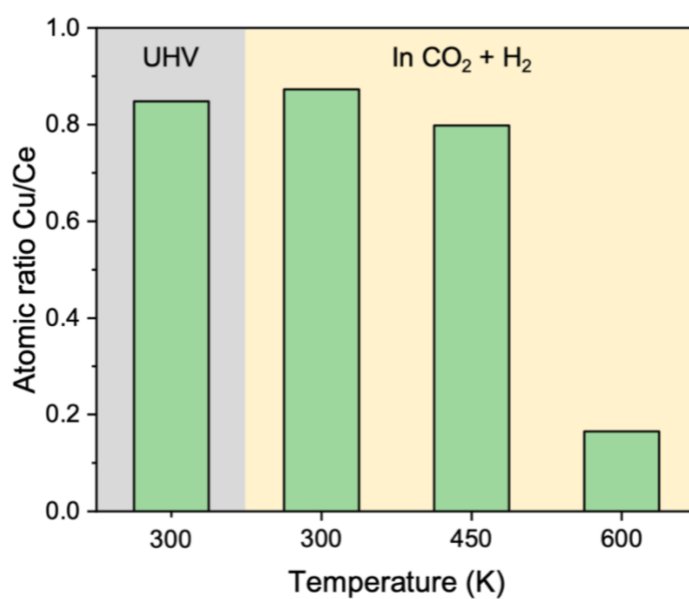


Figure S4.6 The atomic ratio of Cu/Ce on the Cu/CeO_{2-x} model surface under UHV and 0.2 mbar of CO₂ + 0.6 mbar of H₂ at 300, 450, and 600 K, determined by the Cu 2p and Ce 3d peak areas after correction by their corresponding RSFs

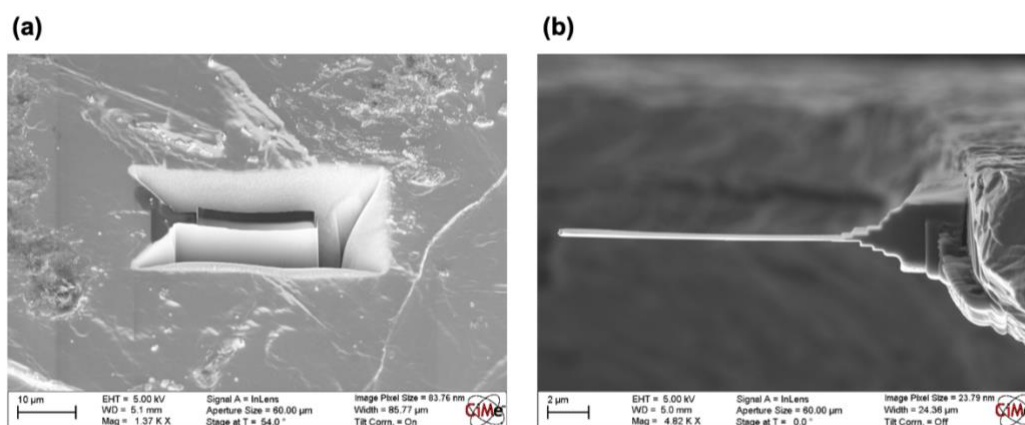


Figure S4.7 TEM lamella of the thin-film Cu/CeO_{2-x} sample prepared by FIB: (a) the cut volume with surface protection by carbon before lift-out, (b) the electron-transparent TEM lamella glued on Mo grid after thinning.

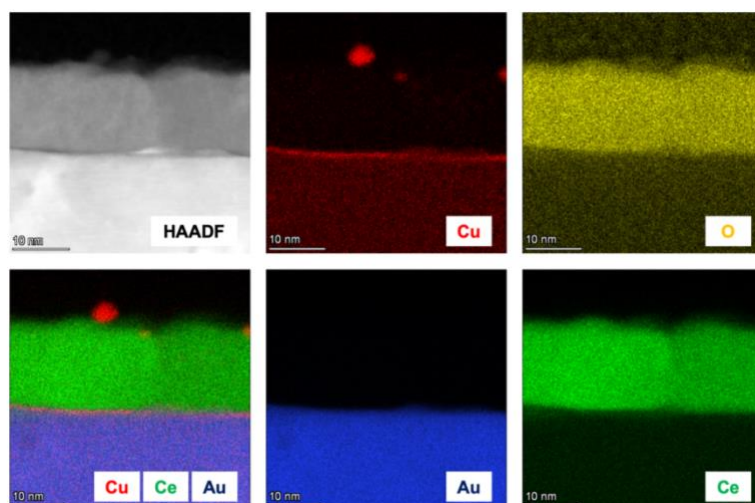


Figure S4.8 Additional cross-sectional STEM-HAADF image, and STEM/EDX elemental map of the Cu/CeO_{2-x} model surface after exposure to 0.2 mbar of CO₂ + 0.6 mbar of H₂ at 600 K for 1 h.

Chapter 5 Support-dependent Cu-In bimetallic catalysts for tailoring the activity of reverse water gas shift reaction

Mo Li^{a,b}, Thi Ha My Pham^{a,b}, Youngdon Ko^{a,b}, Dr. Kun Zhao^c, Dr. Wen Luo^{a,b,d*}, Prof. Dr. Andreas Züttel^{a,b}

a. Laboratory of Materials for Renewable Energy (LMER), Institute of Chemical Sciences and Engineering (ISIC), Basic Science Faculty (SB), École Polytechnique Fédérale de Lausanne (EPFL) Valais/Wallis, Energypolis, Rue de l'Industrie 17, CH-1951 Sion, Switzerland

b. Empa Materials Science & Technology, CH-8600 Dübendorf, Switzerland

c. Department of Chemistry, University of Washington, Seattle, Washington 98195-1700, United States

d. School of Environmental and Chemical Engineering, Shanghai University, 99 Shangda Road, Shanghai 200444, China

*Corresponding author: wen.luo@epfl.ch

Preprint version: preprint version of this manuscript is under review of *Chemical Engineer Journal*.

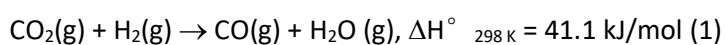
Edit: caption numbers of figures, tables, and equations were edited to match the thesis chapter number.

Abstract

Cu-based bimetallic catalysts have attracted great attentions for the reverse water gas shift (RWGS) reaction due to their high activity and selectivity. In this work, we report the application of Cu-In bimetallic catalysts for the RWGS reaction and demonstrated that the promotion effect of In over Cu is support sensitive. A series of Cu and Cu-In catalysts supported by ZrO₂ or CeO₂ were synthesized and tested for the RWGS reaction. We found that Cu-In/ZrO₂ exhibited significantly higher CO₂ conversion compared to the Cu/ZrO₂ catalyst, while the CO₂ conversion over Cu-In/CeO₂ was much lower than that of Cu/CeO₂. Through systematic characterizations, it was revealed that Cu and In formed Cu-In alloys on ZrO₂ thus promoted the activation of CO₂ by the oxygen vacancies from In₂O₃. While on CeO₂ support, Cu and In were in the form of metallic Cu and In₂O₃, receptivity, and the dispersion of Cu and the formation of oxygen vacancies on CeO₂ were aggravated by the introduction of In, leading to decreased RWGS activity. Among all studied catalysts, Cu supported by CeO₂ has the best RWGS activity because of highly active interfaces between metallic Cu and partially reduced CeO₂, as well as the strong CO₂ activation ability of the partially reduced CeO₂ support. These results demonstrate that a better understanding of the active phases, the surface compositions, and the catalytic performance of supported bimetallic catalysts is of great importance for the design of bimetallic catalysts.

5.1 Introduction

The emission of carbon dioxide has been proven to be responsible for rapid and harmful global environmental changes and thus, there is an urgent need to reduce CO₂ emissions in short term and modify the carbon-based energy structure in long term without compromising our economic growth, national security, and living standards.^{1,2} Since hydrogen is one of the most efficient renewable energy carriers, CO₂ hydrogenation has been considered as a realistic and promising strategies to abate the CO₂ concentration and mitigate the depletion of fossil fuels.^{3–5} The reverse water gas shift (RWGS) reaction (Equation 1) is considered to be one of the most important CO₂ hydrogenation processes because its product, CO, can be converted to various liquid hydrocarbons (e.g. gasoline, diesel) and other value-added chemicals (e.g. olefins) via Fischer-Tropsch and other syngas-related process.^{6–8} Besides, RWGS is also a critical intermediate step of CO₂ hydrogenation to other key products, such as methane and methanol.^{9,10}



Copper-based catalysts supported by metal oxides are widely studied for RWGS reactions due to their high activity and selectivity.^{11–14} But such catalysts often suffer from the loss of Cu dispersion due to the severe sintering of Cu nanoparticles at RWGS working temperature.¹⁵ To increase the stability of Cu, preparation of bimetallic catalysts is a common strategy.^{13,16} Recent work has shown the potential of In₂O₃ and In-based bimetal as high-performance catalysts for RWGS, methanol synthesis, and CO₂ electrochemical reduction to CO.^{17–19} It has been proposed that In₂O₃ promotes the catalytic activity because of the existence of oxygen vacancies^{18,20}, and the formation of intermetallic In-M alloys leads to well-dispersed nanoparticles as the active phase^{21–23}. In our previous study, we have tracked the structural evolution of the Cu-In model catalysts under the CO₂ hydrogenation environment and demonstrated the important synergistic effects of Cu and In in improving the activation of CO₂. Therefore, it would be interesting to further investigate the performance of real working Cu-In catalysts for the RWGS reaction.

On the other hand, the catalytic performance of a Cu-based catalyst can also be enhanced by using proper supporting materials,²⁴ which can introduce oxygen vacancies²⁵, provide anchoring sites¹², tune electronic properties of the active sites²⁶, and/or create metal-oxide interface²⁷. For example, CeO₂ has been extensively studied as the support of RWGS catalysts because the highly active Ce⁴⁺/Ce³⁺ pairs and resulting oxygen vacancies can efficiently promote the dissociative adsorption of CO₂.^{14,25,28,29} Beyond that, supports also affect the compositions of active phases for bimetallic catalysts. Snider et al. and Gao et al. found that on SiO₂ support, In forms alloys with Pd, Ni and Cu, and the resulting alloy particles served as active sites for highly efficient methanol synthesis from CO₂.^{30,31} However, there is a need to deconvolute the effect of different supports on the formation of active phase and catalytic activity of bimetallic catalysts for CO₂ hydrogenation, especially for the Cu-In catalysts. Such an investigation can be achieved by systematically characterizing the surface chemical states of the catalyst and understanding the contribution of different phases and interfaces to the observed catalytic activity.

In the present work, we prepared Cu and Cu-In bimetallic catalysts supported by ZrO₂ and CeO₂ and investigated their performance in the RWGS reaction. We applied transmission electron microscopy (TEM), X-ray diffraction (XRD), X-ray photoelectron spectroscopy (XPS), and temperature-programmed reduction (TPR) to reveal the effect of supports on the formation of metal, oxide and alloy phases, thus to establish the structure-performance relationships. We also compared the adsorption of CO₂ on catalysts supported by ZrO₂ and CeO₂ using temperature-programmed desorption (TPD) and in situ diffuse reflectance infrared

Fourier transform spectroscopy (DRIFTS). We demonstrated that the promotion effect of Cu-In bimetallic interaction is support-dependent, and both surface concentration of the active phase and the CO₂ adsorption ability of the support should be taken into consideration for the design of highly active RWGS catalysts.

5.2 Experimental section

5.2.1 Catalyst preparation

All catalysts were prepared by the impregnation method. The metal precursor solutions consisted of Cu(NO₃)₂·3H₂O (Sigma-Aldrich) and/or In(NO₃)₃·xH₂O (Alfa Aesar) dissolved in 5 mL of deionized water. 2 g of ZrO₂ (Riedel-de Haën) or CeO₂ (Sigma-Aldrich) supports were dispersed in the precursor solutions by sonication followed with continuous stirring at 80 °C until a homogeneous slurry was formed. The slurries were then dried at 80 °C overnight and calcined at 600 °C for 4 h in air with a ramp of 10 °C /min. The calcination temperature was determined by TGA analysis of dried precursor slurries (Figure S2). The concentrations of the metal precursors were chosen to result in a nominal metal fraction of 10 wt.% with a Cu/In ratio of 10:0 or 5:5 (nominated as Cu10 and Cu5In5, respectively).

5.2.2 Catalyst characterizations

Transmission electron microscopy (TEM) images was obtained from a FEI Tecnai G2 Spirit microscope operating with 120 kV high voltage. High-angle annular dark-field scanning transmission electron microscopy (HAADF-STEM) images and coupled energy dispersive X-ray spectroscopy (EDX) element maps were obtained from a FEI Tecnai Osiris microscope with Super-X SDD EDX detectors operating with 200 kV high voltage. The samples were dispersed on Cu grids for TEM, and Ni grids for STEM/EDX to avoid the interference of Cu signal originated from the grid.

Thermogravimetric analysis (TGA) of dried catalyst precursors was carried out using a Netzsch TG209 F1 instrument in a dry air flow of 20 mL/min with 10 mL/min N₂ as purge gas. The sample (~30 mg) was placed in an alumina crucible and heated from 30 to 700 °C at a ramp of 10 °C/min. The specific surface areas (SSA) of calcined catalysts were calculated by multi-point Brunauer-Emmett-Teller (BET) method after N₂ adsorption measurements using a Belsorp Max II system at 77 K. X-ray diffraction (XRD) patterns of reduced catalysts were obtained from a Bruker D8 Advance instrument (40 kV, 40 mA, Cu K α radiation, λ = 0.154 nm). Grain sizes and mass fraction of the components were calculated using the Rietveld refinement with TOPAS 5 software at an accuracy of 10%. The metal (Cu and In) mass fraction in calcined catalysts were analyzed by an Agilent 5110 inductively coupled plasma optical emission spectrometry (ICP-OES) system, results are shown in Table S1.

The X-ray photoelectron spectroscopy (XPS) analysis was performed in Kratos Axis Supra XPS system (analysis chamber base pressure 2×10^{-10} mbar) equipped with a monochromated Al K α (1486.61 eV) X-ray source. The XPS spectra were recorded in the fixed analyzer transmission mode using pass energies of 160 eV for the survey and 20 eV for the narrow scans. A flood gun was used for charge compensation as the samples were poorly conductive. All spectra were calibrated with the binding energy of C 1s of adventitious carbon at 284.8 eV. The XPS spectra were fitted with CasaXPS using linear (only for Ce 3d region) or Shirley-type background subtraction. All symmetric peaks were modeled with Gaussian–Lorentzian line shape (GL90 for metallic Cu 2p and GL30 for the other regions), and the asymmetric peak of metallic In 3d region with the three-parameter Lorentzian line shape. Raman spectra of calcined and reduced catalysts were obtained from a

Renishaw inVia confocal Raman microscope with the 457 nm laser as excitation source. The power of the laser was 10 mW and the exposure time was 10 s.

For H₂ temperature programmed reduction (H₂-TPR), ~ 100 mg of calcined catalyst was fixed in the center of a quartz tube (i.d. = 9 mm) by quartz wool. The catalysts were pretreated in pure He flow at 400 °C for 1 h and cooled down to room temperature. Afterwards, H₂-TPR analysis was carried out in a 10 vol.% H₂/He flow from room temperature to 650 °C at a ramp of 10 °C/min. H₂ consumption was recorded by a quadrupole mass spectrometer (QMS, Pfeiffer Vacuum, OmniStar GSD 320) using the signal of $m/z = 2$ obtained from Faraday detector.

CO₂ temperature programmed desorption (CO₂-TPD) studies were performed with the same instrument as H₂-TPR. ~ 200 mg of calcined catalysts were reduced in a 10 vol.% H₂/He flow at 400 °C for 1 h followed by flushing with pure H₂ for 1 h. The catalysts were then cooled down to 50 °C, saturated with CO₂ in a 20 vol.% CO₂/He flow for 1 h, and the gas flow was switched to pure He to remove physisorbed CO₂ for 1 h. Afterwards, TPD was carried out in He flow from 50 to 650 °C at a ramp of 10 °C/min. The desorbed CO₂ was also recorded with the QMS using the signal of $m/z = 44$ obtained from secondary electron multiplier (SEM) detector.

The *in situ* diffuse reflectance infrared Fourier transform spectroscopy (DRIFTS) experiments were performed on a Bruker Tensor 27 FTIR spectrometer with a liquid N₂ cooled mercury cadmium telluride (MCT) detector at the resolution of 4 cm⁻¹ using 40 scans. ~ 5 mg of catalyst was grinded with KBr (FT-IR grade, Sigma-Aldrich) into fine powder and carefully packed into the sample holder. The samples were firstly reduced at 400 °C with 10 vol.% H₂/He and then flushed with pure He for 30 min. Afterwards, the temperature was cooled down to 300 °C in He and the background spectrum was recorded. Then the gas flow into the cell was switched in the following sequence: CO₂/H₂/He = 1:4:10, pure He, and H₂/He = 4:11. The total gas flow rate was kept at 15 mL/min. The spectra were recorded along all the steps until stable.

5.2.3 Catalyst tests

For the catalytic testing of RWGS reaction, ~ 100 mg of catalyst was placed in a quartz fixed-bed reactor. The calcined catalyst was reduced by 10 vol.% H₂/He at 400 °C and cooled down below 100 °C. Under the mixture of CO₂, H₂, and He (1:4:10), the catalyst was heated to 500 °C with the ramp of 10 °C/min. The total gas flow rate was kept at 15 mL/min and thus the space velocity was 3000 h⁻¹ assuming a voidage of 0.4. The temperature was measured with a K-type thermocouple positioned in the center of the catalyst bed. The outlet pipeline of the reactor was kept above 100 °C to avoid water condensation. The products were analyzed with a QMS using Faraday detector under multi concentration detection (MCD) mode, which has been calibrated using standard gas mixtures previously.

The thermodynamic equilibrium composition of RWGS reaction products were calculated by minimizing the Gibbs free energy using a self-written Matlab code. Thermodynamic data of CO₂, H₂, CO, and H₂O were taken from NIST Chemistry WebBook³².

5.3 Results

5.3.1 Catalytic performance and kinetics

The catalytic activity for RWGS reaction of the ZrO_2 - and CeO_2 -supported Cu10 and Cu5In5 catalysts was summarized and compared in Figure 5.1. The CO_2 conversion increases with the increase of temperature for all studied catalysts (Figure 5.1a and b), while the selectivity for CO maintained at 100% (Figure 5.1c and d), demonstrating the high selectivity of these catalysts for RWGS reaction. Figure 5.1a shows that ZrO_2 is barely active for RWGS reaction. Adding Cu onto ZrO_2 (Cu10/ ZrO_2 catalyst) can only slightly improve the reaction activity, showing an onset CO_2 conversion of 0.6% at 350 °C and a maximum conversion of 5.0% at 600 °C. Nevertheless, simultaneously adding of Cu and In can significantly enhance the catalytic performance: the RWGS rate over Cu5In5/ ZrO_2 is about 10 times that of Cu10/ ZrO_2 within a temperature range of 500–600 °C. In contrast, pure CeO_2 shows much higher CO_2 conversion than that of ZrO_2 , because the reducible nature of CeO_2 is beneficial for the activation and hydrogenation of CO_2 .^{35,36} The activity of CeO_2 can be dramatically improved by adding Cu, as shown in Figure 5.1b, the Cu10/ CeO_2 catalyst displays a CO_2 conversion of 6.8% at 300 °C and close to equilibrium conversions above 400 °C. However, despite that adding of Cu and In can also improve the RWGS rate of CeO_2 , the CO_2 conversion for the Cu5In5/ CeO_2 sample is lower than that of the Cu10/ CeO_2 sample at all temperatures. Therefore, these results clearly indicate that the catalytic performance of Cu and Cu-In based catalysts are highly influenced by the ZrO_2 and CeO_2 supports.

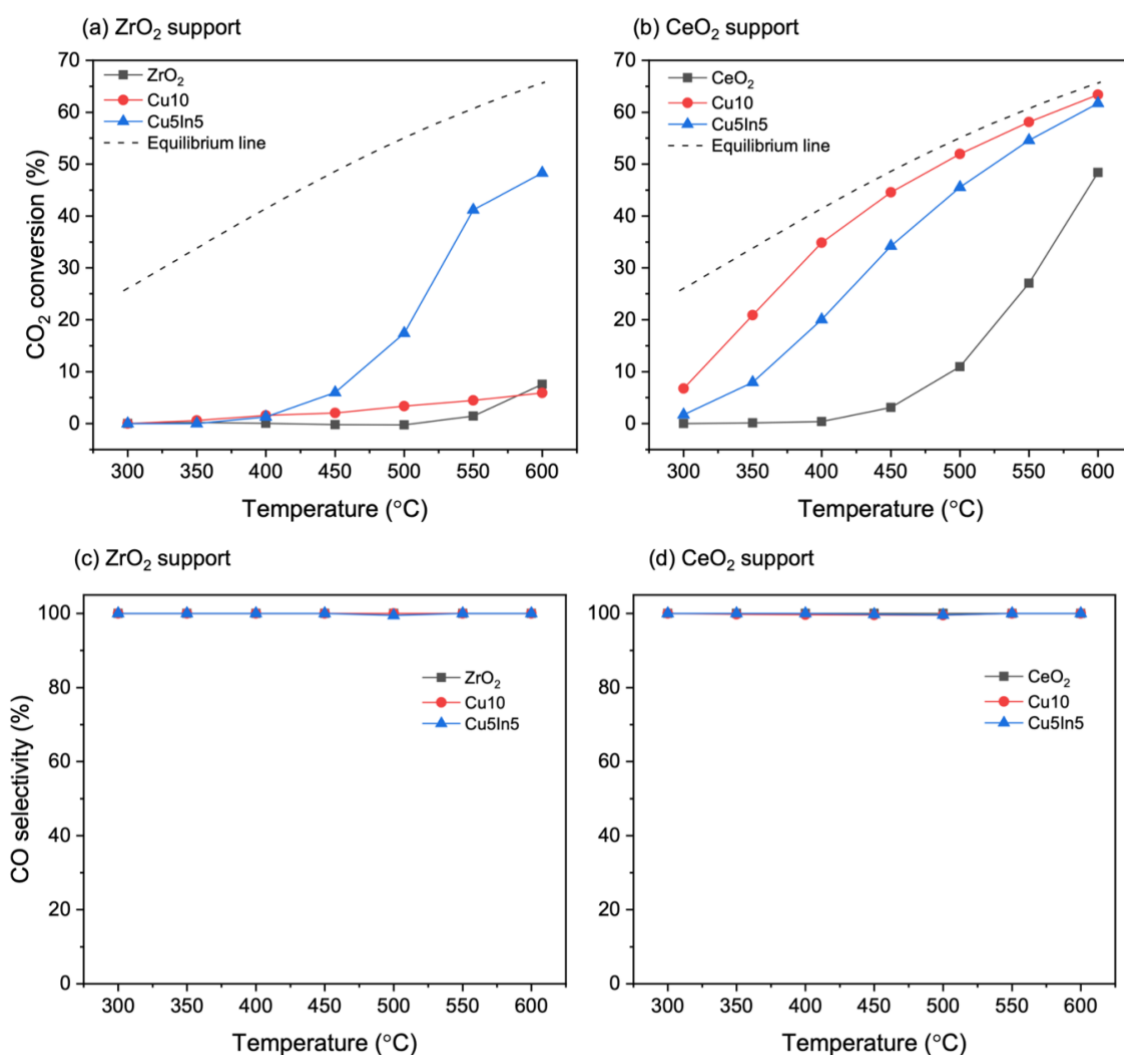


Figure 5.1 CO₂ conversion and CO selectivity of all studied Cu and Cu-In catalysts supported by ZrO₂ (a and c) and CeO₂ (b and d) as well as corresponding supports.

In order to further understand the different catalytic activities of ZrO₂- and CeO₂-supported Cu and Cu-In catalysts, kinetic studies were performed. The kinetically determined reaction temperature range, in which the slope of the Arrhenius plot is approximately constant, was identified for all catalysts. As shown in Table 5.1, this temperature range was found to be about 30 K for all studied catalysts. In addition, temperatures for the Arrhenius plot are generally lower for CeO₂-supported catalysts than those for ZrO₂-supported catalysts, due to that CeO₂-supported catalysts are more active and thus thermodynamic limitations play a role at relatively high temperatures. Based on a good linear fit ($R^2 > 0.99$) of experimental data points in the Arrhenius plot (Figure 5.2), the apparent activation energy (E_a) can be estimated for all catalysts (Table 5.1). It is clear that for ZrO₂-supported catalysts, the E_a decreases from 117 ± 6 for Cu10/ZrO₂ to 85 ± 1 kJ/mol for Cu5In5/ZrO₂, while the E_a of CeO₂-supported catalysts shows an inversed tendency (increase from 67 ± 4 for Cu10/CeO₂ to 78 ± 4 kJ/mol for Cu5In5/CeO₂). This interesting difference in E_a for CO₂ conversion is consistent with the activity differences discussed above, indicating that the introduction of In creates additional active sites for CO₂ hydrogenation on ZrO₂-supported catalysts, but possibly blocks the active sites on CeO₂-

supported catalysts. The above activity and kinetic measurements clearly show that the promotion effect of In on Cu catalysts is support dependent in RWGS reaction.

Table 5.1 Kinetic temperature range ($X_{\text{CO}_2} < 10\%$) for the calculation of activation energy and the determined activation energy (E_a) for CO_2 conversion.

Catalyst	ZrO ₂ support		CeO ₂ support	
	Cu10	Cu5In5	Cu10	Cu5In5
Kinetic temperature range (°C)	570-610	460-500	320-345	325-355
E_a (kJ/mol)	117±6	85±1	67±4	78±3

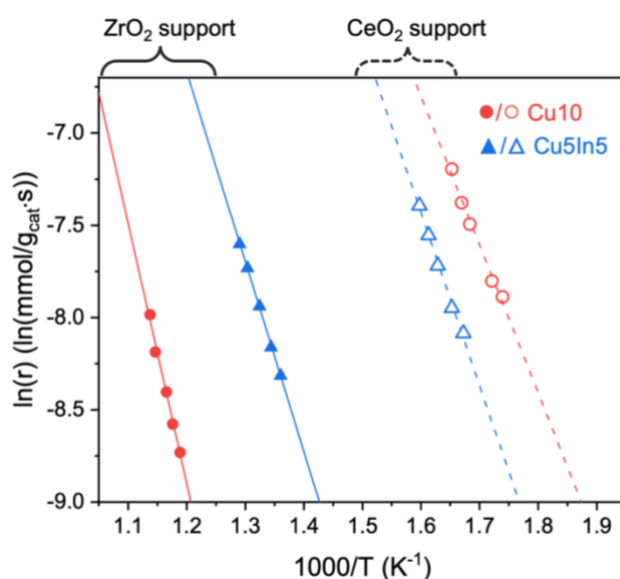


Figure 5.2 Arrhenius plot with the CO_2 conversion experimental data (dots) at the kinetic temperature range for all catalysts supported by ZrO_2 (filled dots and solid lines) or CeO_2 (hollow dots and dash lines).

5.3.2 Structural properties

To understand the origin of the observed performance difference, in-depth characterization was conducted to unravel the structural and chemical differences between ZrO_2 and CeO_2 supported Cu and Cu-In catalysts. TEM measurements were initially performed, where the morphologies of the Cu10 and Cu5In5 catalysts are similar to their corresponding supports (Figure S5.1). STEM/EDX elemental maps were acquired to gain insights into the distribution of Cu and In species of the reduced catalysts (Figure 5.3), and an obvious support dependent distribution of Cu and In on ZrO_2 and CeO_2 was observed. For both Cu10/ ZrO_2 (Figure 5.3a) and Cu5In5/ ZrO_2 sample (Figure 5.3a), Cu distributed all over the ZrO_2 support and formed some aggregations with the size of 20-40 nm. Interestingly, for Cu5In5/ ZrO_2 , the distribution of Cu and In is highly overlapped on the EDX elemental map. One plausible reason for such a spatial concurrence of Cu and In is their alloying, which has been observed in some Cu-In bimetallic catalysts³⁵⁻³⁷, as well as in our previous investigation on Cu-In model surface.³⁸ For the Cu10/ CeO_2 sample (Figure 5.3c), Cu is very well dispersed on the CeO_2 . Figure 5.3d shows that the distribution of Cu and In on the Cu5In5/ CeO_2 sample is not overlapped, different from that on the Cu5In5/ ZrO_2 sample. Meanwhile, more aggregations of Cu are found on the Cu5In5/ CeO_2 (Figure 5.3d) compared to the Cu10/ CeO_2 sample (Figure 5.3c), while In shows a homogeneous dispersion. Altogether, with microscopy analysis, it is speculated that the support dependent dispersion of Cu and In

could be attributed to the different compounds (Cu-In alloys or separated Cu- and In-species) formed on the ZrO_2 and CeO_2 supports.

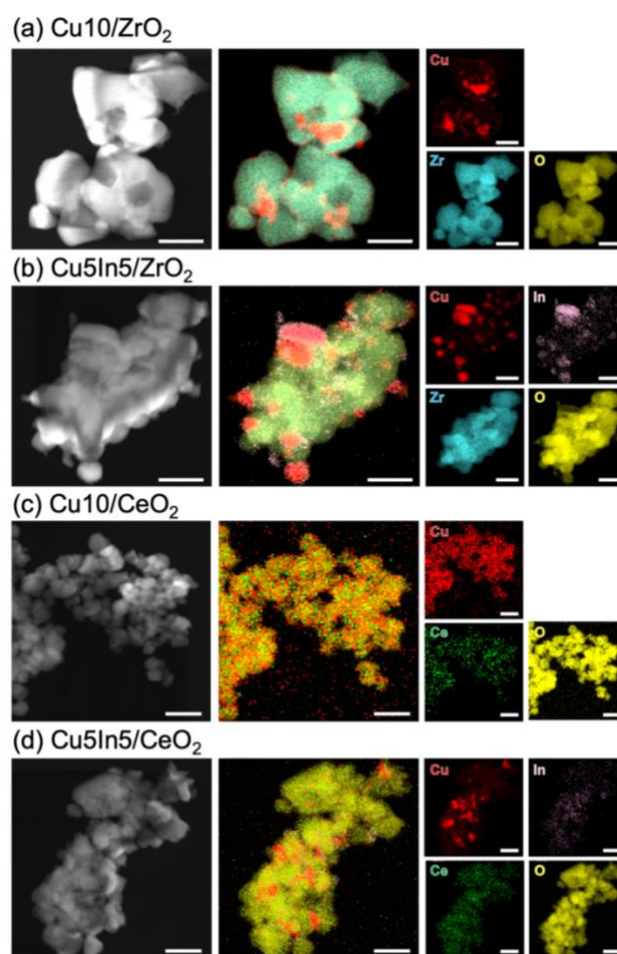


Figure 5.3 STEM-HAADF image and STEM/EDX element maps of Cu10 and Cu5In5 catalysts supported by (a, b) ZrO_2 and (c, d) CeO_2 .

The crystal structure of all samples was further characterized by XRD. The XRD profiles of the reduced catalysts supported by ZrO_2 and CeO_2 are shown in Figure 5.4a and b, respectively. Diffraction peaks of the two supports can be indexed to the monoclinic baddeleyite-type ZrO_2 (PDF 01-081-1314), and cubic cerianite-type CeO_2 (PDF 00-034-0394), respectively. For both Cu10/ZrO_2 and Cu10/CeO_2 samples, except for the diffraction peaks of ZrO_2 and CeO_2 supports, additional peaks at $2\theta = 43.3^\circ$ and 50.4° are observed, which can be assigned to the (111) and (200) reflections of metallic Cu (PDF 00-004-0836). This demonstrates that Cu oxides can be fully reduced under the pre-reduction condition. In contrast, the crystal structure of the Cu-In based samples are strongly influenced by the supports. With ZrO_2 as support, Cu-In alloys, including Cu_7In_3 (PDF 04-007-1137) and $\text{Cu}_{0.932}\text{In}_{0.068}$ (PDF 04-021-6624), are identified as shown in the insets (peaks at $2\theta = 29.5$ and $41.5\text{--}42.5^\circ$) of Figure 5.4a (the detailed assignment of alloy peaks is shown in the Rietveld plot in Figure S5.3). Besides, In_2O_3 (PDF 04-004-3575) can also be observed on the reduced Cu5In5/ZrO_2 sample. When CeO_2 was used as support, Cu and In did not form any alloy phase but only metallic Cu and In_2O_3 . We also performed XRD measurements on the used catalysts (Figure S5.4). After the RWGS reaction, all catalysts showed no significant change compared with the freshly reduced samples, indicating that Cu, Cu-In alloys, and In_2O_3 are stable during the reaction. The mass fractions of each phase are calculated by Rietveld

refinement and shown in Table 1. The content of Cu- and In-containing phases, as well as ZrO₂ and CeO₂ supports is in consistent with the mass fraction of Cu, In, Zr, and Ce in the corresponding calcined catalysts determined by ICP-OES (Table S2).

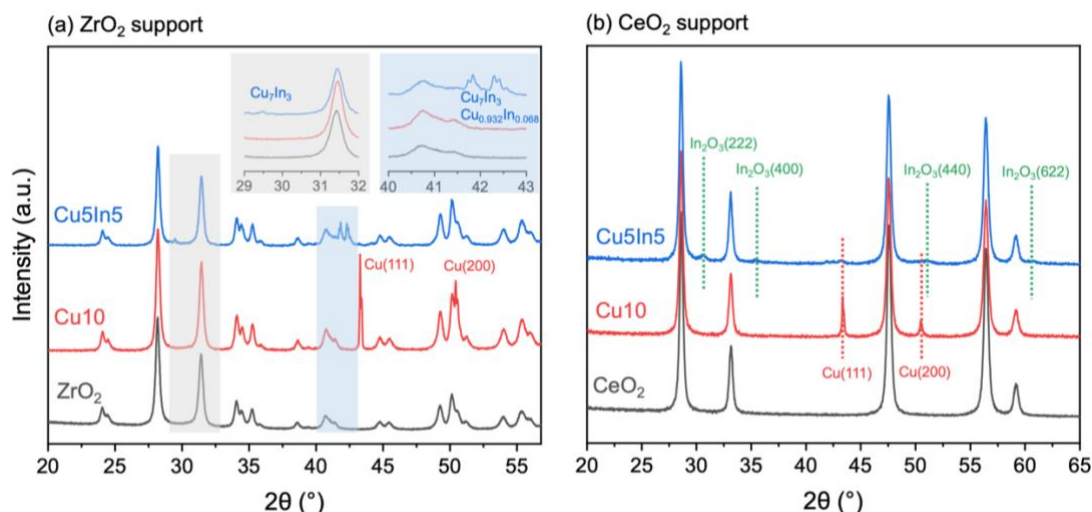


Figure 5.4 XRD patterns of all reduced catalysts supported by (a) ZrO₂ and (b) CeO₂.

The grain sizes of each phase in all reduced catalysts are also obtained from Rietveld refinement (Table S5.3). ZrO₂ and CeO₂ supports have similar grain sizes of ~20 nm. The Cu₇In₃ and Cu_{0.932}In_{0.068} alloys on Cu5In5/ZrO₂ have smaller grain size (48.9 and 25.7 nm, respectively) compared with that of metallic copper (80.1 nm) on Cu10/ZrO₂, which agrees the observations in corresponding TEM images (Figure S5.1). For CeO₂ supported samples, the grain size of Cu is smaller in both Cu10 (64.1 nm) and Cu5In5 (24.4 nm) samples compared with that on ZrO₂, indicating a better Cu dispersion on CeO₂ than on ZrO₂. Besides, In₂O₃ phases have relatively small (< 15 nm) grain sizes in both Cu5In5/ZrO₂ and Cu5In5/CeO₂ samples.

Table 5.2 Quantitative XRD analysis of Cu10 and Cu5In5 catalysts supported by ZrO₂ and CeO₂ obtained from Rietveld refinement.

Samples	Phase content (wt.%)				
	ZrO ₂	Cu	In ₂ O ₃	Cu ₇ In ₃	Cu _{0.932} In _{0.068}
Cu10/ZrO ₂	90.2	9.8	-	-	-
Cu5In5/ZrO ₂	89.46	-	4.04	5.15	1.35
	CeO ₂				
	CeO ₂	Cu	In ₂ O ₃		
Cu10/CeO ₂	92.45	7.55	-		
Cu5In5/CeO ₂	92.26	2.73	5.01		

Due to the existence of highly crystalized primary particles, the change in the dispersion of Cu and In shown in the scale of the STEM/EDX analysis cannot be accurately determined by XRD. Nevertheless, the observations in STEM/EDX and XRD analysis show their consistency after the specific surface areas (SSA) of the reduced samples are taken into consideration. In Table 2, the SSA of all Cu10 and Cu5In5 samples get smaller than the ZrO₂ or CeO₂ supports due to the formation of Cu or Cu-In alloy primary particles shown by the XRD data (Table S3). Meanwhile, a supported-dependent tendency can be observed. With ZrO₂ as the

support, the Cu10 and Cu5In5 samples have similar SSA (10.4 and 12.2 m²/g, respectively), which agrees the similar Cu and In dispersions observed in STEM/EDX images (Figure 5.3a and b) of both catalysts. In CeO₂-supported samples, the SSA of the Cu5In5 catalyst is reduced by 26% compared to the Cu10 catalyst. This is a further evidence for a worse Cu dispersion on the Cu5In5/CeO₂ catalyst than on the Cu10/CeO₂ sample, as shown in Figure 5.3c and d. Thus, despite the primary particle sizes calculated from the XRD data, the influence of the ZrO₂ and CeO₂ supports on the dispersion of Cu and In concluded from STEM/EDX and SSA measurement coincides: on ZrO₂ Cu and In alloy and the dispersion of metals is barely affected, while on CeO₂ the addition of In reduces the dispersion of Cu.

Table 5.3 Specific surface areas (SSA) of all calcined samples determined by N₂ adsorption.

Samples	ZrO ₂	Cu10/ZrO ₂	Cu5In5/ZrO ₂	CeO ₂	Cu10/CeO ₂	Cu5In5/CeO ₂
SSA (m ² /g)	13.9	10.4	12.2	31.8	27.1	20.2

5.3.3 Reducibility and surface properties

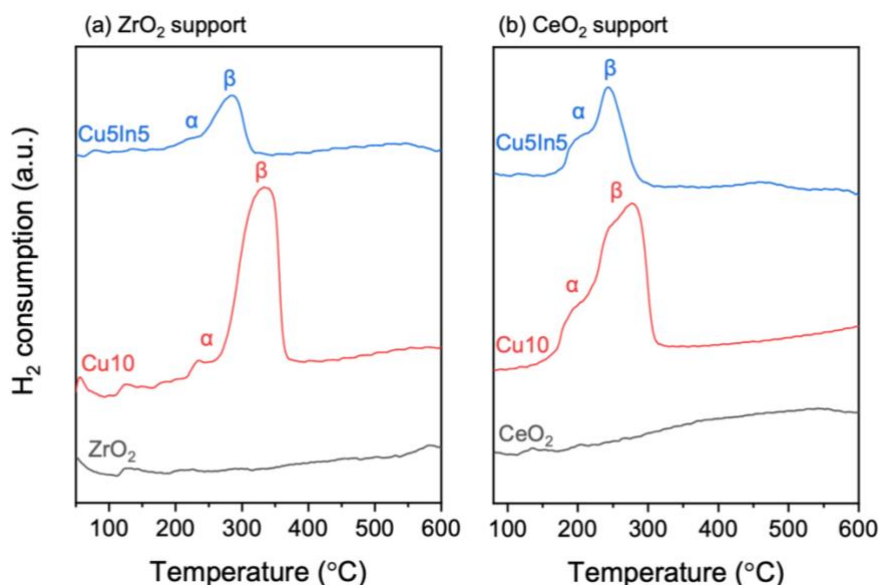


Figure 5.5 H₂-TPR profiles of the calcined Cu10 and Cu5In5 catalysts supported by (a) ZrO₂ and (b) CeO₂.

H₂-TPR was applied to investigate the reducibility of the calcined catalysts and the results are shown in Figure 5.5. While the ZrO₂ support is not reducible, the CeO₂ support shows a broad reduction peak from 300 to 600 °C due to the removal of surface oxygen.^{39,40} All samples containing metallic copper after reduction exhibit two peaks during TPR, where α peak in the low-temperature range corresponding to higher Cu dispersion and stronger metal-support interaction, and β peak in the high-temperature range corresponding to lower Cu dispersion and weaker metal-support interaction^{41–44}. Obviously, Cu10/ZrO₂ has the largest β peak ratio with the highest reduction temperature, which is in agreement with its poor activity and large metallic copper grain size in XRD. On CeO₂-supported samples, the fraction of α peak increases and the reduction temperature decreases due to the strong interaction between Cu species and CeO₂⁴⁵, which has also been proven by the better activity and the smaller metallic copper grain size. The TPR profile becomes a single, and relatively symmetric peak for the Cu5In5/ZrO₂ sample, due to the formation of Cu-In alloys. In contrast,

the Cu5In5/CeO₂ sample showed a TPR profile very similar to the Cu10/CeO₂ sample, which can be attributed to the reduction of CuO to Cu. The H₂-TPR profiles are in consistent with the XRD results, further confirming the formation of Cu-In alloys is dependent on the supports.

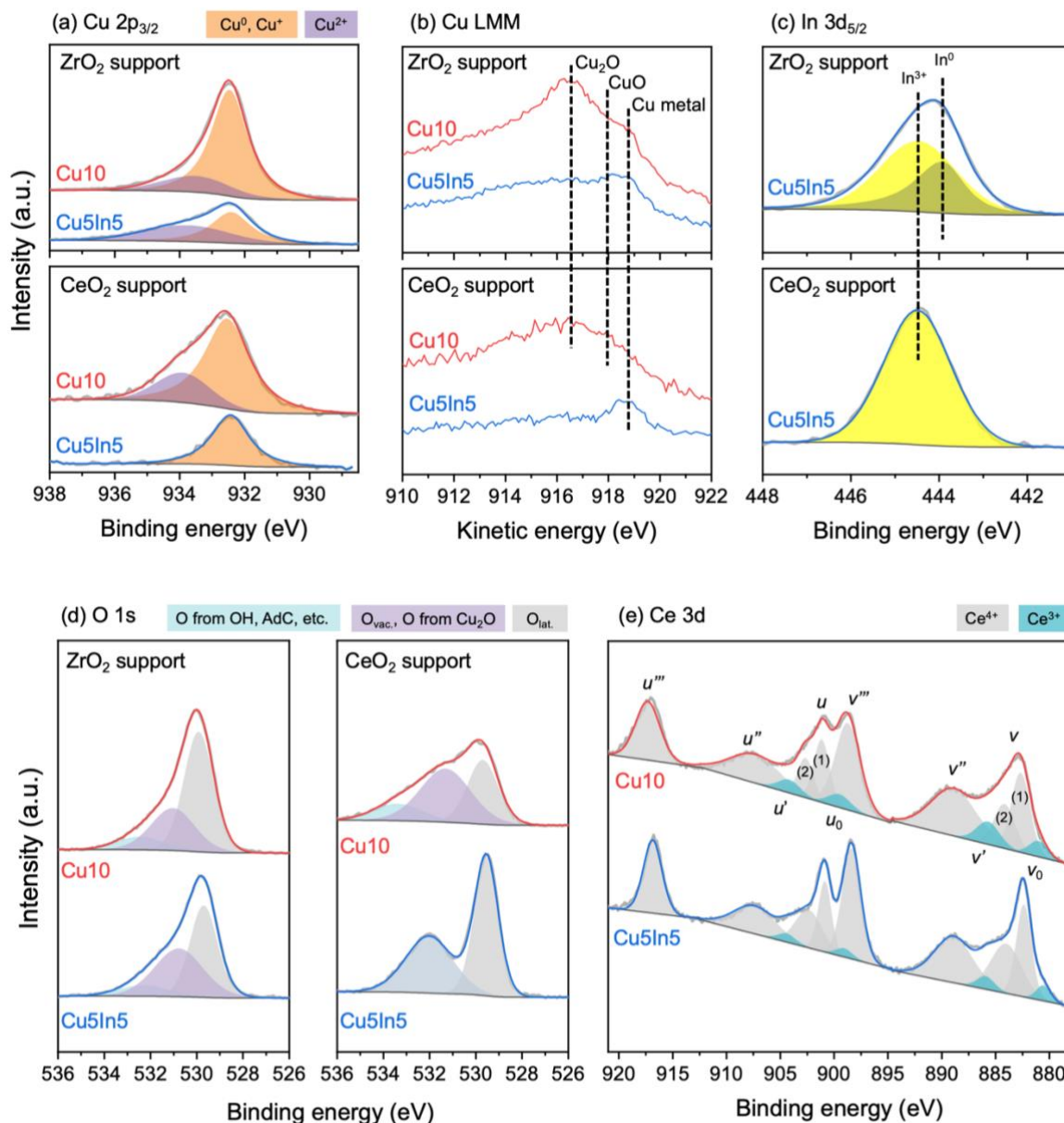


Figure 5.6 XPS spectra of all ZrO₂- and CeO₂-supported Cu10 and Cu5In5 catalysts after reduction (in 5 vol.% H₂, 400 °C, 1h) at different regions: (a) Cu 2p_{3/2}, (b) Cu LMM Auger, (c) In 3d_{5/2}, (d) O 1s, and (e) Ce 3d. For all core level region data, the gray solid lines are the raw data, and the colored solid lines are the fitted spectra. For the Auger region, the colored solid lines are the raw data.

To shed light on the catalyst surface composition and electronic properties, reduced samples were examined by XPS. Both the Cu 2p_{3/2} and Cu LMM Auger peaks were recorded to reveal the oxidation state of Cu (Figure 5.6a and b). For ZrO₂ supported samples, both Cu10/ZrO₂ and Cu5In5/ZrO₂ contain a mixture of metallic Cu, Cu₂O, and CuO, as the corresponding features in Cu LMM region at 918.6, 916.8, and 916.7 eV are identified, respectively.⁴⁶ For In species, the In 3d spectrum of Cu5In5/ZrO₂ can be deconvoluted to In⁰ and In³⁺. The observed Cu and In oxides may originate from slight surface oxidation during the sample transport, while the existence of metallic Cu and In agrees well with existence of Cu-In alloy phases on Cu5In5/ZrO₂ detected by XRD (Figure 5.4a). In the O 1s region (Figure 5.6d), the main components are lattice oxygen (~529.5 eV, in

ZrO₂, In₂O₃, and CuO) and defective oxygen (~531 eV, in In₂O₃). Here, it should be noticed that peaks for the oxygen vacancies in In₂O₃ overlap with the O species from Cu₂O component (~531 eV),⁴⁷ and thus, hinders further quantitative analysis. At ~533 eV, there is another peak associated to the hydroxyl group or carboxylate group in the adventitious carbon adsorbed on the sample surface.^{48,49}

On the CeO₂ support, differences between Cu₁₀/CeO₂ and Cu₅In₅/CeO₂ samples can be clearly observed in the O 1s and Ce 3d regions (Figure 5.6d and e). Compared to Cu₅In₅/CeO₂, the O 1s region of Cu₁₀/CeO₂ shows an additional peak at ~531.3 eV, which, as discussed before, could be attributed to the oxygen vacancies from CeO₂, as well as O atoms from Cu₂O. Supposing that the Cu 2p_{3/2} peak at 932.5 eV was totally contributed by Cu₂O, its corresponding O atom should contribute only 39% of the O 1s peak area at 531.3 eV, and the remaining area should be attributed to the oxygen vacancies from partially reduced CeO₂. For the Cu₅In₅/CeO₂ sample, the peak at ~532.1 eV may be contributed by multiple components with similar binding energies, such as Cu₂O, adsorbed hydroxyl group, defective oxygen from CeO₂ and In₂O₃, and adventitious carbon. Thus, further deconvolution of this peak could result in overinterpretation. Nevertheless, the partial reduction of CeO₂ in the Cu₁₀/CeO₂ and Cu₅In₅/CeO₂ samples was confirmed by the Ce 3d region spectra. As shown in Figure 5.6e, the Ce 3d region consists five sets of the spin-orbit split doublets ($u_0, v_0, u, v, u', v', u'', v'', u''', v''', u''''$), where the u_0, v_0, u' , and v' peaks are contributed by Ce³⁺.^{50,51} Thus, the Ce³⁺ spectral contribution, $x_{\text{Ce(III)}}$ can be calculated by $x_{\text{Ce3+}} = \frac{u_0+v_0+u'+v'}{\sum_i u^i+v^i}$. This way, the Ce³⁺ concentration in the Cu₁₀/CeO₂ sample is calculated to be 14.3%, while the amount of Ce³⁺ is only 6.1% in the Cu₅In₅/CeO₂ sample. Altogether, the effect of In addition on the surface properties of all catalysts is also support dependent: In forms alloys with Cu and remains metallic on the ZrO₂ support, while it reduces the number of surface oxygen vacancies on the CeO₂ support.

Such a difference in surface oxygen vacancies is further confirmed by comparing Raman spectra of calcined and reduced catalysts supported by ZrO₂ and CeO₂ (Figure S5.5). For ZrO₂-supported catalysts, the major observations are characteristic peaks of monoclinic ZrO₂.⁵² The peaks of CuO and In₂O₃ mostly overlap with ZrO₂ peaks, making the identification of changes in the vibration mode challenging. In the range of 100-250 cm⁻¹, the changes of peaks mainly result from thermal-introduced strains in the ZrO₂ lattice.⁵³ Nevertheless, features of CuO at ~290 and ~340 cm⁻¹ can be resolved.⁵⁴ For both Cu₁₀ and Cu₅In₅ samples, reduction leads to the disappearance of these CuO features. Notably, there is a downshift of the CuO peak of the calcined Cu₅In₅ sample at ~290 cm⁻¹ compared to the Cu₁₀ sample. Such a downshift could result from the decrease of the CuO grain size, probably because of the addition of In₂O₃.⁵⁴ The CeO₂ T_{2g} mode at ~460 cm⁻¹⁵⁵ and the longitudinal optical mode activated by the defects in CeO₂ lattice at ~600 cm⁻¹⁵⁵ are clearly observed for all samples. For calcined Cu₁₀ and Cu₅In₅ samples, there is a slight downshift of the T_{2g} band by ~6 cm⁻¹, usually due to the thermal expansion of the lattice.⁵⁶ However, an additional downshift of ~10.7 cm⁻¹ and a significant increase in the full width at half maximum (FWHM) are observed exclusively for the reduced Cu₁₀/CeO₂ sample, which can be attributed to the lattice expansion resulting from the creation of oxygen vacancies.^{57,58} For the Cu₅In₅/CeO₂ catalyst, the CeO₂ lattice is probably stabilized by In₂O₃ and very few oxygen vacancies were generated during the reduction.¹⁸ The findings in Raman spectra are highly consistent with the XPS results, further confirms the support dependence influence of Cu and In on the oxygen vacancies of the ZrO₂ and CeO₂ surfaces.

5.3.4 Adsorption-desorption properties

To gain insights into CO₂ adsorption properties of the samples, CO₂-TPD was performed on reduced catalysts. CO₂-TPD profiles in Figure 5.7 can be divided into three regions: 50~200 °C, 200~400 °C, and >400 °C, corresponding to the desorption of CO₂ from weak, moderate and strong adsorption sites, respectively. Firstly, it is worth noting that the scale of y-axis in Figure 5.7a is one order of magnitude smaller than that in Figure 5.7b, in line with previous findings that CeO₂ adsorbs more CO₂ than ZrO₂. Figure 5.7a shows that CO₂ adsorbs either weakly or strongly on ZrO₂, and deposition of Cu almost completely suppresses the strong adsorption of CO₂ but introduces new moderate adsorption sites. However, such a significant change of CO₂ adsorption property did not change the CO₂ conversion obviously (Figure 5.1a). In addition, the amount of CO₂ desorbed from Cu5In5/ZrO₂ is comparable with that from Cu10/ZrO₂ and ZrO₂, but the CO₂ conversion is much higher. These results indicate that the CO₂ adsorption property on ZrO₂-supported Cu and Cu-In catalysts may not be a main factor affecting the RWGS rate. This conclusion is also applicable for the CeO₂-based catalysts: while the catalytic performance of CeO₂, Cu10/CeO₂, and Cu5In5/CeO₂ are dramatically different, they all show similar desorption peaks of CO₂ in the temperature range of 100-200 °C which is mainly contributed by CeO₂.^{63,64}

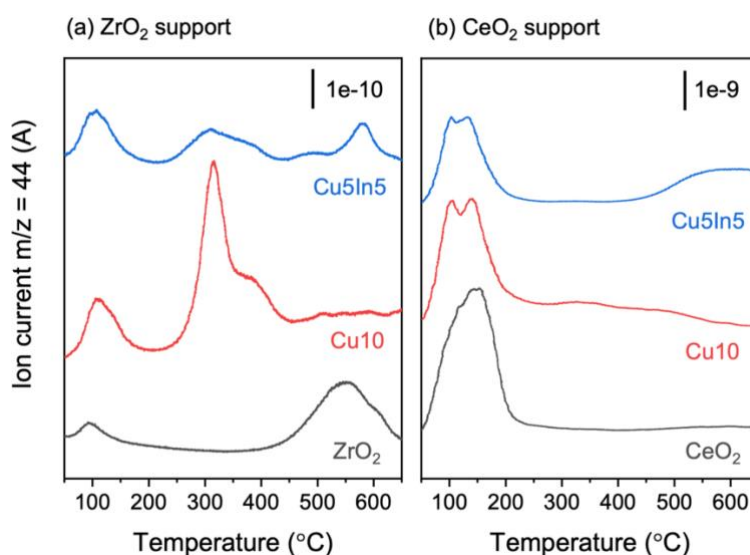


Figure 5.7 CO₂-TPD profiles of all reduced Cu10 and Cu5In5 catalysts supported by (a) ZrO₂ and (b) CeO₂.

5.4 Discussions

Previous studies on CO₂ hydrogenation catalysts show that Cu-In alloys and oxygen vacancies are important active sites for high catalytic performance. In the present experimental study on a series of Cu and Cu-In catalysts, both the catalytic activity of the RWGS reaction and the structural and surface properties of the catalysts show a clear support dependence. Thus, it is reasonable to correlate the support-dependent properties of different catalysts with the corresponding RWGS activities.

Due to its weak reducibility, ZrO₂ support is relatively inactive for CO₂ dissociation.⁶¹ For Cu10/ZrO₂ and Cu5In5/ZrO₂ catalysts, TEM (Figure S5.1) and STEM images (Figure 5.3a and b) show aggregated Cu, which is undesired for high catalytic performance. Thus, it is reasonable that the Cu10/ZrO₂ sample has low activity towards the RWGS reaction. But why does the addition of In improve the RWGS activity significantly without changing the physical property of the catalyst? Characterizations show that Cu and In formed alloys on ZrO₂,

which is confirmed by the overlay of Cu and In in the EDX elemental map (Figure 5.3a and b), the identification of Cu-In alloy phases by XRD (Figure 5.4a), and the existence of metallic Cu and In on catalyst surface detected by XPS (Figure 5.6b and c). Meanwhile, XRD and XPS results also show that reduced Cu₅In₅/ZrO₂ contains defective In₂O₃. It has been proposed that Cu-In alloys have significant influence on promoting the catalytic activity of CO₂ hydrogenation.^{19,31,36,37} Different Cu-In alloys have been found to form during the reduction process of supported Cu-In bimetallic catalysts for hydrogenation reactions, and the alloy phases were proposed to increase the performance of the catalysts in two ways: (i) Cu-In alloys modulate the electron structure of Cu and promote the adsorption and splitting of H₂,³⁶ and (ii) the interface between Cu-In alloys and In₂O₃ can better activate CO₂ than pure In₂O₃.^{31,37} In our previous NAP-XPS study of In/Cu model catalysts, we clearly demonstrated that the formation of Cu-In alloys increases the utility of oxygen vacancies of In₂O₃ in the activation of CO₂.³⁸ Altogether, the superior activity of the Cu₅In₅/ZrO₂ to the Cu₁₀/ZrO₂ catalyst for the RWGS reaction should be attributed to the enhancement of H₂ dissociation on metallic sites and CO₂ activation on In₂O₃ resulting from the formation of different Cu-In alloys.

On CeO₂ support, XRD and XPS characterizations (Figure 5.4b, 5.6d, and 5.6e) show that Cu and In form separated phases, i.e., metallic Cu and In₂O₃. As there was no formation of Cu-In alloys, its promotion effects on CO₂ activation do not exist on CeO₂-supported catalysts. On the contrary, STEM/EDX elemental maps (Figure 5.3c and d) and SSA measurements (Table 5.2) indicate a much better Cu dispersion on the Cu₁₀/CeO₂ than the Cu₅In₅/CeO₂ catalyst. Meanwhile, the oxygen vacancies on defective CeO₂ surfaces, which have been observed using XPS and Raman spectroscopy (Figure 5.6d, 5.6e, and S5.5), are important active sites for the activation of CO₂.^{14,25} Such a good Cu dispersion may provide a highly dense metal-support interfaces for CO₂ activation and H₂ dissociation, where CO₂ dissociates, oxidizes the oxygen vacancy sites, and forms intermediates like carbonates, formates, and Cu⁺-CO.¹⁴ With the reduction of catalyst by H₂ via hydrogen spillover, these oxidized active sites can be rapidly regenerated, and a high catalytic activity is maintained. Thus, the Cu₁₀/CeO₂ sample has the best RWGS activity among all catalysts studied in this work. The influence of In on the surface properties of the CeO₂-supported catalysts was revealed by XPS and Raman spectroscopy (Figure 6d, 6e, and S5) as reducing the percentage of partially reduced CeO₂, resulting in decreased number of oxygen vacancies. So, the reduced number of metal-support interfaces and oxygen vacancies may explain the corresponding lower RWGS activity of the Cu₅In₅/CeO₂ catalyst.

Not only the active phases and surface properties, but also the evolution of adsorbates and intermediates during the RWGS reaction was found to be dependent on different supports and can be correlated to the corresponding activities. Figure S5.6 shows the peaks for the most intense C-O vibration modes of surface carbonate and other oxo-species in the range from 2200 to 1000 cm⁻¹ under RWGS reaction conditions measured by in situ DRIFTS. The detailed assignment of the peaks are shown in the table below Figure S5.6. Despite all the common features, for ZrO₂ supported samples, the Cu₅In₅/ZrO₂ shows the absence of the broad band between 1230 and 1120 cm⁻¹, which has been reported to originate from formaldehyde group, the intermediate of methanol synthesis^{62,63}, compared to the Cu₁₀/ZrO₂ sample. However, the formation of methanol is unfavored under atmospheric pressure, and the methoxy intermediate is stable even after purging the RWGS reactants with He (Figure S5.7). For CeO₂ supported samples, bicarbonate and formate species are observed with the corresponding ~10 times more absorbance higher than on the ZrO₂ supported samples, justifying an easier CO₂ activation on CeO₂ support.

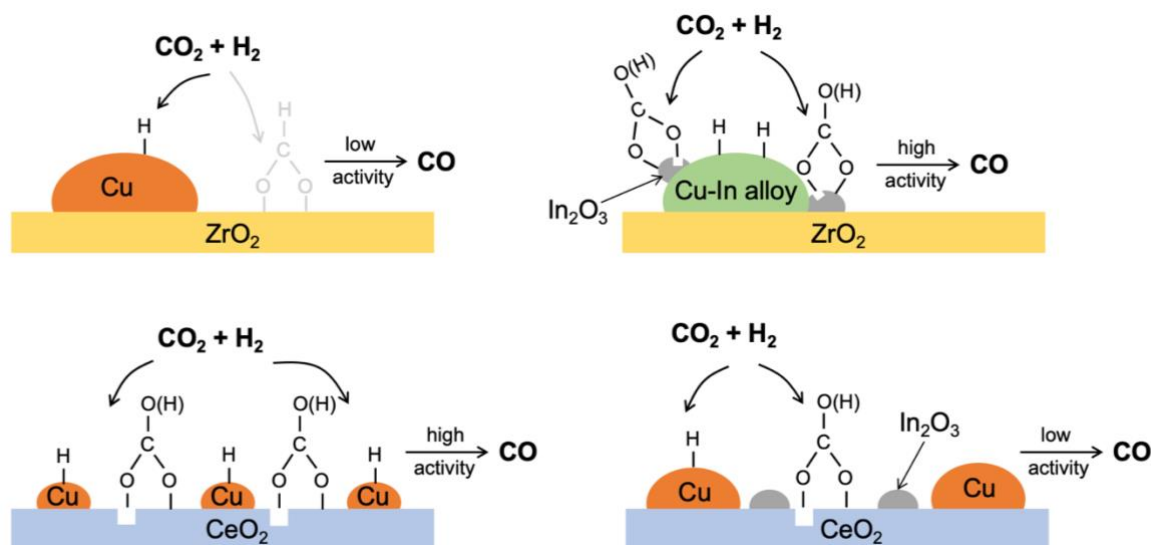


Figure 5.8 Schematic illustration for the dependence of active phases, surface properties, reaction intermediates, and corresponding RWGS activities on different supports investigated in this work on Cu₁₀/ZrO₂, Cu₅In₅/ZrO₂, Cu₁₀/CeO₂, and Cu₅In₅/CeO₂ catalysts.

Here, on supported catalysts, the formation of Cu-In alloys, distribution of Cu, and the content of oxygen vacancies are found to be dependent on supports, and well agrees the activity difference of ZrO₂- and CeO₂-supported catalysts, as summarized in Figure 5.8. On ZrO₂ support, the synergic effect between Cu and In contributes to numerous interfaces between Cu-In alloys and defective In₂O₃, which are active for H₂ dissociation and CO₂ activation in the form of carbonates. As a result, the Cu₅In₅/ZrO₂ has a superior RWGS activity to the Cu₁₀/ZrO₂ catalyst. Oppositely, on CeO₂, a rich interface between highly dispersed Cu and defective CeO₂ leads directly to a high RWGS activity. The addition of In increases extent of Cu aggregation and occupies the oxygen vacancies on CeO₂, resulting in lower RWGS activity of the Cu₅In₅/CeO₂ than the Cu₁₀/CeO₂ catalyst.

5.5 Conclusions

In this work, we demonstrated that the synergy between Cu and In for catalyzing RWGS reaction is support dependent using Cu, In, and Cu-In catalysts supported by ZrO₂ and CeO₂, respectively. The RWGS activity measurements showed that by adding In, the CO₂ conversion was increased over ZrO₂-supported catalysts but decreased over CeO₂-supported catalysts. By means of STEM/EDX, XRD, and XPS, we found that the active phases and surface properties of the catalysts are influenced by different supports. If ZrO₂ was used as the support, CO₂ activation on oxygen vacancies from In₂O₃ can be promoted by the formation of Cu-In alloys. Thus, the Cu₅In₅/ZrO₂ has significantly higher RWGS activity than the Cu₁₀/ZrO₂ catalyst. On CeO₂ support, no formation of Cu-In alloys was observed, but the distribution of Cu and the formation oxygen vacancies on CeO₂ was influenced negatively by the addition of In. Both H₂ dissociation on Cu and CO₂ activation on defective CeO₂ were suppressed on Cu₅In₅/CeO₂ compared to Cu₁₀/CeO₂, giving rise to the highest RWGS activity of the Cu₁₀/CeO₂ catalyst. With CO₂-TPD and *in situ* DRIFTS, CO₂ adsorption on different supports was compared and it turned out that CeO₂ has much stronger CO₂ adsorption ability and thus is generally a more active support for RWGS catalysts compared to ZrO₂. In summary, for the design of bimetallic catalysts for CO₂ hydrogenation, the surface composition, the active phase and the CO₂ adsorption ability of the

support should be comprehensively taken into consideration for the desired metal-support interaction and bimetallic synergy.

References

1. International Energy Agency. *World Energy Outlook 2016*. (Head of Communication and Information Office, 2016).
2. Yu, K. M. K., Curcic, I., Gabriel, J. & Tsang, S. C. E. Recent Advances in CO₂ Capture and Utilization. *ChemSusChem* **1**, 893–899 (2008).
3. Züttel, A. *et al.* Storage of Renewable Energy by Reduction of CO₂ with Hydrogen. *CHIMIA International Journal for Chemistry* **69**, 264–268 (2015).
4. Glenk, G. & Reichelstein, S. Economics of converting renewable power to hydrogen. *Nature Energy* **4**, 216 (2019).
5. V. Kondratenko, E., Mul, G., Baltrusaitis, J., O. Larrazábal, G. & Pérez-Ramírez, J. Status and perspectives of CO₂ conversion into fuels and chemicals by catalytic, photocatalytic and electrocatalytic processes. *Energy & Environmental Science* **6**, 3112–3135 (2013).
6. Ma, Z. & Porosoff, M. D. Development of Tandem Catalysts for CO₂ Hydrogenation to Olefins. *ACS Catal.* **9**, 2639–2656 (2019).
7. Liu, J. *et al.* Selective CO₂ Hydrogenation to Hydrocarbons on Cu-Promoted Fe-Based Catalysts: Dependence on Cu–Fe Interaction. *ACS Sustainable Chem. Eng.* (2018) doi:10.1021/acssuschemeng.8b01491.
8. Wang, J., Zhang, A., Jiang, X., Song, C. & Guo, X. Highly selective conversion of CO₂ to lower hydrocarbons (C₂–C₄) over bifunctional catalysts composed of In₂O₃–ZrO₂ and zeolite. *Journal of CO₂ Utilization* **27**, 81–88 (2018).
9. Miao, B., Ma, S. S. K., Wang, X., Su, H. & Chan, S. H. Catalysis mechanisms of CO₂ and CO methanation. *Catal. Sci. Technol.* **6**, 4048–4058 (2016).
10. Eren, B., Weatherup, R. S., Liakakos, N., Somorjai, G. A. & Salmeron, M. Dissociative Carbon Dioxide Adsorption and Morphological Changes on Cu(100) and Cu(111) at Ambient Pressures. *J. Am. Chem. Soc.* **138**, 8207–8211 (2016).
11. Stone, F. S. & Waller, D. Cu–ZnO and Cu–ZnO/Al₂O₃ Catalysts for the Reverse Water-Gas Shift Reaction. The Effect of the Cu/Zn Ratio on Precursor Characteristics and on the Activity of the Derived Catalysts. *Topics in Catalysis* **22**, 305–318 (2003).
12. Zhang, X. *et al.* Highly Dispersed Copper over β -Mo₂C as an Efficient and Stable Catalyst for the Reverse Water Gas Shift (RWGS) Reaction. *ACS Catal.* **7**, 912–918 (2017).
13. Chen, C.-S., Cheng, W.-H. & Lin, S.-S. Enhanced activity and stability of a Cu/SiO₂ catalyst for the reverse water gas shift reaction by an iron promoter. *Chemical Communications* **0**, 1770–1771 (2001).
14. Yang, S.-C. *et al.* Synergy between Ceria Oxygen Vacancies and Cu Nanoparticles Facilitates the Catalytic Conversion of CO₂ to CO under Mild Conditions. *ACS Catalysis* (2018) doi:10.1021/acscatal.8b04219.
15. Su, X., Yang, X., Zhao, B. & Huang, Y. Designing of highly selective and high-temperature durable RWGS heterogeneous catalysts: recent advances and the future directions. *Journal of Energy Chemistry* **26**, 854–867 (2017).
16. Fernández-García, M., Anderson, J. A. & Haller, G. L. Alloy Formation and Stability in Pd–Cu Bimetallic Catalysts. *J. Phys. Chem.* **100**, 16247–16254 (1996).
17. Martin, O. *et al.* Indium Oxide as a Superior Catalyst for Methanol Synthesis by CO₂ Hydrogenation. *Angew. Chem. Int. Ed.* **55**, 6261–6265 (2016).
18. Wang, W. *et al.* Reverse water gas shift over In₂O₃–CeO₂ catalysts. *Catalysis Today* **259**, 402–408 (2016).
19. Luo, W. *et al.* Selective and Stable Electroreduction of CO₂ to CO at the Copper/Indium Interface. *ACS Catal.* **8**, 6571–6581 (2018).
20. Ye, J., Liu, C. & Ge, Q. DFT Study of CO₂ Adsorption and Hydrogenation on the In₂O₃ Surface. *J. Phys. Chem. C* **116**, 7817–7825 (2012).
21. Ye, J., Ge, Q. & Liu, C. Effect of PdIn bimetallic particle formation on CO₂ reduction over the Pd–In/SiO₂ catalyst. *Chemical Engineering Science* **135**, 193–201 (2015).
22. García-Trenco, A. *et al.* PdIn intermetallic nanoparticles for the Hydrogenation of CO₂ to Methanol. *Applied Catalysis B: Environmental* **220**, 9–18 (2018).
23. Richard, A. R. & Fan, M. Low-Pressure Hydrogenation of CO₂ to CH₃OH Using Ni–In–Al/SiO₂ Catalyst Synthesized via a Phyllosilicate Precursor. *ACS Catal.* **7**, 5679–5692 (2017).
24. Ahmadi, M., Mistry, H. & Roldan Cuenya, B. Tailoring the Catalytic Properties of Metal Nanoparticles via Support Interactions. *J. Phys. Chem. Lett.* **7**, 3519–3533 (2016).
25. Lin, L. *et al.* In Situ Characterization of Cu/CeO₂ Nanocatalysts for CO₂ Hydrogenation: Morphological Effects of Nanostructured Ceria on the Catalytic Activity. *J. Phys. Chem. C* **122**, 12934–12943 (2018).
26. Cao, Y. *et al.* Defect-induced efficient dry reforming of methane over two-dimensional Ni/h-boron nitride nanosheet catalysts. *Applied Catalysis B: Environmental* **238**, 51–60 (2018).
27. Suo, Z., Kou, Y., Niu, J., Zhang, W. & Wang, H. Characterization of TiO₂-, ZrO₂- and Al₂O₃-supported iron catalysts as used for CO₂ hydrogenation. *Applied Catalysis A: General* **148**, 301–313 (1997).
28. Wang, L., Liu, H., Chen, Y. & Yang, S. Reverse water–gas shift reaction over co-precipitated Co–CeO₂ catalysts: Effect of Co content on selectivity and carbon formation. *International Journal of Hydrogen Energy* **42**, 3682–3689 (2017).
29. Dai, B. *et al.* CO₂ reverse water-gas shift reaction on mesoporous M–CeO₂ catalysts. *The Canadian Journal of Chemical Engineering* **95**, 634–642 (2017).
30. Snider, J. L. *et al.* Revealing the Synergy between Oxide and Alloy Phases on the Performance of Bimetallic In–Pd Catalysts for CO₂ Hydrogenation to Methanol. *ACS Catal.* 3399–3412 (2019) doi:10.1021/acscatal.8b04848.
31. Gao, J. *et al.* Cu₂In Nanoalloy Enhanced Performance of Cu/ZrO₂ Catalysts for the CO₂ Hydrogenation to Methanol. *Ind. Eng. Chem. Res.* **59**, 12331–12337 (2020).
32. *NIST Chemistry WebBook, NIST Standard Reference Database Number 69*. (National Institute of Standards and Technology).

33. Kong, D., Zhu, J. & Ernst, K.-H. Low-Temperature Dissociation of CO₂ on a Ni/CeO₂(111)/Ru(0001) Model Catalyst. *The Journal of Physical Chemistry C* **120**, 5980–5987 (2016).
34. Senanayake, S. D. *et al.* Hydrogenation of CO₂ to Methanol on CeO_x/Cu(111) and ZnO/Cu(111) Catalysts: Role of the Metal–Oxide Interface and Importance of Ce³⁺ Sites. *J. Phys. Chem. C* **120**, 1778–1784 (2016).
35. Yao, L., Shen, X., Pan, Y. & Peng, Z. Synergy between active sites of Cu–In–Zr–O catalyst in CO₂ hydrogenation to methanol. *Journal of Catalysis* **372**, 74–85 (2019).
36. Shi, Z. *et al.* CO₂ hydrogenation to methanol over Cu–In intermetallic catalysts: Effect of reduction temperature. *Journal of Catalysis* **379**, 78–89 (2019).
37. Shi, Z., Tan, Q. & Wu, D. A novel Core–Shell structured CuIn@SiO₂ catalyst for CO₂ hydrogenation to methanol. *AIChE Journal* **65**, 1047–1058 (2019).
38. Li, M., Luo, W. & Züttel, A. Near ambient-pressure X-ray photoelectron spectroscopy study of CO₂ activation and hydrogenation on indium/copper surface. *Journal of Catalysis* (2021) doi:10.1016/j.jcat.2021.01.010.
39. Giordano, F., Trovarelli, A., de Leitenburg, C. & Giona, M. A Model for the Temperature-Programmed Reduction of Low and High Surface Area Ceria. *Journal of Catalysis* **193**, 273–282 (2000).
40. Yi, G., Xu, Z., Guo, G., Tanaka, K. & Yuan, Y. Morphology effects of nanocrystalline CeO₂ on the preferential CO oxidation in H₂-rich gas over Au/CeO₂ catalyst. *Chemical Physics Letters* **479**, 128–132 (2009).
41. Zimmer, P., Tschöpe, A. & Birringer, R. Temperature-Programmed Reaction Spectroscopy of Ceria- and Cu/Ceria-Supported Oxide Catalyst. *Journal of Catalysis* **205**, 339–345 (2002).
42. Liu, J. *et al.* Surface active structure of ultra-fine Cu/ZrO₂ catalysts used for the CO₂+H₂ to methanol reaction. *Applied Catalysis A: General* **218**, 113–119 (2001).
43. Ko, J. B., Bae, C. M., Jung, Y. S. & Kim, D. H. Cu–ZrO₂ Catalysts for Water-gas-shift Reaction at Low Temperatures. *Catal Lett* **105**, 157–161 (2005).
44. Chary, K. V. R., Sagar, G. V., Srikanth, C. S. & Rao, V. V. Characterization and Catalytic Functionalities of Copper Oxide Catalysts Supported on Zirconia. *J. Phys. Chem. B* **111**, 543–550 (2007).
45. Tamura, M., Kitanaka, T., Nakagawa, Y. & Tomishige, K. Cu Sub-Nanoparticles on Cu/CeO₂ as an Effective Catalyst for Methanol Synthesis from Organic Carbonate by Hydrogenation. *ACS Catal.* **6**, 376–380 (2016).
46. Biesinger, M. C. Advanced analysis of copper X-ray photoelectron spectra. *Surface and Interface Analysis* **49**, 1325–1334 (2017).
47. Losev, A., Rostov, K. & Tyuliev, G. Electron beam induced reduction of CuO in the presence of a surface carbonaceous layer: an XPS/HREELS study. *Surface Science* **213**, 564–579 (1989).
48. Stoch, J. & Gablankowska-Kukucz, J. The effect of carbonate contaminations on the XPS O 1s band structure in metal oxides. *Surface and Interface Analysis* **17**, 165–167 (1991).
49. McCafferty, E. & Wightman, J. P. Determination of the concentration of surface hydroxyl groups on metal oxide films by a quantitative XPS method. *Surface and Interface Analysis* **26**, 549–564 (1998).
50. Fujimori, A. Mixed-valent ground state of Ce $\{\mathrm{O}\}_2$. *Phys. Rev. B* **28**, 2281–2283 (1983).
51. Mullins, D. R., Overbury, S. H. & Huntley, D. R. Electron spectroscopy of single crystal and polycrystalline cerium oxide surfaces. *Surface Science* **409**, 307–319 (1998).
52. Keramidas, V. G. & White, W. B. Raman Scattering Study of the Crystallization and Phase Transformations of ZrO₂. *Journal of the American Ceramic Society* **57**, 22–24 (1974).
53. Ishigame, M. & Sakurai, T. Temperature Dependence of the Raman Spectra of ZrO₂. *Journal of the American Ceramic Society* **60**, 367–369 (1977).
54. Xu, J. F. *et al.* Raman spectra of CuO nanocrystals. *Journal of Raman Spectroscopy* **30**, 413–415 (1999).
55. Weber, W. H., Hass, K. C. & McBride, J. R. Raman study of $\{\mathrm{CeO}\}_2$: Second-order scattering, lattice dynamics, and particle-size effects. *Phys. Rev. B* **48**, 178–185 (1993).
56. Spanier, J. E., Robinson, R. D., Zhang, F., Chan, S.-W. & Herman, I. P. Size-dependent properties of $\{\mathrm{CeO}\}_2$ nanoparticles as studied by Raman scattering. *Phys. Rev. B* **64**, 245407 (2001).
57. Lee, Y. *et al.* Raman Analysis of Mode Softening in Nanoparticle CeO₂– δ and Au–CeO₂– δ during CO Oxidation. *J. Am. Chem. Soc.* **133**, 12952–12955 (2011).
58. Silva, I. de C., Sigoli, F. A. & Mazali, I. O. Reversible Oxygen Vacancy Generation on Pure CeO₂ Nanorods Evaluated by in Situ Raman Spectroscopy. *J. Phys. Chem. C* **121**, 12928–12935 (2017).
59. Liu, B. *et al.* Oxygen Vacancy Promoting Dimethyl Carbonate Synthesis from CO₂ and Methanol over Zr-Doped CeO₂ Nanorods. *ACS Catal.* **8**, 10446–10456 (2018).
60. Meng-fei Luo, Yi-jun Zhong, Bo Zhu, Xian-xin Yuan, & Xiao-ming Zheng. Temperature-programmed desorption study of NO and CO₂ over CeO₂ and ZrO₂. *Applied Surface Science* **115**, 185–189 (1997).
61. Li, H. *et al.* CO₂ activation on ultrathin ZrO₂ film by H₂O co-adsorption: In situ NAP-XPS and IRAS studies. *Surface Science* **679**, 139–146 (2019).
62. Ihm, S.-K., Park, Y.-K., Jeon, J.-K., Park, K.-C. & Lee, D.-K. A study on methanol synthesis through CO₂ hydrogenation over copper-based catalysts. in *Studies in Surface Science and Catalysis* (eds. Inui, T., Anpo, M., Izui, K., Yanagida, S. & Yamaguchi, T.) vol. 114 505–508 (Elsevier, 1998).
63. Kattel, S., Yan, B., Yang, Y., Chen, J. G. & Liu, P. Optimizing Binding Energies of Key Intermediates for CO₂ Hydrogenation to Methanol over Oxide-Supported Copper. *J. Am. Chem. Soc.* **138**, 12440–12450 (2016).

Supporting information

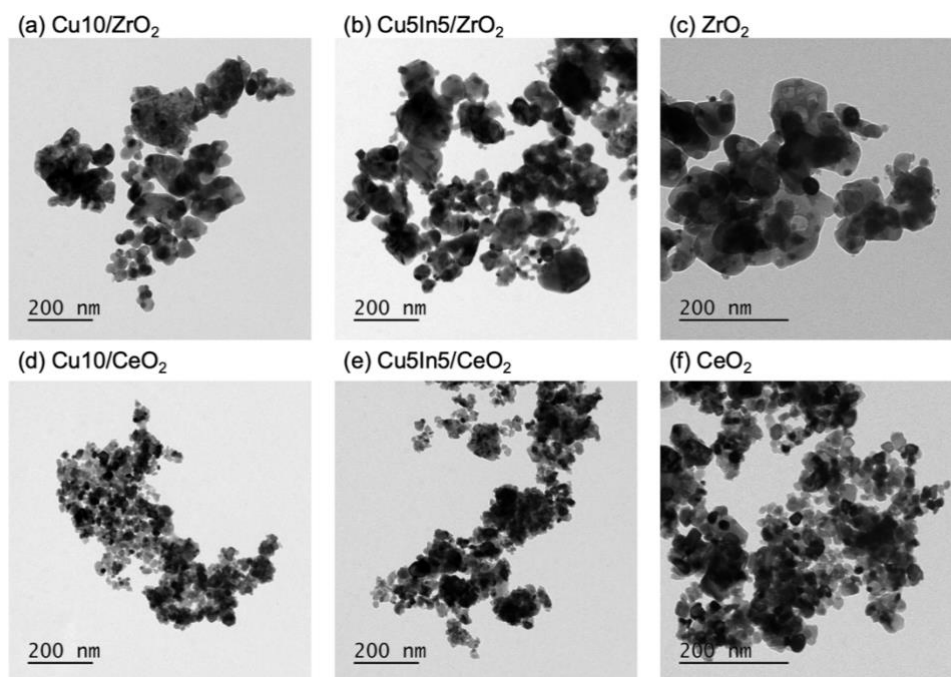


Figure S5.1 TEM images of all Cu, Cu-In catalysts and their corresponding supports: (a) $\text{Cu}_{10}/\text{ZrO}_2$, (b) $\text{Cu}_{5\text{In}5}/\text{ZrO}_2$, (c) ZrO_2 , (d) $\text{Cu}_{10}/\text{CeO}_2$, (e) $\text{Cu}_{5\text{In}5}/\text{CeO}_2$, and (f) CeO_2 .

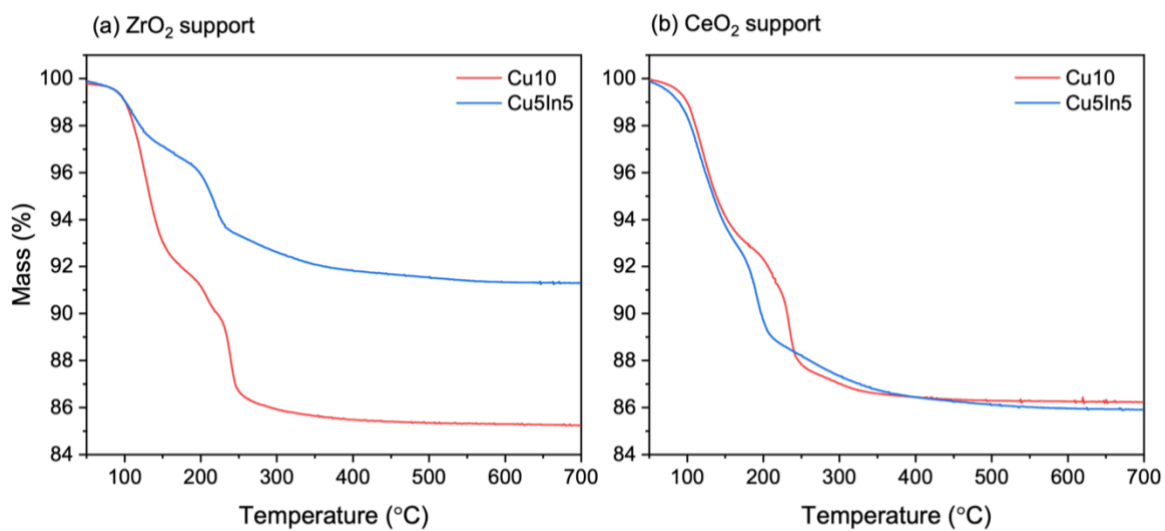


Figure S5.2 TGA curves of the dried precursors of Cu_{10} and $\text{Cu}_{5\text{In}5}$ samples supported by (a) ZrO_2 and (b) CeO_2 .

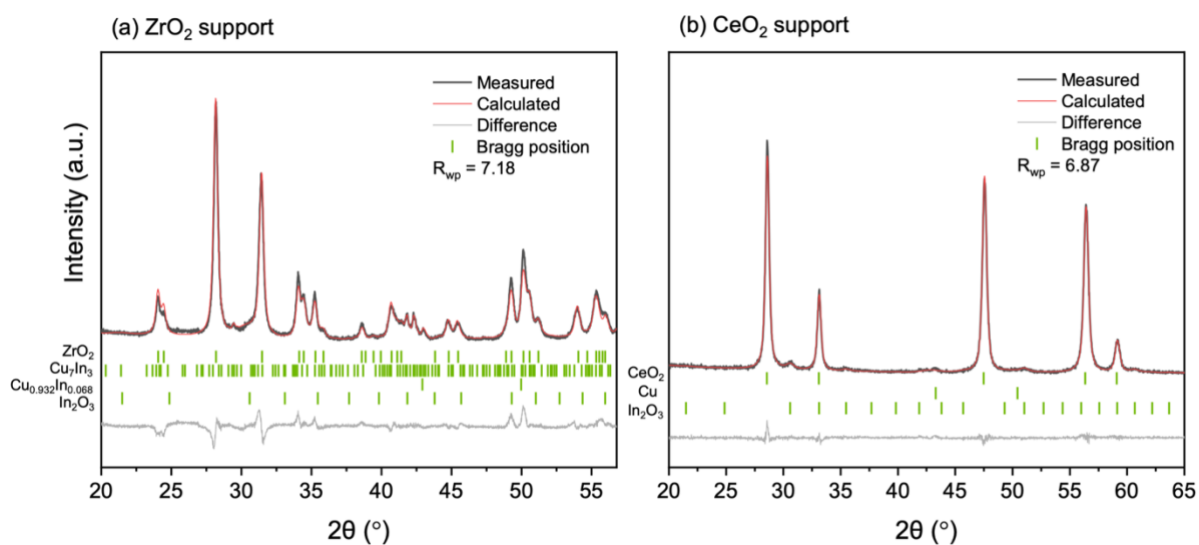


Figure S5.3 Rietveld plot of the reduced $\text{Cu}_5\text{In}_5/\text{ZrO}_2$ and $\text{Cu}_5\text{In}_5/\text{CeO}_2$ catalysts.

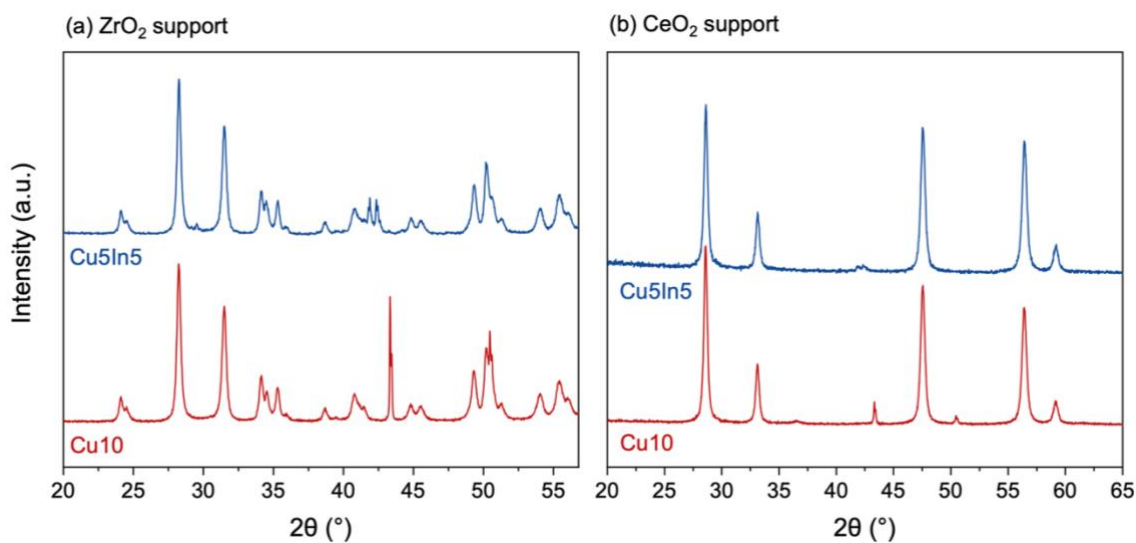


Figure S5.4 XRD of used Cu_{10} and Cu_5In_5 catalysts supported by (a) ZrO_2 and (b) CeO_2 .

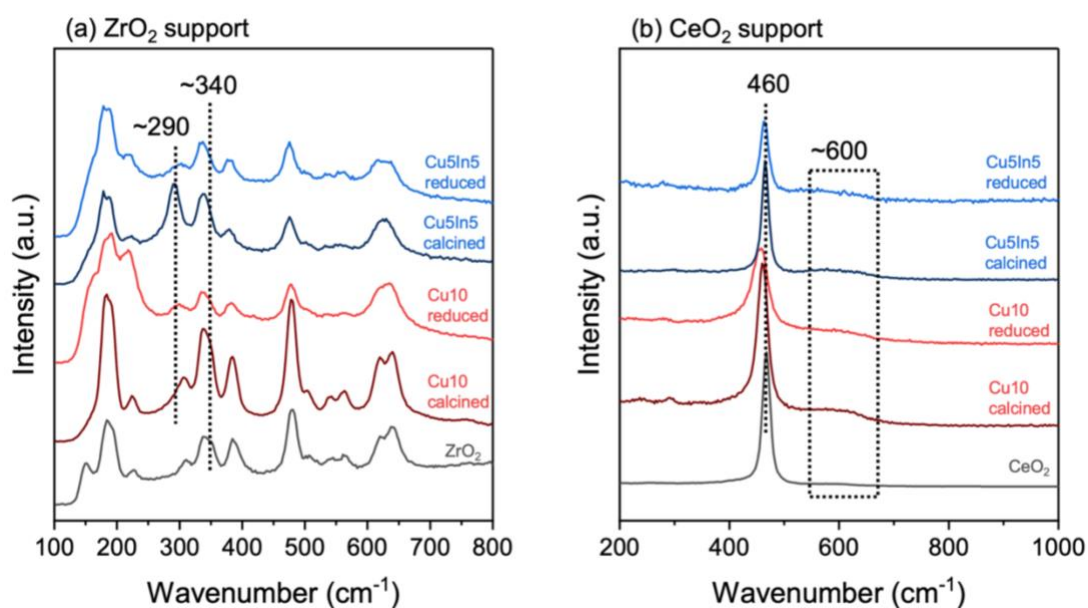


Figure S5.5 Raman spectra of all calcined and reduced Cu10 and Cu5In5 catalysts supported by (a) ZrO₂ and (b) CeO₂.

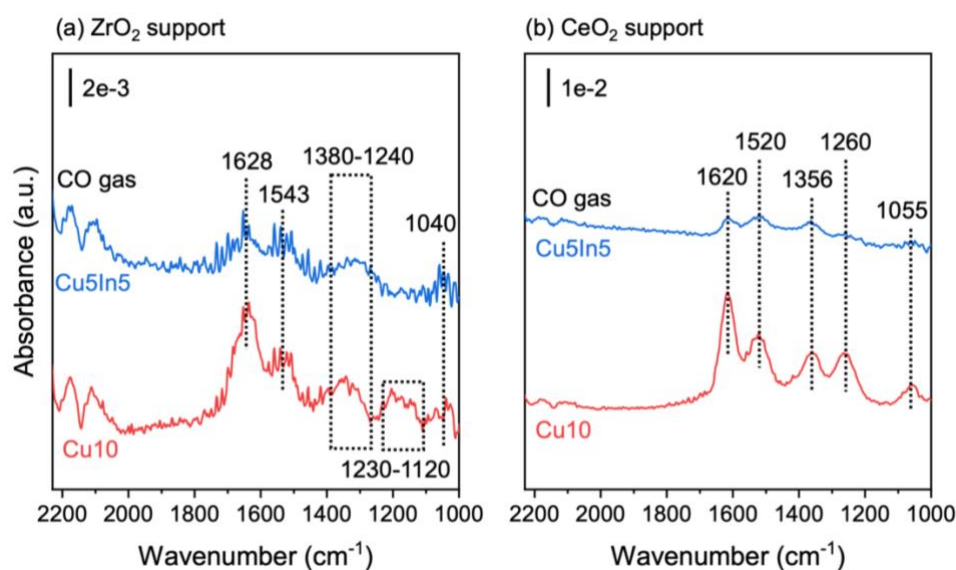


Figure S5.6 *In situ* DRIFT spectra of all reduced catalysts supported by (a) ZrO₂ and (b) CeO₂ under RWGS conditions (300 °C, 4 mL/min H₂, 1 mL/min CO₂, 10 mL/min He). The background was obtained in 15 mL/min He at 300 °C after the samples were reduced. The assignment of different peaks is shown in the table below.

Species	Wavenumber/cm ⁻¹	Vibration mode
Formate	1550-1520	$\nu_{as}(\text{OCO})$
	1260-1230	$\nu_s(\text{OCO})$
Carbonate, bicarbonate	1630-1620	$\nu_{as}(\text{OCO})$
	1380-1350	$\nu_s(\text{CO})$
	1060-1040	$\nu(\text{C-OH})$
Formaldehyde	1160-1120	$\nu(\text{CO})$

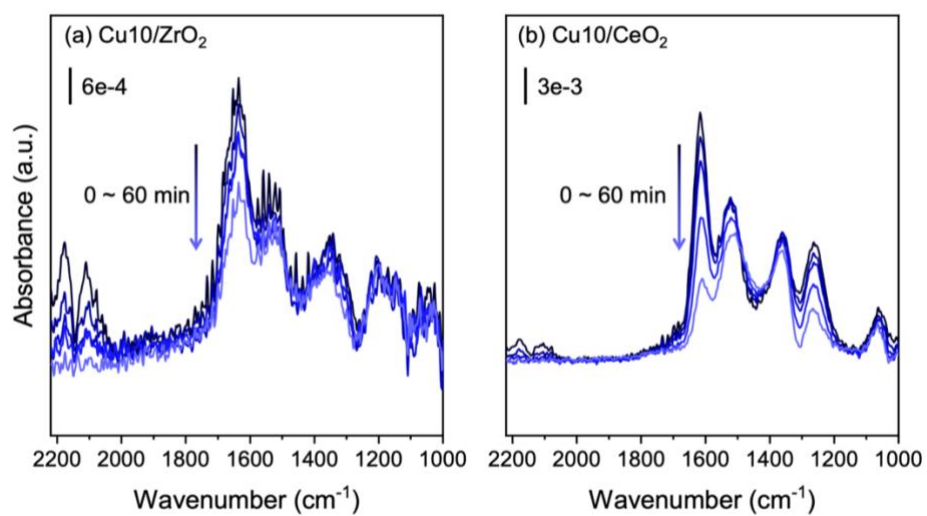


Figure S5.7 Time-resolved DRIFT spectra of Cu10 catalysts supported by (a) ZrO₂ and (b) CeO₂ collected at 300 °C after the gas was switched from feed mixture to pure He.

Table S5.1 Kinetic temperature range ($X_{\text{CO}_2} < 10\%$) for the calculation of activation energy and the determined activation energy (E_a) for CO_2 conversion.

Catalyst	ZrO ₂ support		CeO ₂ support	
	Cu10	Cu5In5	Cu10	Cu5In5
Kinetic temperature range (°C)	570-610	460-500	320-345	325-355
E_a (kJ/mol)	117±6	85±1	67±4	78±3

Table S5.2 Mass fraction of Cu and In in all calcined catalysts determined by ICP-OES

Samples	Mass fraction/wt.%	
	Cu	In
Cu10/ZrO ₂	6.03	0
Cu5In5/ZrO ₂	4.31	3.79
Cu10/CeO ₂	6.73	0
Cu5In5/CeO ₂	4.07	3.73

Table S5.3 Grain sizes of each phase in Cu10 and Cu5In5 catalysts supported by ZrO₂ and CeO₂ obtained from Rietveld refinement.

Samples	Grain size (nm)				
	ZrO ₂	Cu	In ₂ O ₃	Cu ₇ In ₃	Cu _{0.932} In _{0.068}
Cu10/ZrO ₂	19.1	80.1	-	-	-
Cu5In5/ZrO ₂	18.8	-	5.3	48.9	25.7
Samples	Grain size (nm)				
	CeO ₂	Cu	In ₂ O ₃		
Cu10/CeO ₂	18.6	64.1	-		
Cu5In5/CeO ₂	18.5	24.4	7.9		

Chapter 6 Conclusion and perspectives

6.1 Achieved results

With the aim of understanding the gas-surface interaction and the structure-performance relationships of CO₂ hydrogenation catalysts, Cu-based model and practical catalysts were prepared and systematically investigated by NAP-XPS and other conventional characterization/evaluation techniques. Under CO₂ hydrogenation atmosphere, the stability of Cu NPs and its dependence on sizes and supports, the bimetallic synergy between Cu and In for CO₂ activation, and the evolution of surface species on Cu/CeO_{2-x} surfaces were revealed. The influence of supports on Cu-In bimetallic catalysts for the RWGS reaction was also studied.

In Chapter 2, size-selected Cu nanoparticles (Cu NPs) were deposited on different supports as model catalysts. The influence of particle size, support, temperature, as well as CO₂ hydrogenation atmosphere was systematically investigated by XPS and TEM. Under UHV, carbon supported 4 nm Cu NPs were found to be less stable than 8 nm Cu NPs, due to the sintering through particle migration at 220 °C. At higher temperatures (320 and 460 °C), Ostwald ripening was suggested to be the dominant mechanism for both 4 and 8 nm Cu NPs. Compared with carbon support, SiO₂ support can better stabilize Cu NPs upon heat treatment under both UHV and CO₂ hydrogenation atmosphere due to the stronger interaction between SiO₂ and Cu. Upon exposure to CO₂/H₂ mixture, the stability of Cu NPs is suggested to be influenced by the interplay of redispersion, agglomeration, and volatilization. These findings from model systems can offer new insights in the deactivation of Cu-based catalysts.

To meet the general interest in improving the activity of highly selective indium-based catalysts for CO₂ hydrogenation, more complex bimetallic In/Cu model catalysts were studied in Chapter 3. NAP-XPS was employed to investigate the chemical properties and the catalytic role of In/Cu model catalysts under CO₂ hydrogenation conditions. It was found that the deposition of In on the surface of a Cu foil leads to the formation of Cu-In alloy, whereas upon CO₂ exposure, In was partially oxidized to In₂O_{3-x} and Cu remains metallic. Due to the presence of In₂O_{3-x}, CO₂ was activated on the surface of In/Cu samples mainly in the form of carbonate. By quantifying the surface density of oxygen vacancies and carbonates, CO₂ was found to be more easily activated on the In₂O_{3-x} sites adjacent to Cu-In alloys. These results reveal the evolution of the active sites of In/Cu catalysts and inspire the design of advanced In-based bimetallic catalysts for CO₂ hydrogenation.

Considering the significant influence of oxide supports on the catalytic processes, in Chapter 4, Cu/CeO_{2-x} model catalysts were prepared and applied for CO₂ hydrogenation. Under atmospheric pressure, CO₂ hydrogenation occurred on the Cu/CeO_{2-x} surface via the RWGS reaction, leading to CO production. Partially reduced ceria with oxygen vacancies is responsible for CO₂ activation in the form of carbonate. Meanwhile, H₂ dissociates on metallic Cu, and spillovers to the ceria sites, engaging in two processes: the conversion from carbonate to CO via formate intermediate, and the regeneration of the oxygen vacancies healed by CO₂. The presence of numerous partially buried metal-support interfaces were detected by visualizing the cross-sectional structure and chemical composition of the Cu/CeO_{2-x} model catalyst. Combining the NAP-XPS and

STEM/EDX results, the high performance of the Cu/CeO_{2-x} catalyst in the RWGS reaction was attributed to an effective CO₂ activation and hydrogenation via carbonate/formate intermediates over the coupled Cu⁺/Cu⁰ and Ce⁴⁺/Ce³⁺ redox pairs at the metal-oxide interfaces.

In order to apply the knowledge obtained from the above model catalysts to practical catalysts, a series of practical catalysts consisting of ZrO₂ and CeO₂ supported Cu and Cu-In were systematically studied in Chapter 4. The performance of Cu and Cu-In based catalysts in RWGS reaction was demonstrated to be support dependent. By adding In, the CO₂ conversion was increased over ZrO₂-supported catalysts but decreased over CeO₂-supported catalysts. Characterizations revealed that different supports influence the active phases and the chemical states of the surface in a different way. Cu-In alloys, which promotes CO₂ activation in the form of carbonate, are formed exclusively on ZrO₂ supports. On the contrary, Cu and In precursors form separated oxides on CeO₂ and suppressed the RWGS activity. Thus, for the design of bimetallic catalysts for CO₂ hydrogenation, the surface composition, the active phase and the CO₂ adsorption ability of the support should be comprehensively taken into consideration for an optimized performance.

Overall, in this thesis, we performed fundamental studies over model and practical CO₂ hydrogenation catalysts, revealed and interpreted various surface phenomena, which cannot be observed using conventional ex situ and in situ characterizations, by NAP-XPS and other conventional characterization techniques. The achieved results cover the stability of Cu NPs and its dependence on sizes and supports, the bimetallic synergy of Cu and In for CO₂ activation, the evolution of surface species on Cu/CeO_{2-x} surfaces, and the influence of supports on Cu-In bimetallic catalysts for the RWGS reaction. Although the scope of this thesis limits to Cu-based catalysts for CO₂ hydrogenation, the methodology and fundamental insights obtained in this work can be expanded to other heterogeneous catalysts and reactions.

6.2 Perspectives

In this thesis, efforts were devoted to narrowing down the “pressure gap” and “material gap” between conventional surface science studies under UHV and activity studies on heterogeneous catalysts for CO₂ hydrogenation under reactivity by utilizing NAP-XPS and well-defined model catalysts. Although the consistency in both surface properties and catalytic activities of model and practical catalysts has been proven for several Cu-based catalysts, some further studies can be carried out in the future focusing on the investigation of model surfaces, in operando characterization of practical catalysts, and overcoming the limitations of current NAP-XPS techniques.

6.2.1 In-based model catalysts

In-based model catalysts can be studied to understand the high methanol selectivity during CO₂ hydrogenation. On In₂O₃ powder catalysts, the active phase and the surface intermediates during CO₂ hydrogenation are still not clear, neither are the In-based bimetallic alloy catalysts aiming for a higher CO₂ conversion. Thus, NAP-XPS study on a clean poly- or single-crystalline In₂O₃ thin film without adventitious carbon (AdC) contamination can contribute to revealing the activation process of CO₂ on related catalysts. Similarly, alloy model catalysts prepared by depositing In onto another metal are ideal for the investigation of bimetallic synergies, e.g., In/Pd, In/Au, and In/Ni. Furthermore, by integrating the size-selective magnetron sputtering setup to the NAP-XPS system, the composition and structure of model catalysts can be even better

tailored for the investigation of size effect. Beyond these, other surface techniques which have been applied on single crystal model catalysts, such as infrared reflection adsorption spectroscopy (IRRAS) and scanning probe microscopy (SPM), can also be combined with NAP-XPS investigations for more reliable determination of surface intermediates and the visualization of the catalyst surface.

Meanwhile, laboratory- and synchrotron-based NAP-XPS experiments can be combined. One disadvantage of laboratory based XPS is the fixed photon energy, leading to a difference in the information depth of different core levels. For example, with Al K α radiation (1486.8 eV), the information depth is ~ 10 nm for C 1s and ~ 3 nm for Cu 2p. However, for the investigation of CO₂ activation, the information obtained from roughly the same depth is more desired. Such a problem can only be solved by using synchrotron X-ray source with adjustable photon energy. Thus, the flexibility of lab-based and the power of synchrotron-based NAP-XPS should be simultaneously considered for the most reliable surface analysis.

6.2.2 Practical catalysts

NAP-XPS can also be applied directly to practical powder catalysts for CO₂ hydrogenation. The investigation of the change in chemical states of the catalysts is not challenging. However, if surface intermediates can also be observed from powder catalysts, it will be a great improvement in eliminating the material gap. To achieve this, it is important to develop appropriate pre-treatment procedures to reduce the degassing from the catalyst bed during the in operando measurement and remove the surface AdC. O₂ plasma treatment is a potential method for such a procedure due to its UHV compatibility. Meanwhile, it will also be interesting to compare the surface phenomena observed over a practical catalyst and its model counterpart by NAP-XPS, thus, to reveal the influence of pressure and structure on the catalytic performance.

For example, the consistency in the RWGS activity of Cu/CeO_{2-x} model and practical catalysts has been revealed in Chapter 4 of this thesis. As a next step, the active site and surface intermediates can also be investigated using NAP-XPS with simultaneous activity measurement by mass spectroscopy. The results will be compared with the corresponding model surface. This way, a genuine in operando surface-sensitive study on CO₂ hydrogenation catalysts can be realized by NAP-XPS, in concord with other in operando techniques, such as DRIFTS and Raman spectroscopy.

Furthermore, the activation process of bimetallic catalysts can also be investigated by NAP-XPS. In Chapter 5, the reduction products of mixed Cu and In oxides were found to be support dependent. However, it has not been resolved how different supports affect the reducing process. As a following step, NAP-XPS can be used to track the formation of Cu-In alloys or separated Cu and In metals on different supports and discover potential oxygen exchanges between the metal precursors and the supports. Valuable knowledge will be obtained for the design of alloy catalysts and the selection of appropriate support.

Curriculum vitae

LI Mo

E-mail mo.li@epfl.ch
Address Chemin des Pâquerettes 39, 1950 Sion, Switzerland
Tel. +41 76 249 3812
Nationality Chinese



Education

2017.12 – now	PhD student in Chemical Science and Engineering at École Polytechnique fédérale de Lausanne (EPFL), Switzerland
2015.09 – 2018.03	PhD student (unfinished) in Chemical Engineering at ETH Zürich, Switzerland
2012.09 – 2015.06	M. Sc. in Chemical Engineering at Dalian University of Technology, China
2007.09 – 2012.06	B. Sc. in Chemical Engineering at Dalian University of Technology, China

Teaching activities

2018.09 – 2021.06	Teaching assistant on “ <i>Introduction to chemical engineering laboratory works</i> ”, “ <i>Thermodynamics of energy conversion and storage</i> ”, and “ <i>Fluid mechanics and transport phenomena</i> ” at EPFL Supervision on master thesis “ <i>Stability of size-selected Cu-based model catalysts for CO₂ hydrogenation</i> ” at EPFL
2015.09 – 2018.03	Teaching assistant on “ <i>Mass transfer</i> ” and “ <i>Process engineering laboratory works</i> ” at ETH Zürich

Professional qualifications

Basis of inorganic synthesis for catalysts and nanomaterials
Thin film deposition: PVD, ALD, magnetron sputtering
Surface science: UHV- and NAP-XPS, UPS, Raman spectroscopy
Characterizations: SEM, XRD, FTIR, physical adsorption, chemical adsorption, thermal analysis, etc.
Software: OriginPro, AutoCAD, AspenPlus, 3Dsmx, Adobe Illustrator, CasaXPS, GSAS-II, TOPAS

Publications

1. M. Li, T. H. M. Pham, E. Oveisi, Y. Ko, W. Luo, A. Züttel, Revealing the surface chemistry for CO₂ hydrogenation on Cu/CeO_{2-x} using near-ambient pressure X-ray photoelectron spectroscopy. Submitted to **ACS Applied Energy Materials**. Under review.
2. M. Li, T. H. M. Pham, Y. Ko, K. Zhao, W. Luo, A. Züttel, Support-dependent Cu-In bimetallic catalysts for tailoring the activity of reverse water gas shift reaction. Submitted to **Chemical Engineering Journal**. Under review.
3. M. Li, W. Luo, A. Züttel, Near ambient-pressure X-ray photoelectron spectroscopy study of CO₂ activation and hydrogenation on indium/copper surface, **Journal of Catalysis**. 395 (2021) 312-324.
4. M. Li, A. Borsay, M. Dakhchoune, K. Zhao, W. Luo, A. Züttel, Thermal stability of size-selected copper nanoparticles: Effect of size, support and CO₂ hydrogenation atmosphere, **Applied Surface Science**. 510 (2020) 145439.
5. M. Li, X. Li, X. Qi, F. Luo, G. He, Shape-Controlled Synthesis of Magnetic Iron Oxide@SiO₂-Au@C Particles with Core-Shell Nanostructures, **Langmuir**. 31 (2015) 5190-5197.
6. M. Li, X. Li, G. Jiang, G. He, Hierarchically macro-mesoporous ZrO₂-TiO₂ composites with enhanced photocatalytic activity, **Ceramics International**. 41 (2015) 5749-5757.
7. M. Li, X. Jiang, G. He, Application of membrane separation technology in postcombustion carbon dioxide capture process, **Frontiers of Chemical Science and Engineering**. 8 (2014) 233-239.

8. K. Zhao, M. Calizzi, E. Moioli, **M. Li**, A. Borsay, L. Lombardo, R. Mutschler, W. Luo, A. Züttel, Unraveling and optimizing the metal-metal oxide synergistic effect in a highly active $\text{Co}(\text{CoO})_{1-x}$ catalyst for CO_2 hydrogenation, *Journal of Energy Chemistry*. 53 (2021) 241–250.
9. Y. Ko, L. Lombardo, **M. Li**, E. Oveisi, H. Yang, A. Züttel, Interfacial Effect between Aluminum-Based Complex Hydrides and Nickel-Containing Porous Carbon Sheets, *ACS Applied Energy Materials*. 3 (2020) 9685–9695.
10. K. Zhao, J. Zhang, W. Luo, **M. Li**, E. Moioli, M. Spodyryk, A. Züttel, A combined diffuse reflectance infrared Fourier transform spectroscopy–mass spectroscopy–gas chromatography for the operando study of the heterogeneously catalyzed CO_2 hydrogenation over transition metal-based catalysts, *Review of Scientific Instruments*. 91 (2020) 074102.
11. Y. Yang, C. Liu, A. Mahata, **M. Li**, C. Roldán-Carmona, Y. Ding, Z. Arain, W. Xu, Y. Yang, P. Alexander Schouwink, A. Züttel, F.D. Angelis, S. Dai, M. Khaja Nazeeruddin, Universal approach toward high-efficiency two-dimensional perovskite solar cells via a vertical-rotation process, *Energy & Environmental Science*. 13 (2020) 3093–3101.
12. H. Kanda, N. Shibayama, A. Joel Huckaba, Y. Lee, S. Paek, N. Klipfel, C. Roldán-Carmona, V.I. Emmanuel Queloz, G. Grancini, Y. Zhang, M. Abuhelaiqa, K. Taek Cho, **M. Li**, M. Driss Mensi, S. Kinge, M. Khaja Nazeeruddin, Band-bending induced passivation: high performance and stable perovskite solar cells using a perhydropoly(silazane) precursor, *Energy & Environmental Science*. 13 (2020) 1222–1230.
13. S. Huang, L.F. Villalobos, D.J. Babu, G. He, **M. Li**, A. Züttel, K.V. Agrawal, Ultrathin Carbon Molecular Sieve Films and Room-Temperature Oxygen Functionalization for Gas-Sieving, *ACS Applied Materials and Interfaces*. 11 (2019) 16729–16736.
14. W. Luo, J. Zhang, **M. Li**, A. Züttel, Boosting CO Production in Electrocatalytic CO_2 Reduction on Highly Porous Zn Catalysts, *ACS Catalysis*. (2019) 3783–3791.
15. W. Luo, W. Xie, **M. Li**, J. Zhang, A. Züttel, 3D hierarchical porous indium catalyst for highly efficient electroreduction of CO_2 , *Journal of Materials Chemistry A*. 7 (2019) 4505–4515.
16. F. Luo, X. Li, G. He, **M. Li**, H. Zhang, Preparation of Double-Shelled C/SiO_2 Hollow Spheres with Enhanced Adsorption Capacity, *Industrial & Engineering Chemistry Research*. 54 (2015) 641–648.
17. J. Shi, X. Li, G. He, L. Zhang, **M. Li**, Electrodeposition of high-capacitance 3D CoS /graphene nanosheets on nickel foam for high-performance aqueous asymmetric supercapacitors, *Journal of Materials Chemistry A*. 3 (2015) 20619–20626.
18. C. Dong, G. He, W. Zheng, T. Bian, **M. Li**, D. Zhang, Study on antibacterial mechanism of $\text{Mg}(\text{OH})_2$ nanoparticles, *Materials Letters*. 134 (2014) 286–289.
19. X. Jiang, **M. Li**, G. He, J. Wang, Research Progress and Model Development of Crystal Layer Growth and Impurity Distribution in Layer Melt Crystallization: A Review, *Industrial & Engineering Chemistry Research*. 53 (2014) 13211–13227.

Conference contributions

1. **M. Li**, W. Luo, A. Züttel, CO_2 activation on Cu-In surface alloy: a near ambient-pressure X-ray photoelectron spectroscopy study, 2020 Swiss Chemistry Society Fall Meeting, Bern, Switzerland, 2020.08
2. **M. Li**, W. Luo, A. Züttel, Size-selected copper nanoparticles as model catalysts for understanding CO_2 hydrogenation mechanisms, The 13th International Symposium Hydrogen & Energy, Incheon, Korea, 2019.02
3. **M. Li**, W. Luo, A. Züttel, Investigation of gas-surface interaction of well-defined model catalysts for CO_2 hydrogenation, The 12th International Symposium Hydrogen & Energy, Lausanne, Switzerland, 2018.02
4. **M. Li**, S. Huang, Y. Dai, G. He, Effect of coating conditions on performance of polyetherimide hollow fiber composite membrane, The 10th International Congress on Membranes and Membrane Processes, Suzhou, China, 2014.07

Honors and awards

2015.09	PhD scholarship of China Scholarship Council
2015.06	Outstanding postgraduate scholarship
2012.06	Outstanding graduate award of Dalian City
2011.09	The second prize in National Chemical Engineering Design Competition
2009.10	National scholarship of China

Interests

Photography on railway transportation, classical music, hiking